UNIVERSITY OF CALIFORNIA

Los Angeles

Effects of Transient Deoxygenation on Sulfur Cycling in Aquatic Systems

A dissertation submitted in partial satisfaction of the requirements for the degree Doctor of Philosophy in Geochemistry

by

David John Yousavich

2024

ABSTRACT OF THE DISSERTATION

Effects of Transient Deoxygenation on Sulfur Cycling in Aquatic Systems

by

David John Yousavich

Doctor of Philosophy in Geochemistry

University of California, Los Angeles, 2024

Professor Tina Irene Treude, Chair

The rise of oxygen in the early Earth atmosphere allowed for a vast expansion of life, including the proliferation of animal life, that could utilize this powerful electron acceptor for new metabolisms. This oxygen requirement has left many organisms vulnerable to oxygen-depleted conditions (i.e., anoxia). These anoxic events in Earth's aquatic environments allow for free iron (ferruginous) or free sulfide (euxinic) conditions to develop. While much research has been done on the past and present of aquatic anoxia, transiently deoxygenated systems that cycle annually between oxygenated and anoxic states are underexplored. Questions about these cycles of aquatic redox state abound; for example, 1) if benthic sulfur-oxidizing bacteria promote free sulfide at the sediment-water interface in transiently deoxygenated systems 2) if these cycles of anoxia can promote a loss of free iron from the benthic marine environment and 3) if sulfate reducing bacteria are quickly established in lacustrine waters after anoxia develops.

The first and second questions will be addressed in this dissertation through a suite of

investigations in the transiently deoxygenated Santa Barbara Basin. Porewater geochemistry, sulfate reduction rates, and benthic flux measurements were collected between 2019-2023 under varying oxygen concentrations. We found that sulfur-oxidizing bacterial mats in the basin are associated with high rates of dissimilatory nitrate reduction to ammonium and require an elevation of the sulfate reduction zone to the sediment-water interface in order to proliferate. Mat proliferation also requires an exhaustion of iron oxides in the surface sediment. Mat formation is also associated with extremely high fluxes of iron into the water column. This free iron is potentially lost from the basin through bottom water currents that carry mid-waters upslope during the anoxic events.

The third question will be addressed in this dissertation by several geochemical and ex-situ sulfate reduction measurements taken in the Salton Sea between 2020-2023 under a variety of water column redox conditions. We found that sulfate reduction is present in waters that contained oxygen, most likely occurring inside organic particles in the water. We also found that sulfate reduction is quickly established after the onset of anoxia in the lake.

The dissertation of David John Yousavich is approved.

Edwin Arthur Schauble

Daniele Bianchi

David Clifford Jewitt

David L Valentine

Tina Irene Treude, Committee Chair

University of California, Los Angeles

2024

Dedication Page

I dedicate this dissertation to my family: My mother Margaret McLean, father Robert Yousavich and his wife Cheryl Yousavich, my siblings Debra Yousavich and Christina Cox, my grandfather Charles McLean and his wife Barbara McLean, and all the members of my extended family. Additionally, I would like to dedicate this work to the amazing friends I have made along this journey. Their love and support has made this work possible.

Table of Contents

List of Figures

List of Tables

List of Acronyms

°C - Degrees Celsius

AOM - Anaerobic Oxidation of Methane

Approx. - Approximately

ADP - Adenosine Diphosphate

ATP - Adenosine Triphosphate

AMP - Adenosine Monophosphate

AUV - Automated Underwater Vehicle

BIF - Banded Iron Formations

$CaCl_2$ - Calcium Chloride

$CaCO_3$ - Calcium Carbonate

CH_3COO^- - Acetate

CH_4 - Methane

cm - Centimeter

cm^{-3} - Centimeter Cubed

CO_2 - Carbon Dioxide

CPM - Counts Per Minute

csSRR - Cell Specific Sulfate Reduction Rate

D - Deuterium

d - Days

d^{-1} - Per Day

DIC - Dissolved Inorganic Carbon

DOI - Digital Online Identifier

Fe(II) - Iron (II)

Fe(III) - Iron (III)

FeS - Iron monosulfides

FeS_2 - Pyrite

g - Grams

GC - Gas Chromatography

H - Hydrogen

h - Hours

H^+- Proton

H_2O -Water

HCO_3^- - Bicarbonate

HS^- - Hydrogen Sulfide

i.d. - Inner Diameter

k - Rate Constant

K - Kelvin

KBq - Kilo Becquerel

KIE - Kinetic Isotope Effects

K_m - Michaelis Menten Constant

KNO_3^- - Potassium Nitrate

kPa - Kilo Pascals

L - Liter

L^{-1} - Per Liter

M - Molar

m - Meters

m^{-2} - Per Meters Squared

$MgSO_4$ - Magnesium Sulfate

mL - Milliliter

mM - Millimolar

Mn (IV) - Manganese (IV)

mol - Moles

MOx - Aerobic Oxidation of Methane

MUC - Multicorer

N_2 - Dinitrogen

NaOH - Sodium Hydroxide

NDRO - Northern Depositional Radial Origin

NDT3A - Northern Depositional Transect 3 A

NDT3B - Northern Depositional Transect 3 B

NDT3C - Northern Depositional Transect 3 C

NDT3D - Northern Depositional Transect 3 D

NH_4^+ - Ammonium nmol - Nano Moles

nM - Nanomolar

NO_3^- - Nitrate

NO_2^- - Nitrate

NOAA - National Oceanic and Atmospheric Administration

NSF - National Science Foundation

O_2 - Oxygen

OD - Outer Diameter

OMZ - Oxygen Minimum Zone

PCR - Polymerase Chain Reaction

PO_4^{3-} - Phosphate

PSED - Sediment Porosity

PSU - Practical Salinity Unit

R/V - Research Vessel

RF - Recovery Factor

RFU - Relative Fluorescence Units

ROV - Remote Operated Vehicle

SBB - Santa Barbara Basin

SDRO - Southern Depositional Radial Origin

SDT1A - Southern Depocenter Transect 1 A

SDT3A - Southern Depocenter Transect 3 A

SDT3B - Southern Depocenter Transect 3 B

SDT3C - Southern Depocenter Transect 3 C

SDT3D - Southern Depocenter Transect 3 D

SMTZ - Sulfate Methane Transition Zone

SO_2 – Sulfur dioxide

SO_3^- - Sulfite

$SO4^{2-}$ - Sulfate

$S_2O_3^{2-}$ - Thiosulfate

SR - Sulfate Reduction

SRR - Sulfate Reduction Rate

t - Time

TBq - Tera Becquerel

Tg - Tera-grams

TIC - Total Inorganic Carbon

TRIS - Total Reduced Inorganic Sulfur

USA - United States of America

UV - Ultraviolet

wk - Week

Yr^{-1} - Per Year

µL - Micro Liters

µM - Micro Molar

µmol - Micro Moles

Acknowledgements

My many mentors and friends were integral to the completion of the work presented in this dissertation. First and foremost, I would like to acknowledge my Ph.D. advisor and mentor, Dr. Tina Treude, who recruited me to work on this amazing science and provided me with the resources and guidance to explore my scientific curiosities. I would also like to acknowledge my gratitude to the Ph.D. committee, Dr. Edwin Schauble, Dr. Daniele Bianchi, Dr. David Jewitt of UCLA, and Dr. David Valentine of UCSB, all of whom dedicated their expertise, time, and resources to benefit the work presented in this dissertation.

I would like to acknowledge those who mentored me and provided advice throughout my doctoral program: Dr. Jeana Drake, Dr. Kira Homola, Dr. Samuel Howell, Dr. Peter Girguis, Dr. Donald Canfield, Dr. Ronnie Guld, Dr. Bo Thamdrup, Dr. Joan Bernhard, Dr. Beth Orcutt, Dr. Xuefeng Peng, Dr. Jessica Kozlowski, Dr. Dimitri Kits, Dr. Timothy Lyons, Dr. Morgan Raven, Dr. Mackenzie Day, Dr. Andrew Stewart, Dr. James McWilliams, Dr. Aradhna Tripati, Dr. Carolina Lithgow-Bertelloni, Dr. Jean-Luc Margot, Dr. Edward Young, Dr. David Jacobs, and Dr. William Schopf. I would also like to thank the UCLA Earth, Planetary and Space Sciences Department, past and present staff, especially Tasha Taylor, Lauri Holbrook, Carlene Brown, Richard Fort, Kelli Yang, Michelle Pang, Roderic O'Connor, Eric Wessenauer, Henry Gonzalez, Bill Harris, Emmanuel Masongsong, Jim Nakatsuka, Sean Silverstein, Evgenia Grigorova, and Pierpaolo Muti.

I feel particularly privileged to have made new and maintained old friendships which has been essential to the completion of my dissertation. To all of the close friends I have made at UCLA and from other institutions, I want to especially acknowledge Sebastian Krause,

Jeffrey Osterhout, Jon Tarn, Eleanor Arrington, Emma Qin, Na Liu, Andrew Parisi, Ashley Schoenfeld, Heather Kirkpatrick, De'Marcus Robinson, Akash Gupta, Jiarui Liu, Tyler Powell, Robert Ulrich, Kirellos Sefien, Ariel Graykowski, Mark Hubbert, Leslie Insixiengmay, Jason Utas, Deepshikha Upadhyay, Hannah Tandy, Nathan Pulver, Valeria Jaramillo-Hernandez, Emily Klonicki, William Misener, and Yufan Xu. I also want to acknowledge the great friends I have made in organizing Exploring Your Universe: Abijah Simon, Sophia Uemura, Yutong Wu, Danny Ying, Hayley Bricker, David James, and Megan Li. I have been privileged to have some amazing and supportive friends and mentors outside of academia; a special thanks to my fraternity brothers Eric Cooke, Michael George, Patrick Maney, Tyler Hoops, Michael Eyler, Eric Mueller, and Ian Mullenhour. Additional special thanks to Nicolé Bibb, Ingrid Van Eckert, Linda Chang, Rebecca Gale, Chi Bui, Aaron Lai, Jonathon Tran, Daniel Harnack, Dawn York, Belinda Fowler, Rachel Cooke, LaQuana Askew, Kelly Wills, Sarah Mack, Thomasina and Ian Merkel, Matthew Savary, and Sidney Thomas. I would also like to shout out the amazing and talented undergraduates I have mentored at UCLA: Marcus Lin, Alexandra Fowler, Tessa Holzmann, Zoe Collins, Ashley Huh, Nick Leong, Ben Clautier, and George Vetushko.

Lastly, I would like to acknowledge the funding sources for my research: The University of California, The Center for Diverse Leadership in Science at UCLA, and the National Science Foundation (NSF). I would also like to thank the crews of the research vessels *Atlantis, Nautilus,* and *Shearwater*, the teams who operate the remote operated vehicles (ROV) *Jason* and *Hercules* and the team who operates the submersible *Alvin* as the field work that produced the research within this dissertation was the highlight of my doctoral studies.

Vita/Biographical Sketch

David John Yousavich

Education

2024, PhD Candidate in Geochemistry, University of California Los Angeles

2021, M.S. in Geology, University of California Los Angeles

2018, M.S. in Geology, California State University Los Angeles

2010, B.A. in Zoology and Chemistry, Miami University

Publications

1. **Yousavich, David J**., D. Robinson, X. Peng, S.J.E. Krause, F. Wenzhöfer, F. Janssen, N. Liu et al. "Marine anoxia initiates giant sulfur-oxidizing bacterial mat proliferation and associated changes in benthic nitrogen, sulfur, and iron cycling in the Santa Barbara Basin, California Borderland." *Biogeosciences* 21, no. 3 (2024): 789-809.
2. Robinson, De'Marcus, A.L.D. Pham, **David J. Yousavich**, F. Janssen, F. Wenzhöfer, E. C. Arrington, K. M. Gosselin et al. "Iron “ore” nothing: benthic iron fluxes from the oxygen-deficient Santa Barbara Basin enhance phytoplankton productivity in surface waters." *Biogeosciences* 21, no. 3 (2024): 773-788.
3. Krause, Sebastian JE, J. Liu, **David J. Yousavich**, D. Robinson, D. W. Hoyt, Q. Qin, F. Wenzhöfer, F. Janssen, D. L. Valentine, and T. Treude. "Evidence of cryptic methane cycling and non-methanogenic methylamine consumption in the sulfate-reducing zone of sediment in the Santa Barbara Basin, California." *Biogeosciences* 20, no. 20 (2023): 4377-4390.
4. Lindsay, M. R., Angelo, T. D., Munson-McGee, J. H., Saidi-Mehrabad, A., Devlin, M., McGonigle, J., Goodell, E., Herring, M., Lubelcyzk, L., Mascena, C., Brown, J., Gavelis, G., Liu, J., **Yousavich D.J.**, Hamilton-Brehm S. D., Hedlund, B. P., Lang, S., Treude, T.,

Poulton, N. J., Stepanuskas, R., Moser D. P., Emerson, D., Orcutt, B. N. "Species-resolved, single-cell respiration rates reveal dominance of sulfate reduction in a deep continental subsurface ecosystem." *Proceedings of the National Academy of Sciences*, (2024): e2309636121.

Talks and Posters

2022 European Geosciences Union, Talk

2022 UCLA Geocheminar Series, Talk

2021 UCLA Geocheminar Series, Talk

2020 American Geophysical Union, Poster

2020 Ocean Sciences Meeting, Poster

2017 American Geophysical Union, Poster

Teaching

2019 – 2023 (4 Quarters taught) **UCLA Introduction to Oceanography** (EPSS 15)

2018 – 2021 (3 Quarters taught) **UCLA Astrobiology** (EPSS 3)

Field Experience

June 2023 **AT50-11 R/V Atlantis** (Santa Barbara Basin, CA)

July 2022 **R/V Sheerwater** (Santa Barbara Basin, CA)

July 2021 **NA-127 R/V Nautilus** (Santa Barbara Basin, CA)

July 2018, Jan 2020, Aug 2020, Sep 2021, Nov 2023 **Salton Sea** (Calipatria, CA)

Oct 2019 **AT42-19 R/V Atlantis** (Santa Barbara Basin, CA)

July 2019 **Carpinteria Salt Marsh Reserve** (Carpinteria, CA)

May 2017, Sep 2017 **Culver City Rain Garden** (Culver City, CA)

Fellowships and Awards

2024 UCLA Earth, Planetary and Space Science Departmental Fellowship

2023 UCLA Excellence in Science Communication Award

2019 – 2023 UCLA Center for Diverse Leadership in Science, Early Career Fellow

Chapter 1

Part I. How Life Derives Energy on Earth

Introduction to Metabolism

All life on Earth utilizes the transfer of electrons, negatively charged subatomic particles, to gain the energy required to build biomass. Metabolism encompasses the series of complex biochemical processes required for this transfer of electrons for energy derivation and subsequent biosynthesis (Nielsen 2017). There are two general categories of metabolism: catabolism and anabolism. The specific pathways of catabolism differ depending on the electron donor (ED) and terminal electron acceptor (TEA). The energy yielded from different pairs of ED and TEA is governed by the laws of thermodynamics (see 'Anaerobic Chemoheterotrophy' section for more details). In general, electrons are first stored in a transfer molecule such as nicotinamide adenine dinucleotide phosphate (NADPH). This molecule then transfers the electrons gained from the ED to the first molecule of the electron transport chain. Then a series of redox reactions, or coupled oxidation and reduction reactions, carry the electron through the transport chain. At the end of this process, the electron is transferred to the TEA, which is usually transported out of the cell (if the TEA is not already extracellular). During the electron transfer, the cell utilizes the energy gained from these redox reaction to pump H^+ (protons) across a membrane within the cell. In many organisms, this proton gradient is then used to generate adenosine triphosphate (ATP), the cell's main currency for energy transfer; one phosphate molecule from ATP is cleaved to form Adenosine Diphosphate (ADP), releasing approx. 30.5 Kilijoules mol^{-1}ATP (Hinkle and McCarty 1978).

Anabolism differs greatly depending on whether the ED is organic or inorganic carbon, and whether energy from redox reactions (chemosynthesis) or light (photosynthesis) is used to

incorporate the carbon. Heterotrophs are organisms that utilize organic carbon to build their biomass, whereas autotrophs utilize inorganic carbon molecules like carbon dioxide (CO_2) to build their biomass. Metabolisms can be further divided by where their energy is derived; phototrophs derive energy from sunlight whereas chemotrophs derive energy from chemical reactions. This leads to four general metabolic genres in which life on Earth exists: chemoheterotrophs, chemoautotrophs, photoautotrophs, and photoheterotrophs. The myriad different possibilities for metabolisms, each utilizing and generating different molecules in their catabolic and anabolic processes, some of which incorporating light energy, yields a complex web of interactions between organisms conducting these different metabolisms, fueling the diversity of life on Earth.

Chemoheterotrophy

As humans (assuming you reading this, are a human), we are most familiar with a metabolism based around aerobic respiration paired with organic matter degradation. This process of aerobic respiration is the most energetically favorable chemoheterotrophic metabolism on Earth (Table 1-1). In this process, oxygen is used as a TEA, and reduced carbon is used as both a source of ED and for the production of biomass via anabolic processes. O_2 (oxygen) is the energetically most favorable TEA for respiration on Earth (Thauer et al. 1977). Aerobic respiration is, however, only one potential metabolism in a vast array of possibilities. Aerobic respiration likely followed the appearance of oxygenic photosynthesis, i.e., the production of oxygen from photosynthetic organisms, in the early Proterozoic eon approx. 2.3 billion years ago (Bekker et al. 2004; Lyons et al. 2014; Soo et al. 2017). O_2 reductases, enzymes used in aerobic respiration, were likely present in bacteria and archaea prior to the rise of photosynthesis, though these microorganisms probably used O_2 reductases as a means of surviving the powerful

oxidizing effects of (likely chemically produced) oxygen rather than utilizing it for a metabolic process (Brochier-Armanet et al. 2009). The rise in atmospheric (and oceanic) oxygen concentrations following the advent of oxygenic photosynthesis is marked by banded iron formations (BIF, Fig. 1), oxidized iron found in the geological record dating to 2.5 billion years ago (Cloud 1973; James 1966; Johnson et al. 2008) though evidence of periodic pulses of oxygen prior to BIF formation exist in the geological record (Anbar et al. 2007). The earliest signs of life on Earth are from approx. 4 billion years ago, at the beginning of the Archean eon (Bell et al. 2015) leaving approx. 1.5 billion years between the emergence of life and geological evidence of long-lasting oxygen accumulation in Earth's atmosphere. This early life on Earth utilized a myriad of metabolic pathways that did not require oxygen to derive energy. We can find traces of these metabolisms in the geological record, and we also find these metabolisms dispersed across Earth in the present day.

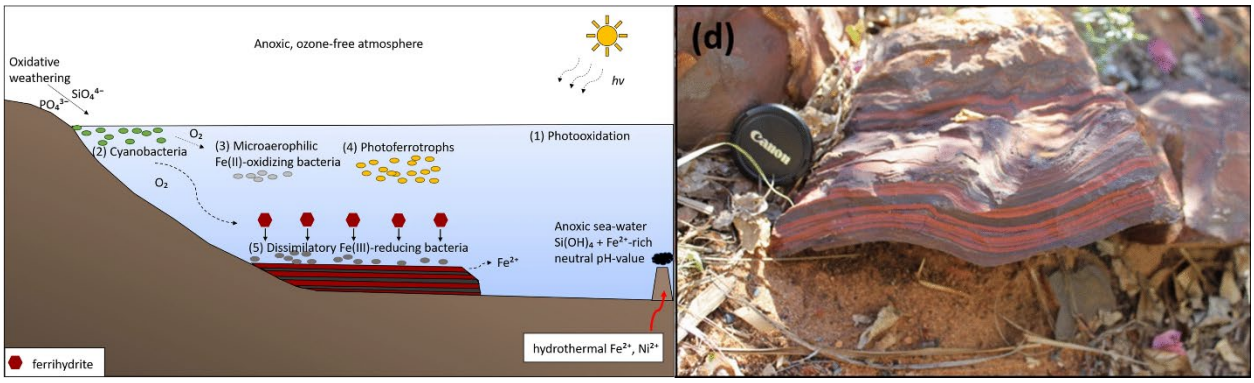

Figure 1-1. **Left:** Schematic of the genesis of banded iron formation. **1)** Photooxidation of Fe^{2+} provides Fe^{3+} in Precambrian Oceans. **2)** Weathering of continental crust provides nutrients for cyanobacteria growth in the photic zone, producing O_2 as a byproduct. **3)** Some of the O_2 from these cyanobacteria provides the oxidant for iron-oxidizing bacteria, generating Fe^{3+}. **4)** Oxidation of Fe^{2+} to Fe^{3+} by photoferrotrophs performing anoxygenic photosynthesis. **5)** Some O_2 from step (2) combines with Fe^{3+} to form iron oxides (e.g., ferrihydrite), an insoluble solid which settles on the seafloor. Some of these iron oxides are reduced to mixed valence iron (e.g., magnetite) or back to Fe^{2+}, some of which could be re-oxidized by processes (1), (3), or (4). **Right:** A representative banded iron formation from Western Australia. Taken from Figs. 1 & 2 from Dreher et al. (2021).

Heterotrophy is not limited to using O_2 as an electron acceptor, and the exact organic molecule used as an electron donor can vary. Reduced carbon in the form of simple organic molecules (e.g., acetate) is one of the strongest electron donors available to organisms on Earth. Chemoheterotrophic aerobes are able to break down complex organic molecules (e.g., polysaccharides like starch) into simpler molecules (e.g., glucose). These organisms can then further process the organic molecules via glycolysis, a multi-step enzymatic process that converts one glucose molecule into two pyruvate molecules, generating two ATP and two NADH (the non-phosphorylated form of NADPH) molecules as by-products. Pyruvate then can enter the Krebs Cycle, also called the Citric Acid Cycle to produce more ATP and NADH, along with several other intermediates important to both catabolic and anabolic processes. The NADH produced by the Krebs Cycle then carries the electrons gained from these reduced organic compounds to the electron transport chain, to eventually be transferred to the TEA. An alternative to the Krebs Cycle is fermentation, which involves direct transformation of substrates to ATP and NADH and does not involve an electron transport chain (and thus does not need a TEA).

In anoxic (i.e., oxygen free) aquatic environments, the order of terminal electron acceptors utilized in chemoheterotrophic metabolisms follows a sequential cascade depending on the Gibbs Free Energy of the redox reaction involved. The concentrations of both products and reactants are important to this cascade as well. The Gibbs Free Energy equation can be used to determine how energetically favorable a particular metabolic process is:

$$\Delta G = \left(\left(\Sigma \Delta G_f^{\circ}\, products\right) - \left(\Sigma \Delta G_f^{\circ}\, reactants\right) + RTln(K) \right. \quad [1]$$

Where ΔG is the Gibbs Free Energy produced by the reaction (in kJ mol^{-1}), ΔG_f° is the energy of formation of each compound that participates in the reaction, R is the ideal gas constant, T is the

temperature (in Kelvin), and K is the equilibrium constant, derived from the concentration (more accurately, the activity) of each chemical that participates in the reaction. By assuming a temperature of 298°K and all concentrations to be 1 M (known as ΔG°) at the beginning of the reaction, the metabolic processes common in anoxic environments can be ordered by their energy yield in a predictable redox cascade (Table 1).

Pathway and stoichiometry of reaction	ΔG^0 (kJ mol-1)
Oxic respiration:	
$CH_2O + O_2 \rightarrow CO_2 + H_2O$	-479
Denitrification:	
$5CH_2O + 4NO_3^- \rightarrow 2N_2 + 4HCO_3^- + CO_2 + 3H_2O$	-453
Mn(IV) reduction:	
$CH_2O + 3CO_2 + H_2O + 2MnO_2 \rightarrow 2Mn^{2+} + 4HCO_3^-$	-349
Fe(III) reduction:	
$CH_2O + 7CO_2 + 4Fe(OH)_3 \rightarrow 4Fe^{2+} + 8HCO_3^- + 3H_2O$	-114
Sulfate reduction:	
$2CH_2O + SO_4^{2-} \rightarrow H_2S + 2HCO_3^-$	-77
$4H_2 + SO_4^{2-} + H^+ \rightarrow HS^- + 4H_2O$	-152
$CH_3COO^- + SO_4^{2-} + 2H^+ \rightarrow 2CO_2 + HS^- + 2H_2O$	-41
Methane production:	
$4H_2 + HCO_3^- + H^+ \rightarrow CH_4 + 3H_2O$	-136
$CH_3COO^- + H^+ \rightarrow CH_4 + CO_2$	-28
Acetogenesis:	
$4H_2 + 2CO_3^- + H^+ \rightarrow CH_3COO^- + 4H_2O$	-105
Fermentation:	
$CH_3CH_2OH + H_2O \rightarrow CH_3COO^- + 2H_2 + H^+$	10
$CH_3CH_2COO^- + 3H_2O \rightarrow CH_3COO^- + HCO_3^- + 3H_2 + H^+$	77

Table 1-1: Selected reactions important to chemoheterotrophic metabolisms with associated ΔG° for each reaction taken from (Jørgensen 2000). The more negative a value for ΔG° the more thermodynamically favorable the reaction is (and thus the more energy yielded).

After aerobic respiration, the next most energetically favorable reaction is the reduction of NO_3^- (nitrate). This process can occur as NO_3^- (nitrate) reduction to N_2 (dinitrogen; this process is known as denitrification) or dissimilatory nitrate reduction to NH_4^+ (ammonium; this process is known as DNRA). Nitrate is first imported into the cell, usually via active transport,

where it$^-$ is pumped against a diffusion gradient at the expense of the proton motive force or ATP hydrolysis. During denitrification, nitrate is first reduced to NO_2^- (nitrite) by the nitrate reductase enzyme. NO_2^- is then further reduced to NO (nitric oxide) by nitrite reductase, which is then further reduced to N_2O (nitrous oxide) by nitrous oxide reductase. The final step is the conversion of N_2O to N_2 by nitrous oxide reductase (Gruber and Sarmiento 1997; Stüeken et al. 2016). As denitrification leads to N_2, a diatomic element with a strong triple bond, it is responsible for reactive nitrogen loss from the environment. Denitrifiers can use a variety of organic and inorganic ED's for their metabolism and can secrete extracellular hydrolysis similar to aerobic organisms (Andersson et al. 2009). DNRA on the other hand reduces NO_3^- to ammonium (NH_4^+) by first converting NO_3^- to NO_2^- and then reducing NO_2^- to NH_4^+ using a different type of nitrite reductase (Stüeken et al. 2016).

Once NO_3^- is exhausted, manganese (Mn^{4+}) and iron (Fe^{3+}) become the most favorable TEA's, particularly in sediment porewaters and soils. In the following, I will focus on iron reduction, as iron is the fourth most abundant element in Earth's crust (approx. 6%), manganese compromises less than 0.1% of the Earth's crust (Lide 2005). Iron(III) (oxidized iron) was likely originally produced on Earth through the photolytic oxidation of Fe(II), which also produces molecular hydrogen (H_2), a favorable ED (Cairns-Smith 1978; Lovley et al. 2004; Weber et al. 2006).

$$2Fe(II) + 2H^+ \xrightarrow{hv} 2Fe(III) + H_2 \quad [2]$$

This oxidized Fe(III) was then available as a TEA for primordial iron-reducing organisms. Unlike denitrifying organisms, the TEA used in iron reduction is solid Fe(III), usually in the form of poorly crystalline iron oxide minerals (e.g., ferrihydrite), though more highly crystalline iron oxides (e.g., hematite) can also be utilized, albeit with a higher energy input required for

electron transfer (Fredrickson et al. 1998; Kostka and Nealson 1995; Weber et al. 2006). Therefore, iron-reducing organisms cannot actively pump the TEA into their cells; instead, they must perform extracellular electron transfer as the last step of their electron transport chain. This transfer can either be done by directly transferring electrons to solid Iron(III) (Reguera et al. 2005) or by using intermediate electron shuttles such as humic acid that diffuse into the surrounding porewater and reduce the Iron(III) abiotically (Lovley et al. 1996). The resultant Fe^{2+} can re-mineralize (e.g., with sulfide to form iron sulfides), but it is also soluble in water at standard pH and can thus diffuse into surrounding sediment porewaters and potentially leave the system. Heterotrophic iron-reducing bacteria usually utilize simpler organic molecules produced by fermentation reactions (e.g., lactate) as ED (Weber et al. 2006) though they can degrade more complex organic matter like polycyclic aromatic compounds (Lovley et al. 1989).

Once manganese and iron oxides are exhausted, sulfate reduction becomes the next most favorable common metabolism in anoxic aquatic environments, which will be discussed in detail in part II, 'Sulfate Reduction'. Methanogenesis, the last step in organic matter degradation in anoxic aquatic environments, is typically limited (though not always) to sediment below the sulfate methane transition zone (SMTZ). Sulfate reduction within the SMTZ is fueled by the anaerobic oxidation of methane (AOM) (Alperin and Reeburgh 1985). Methanogenesis is restricted with the respect to usable substrates, with three main pathways existing: Acetoclastic (using acetate), hydrogenotrophic (using H_2 as an ED and CO_2 as a TEA), and methylotrophic (using methylated compounds like methanol and methylamines). While there are many more possible heterotrophic metabolisms that utilize alternative TEA in anoxic environments (e.g., iodate reduction; (Amachi et al. 2007)), the reactions detailed in this section are the most common on Earth based on the abundance of the respective TEAs.

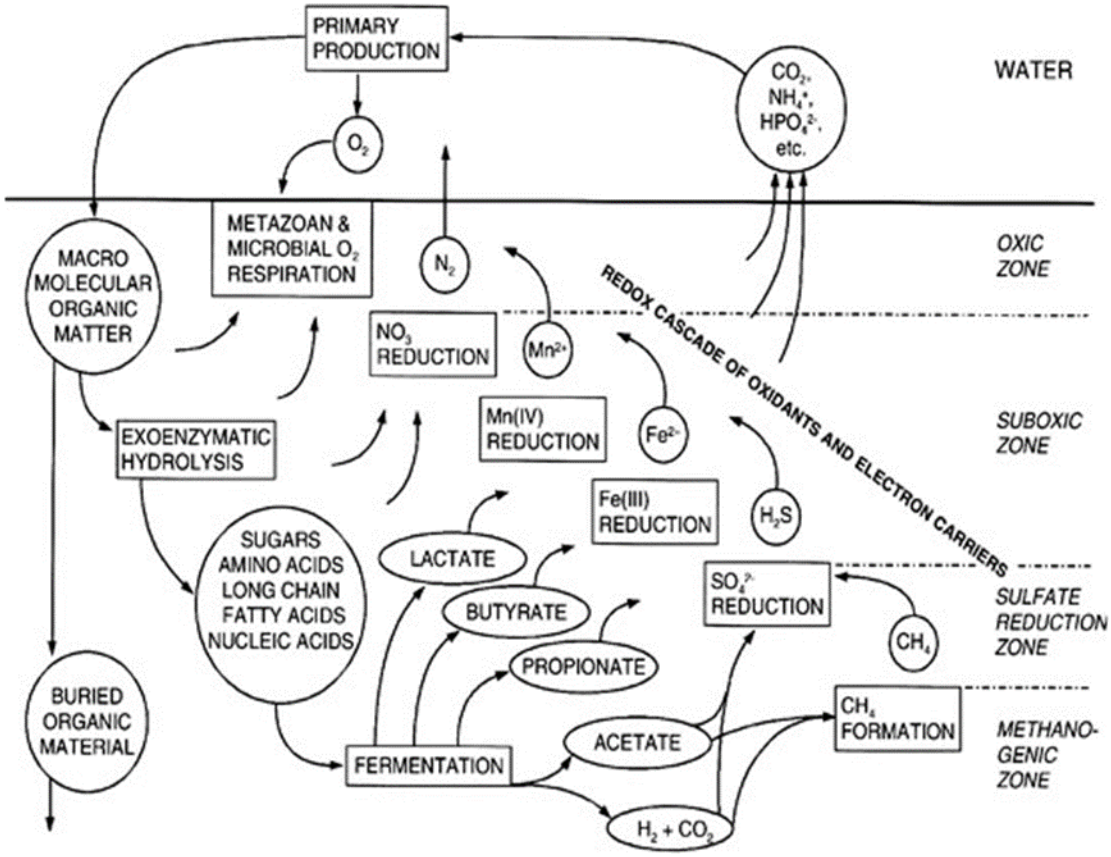

Figure 1-2. Schematic for the heterotrophic redox cascade in marine sediments, originally from (Jørgensen 2000). Aerobic respiration and nitrate reduction consumes complex organic matter that has been enzymatically processed into simpler molecules (e.g., sugars and amino acids). Bacteria below the oxycline and nitracline break down sugars through glycolysis and subsequent fermentation reactions into even simpler organic molecules like lactate ($C_3H_6O_3$) and acetate (CH_3COO). After nitrate is exhausted, manganese and iron reduction become dominant and utilize these fermentation products as electron donors.

Photosynthetic Life

The evolution of photosynthesis, or the derivation of energy via sunlight, is considered instrumental to the diversification of life on Early Earth (Des Marais 2000). Photosynthesis can be oxygenic (i.e., producing O_2 by splitting apart H_2O molecules) or anoxygenic (using reduced

compounds like Fe^{2+} or H_2S). Anoxygenic photosynthesis proceeds through a similar biochemical pathway as oxygenic photosynthesis, with the major differences being the ED and the presence of two photosystems, and will be covered in more depth in Part II, 'Sulfur Oxidation'. In oxygenic photosynthesis, light energy is absorbed by pigment molecules (e.g., chlorophyll) located in the prokaryotic cytoplasm or within specialized organelles called chloroplasts in eukaryotes (Blankenship 2021; Hall and Rao 1999). The primary sites where light energy is absorbed are called photosystems. Electrons in photosystem II are excited by light energy and then transported through an electron transport chain which, similar to chemoheterotrophic electron transport, creates a proton gradient. The electrons lost by photosystem II are replaced by the oxidation of water molecules, creating O_2 as a by-product. Photosystem I lies at the end of the electron transport chain, where light energy again excites the electrons that have been transferred from photosystem II. Another electron transport chain is initiated, ultimately creating NADPH. This NADPH, in conjunction with ATP that is generated by the proton gradient, can then be used by the photosynthetic organisms in the light-independent Calvin Cycle (Blankenship 2021). In the Calvin Cycle, an enzyme called Ribulose-1,5-biphosphate carboxylase/oxygenase (Rubisco) fixes carbon dioxide to a sugar molecule called ribulose-1,5-biphosphate (RuBP). The ATP and NADPH created during the light-dependent reaction are then used to phosphorylate and reduce this molecule further in a multi-step process, eventually leading to glyceraldehyde-3-phosphate (G3P). Some of the produced G3P will be converted back into RuBP, while some of it will be used to create sugar molecules and subsequently biomass (Blankenship 2021). Photosynthetic organisms can either be heterotrophs or autotrophs, with the latter being more common. Photoheterotrophs may still perform the Calvin Cycle but are generally incapable of creating all of their biomass through

CO_2 fixation (Kirchman and Hanson 2013). Photoautotrophs on the other hand, solely rely on CO_2 fixation to build their biomass (Blankenship 2021).

Chemoautotrophy

Similar to photoautotrophs, chemoautotrophic organisms conduct CO_2 fixation to build biomass, but inorganic reactions are used in energy derivation instead of light. In most aquatic environments, inorganic electron donors (e.g., NH_4^+, Fe^{2+}, H_2S) utilized by chemoautotrophic microbes are mainly produced by heterotrophic processes (Jørgensen 2000). While O_2 is the most potent TEA for chemoautotrophic metabolisms, the same redox cascade of TEAs for chemoheterotrophic metabolisms applies for chemoautotrophic metabolisms. Chemoautotrophic organisms utilize the energy gained from the oxidation of these reduced compounds to fix CO_2 (as opposed to utilizing light energy to achieve the same means). In most chemoautotrophs, carbon fixation is achieved through roughly the same pathway as photosynthesis (i.e., the Calvin Cycle), however the exact form of Rubisco used could differ for different organisms and EDs (Tabita et al. 2007).

In aerobic ammonium oxidation, NH_4^+ is first oxidized to hydroxylamine (NH_2OH) using ammonia mono-oxygenase, which is further oxidized to NO_2^- by ammonium-oxidizing bacteria or archaea. NO_2^- is then oxidized to NO_3^- by nitrite-oxidizing bacteria (Zhang et al. 2020). Each step in the process is usually carried out by multiple organisms, however, complete nitrification by a single organism (comammox) has recently been discovered (Kits et al. 2017; Van Kessel et al. 2015). Ammonium oxidation can also occur anaerobically (annamox) by bacteria within the phylum *Planctomycetes* with NO_2^- as the electron acceptor instead of O_2 (Van de Graaf et al. 1995; Zhang et al. 2020). Anammox occurs in specialized organelles called “anammoxosomes”. First, NH_4^+ is oxidized to hydroxylamine (NH_2OH) by hydrazine synthase while NO_2^- is reduced

first to NO, and then to NH_2OH. Two NH_2OH molecules are then oxidized to hydrazine (N_2H_4) by hydrazine synthase, which is then converted to N_2 by hydrazine dehydrogenase (Zhang et al. 2020). Similar to denitrification, annamox leads to a loss of reactive nitrogen in biological systems.

The oxidation of Fe^{2+} or (as it is referred to if present in its solid form) Fe(II) by oxygen happens rapidly without biological input, but can also be biologically mediated in low-oxygen (Edwards et al. 2003; Emerson and Weiss 2004; Weber et al. 2006) or acidic environments (Abramov et al. 2022). Anaerobic iron oxidation is considered a primordial respiration metabolism available to Precambrian microbes; these microbes either utilize light energy (iron-dependent anoxygenic photosynthesis) or NO_3^- as an electron acceptor (Hafenbradl et al. 1996; Widdel et al. 1993). Additionally, recently discovered cable bacteria are able to span the gap between oxygenated bottom waters and ferruginous (free Fe^{2+}) sediment porewaters via the use of cm-long nanowire filaments and perform aerobic or anaerobic iron oxidation (Kessler et al. 2019; Kjeldsen et al. 2019; Pfeffer et al. 2012). Cable bacteria are also capable of conducting chemoautotrophic sulfide oxidation, which will be covered in more detail in Part II, 'Sulfur Oxidation'. Methanotrophy, or the oxidation of methane, can occur aerobically or anaerobically. Methanotrophs utilize methane as both an ED as well as a source of carbon for biomass, and can use some C_1 compounds to build biomass, therefore they are not considered strictly autotrophs (Ouboter et al. 2023). The first step in aerobic oxidation of methane is the oxidation of methane to methanol via methane monooxygenase and subsequent oxidation to formaldehyde (CH_2O) by methanol dehydrogenase (Anthony 1982; Hakemian and Rosenzweig 2007; Hanson and Hanson 1996). At this step, CH_2O can either go through anabolic processes via the ribulose monophosphate pathway (Type I) or serine pathway (Type II), or go through catabolic processes,

eventually being oxidized to CO_2 (Anthony 1982; Hanson and Hanson 1996; Lieberman and Rosenzweig 2004). Anaerobic oxidation of methane can be coupled to Fe^{3+}, NO_3^-, or SO_4^{2-} reduction.

Part II. Sulfur Cycling and Associated Metabolisms

Introduction to Sulfur

Sulfur, the 16th element on the periodic table, is an essential element of several amino acids and vitamins critical for life. In solution and mineral form, it most commonly exists as either sulfide (H_2S, HS-, S^{2-}) or sulfate (SO_4^{2-}) and has an oxidation state ranging from -2 to +6. There are four stable isotopes of sulfur: ^{32}S, ^{33}S, ^{34}S and ^{36}S with natural abundance ratios of 95.02 : 0.75 : 4.21 : 0.02. ^{35}S, with a half-life of approx. 87 days, is the only radioactive isotope of sulfur with a half-life of more than three hours. The melting point of elemental sulfur is 115°C, close to the boiling point of water (100°C), which attracted the attention of Earth's earliest chemists (Kutney 2023).

The first documented evidence in history of human's using sulfur is from the Ebers Papyrus, written in approx. 1550 B.C., where it was used as an ingredient in an eye salve to treat conjunctivitis (Ebers and Stern 1875). Aristotle's student Theophrastus describes the transformation of cinnabar (HgS) to elemental mercury (Hg) in his book 'On Stones', written in the 4th century B.C., one of the first known descriptions of a chemical reaction (Caley and Richards 1956; Kutney 2023; Takacs 2000). The production of sulfur dioxide (SO_2) by burning sulfur with oxygen is considered one of the earliest industrial applications of chemical reactions, and the noxious gas was used to spiritually purify buildings and as an ancient form of pesticide (Kutney 2023). Sulfur was also an important foundation to the art of alchemy, specifically the transformation of pyrite to sulfuric acid circa the 15th century A.D., which is widely considered to be the foundation of modern chemistry (Davis 1930; Kutney 2023). The creation of gunpowder in the 8th century A.D., and specifically its use in the siege of Constantinople in 1453, created the first large-scale industrial application for sulfur, follow by the production of

sulfuric acid in the 18th century, which was critical to the invention of the fertilizer industry and modern agriculture (Kutney 2023).

Investigations into the biological transformations of sulfur for metabolic processes can be traced back to the work of Sergei Winogradsky, who's discovery of sulfur cycling organisms via the study of *Beggiatoa* (Fig. 3), is considered the foundation of environmental microbiology (Dworkin and Gutnick 2012). Furthermore, when isotope geochemistry was identified as a powerful tool to study past climates through the investigation of mineralogical clues, sulfur isotope analyses quickly became an important investigation. Several processes within biological sulfur cycling impart a kinetic isotope effect (KIE); biological processes prefer the lighter isotope (or isotopologue) of any given compound during anabolic and catabolic processes (O'Neil 1986). Thus, the presence and magnitude of any deviation of relative isotope abundance (e.g., $^{34}S/^{32}S$) in a mineral from a reference material can signal biological activity at the time of formation. Both sulfate minerals (e.g., evaporites) and sulfide minerals (e.g., pyrite) have been crucial in reconstructing ancient environments using these isotope fractionations (Canfield 1991; Claypool et al. 1980; Fike et al. 2015). Biological sulfur cycling is important in many environments, including hydrothermal vents (Childress and Fisher 1992), terrestrial hot springs (Kubo et al. 2011), methane seeps (Orcutt et al. 2005), and whale falls (Treude et al. 2009). In this section, I will focus on sulfur cycling within the water column and sediment of eutrophic marine and lacustrine low oxygen environments.

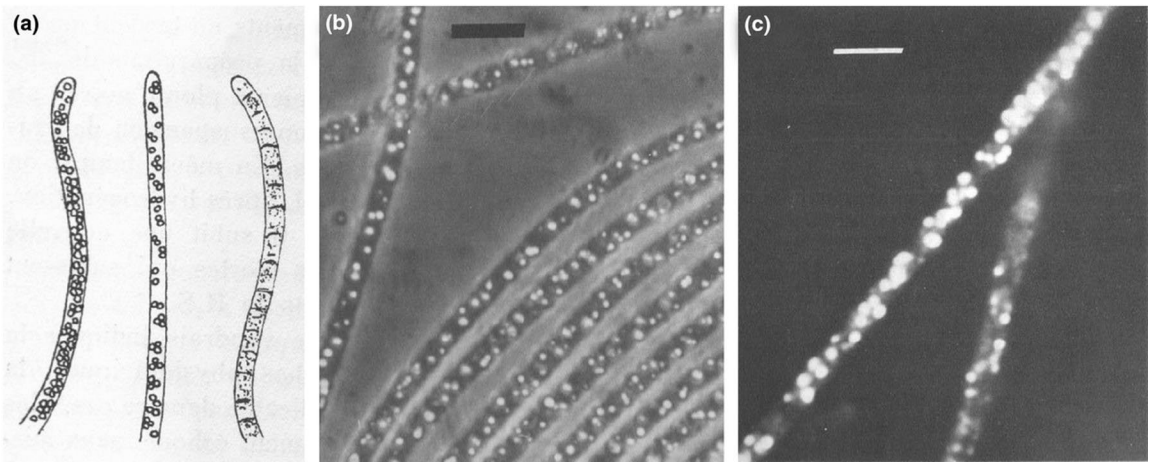

Figure 1-3. Early depictions of the sulfur-oxidizing bacteria *Beggiatoa* from (a) Winogradsky and (b,c) Strohl & Larkin (Strohl and Larkin 1978).

Sulfur Mineralization

Sulfur can form minerals at several oxidation states, most commonly in the form of sulfate (SO_4^{2-}) or sulfide (S^{2-}) ions. Common sulfate minerals include the calcium bearing gypsum ($CaSO_4*2H_2O$) and anhydrite ($CaSO_4$), which primarily form as evaporites in desiccating, saline environments or from interactions between hydrothermal fluids and rock. Gypsum typically forms under lower pressure and temperature conditions, and where desiccation rates are slow enough to allow the inclusion of water into its crystal structure. Anhydrite often forms secondary to gypsum; in evaporites from the Messinian salt layer, gypsum is found to be the primary evaporite mineral produced directly from the desiccating Mediterranean brine, whereas anhydrite is a product of secondary mineralization through further desiccation (Testa and Lugli 2000). Dissolution of calcium sulfate minerals occurs when these evaporite layers come in contact with neutral to acidic waters, which can hydrolyze the calcium sulfate bond and free both minerals to dissolve into the water, potentially increasing the salinity of surrounding water bodies (Lebedev 2015; Wardlaw and Valentine 2005).

Metal sulfides, especially iron sulfides are of particular interest to biological sulfur

cycling in anoxic environments (Rickard and Luther 2007). There are many mineral forms that iron sulfides can take, however amorphous iron mono-sulfides (FeS) and pyrite (FeS_2) are of particular importance in early diagenesis of marine sediment. When the water column above marine sediment is oxygenated (i.e., containing free dissolved oxygen) or ferruginous (i.e., containing dissolved Fe^{2+}), iron mono-sulfides with poorly organized crystalline structures form near the sediment-water interface (de Koff et al. 2008; Rickard and Luther 2007). The sulfur in these iron minerals can later be oxidized to a -1 oxidation state by elemental sulfur during early diagenesis, allowing for the creation of pyrite (Liu et al. 2020). When the water column is euxinic (i.e., containing dissolved sulfide), Fe^{2+} initially forms iron-mono-sulfides in the water column, which act as nucleation centers for the creation of framboidal pyrite, which then sinks to the seafloor (Wilkin and Barnes 1997, Rickard and Luther 2007).

In transiently deoxygenated systems, when oxygenated bottom waters return, iron sulfides can be re-oxidized back to sulfate and Fe(III), with the latter being insoluble at neutral pH. This effectively transforms iron sulfide minerals into iron oxide minerals at the sediment-water interface, and sometimes deeper in the sediment in the presence of bioturbation and bioirrigation that introduce oxygen (Bonaglia et al. 2019; Peterson et al. 1996). This repeating cycle of Fe(III) mineral reduction to Fe(II) minerals during anoxia and re-oxidation of Fe(II) minerals to Fe(III) minerals upon oxygenation can lead to high benthic iron fluxes (Kuwabara et al. 1999). In addition to abiotic oxidation of iron sulfides, several types of sulfur- and iron-oxidizing chemoautotrophic organisms, such as cable bacteria, are capable of oxidizing these minerals to gain access to the powerful ED (Hermans et al. 2019; Preisler et al. 2007; Seitaj et al. 2015). Iron delivery to coastal marine sediment is largely terrigenous, while the sulfide in marine sediment is largely sourced from biological sulfate reduction, though both sulfide and iron in

marine systems can also be chemogenic in origin (Rickard and Luther 2007).

Sulfate Reduction

Sulfate reduction typically uses fermentation products (e.g., hydrogen, acetate, lactate; Fig. 2, Table 1) for electron donors, and hydrogenotrophic sulfate reduction ($\Delta G° = -152$ kj mol^{-1}) is much more energetically favorable than organoclastic sulfate reduction (e.g., $\Delta G° = -41$ kJ mol^{-1} when paired with acetate oxidation) (Jørgensen 2000). Hydrogenotrophic sulfate reduction is a chemoautotrophic process, and is considered one of Earth's primordial metabolisms, having been widespread by the early Archean eon (Shen and Buick 2004). Sulfate-reducing bacteria can also act in a consortium with methanotrophic archaea to perform the anaerobic oxidation of methane (Boetius et al. 2000; Orphan et al. 2001; Treude 2003). They can also utilize thermogenic compounds such as propane as ED (Kniemeyer et al. 2007).

Despite being much less energetically favorable than nitrate or iron reduction, sulfate reduction is still an incredibly important metabolic process in marine sediment, particularly those under surface waters marked with high amounts of primary productivity (Canfield et al. 2005, Treude 2011). The sulfate reduction zone develops once O_2, NO_3^-, Mn(IV), and Fe(III) are exhausted; while some sulfate reducers can tolerate oxygen (Cypionka 2000), biological sulfate reduction is an anaerobic process.

Biological sulfate reduction (Fig. 4) begins with either active or passive transport of sulfate into the cell. Active transport is usually done by symporters that recruit several other ions into to the cell (e.g., Na^+) along with sulfate, though, most sulfate recruitment likely occurs through passive transport because active transport would make the process not energetically favorable (Cypionka 1995). Once transported into the cell, sulfate is first transformed to adenosine 5'-phosphosulfate (APS), requiring one molecule of ATP. This intermediate step

happens because APS reduction to sulfite by the enzyme APS reductase is more energetically favorable than direct reduction of sulfate to sulfite (Michaels et al. 1970). Sulfite is then reduced by dissimilatory sulfite reductase (DsrABC) to H_2S, $S_2O_3^{2-}$, or elemental sulfur which is transported out of the cell by the c-subunit of the reductase (DsrC, (Oliveira et al. 2008; Santos et al. 2015)). DsrC then acts as the terminal electron acceptor for the electron transport chain within sulfate-reducing cells (Venceslau et al. 2014).

A diverse array of organisms are capable of conducting sulfate reduction, mainly belonging to the class Deltaproteobacteria, a class of gram-negative bacteria (Robador et al. 2016). For example, in the upper margins of marine sediment in Aarhus Bay, Desulfobacteracae and Desulfobulbaceae are the most abundant (LeLoup et al. 2009), while in the upper margins of the Black Sea, uncultured gram-positive sulfate-reducing bacteria dominate (LeLoup et al. 2007). In deeper sediment and in the water column of anoxic lakes, where there is sulfate limitation, other taxa like Chloroflexi and Firmicutes become dominant sulfate reducers (Phillips et al. 2021; Wasmund et al. 2017). Additionally, some archaea such as Archeaoglobus (Burggraf et al. 1990) and Thorarchaeota (Seitz et al. 2016) have the genes necessary to conduct sulfate reduction, though their contribution to sulfur cycling in the environment remains unclear. Ultimately, the distribution, abundance, and diversity of sulfate-reducing bacteria correlates with availability of ED and TEA

The kinetic isotope effect (KIE) associated with sulfate reduction leads to an isotopically heavy reserve of sulfate and the production of isotopically light reduced sulfur compounds. This fractionation of ^{34}S relative to the lighter isotope ^{32}S is measured against the Vienna Canyon Diablo Triolite standard (VCDT):

$$\partial^{34}S\ (‰) = \left(\frac{[^{34}S\ /\ ^{32}S]_{sample}}{[^{34}S\ /\ ^{32}S]_{VCDT}} - 1\right) x\ 1000 \qquad [3]$$

Where $\delta^{34}S$ is the deviation of the fraction of $^{34}S/^{32}S$ from the standard. The maximum depletion of $\delta^{34}S$ of sulfide produced from sulfate reduction in pure culture experiments has been constrained to be approx. 47‰ (Canfield and Teske 1996), however larger values have been recorded in mixed cultures and chemostat experiments (Canfield et al. 2010a; Leavitt et al. 2013). These fractionations appear to occur primarily during APS reduction to sulfite and sulfite reduction to H_2S by DsrABC (Rees 1973). Sulfate reducers that do not completely oxidize their ED (e.g., to CO_2) yield lower isotope fractionations (depleted in $\delta^{34}S$ by < 19‰, (Detmers et al. 2001)). The major factors governing isotope fractionation during sulfate reduction appear to be 1) sulfate concentration, whereby higher concentrations lead to increased fractionation (Habicht et al. 2002) and 2) cell-specific sulfate reduction rate (csSRR), where higher csSRR produces less fractionation (Chambers et al. 1975; Harrison and Thode 1958; Sim et al. 2011a; Wing and Halevy 2014). Additionally, the use of triplicate isotope analyses (^{32}S, ^{33}S, ^{34}S) have shown that csSRR related sulfur isotope fractionation is impacted by ED quality and availability, with more consistent input of ED (i.e., in eutrophic shallow marine environments) leading to higher csSRR and less fractionation (Leavitt et al. 2013; Sim et al. 2011b). This KIE associated with sulfate concentrations, csSRR, and ED availability has been used to inform our understanding of paleoenvironments (Fike et al. 2015). One potential complication with these interpretations, however, is that other biologically-mediated reactions within the sulfur cycle (e.g., sulfur disproportionation reactions) can impart their own KIE and mask the fractionation signal (Jørgensen et al. 2019). While these sulfur disproportionation reactions can lead to $\delta^{34}S$ of sulfide depleted by greater than 47 ‰ (Canfield and Thamdrup 1994) the impact of these reactions on isotope fractionation in modern marine sediment appears marginal (Fike et al. 2015).

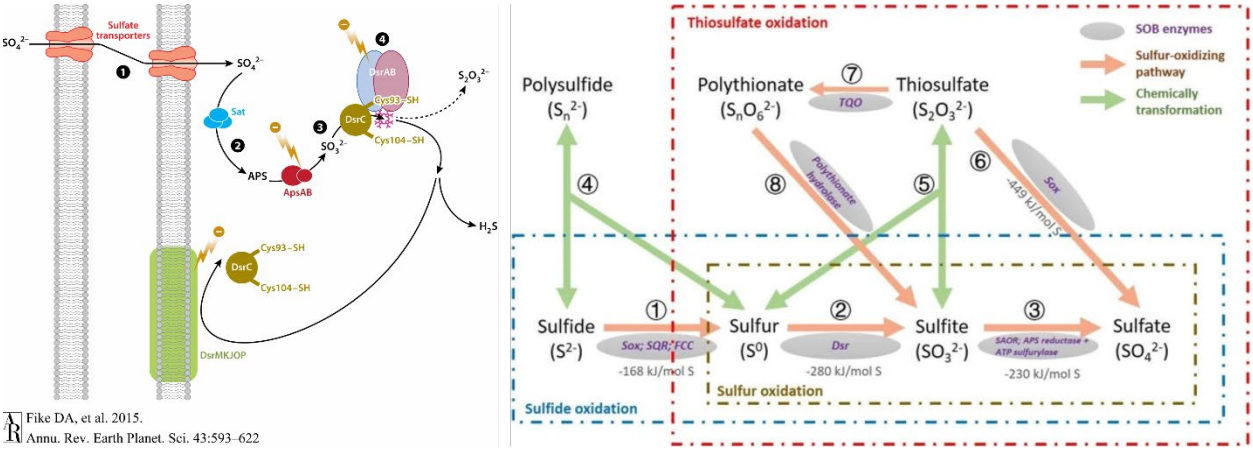

Figure 1-4. **Left:** Schematic of sulfate reduction, taken from (Fike et al. 2015). **1)** Sulfate is transported into the cell using a sulfate transporter (or via passive diffusion). **2)** Sulfate is reduced to APS. **3)** APS is reduced to sulfite. **4)** The DSR protein complex reduces sulfite to thiosulfate and hydrogen sulfide. DsrC then acts as an electron acceptor in the electron transport chain of sulfate-reducing bacteria. **Right:** Schematic of common microbial sulfur oxidation pathways, taken from (Cui et al. 2019). Focusing on the transformation of sulfide to sulfate: **1)** Oxidation of sulfide to elemental sulfur via Sox, SQR, or FCC enzymes. **2)** Oxidation of elemental sulfur to sulfite by Dsr enzyme. **3)** Oxidation of sulfite to sulfate by APS reductase and ATP sulfurylase.

Sulfur Oxidation

The reduced products of sulfate reduction, typically sulfide, can be used as an ED for autotrophic organisms, coupled to either anoxygenic photosynthesis, O_2 reduction, or NO_3^- reduction. Unlike sulfate reduction and sulfur disproportionation reactions, sulfide oxidation seems to have little effect on isotope fractionation. Anoxygenic photosynthesis coupled to sulfide oxidation is conducted in much the same manner as oxygenic photosynthesis, with reduced sulfur compounds as the electron donor instead of water. One key difference between oxygenic and anoxygenic photosynthesis is that the former requires two photosystems to cleave electrons off of H_2O molecules, but anoxygenic photosynthesis substrates such as H_2S only require one photosystem (Allen 2005). Green sulfur bacteria such as *Chlorobi* can oxidize either sulfide or

ferrous iron using different bacteriochlorophylls as their photosynthetic pigments (Bryant and Frigaard 2006). These green sulfur bacteria have also been observed conducting photosynthesis off of infrared radiation from hydrothermal vents (Beatty et al. 2005), contributing to primary productivity in a system devoid of sunlight. Purple sulfur bacteria from the Proteobacteria class such as *Roseobacter* are facultative phototrophs under anoxic conditions but can also perform heterotrophic metabolisms when environmental conditions are favorable (Bryant and Frigaard 2006). Despite the diversity (in species and metabolism) of organisms capable of doing anoxygenic photosynthesis, several questions regarding the evolution and biochemistry of sulfur-oxidizing photoautotrophs remain (Bryant and Frigaard 2006). The importance of anoxygenic photosynthesizers to sulfur cycling, particularly in the oxycline of stratified lakes where they can represent up to 50% of microbial species, necessitates much further analyses (Block et al. 2021; Gregersen et al. 2009).

Aerobic sulfide oxidation occurs abiotically, however microbes are able to catalyze sulfide oxidation orders of magnitude faster than the abiotic process (Jørgensen 1982; Luther III et al. 2011). While several pathways exist for the oxidation of sulfide (some to sulfate, some terminate in intermediary compounds like elemental sulfur) the *sox* pathway is the most well understood (Friedrich et al. 2001). Aerobic sulfide oxidation must occur in an environment where the oxidant and ED come in close contact with each other, such as in the chemocline in anoxic pelagic environments (Lavik et al. 2009; Phillips et al. 2021) or at the marine sediment-water interface (Canfield and Thamdrup 2009; Wasmund et al. 2017). The majority of aerobic sulfur-oxidizing bacteria that colonize the marine sediment-water interface are *Gammaproteobacteria* (Dyksma et al. 2016), though other genera such as *Thiobacillus* and *Thiomicrospira* are plentiful (Brinkhoff et al. 1998). Sulfur oxidizers in surface sediments are

often concomitant with high amounts of surface organic carbon content and consequentially high rates of sulfate reduction near the sediment-water interface, giving them ample access to both their ED and TEA (Canfield 1989b; Thamdrup et al. 1994a; Thamdrup et al. 1994b). Cable bacteria and some genera of filamentous sulfur-oxidizing bacteria with vacuolated nitrate are able to bridge the gap between reduced sediment and oxygenated bottom waters, either through the use of nanowires or through vertical migration into the sediment, respectively (Larkin and Strohl 1983; Schauer et al. 2014).

The sulfur cycle and nitrogen cycle can interact via Giant Sulfur-Oxidizing Bacteria (GSOB) such as the filamentous *Beggiatoa* and *Thioploca* and the spherical *Thiomargarita* which can couple sulfide oxidation to nitrate reduction (Jørgensen and Nelson 2004; Larkin and Strohl 1983). These GSOB can hyper-accumulate nitrate in intracellular vacuoles up to 500 mM (Fossing et al. 1995a) and also hold reserves of elemental sulfur within their cells (Otte et al. 1999). These gammaproteobacteria (Salman et al. 2011) utilize different pathways for sulfide oxidation (Fig. 4). Some strains of *Beggiatoa* utilize adenosine mono phosphate (AMP) to oxidize sulfite to APS using the APS reductase enzyme, then ATP sulfurylase oxidize sulfite to sulfate, producing an ATP in the process (Hagen and Nelson 1997). However, this complete oxidation to sulfate is not the preferred pathway for GSOB to oxidize sulfide; the sulfur globules within these bacterial cells indicate that sulfide is first oxidized to elemental sulfur which is then stored and subsequently oxidized to sulfate in a secondary step by c-type cytochromes (Prince et al. 1988, Fike et al. 2015). These GSOB in marine sediment can conduct either denitrification or DNRA (De Brabandere et al. 2015; Otte et al. 1999; Schutte et al. 2018); the environmental conditions that preference nitrate reduction pathway and ergo which organisms will dominate may depend on the duration of anoxia and nitrate depletion.

Part III: Transiently Deoxygenated Environments

Open Ocean Oxygen Minimum Zones

The oxygen minimum zone (OMZ) that was described first was the OMZ in the tropical East Pacific, off the coast of Mexico (Cline and Richards 1972). Since this time, the term OMZ has sometimes been used to refer to ubiquitously distributed areas of the ocean where oxygen concentrations reach a minima between approx. 1,000 and 1,500 m depth (Paulmier and Ruiz-Pino 2009; Wyrtki 1962). These naturally occurring ubiquitously distributed areas of the ocean are now referred to as "classical O_2-minima" and instead the term "OMZ" is reserved for more intense areas of deoxygenation where waters become hypoxic (< 63 μM) or even approach anoxia (Paulmier and Ruiz-Pino 2009). Open ocean OMZ are believed to be created in part by the transport of low oxygen waters from areas with higher rates of organic matter degradation (Davila et al. 2023; Karstensen et al. 2008; Wyrtki 1962). However, in many places high primary productivity in surface waters also contributes to the appearance of OMZ (Rabalais et al. 2014). These open ocean OMZ are expanding and intensifying (Stramma et al. 2008) with consequences on aquatic organisms and biogeochemical cycling in Earth's oceans (Stramma et al. 2010). The exact level deoxygenation used to define and study OMZ depends on the research question, but 90, 45, and 4.5 μM have all been used (Karstensen et al. 2008; Paulmier and Ruiz-Pino 2009; Stramma et al. 2008). A map of the oxygen minimum throughout Earth's oceans can be seen in Fig. 5.

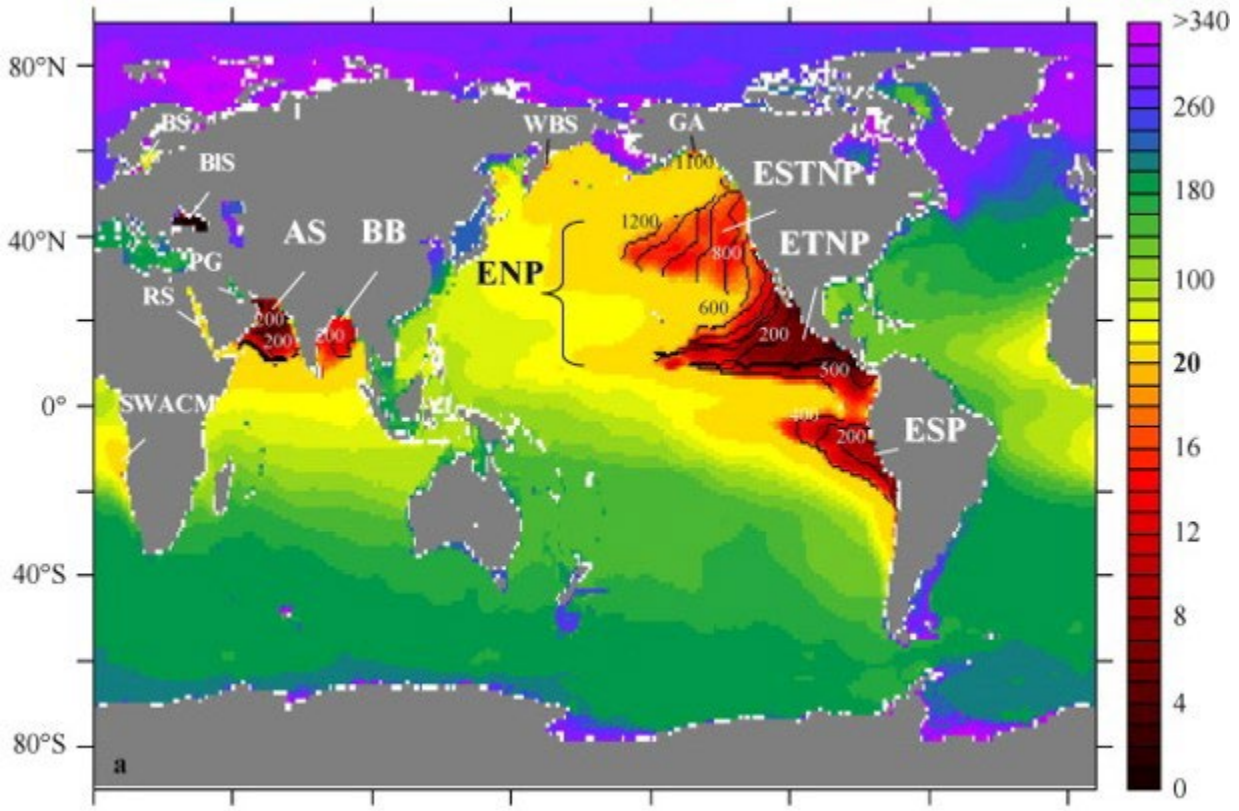

Figure 1-5. Map of O_2 distribution at depth where O_2 concentration is minimal (O_2 in µM) throughout Earth's oceans, taken from Fig. 1 of (Paulmier and Ruiz-Pino 2009). Oxygen minimum zones are pointed out in white letters: Arabian Sea (AS), Bay of Bengal (BB), Black Sea (BIS), Baltic Sea (BS), Eastern Northern Pacific (ENP), Eastern South Pacific (ESP), Eastern Sub-Tropical North Pacific (ESTNP), Eastern Tropical North Pacific (ETNP), Gulf of Alaska (GA), Persian Gulf (PG), Red Sea (RS), South Western African Continental Margin (SWACM), and Western Bering Sea (WBS).

While the vast majority of modern oceans are well oxygenated, approx. 4% of the global ocean has less than 90 µM O_2, considered too low to support most marine animals, and around 0.05% has less than 4.5 µM O_2, low enough for anaerobic metabolisms to take hold (Karstensen et al. 2008; Keeling et al. 2010; Lam and Kuypers 2011). According to the thermodynamics (Table 1) denitrification should be the dominant pathway once OMZ waters approach anoxia; the accumulation of NO_2^- in waters below the mixed layer inspired scientists to study denitrification in the oceans in the first place (Brandhorst 1959; Gilson 1933; Lam and Kuypers 2011; Wooster

et al. 1965). However, even though there is ample evidence of active denitrifiers in these OMZ waters (Castro-González et al. 2005; Lam et al. 2009) there is an apparent lack of complete denitrification along with a lack of transcription of *NirS* (Lam et al. 2009), the gene responsible for NO_2^- to NO conversion during denitrification. In the Eastern Tropical South Atlantic (ETSA) OMZ (Kuypers et al. 2005) and in the Eastern Tropical South Pacific (ETSP) OMZ (Thamdrup et al. 2006) annamox was found to be the primary mechanism for N_2 and N_2O production. Annamox was further found to be the key pathway responsible for reactive nitrogen loss from OMZ waters using paired isotope rate determinations (Holtappels et al. 2011). The NO_2^- needed for annamox is likely sourced from aerobic ammonium oxidation in the upper and lower portions of the OMZ; Thaumarchaeota, an aerobic ammonium-oxidizing archaea (Kozlowski et al. 2016) are rife in the upper OMZ waters but not found in the OMZ core (Ulloa et al. 2012). Some NO_2^- likely comes from incomplete denitrification (i.e., nitrate reduction to nitrite) as well, while the NH_4^+ is sourced from both organic matter degradation and DNRA within the OMZ (Holtappels et al. 2011; Lam et al. 2009). This complex web of nitrogen cycling within OMZ waters (Fig 6) is an active area of research, and not all OMZ appear to have the same nitrogen cycles (Ward et al. 2009).

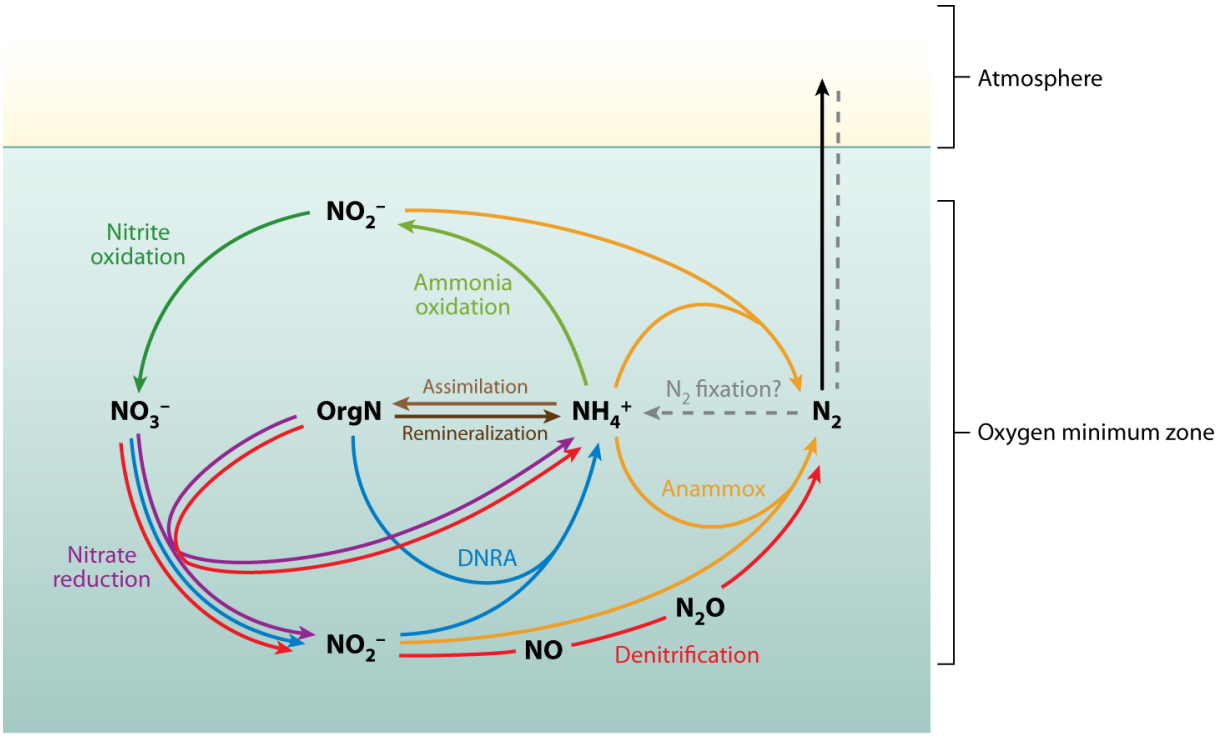

Figure 1-6: Schematic of nitrogen transformations that occur in oxygen minimum zones, taken from (Lam and Kuypers 2011). Nitrate reduction transforms NO_3^- to NO_2^-, which can either be further reduced to N_2 via canonical denitrification or to NH_4^+ via dissimilatory nitrate reduction to ammonium (DNRA). This NH_4^+ can then be assimilated into organic matter, oxidized to NO_2^- during aerobic ammonium oxidation, or reduced to N_2 via anaerobic ammonium oxidation (annamox).

Iron reduction is not likely to occur in most OMZ waters because Fe(III) is not soluble at standard ocean pH, and iron is an essential (and often limiting) micronutrient for primary productivity (Gervais et al. 2002). Microniches in sinking particles within OMZ waters were hypothesized to support sulfate reduction, and this particle-associated sulfate reduction (and resultant sulfide) was offered as a solution to explain the enrichment of trace metals in particles of OMZ waters (Bianchi et al. 2018). This particle-associated sulfate reduction was later confirmed in the Eastern Tropical North Pacific (ETNP) OMZ, where the resultant reduced sulfur compounds create recalcitrant organic sulfides which may promote carbon burial in the sediment underlying these OMZ (Raven et al. 2021).

Coastal Oxygen Minimum Zones

When OMZs occur in coastal waters, the anoxic water column can extend to the seafloor, leading to altered biogeochemical cycling within the marine sediment below the OMZ (Dale et al. 2016). These coastal anoxic environments are usually due to either eutrophication from upwelling (e.g., the Peruvian Margin, (Bohlen et al. 2011; Dale et al. 2016; Sommer et al. 2016)) or restricted ventilation in enclosed basins (e.g., the Eastern Gotland Basin of the Baltic Sea, (Noffke et al. 2016)). Some of these environments, like the Black Sea, are permanently anoxic at certain depths (Deuser 1974), however many are transiently deoxygenated environments that are periodically flushed with oxygenated water (Bograd et al. 2002; van de Velde et al. 2020a). The benthic biogeochemistry of these transiently deoxygenated coastal OMZ is heavily affected by processes at the sediment-water interface and in the sediment. For example, in the Santa Barbara Basin, the bulk of nitrogen loss via denitrification occurs at the sediment-water interface, not in the water column (Sigman et al. 2003). On the Peruvian shelf, fluxes of ammonium from the seafloor are concomitant with O_2 and NO_3^- depletion in the bottom waters and the development of thick benthic microbial mats of GSOB bacteria (Sommer et al. 2016). These GSOB mats (Fig 7) appear in transiently deoxygenated environments when the bottom waters reach anoxia and nitrate is still present (Noffke et al. 2016; Valentine et al. 2016). While some GSOB bacteria perform aerobic sulfide oxidation, this niche in transiently deoxygenated marine environments appears to be dominated by cable bacteria at the exclusion of GSOB, whereas GSOB appear to dominate once anoxia is established (Kessler et al. 2019; Marzocchi et al. 2018; Schauer et al. 2014). Because of their ability to rapidly oxidize sulfide and their appearance at the sediment-water interface, both cable bacteria and GSOB mats are seen as the last prevention towards the

development of euxinia in the anoxic bottom waters of coastal OMZ (Fossing et al. 1995a; Gutiérrez et al. 2008; Seitaj et al. 2015; Sommer et al. 2016). While GSOB mats are able to persist on their intracellular stores of nitrate (Fig. 7), persistent anoxia and nitrate depletion leads to a collapse of the mats and sulfide fluxes into the bottom waters (Gutiérrez et al. 2008). The exact conditions in both the sediment and bottom waters that allow for the proliferation of these thick GSOB mats, and the duration of anoxia and NO_3^- depletion that lead to their collapse, is an area requiring further research (Kuwabara et al. 1999; Sommer et al. 2016; Valentine et al. 2016).

Hypotheses for Coastal OMZ

The primary goal of the original research detailed in this dissertation is to increase our understanding of how sulfur, and associated redox-sensitive elements, are cycled in transiently deoxygenated aquatic environments. The Santa Barbara Basin is a coastal OMZ that experiences transient deoxygenation and hosts ephemeral GSOB mats during times of anoxia. We build off research conducted on these mats by Reimers et al. (1996), Kuwabara et al. (1999), and Valentine et al. (2016) amongst others. In particular, we set out to determine whether these mats establish a feedback loop with sulfate reducing bacteria in the sediment below to help them proliferate. These mats occupy an ecological niche between anoxic and euxinic water column conditions and are associated with declining nitrate values in the basin's bottom waters (Valentine et al. 2016). If their appearance prohibits the penetration of nitrate into the sediment, it could allow for a shallowing of the sulfate reduction zone to the near-surface, providing the mats with more electron donor. Additionally, we seek to determine if increasingly long periods of anoxia in the basin are leading to a shift from a ferruginous to a sulfidic sediment state. This

research will aid in the broader understanding of how expanding oxygen minimum zones could affect benthic geomicrobiology and the global sulfur cycle.

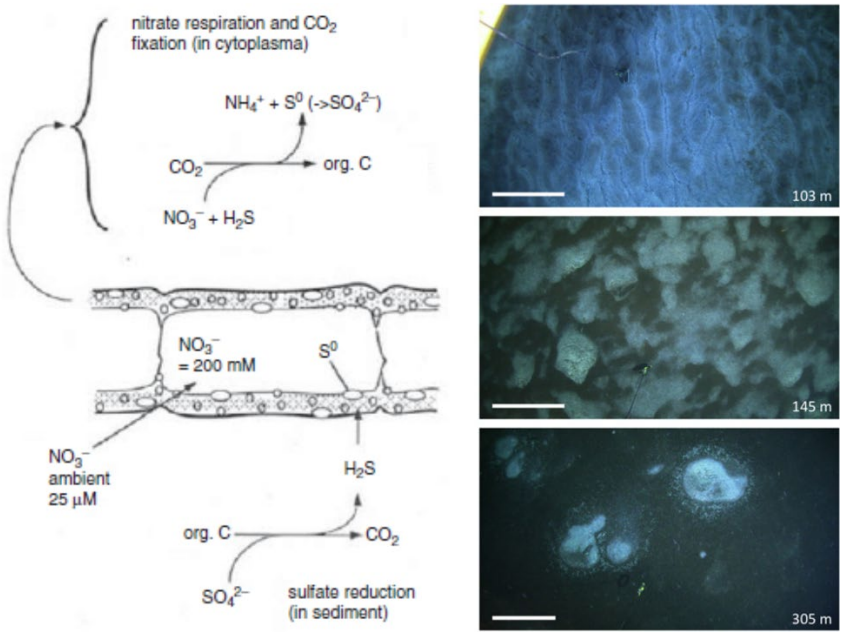

Figure 1-7. Left: Schematic of giant sulfur-oxidizing bacteria (GSOB) metabolism taken from (Teske and Nelson 2006). Nitrate (NO_3^-) is stored in intracellular vacuoles to >100 mM concentrations. Sulfide (H_2S) is oxidized to elemental sulfur (S^0), which is stored within the cell and is later further oxidized to sulfate (SO_4^{2-}). Right: Images from the Peruvian shelf of GSOB mats taken at 103, 145, and 305 m depth (Sommer et al. 2016).

Lake Hypolimnion

Marine environments are not the only systems that experience transient deoxygenation, many lacustrine environments experience stagnation in their deeper waters due to density stratification at least once per year. Some lakes are meromictic, meaning they have permanent stratification (e.g., Green Lake, NY) while other lakes experience annual (or more frequent) deoxygenation in their bottom waters, which are called holomictic lakes (e.g., Lake Titicaca). In the layer beneath the thermocline (the hypolimnion) anaerobic metabolisms, including those that

cycle sulfur, are prevalent (Foti et al. 2007). Of particular interest to sulfur cycling are endorheic lakes that serve as the hydrological sink for inland watersheds with no connection to the ocean. A common feature of these endorheic lakes is increasing salinity due to cycles of evaporation and re-hydration, though overall these lakes are desiccating around the world (Williams 2002). The dissolution of evaporites like gypsum and epsomite into the water column can lead to high concentrations of sulfate within these lakes which can promote sulfate reduction in the sediment and anoxic water column of these lakes (Margalef-Marti et al. 2023; Wardlaw and Valentine 2005). Chemoautotrophic sulfide oxidation and anoxygenic photosynthesis are common sulfur-oxidizing metabolisms found at the chemocline within these lakes (Gilhooly III et al. 2016; Gregersen et al. 2009). Besides biological sulfide oxidation, a common sink for sulfide in these lakes is the formation of framboidal pyrite in the oxycline of the water column (de Koff et al. 2008; Gilhooly III et al. 2016). As these lakes dry, the changes of sulfur cycling metabolisms and their impact on the surrounding ecosystem and human populations need to be assessed (Fogel et al. 2021; Frie et al. 2017). Additionally, these drying inland lakes can act as an analogue for studying biogeochemical progressions involved in past drying events, like the Messinian Salinity Crisis (Krijgsman et al. 1999) and the potential for life on early Mars (Pontefract et al. 2017).

Hypotheses for Lake Hypolimnions

The Salton Sea in California offers an additional system to study sulfur cycling during transient deoxygenation. Water column sulfate reduction likely occurs in the lake when the hypolimnion becomes anoxic, as evidenced by the extreme euxinia (>2 mM) that has been measured in the lake (Reese et al., 2008). We hypothesize that sulfate reduction in the Salton Sea water column contributes to this euxinia, and we set out to quantify sulfate reduction rates in the

lake's waters during oxygenated and deoxygenated conditions. This research will aid in understating how microbial rates in the Salton Sea's water column change with different seasons and help further refine the sulfur budget for the lake. This research will also give us clues into how rapid desiccation can affect the sulfur cycle in transiently deoxygenated saline lakes.

Part V. Dissertation outlook

This dissertation contains this introductory chapter, three separate manuscript chapters, and a conclusion chapter. Each manuscript chapter presents novel research that has either already been published (chapter 2) or is in preparation for publication (chapters 3 & 4). Chapter 2 was recently published in *Biogeosciences* (Yousavich et al. 2024) and details conditions necessary for benthic microbial mat proliferation in the Santa Barbara Basin, California. Chapter 3 has gone through several rounds of co-author review and will be submitted to *Nature Geosciences* in summer 2024. This manuscript documents how increasing deoxygenation within the Santa Barbara Basin, associated with increasing El Niño events, is forcing a shift from a ferruginous to sulfidic sediment state and a loss of highly reactive iron from the sediment-water interface. This chapter builds upon the work done in Chapter 2 and incorporates a wealth of historical data and statistical techniques to elucidate correlations within the sediment redox state to bottom water oxidant concentrations. Chapter 4 examines the effect of transient deoxygenation on sulfur cycling in the Salton Sea, California and reports the first microbial rates of sulfate reduction, methane oxidation, and nitrogen cycling from the Salton Sea. This manuscript is in preparation for submission to *Limnology and Oceanography*. The last chapter of this dissertation (chapter 5) summarizes the most important findings and places the research within the greater context of microbiology and geochemistry of anoxic and transiently deoxygenated aquatic environments.

References

Abramov, S. M. and others 2022. Biogeochemical niches of Fe-cycling communities influencing heavy metal transport along the Rio Tinto, Spain. Applied and Environmental Microbiology **88**: e02290-02221.

Allen, J. F. 2005. A redox switch hypothesis for the origin of two light reactions in photosynthesis. FEBS letters **579**: 963-968.

Alperin, M. C., and W. S. Reeburgh. 1985. Inhibition experiments on anaerobic methane oxidation. Appl. Environ. Microbiol. **50:** 940-945.

Amachi, S. and others 2007. Dissimilatory iodate reduction by marine Pseudomonas sp. strain SCT. Applied and environmental microbiology **73**: 5725-5730.

Anbar, A. D. and others 2007. A whiff of oxygen before the great oxidation event? Science **317:** 1903-1906.

Andersson, S., G. Dalhammar, C. J. Land, and G. Kuttuva Rajarao. 2009. Characterization of extracellular polymeric substances from denitrifying organism Comamonas denitrificans. Applied microbiology and biotechnology **82:** 535-543.

Anthony, C. 1982. The biochemistry of methylotrophs.

Beatty, T. J. and others 2005. An obligately photosynthetic bacterial anaerobe from a deep-sea hydrothermal vent. PNAS **102:** 9306-9310.

Bekker, A. and others 2004. Dating the rise of atmospheric oxygen. Nature **427:** 117-120.

Bell, E. A., P. Boehnke, T. M. Harrison, and W. L. Mao. 2015. Potentially biogenic carbon preserved in a 4.1 billion-year-old zircon. Proceedings of the National Academy of Sciences **112:** 14518-14521.

Bianchi, D., T. S. Weber, R. Kiko, and C. Deutsch. 2018. Global niche of marine anaerobic metabolisms expanded by particle microenvironments. Nature Geoscience **11:** 263-268.

Blankenship, R. E. 2021. Molecular mechanisms of photosynthesis. John Wiley & Sons.

Block, K. R., J. M. O'Brien, W. J. Edwards, and C. L. Marnocha. 2021. Vertical structure of the bacterial diversity in meromictic Fayetteville Green Lake. MicrobiologyOpen **10:** e1228.

Boetius, A. and others 2000. A marine microbial consortium apparently mediating anaerobic oxidation of methane. Nature **407:** 623-626.

Bograd, S. J., F. B. Schwing, C. G. Castro, and D. A. Timothy. 2002. Bottom water renewal in the Santa Barbara Basin. Journal of Geophysical Research: Oceans **107:** 9-1-9-9.

Bohlen, L. and others 2011. Benthic nitrogen cycling traversing the Peruvian oxygen minimum zone. Geochim. Cosmochim. Acta **75:** 6094-6111.

Bonaglia, S., U. Marzocchi, N. Ekeroth, V. Brüchert, S. Blomqvist, and P. O. Hall. 2019. Sulfide oxidation in deep Baltic Sea sediments upon oxygenation and colonization by macrofauna. Marine biology **166:** 1-12.

Brandhorst, W. 1959. Nitrification and denitrification in the eastern tropical North Pacific. ICES Journal of Marine Science **25:** 3-20.

Brinkhoff, T., C. M. Santegoeds, K. Sahm, J. Kuever, and G. Muyzer. 1998. A polyphasic approach to study the diversity and vertical distribution of sulfur-oxidizing Thiomicrospira species in coastal sediments of the German Wadden Sea. Applied and Environmental Microbiology **64:** 4650-4657.

Brochier-Armanet, C., E. Talla, and S. Gribaldo. 2009. The multiple evolutionary histories of dioxygen reductases: implications for the origin and evolution of aerobic respiration. Molecular biology and evolution **26:** 285-297.

Bryant, D. A., and N.-U. Frigaard. 2006. Prokaryotic photosynthesis and phototrophy illuminated. Trends in microbiology **14:** 488-496.

Burggraf, S., H. W. Jannasch, B. Nicolaus, and K. O. Stetter. 1990. Archaeoglobus profundus sp. nov., represents a new species within the sulfate-reducing archaebacteria. Systematic and applied microbiology **13**: 24-28.

Cairns-Smith, A. 1978. Precambrian solution photochemistry, inverse segregation, and banded iron formations. Nature **276:** 807-808.

Caley, E. R., and J. F. Richards. 1956. Theophrastus on Stones: Introduction, Greek text, English translation, and commentary. The Ohio State University Press.

Canfield, D. E. 1989. Sulfate reduction and oxic respiration in marine sediments: implications for organic carbon preservation in euxinic environments. Deep-Sea Res. **36:** 121-138.

Canfield, D. E. 1991. Sulfate reduction in deep-sea sediments. American Journal of Science **291:** 177-188.

Canfield, D. E., J. Farquhar, and A. L. Zerkle. 2010. High isotope fractionations during sulfate reduction in a low-sulfate euxinic ocean analog. Geology **38:** 415–418.

Canfield, D. E., and A. Teske. 1996. Late Proterozoic rise in atmospheric oxygen concentration inferred from phylogenetic and sulfur-isotope studies. Nature **382:** 127-132.

Canfield, D. E., and B. Thamdrup. 1994. The production of 34S-depleted sulfide during bacterial disproportionation of elemental sulfur. Science **266:** 1973-1975.

Canfield, D. E., E. Kristensen, and B. Thamdrup. 2005. The sulfur cycle, p. 313-381. Advances in Marine Biology. Elsevier.

Canfield D.E. and B. Thamdrup. 2009. Towards a consitent classification scheme for geochemical environments, or, why we wish the term "suboxic" would go away. Geobiology **7:** 385-392.

Castro-González, M., G. Braker, L. Farías, and O. Ulloa. 2005. Communities of nirS-type denitrifiers in the water column of the oxygen minimum zone in the eastern South Pacific. Environmental Microbiology **7:** 1298-1306.

Chambers, L. A., P. A. Trudinger, J. W. Smith, and M. S. Burns. 1975. Fractionation of sulfur isotopes by continuous cultures of Desulfovibrio desulfuricans. Canadian Journal of Microbiology **21:** 1602-1607.

Childress, J. J., and C. R. Fisher. 1992. The biology of hydrothermal vent animals: physiology, biochemistry, and autotrophic symbioses. Oceanogr. and Mar. Biol. **30:** 337-441.

Claypool, G. E., W. T. Holser, I. R. Kaplan, H. Sakai, and I. Zak. 1980. The age curves of sulfur and oxygen isotopes in marine sulfate and their mutual interpretation. Chemical geology **28:** 199-260.

Cline, J. D., and F. A. Richards. 1972. Oxygen deficient conditions and nitrate reduction in the eastern tropical North Pacific Ocean 1. Limnology and Oceanography **17:** 885-900.

Cloud, P. 1973. Paleoecological significance of the banded iron-formation. Economic Geology **68:** 1135-1143.

Cui, Y.-X. and others 2019. Biological nitrogen removal from wastewater using sulphur-driven autotrophic denitrification. Applied microbiology and biotechnology **103:** 6023-6039.

Cypionka, H. 1995. Solute transport and cell energetics, p. 151-184. Sulfate-reducing bacteria. Springer.

Cypionka, H. 2000. Oxygen respiration by Desulfovibrio species. Annual Reviews in Microbiology **54:** 827-848.

Dale, A. W., S. Sommer, U. Lomnitz, A. Bourbonnais, and K. Wallmann. 2016. Biological nitrate transport in sediments on the Peruvian margin mitigates benthic sulfide emissions and drives pelagic N loss during stagnation events. Deep Sea Research Part I: Oceanographic Research Papers **112:** 123-136.

Davila, X., A. Olsen, S. K. Lauvset, E. L. McDonagh, A. Brakstad, and G. Gebbie. 2023. On the origins of open ocean oxygen minimum zones. Journal of Geophysical Research: Oceans **128:** e2023JC019677.

Davis, T. L. 1930. Questions for the student of elementary chemistry. Journal of Chemical Education **7:** 1141.

De Brabandere, L. and others 2015. Oxygenation of an anoxic fjord basin strongly stimulates benthic denitrification and DNRA. Biogeochemistry **126:** 131-152.

de Koff, J. P., M. A. Anderson, and C. Amrhein. 2008. Geochemistry of iron in the Salton Sea, California, p. 111-121. The Salton Sea Centennial Symposium: Proceedings of a Symposium Celebrating a Century of Symbiosis Among Agriculture, Wildlife and People, 1905–2005, held in San Diego, California, USA, March 2005. Springer.

Des Marais, D. J. 2000. When did photosynthesis emerge on Earth? Science **289:** 1703-1705.

Detmers, J., V. Brüchert, K. S. Habicht, and J. Kuever. 2001. Diversity of sulfur isotope fractionations by sulfate-reducing prokaryotes. Applied and environmental microbiology **67:** 888-894.

Deuser, W. 1974. Evolution of anoxic conditions in Black Sea during Holocene: Water.

Dreher, C. L., M. Schad, L. J. Robbins, K. O. Konhauser, A. Kappler, and P. Joshi. 2021. Microbial processes during deposition and diagenesis of Banded Iron Formations. PalZ **95:** 593-610.

Dworkin, M., and D. Gutnick. 2012. Sergei Winogradsky: a founder of modern microbiology and the first microbial ecologist. FEMS microbiology reviews **36:** 364-379.

Dyksma, S. and others 2016. Ubiquitous Gammaproteobacteria dominate dark carbon fixation in coastal sediments. The ISME journal **10:** 1939-1953.

Ebers, G., and L. Stern. 1875. Papyros Ebers: das Hermetische Buch über die Arzneimittel der alten Ägypter in hieratischer Schrift.

Edwards, K. J., D. R. Rogers, C. O. Wirsen, and T. McCollom. 2003. Isolation and characterization of novel psychrophilic, neutrophilic, Fe-oxidizing, chemolithoautotrophic α-and γ-Proteobacteria from the deep sea. Applied and Environmental Microbiology **69:** 2906-2913.

Emerson, D., and J. V. Weiss. 2004. Bacterial iron oxidation in circumneutral freshwater habitats: findings from the field and the laboratory. Geomicrobiology Journal **21:** 405-414.

Fike, D. A., A. S. Bradley, and C. V. Rose. 2015. Rethinking the ancient sulfur cycle. Annual Review of Earth and Planetary Sciences **43:** 593-622.

Fogel, M. and others 2021. Crisis at the Salton Sea: The Vital Role of Science.

Fossing, H. and others 1995. Concentration and transport of nitrate by the mat-forming sulphur bacterium Thioploca. Nature **374:** 713-715.

Foti, M. and others 2007. Diversity, activity, and abundance of sulfate-reducing bacteria in saline and hypersaline soda lakes. Applied and environmental microbiology **73:** 2093-2100.

Fredrickson, J. K. and others 1998. Biogenic iron mineralization accompanying the dissimilatory reduction of hydrous ferric oxide by a groundwater bacterium. Geochimica et Cosmochimica Acta **62:** 3239-3257.

Frie, A. L., J. H. Dingle, S. C. Ying, and R. Bahreini. 2017. The effect of a receding saline lake (the Salton Sea) on airborne particulate matter composition. Environmental science & technology **51:** 8283-8292.

Friedrich, C. G., D. Rother, F. Bardischewsky, A. Quentmeier, and J. Fischer. 2001. Oxidation of reduced inorganic sulfur compounds by bacteria: emergence of a common mechanism? Applied and environmental microbiology **67:** 2873-2882.

Gervais, F., U. Riebesell, and M. Y. Gorbunov. 2002. Changes in primary productivity and chlorophyll a in response to iron fertilization in the Southern Polar Frontal Zone. Limnology and Oceanography **47:** 1324-1335.

Gilhooly III, W. P., C. T. Reinhard, and T. W. Lyons. 2016. A comprehensive sulfur and oxygen isotope study of sulfur cycling in a shallow, hyper-euxinic meromictic lake. Geochimica et Cosmochimica Acta **189:** 1-23.

Gilson, H. C. 1933. The nitrogen cycle. The John Murray Expedition **1934:** 21-81.

Gregersen, L. H. and others 2009. Dominance of a clonal green sulfur bacterial population in a stratified lake. FEMS microbiology ecology **70:** 30-41.

Gruber, N., and J. L. Sarmiento. 1997. Global patterns of marine nitrogen fixation and denitrification. Global biogeochemical cycles **11:** 235-266.

Gutiérrez, D. and others 2008. Oxygenation episodes on the continental shelf of central Peru: Remote forcing and benthic ecosystem response. Prog. Oceanogr. **79:** 171-189.

Habicht, K. S., M. Gade, B. Thamdrup, P. Berg, and D. E. Canfield. 2002. Calibration of sulfate levels in the Archean ocean. Science **298:** 2372-2374.

Hafenbradl, D. and others 1996. Ferroglobus placidus gen. nov., sp. nov., a novel hyperthermophilic archaeum that oxidizes Fe2+ at neutral pH under anoxic conditions. Archives of microbiology **166:** 308-314.

Hagen, K. D., and D. C. Nelson. 1997. Use of reduced sulfur compounds by Beggiatoa spp.: enzymology and physiology of marine and freshwater strains in homogeneous and gradient cultures. Applied and environmental microbiology **63:** 3957-3964.

Hakemian, A. S., and A. C. Rosenzweig. 2007. The biochemistry of methane oxidation. Annu. Rev. Biochem. **76:** 223-241.

Hall, D. O., and K. Rao. 1999. Photosynthesis. Cambridge University Press.

Hanson, R. S., and T. E. Hanson. 1996. Methanotrophic bacteria. Microbiol. Rev. **60:** 439-471.

Harrison, A., and H. Thode. 1958. Mechanism of the bacterial reduction of sulphate from isotope fractionation studies. Transactions of the Faraday Society **54:** 84-92.

Hermans, M. and others 2019. Abundance and biogeochemical impact of cable bacteria in Baltic Sea sediments. Environmental science & technology **53:** 7494-7503.

Hinkle, P. C., and R. E. McCarty. 1978. How cells make ATP. Scientific American **238:** 104-123.

Holtappels, M., G. Lavik, M. M. Jensen, and M. M. Kuypers. 2011. 15N-labeling experiments to dissect the contributions of heterotrophic denitrification and anammox to nitrogen removal in the OMZ waters of the ocean, p. 223-251. Methods in enzymology. Elsevier.

James, H. L. 1966. Chemistry of the iron-rich sedimentary rocks. US Government Printing Office.

Johnson, C. M., B. L. Beard, C. Klein, N. J. Beukes, and E. E. Roden. 2008. Iron isotopes constrain biologic and abiologic processes in banded iron formation genesis. Geochimica et Cosmochimica Acta **72:** 151-169.

Jørgensen, B. B. 1982. Ecology of the bacteria of the sulphur cycle with special reference to anoxic-oxic interface environments. Phil. Trans. R. Soc. Lond. B **298:** 543-561.

Jørgensen, B. B. 2000. Bacteria and marine biogeochemistry, p. 173-201. *In* H. D. Schulz and M. Zabel [eds.], Marine biogeochemistry. Springer Verlag.

Jørgensen, B. B., A. J. Findlay, and A. Pellerin. 2019. The biogeochemical sulfur cycle of marine sediments. Frontiers in microbiology **10:** 436320.

Jørgensen, B. B., and D. C. Nelson. 2004. Sulfide oxidation in marine sediments: Geochemistry meets microbiology. Geological Society of America **Special Paper 379:** 63-81.

Karstensen, J., L. Stramma, and M. Visbeck. 2008. Oxygen minimum zones in the eastern tropical Atlantic and Pacific oceans. Progress in Oceanography **77:** 331-350.

Keeling, R. F., A. Körtzinger, and N. Gruber. 2010. Ocean Deoxygenation in a Warming World. Annual Review of Marine Science. Ann. Rev. Mar. Sci. **2:** 199-229.

Kessler, A. J. and others 2019. Cable bacteria promote DNRA through iron sulfide dissolution. Limnology and Oceanography **64:** 1228-1238.

Kirchman, D. L., and T. E. Hanson. 2013. Bioenergetics of photoheterotrophic bacteria in the oceans. Environmental microbiology reports **5:** 188-199.

Kits, K. D. and others 2017. Kinetic analysis of a complete nitrifier reveals an oligotrophic lifestyle. Nature **549:** 269-272.

Kjeldsen, K. U. and others 2019. On the evolution and physiology of cable bacteria. Proceedings of the National Academy of Sciences **116:** 19116-19125.

Kniemeyer, O. and others 2007. Anaerobic oxidation of short-chain hydrocarbons by marine sulfate-reducing bacteria. Nature **449:** 898-902.

Kostka, J. E., and K. H. Nealson. 1995. Dissolution and reduction of magnetite by bacteria. Environmental Science & Technology **29:** 2535-2540.

Kozlowski, J. A., M. Stieglmeier, C. Schleper, M. G. Klotz, and L. Y. Stein. 2016. Pathways and key intermediates required for obligate aerobic ammonia-dependent chemolithotrophy in bacteria and Thaumarchaeota. The ISME journal **10:** 1836-1845.

Krijgsman, W., F. J. Hilgen, I. Raffi, F. J. Sierro, and D. Wilson. 1999. Chronology, causes and progression of the Messinian salinity crisis. Nature **400:** 652-655.

Kubo, K., K. Knittel, R. Amann, M. Fukui, and K. Matsuura. 2011. Sulfur-metabolizing bacterial populations in microbial mats of the Nakabusa hot spring, Japan. Systematic and applied microbiology **34:** 293-302.

Kutney, G. 2023. Sulfur: history, technology, applications and industry. Elsevier.

Kuwabara, J. S., A. van Geen, D. C. McCorkle, and J. M. Bernhard. 1999. Dissolved sulfide distributions in the water column and sediment pore waters of the Santa Barbara Basin. Geochimica et Cosmochimica Acta **63:** 2199-2209.

Kuypers, M. M. M. and others 2005. Massive nitrogen loss from the Benguela upwelling system through anaerobic ammonium Oxidation. PNAS **102:** 6478-6483.

Lake, J. A. and others 1985. Eubacteria, halobacteria, and the origin of photosynthesis: the photocytes. Proceedings of the National Academy of Sciences **82:** 3716-3720.

Lam, P., and M. M. M. Kuypers. 2011. Microbial nitrogen cycling processes in oxygen minimum zones. Annu. Rev. Mar. Sci. **3:** 317-345.

Lam, P. and others 2009. Revising the nitrogen cycle in the Peruvian oxygen minimum zone. Proceedings of the National Academy of Sciences **106:** 4752-4757.

Lanyi, J. K. 2004. Bacteriorhodopsin. Annu. Rev. Physiol. **66:** 665-688.

Larkin, J. M., and W. R. Strohl. 1983. Beggiatoa, Thiothrix, and Thioploca. Ann. Rev. Microbiol. **37:** 341-367.

Lavik, G. and others 2009. Detoxification of sulphidic African shelf waters by blooming chemolithotrophs. Nature **457:** 581-584.

Leavitt, W. D., I. Halevy, A. S. Bradley, and D. T. Johnston. 2013. Influence of sulfate reduction rates on the Phanerozoic sulfur isotope record. Proceedings of the National Academy of Sciences **110:** 11244-11249.

Lebedev, A. 2015. Kinetics of gypsum dissolution in water. Geochemistry International **53:** 811-824.

LeLoup, J., H. Fossing, K. Kohls, L. Holmkvist, C. Borowski, and B. B. Jørgensen. 2009. Sulfate-reducing bacteria in marine sediments (Aarhus Bay, Denmark): abundance and diversity related to geochemical zonation. Environ. Microbiol. **11:** 1278-1291.

LeLoup, J., A. Loy, N. J. Knab, C. Borowski, M. Wagner, and B. B. Jørgensen. 2007. Diversity and abundance of sulfate-reducing microorganisms in the sulfate and methane zones of a marine sediment, Black Sea. Environ. Microbiol. **9:** 131-142.

Lide, D. R. 2005. Abundance of Elements in the Earth's Crust and in the Sea. CRC handbook of chemistry and physics, Internet Version**:** 14-17.

Lieberman, R. L., and A. C. Rosenzweig. 2004. Biological methane oxidation: regulation, biochemistry, and active site structure of particulate methane monooxygenase. Critical reviews in biochemistry and molecular biology **39:** 147-164.

Liu, J. and others 2020. Early diagenesis of iron and sulfur in Bornholm Basin sediments: The role of near-surface pyrite formation. Geochimica et Cosmochimica Acta **284:** 43-60.

Lovley, D. R., M. J. Baedecker, D. J. Lonergan, I. M. Cozzarelli, E. J. Phillips, and D. I. Siegel. 1989. Oxidation of aromatic contaminants coupled to microbial iron reduction. Nature **339:** 297-300.

Lovley, D. R., J. D. Coates, E. L. Blunt-Harris, E. J. Phillips, and J. C. Woodward. 1996. Humic substances as electron acceptors for microbial respiration. Nature **382:** 445-448.

Lovley, D. R., D. E. Holmes, and K. P. Nevin. 2004. Dissimilatory fe (iii) and mn (iv) reduction. Advances in microbial physiology **49:** 219-286.

Lovley, D. R., and E. J. P. Phillips. 1987. Competitive mechanisms for inhibition of sulfate reduction and methane production in the zone of ferric iron reduction in sediments. Appl. Environm. Microbiol. **53:** 2636-2641.

Luther III, G. W. and others 2011. Thermodynamics and kinetics of sulfide oxidation by oxygen: a look at inorganically controlled reactions and biologically mediated processes in the environment. Frontiers in microbiology **2:** 62.

Lyons, T. W., C. T. Reinhard, and N. J. Planavsky. 2014. The rise of oxygen in Earth's early ocean and atmosphere. Nature **506:** 307-315.

Lyu, Z., N. Shao, T. Akinyemi, and W. B. Whitman. 2018. Methanogenesis. Current Biology **28:** R727-R732.

Margalef-Marti, R. and others 2023. Upside down sulphate dynamics in a saline inland lake. Scientific Reports **13:** 3032.

Marzocchi, U. and others 2018. Transient bottom water oxygenation creates a niche for cable bacteria in long-term anoxic sediments of the Eastern Gotland Basin. Environmental microbiology **20:** 3031-3041.

Michaels, G. B., J. Davidson, and H. D. Peck Jr. 1970. A flavin-sulfite adduct as an intermediate in the reaction catalyzed by adenylyl sulfate reductase from Desulfovibriovulgaris. Biochemical and Biophysical Research Communications **39:** 321-328.

Nielsen, J. 2017. Systems biology of metabolism. Annual review of biochemistry **86:** 245-275.

Noffke, A., S. Sommer, A. Dale, P. Hall, and O. Pfannkuche. 2016. Benthic nutrient fluxes in the Eastern Gotland Basin (Baltic Sea) with particular focus on microbial mat ecosystems. Journal of Marine Systems **158:** 1-12.

O'Neil, J. R. 1986. Theoretical and experimental aspects of isotopic fractionation. Reviews in Mineralogy **16:** 1-40.

Oliveira, T. F., C. Vonrhein, P. M. Matias, S. S. Venceslau, I. A. Pereira, and M. Archer. 2008. The crystal structure of Desulfovibrio vulgaris dissimilatory sulfite reductase bound to DsrC provides novel insights into the mechanism of sulfate respiration. Journal of Biological Chemistry **283:** 34141-34149.

Orcutt, E., A. Boetius, M. Elvert, V. Samarkin, and S. B. Joye. 2005. Molecular biogeochemistry of sulfate reduction, methanogenesis and anaerobic oxidation of methane at Gulf of Mexico cold seeps. Geochim. Cosmochim. Acta **69:** 4267-4281.

Orphan, V. J. and others 2001. Comparative analysis of methane-oxidizing archaea and sulfate-reducing bacteria in anoxic marine sediments. Appl. Environ. Microbiol. **67:** 1922-1934.

Otte, S. and others 1999. Nitrogen, carbon, and sulfur metabolism in natural Thioploca samples. Applied and Environmental Microbiology **65:** 3148-3157.

Ouboter, H. T. and others 2023. Acetate and acetyl-CoA metabolism of ANME-2 anaerobic archaeal methanotrophs. Applied and Environmental Microbiology **89**: e00367-00323.

Paulmier, A., and D. Ruiz-Pino. 2009. Oxygen minimum zones (OMZs) in modern ocean. Progr. Oceanog. **80:** 113-128.

Peterson, G. S., G. T. Ankley, and E. N. Leonard. 1996. Effect of bioturbation on metal-sulfide oxidation in surficial freshwater sediments. Environmental Toxicology and Chemistry: An International Journal **15:** 2147-2155.

Pfeffer, C. and others 2012. Filamentous bacteria transport electrons over centimetre distances. Nature **491:** 218-221.

Phillips, A. A. and others 2021. Microbial succession and dynamics in meromictic Mono Lake, California. Geobiology **19:** 376-393.

Pontefract, A. and others 2017. Microbial diversity in a hypersaline sulfate lake: a terrestrial analog of ancient Mars. Frontiers in microbiology **8:** 1819.

Preisler, A., D. De Beer, A. Lichtschlag, G. Lavik, A. Boetius, and B. B. Jørgensen. 2007. Biological and chemical sulfide oxidation in a Beggiatoa inhabited marine sediment. ISME Journal**:** 341-351.

Prince, R. C., K. E. Stokley, C. E. Haith, and H. W. Jannasch. 1988. The cytochromes of a marine Beggiatoa. Archives of microbiology **150:** 193-196.

Rabalais, N. N. and others 2014. Eutrophication-driven deoxygenation in the coastal ocean. Oceanography **27:** 172-183.

Raven, M., R. Keil, and S. Webb. 2021. Microbial sulfate reduction and organic sulfur formation in sinking marine particles. Science **371:** 178-181.

Rees, C. 1973. A steady-state model for sulphur isotope fractionation in bacterial reduction processes. Geochimica et Cosmochimica Acta **37:** 1141-1162.

Reimers, C. E., K. C. Ruttenberg, D. E. Canfield, M. B. Christiansen, and J. B. Martin. 1996. Porewater pH and authigenic phases formed in the uppermost sediments of Santa Barbara Basin. Geochim. Cosmochim. Acta **60**: 4037-4057.

Reguera, G., K. D. McCarthy, T. Mehta, J. S. Nicoll, M. T. Tuominen, and D. R. Lovley. 2005. Extracellular electron transfer via microbial nanowires. Nature **435:** 1098-1101.

Rickard, D., and G. W. Luther. 2007. Chemistry of iron sulfides. Chemical reviews **107:** 514-562.

Robador, A. and others 2016. Activity and community structures of sulfate-reducing microorganisms in polar, temperate and tropical marine sediments. The ISME journal **10:** 796-809.

Salman, V. and others 2011. A single-cell sequencing approach to the classification of large, vacuolated sulfur bacteria. Systematic and applied microbiology **34:** 243-259.

Santos, A. A. and others 2015. A protein trisulfide couples dissimilatory sulfate reduction to energy conservation. Science **350:** 1541-1545.

Schauer, R. and others 2014. Succession of cable bacteria and electric currents in marine sediment. The ISME journal **8:** 1314-1322.

Schutte, C. A. and others 2018. Filamentous giant Beggiatoaceae from the Guaymas Basin are capable of both denitrification and dissimilatory nitrate reduction to ammonium. Applied and environmental microbiology **84:** e02860-02817.

Seitaj, D. and others 2015. Cable bacteria generate a firewall against euxinia in seasonally hypoxic basins. Proceedings of the National Academy of Sciences **112:** 13278-13283.

Seitz, K. W., C. S. Lazar, K.-U. Hinrichs, A. P. Teske, and B. J. Baker. 2016. Genomic reconstruction of a novel, deeply branched sediment archaeal phylum with pathways for acetogenesis and sulfur reduction. The ISME journal **10:** 1696-1705.

Shen, Y., and R. Buick. 2004. The antiquity of microbial sulfate reduction. Earth-Science Reviews **64:** 243-272.

Sigman, D. M. and others 2003. Distinguishing between water column and sedimentary denitrification in the Santa Barbara Basin using the stable isotopes of nitrate. Geochemistry, Geophysics, Geosystems **4**.

Sim, M. S., T. Bosak, and S. Ono. 2011a. Large sulfur isotope fractionation does not require disproportionation. Science **333:** 74-77.

Sim, M. S., S. Ono, K. Donovan, S. P. Templer, and T. Bosak. 2011b. Effect of electron donors on the fractionation of sulfur isotopes by a marine Desulfovibrio sp. Geochimica et Cosmochimica Acta **75:** 4244-4259.

Sommer, S. and others 2016. Depletion of oxygen, nitrate and nitrite in the Peruvian oxygen minimum zone cause an imbalance of benthic nitrogen fluxes. Deep-Sea Res. I **112:** 113–122.

Soo, R. M., J. Hemp, D. H. Parks, W. W. Fischer, and P. Hugenholtz. 2017. On the origins of oxygenic photosynthesis and aerobic respiration in Cyanobacteria. Science **355:** 1436-1440.

Stramma, L., G. C. Johnson, J. Sprintall, and V. Mohrholz. 2008. Expanding oxygen-minimum zones in the tropical oceans. Science **320:** 655-658.

Stramma, L., S. Schmidtko, L. A. Levin, and G. C. Johnson. 2010. Ocean oxygen minima expansions and their biological impacts. Deep-Sea Research I **57:** 587-595.

Strohl, W. R., and J. M. Larkin. 1978. Enumeration, isolation, and characterization of Beggiatoa from freshwater sediments. Applied and Environmental Microbiology **36:** 755-770.

Stüeken, E. E., M. A. Kipp, M. C. Koehler, and R. Buick. 2016. The evolution of Earth's biogeochemical nitrogen cycle. Earth-Science Reviews **160:** 220-239.

Tabita, F. R., T. E. Hanson, H. Li, S. Satagopan, J. Singh, and S. Chan. 2007. Function, structure, and evolution of the RubisCO-like proteins and their RubisCO homologs. Microbiology and Molecular Biology Reviews **71:** 576-599.

Takacs, L. 2000. Quicksilver from cinnabar: The first documented mechanochemical reaction? JOM **52:** 12-13.

Teske, A., and D. C. Nelson. 2006. The genera beggiatoa and thioploca. Prokaryotes **6:** 784-810.

Testa, G., and S. Lugli. 2000. Gypsum–anhydrite transformations in Messinian evaporites of central Tuscany (Italy). Sedimentary Geology **130:** 249-268.

Thamdrup, B., T. Dalsgaard, M. M. Jensen, O. Ulloa, L. Farías, and R. Escribano. 2006. Anaerobic ammonium oxidation in the oxygen-deficient waters off northern Chile. Limnology and Oceanography **51:** 2145-2156.

Thamdrup, B., K. Finster, H. Fossing, J. W. Hansen, and B. B. Jørgensen. 1994a. Thiosulfate and sulfite distributions in porewater of marine sediments related to manganese, iron, and sulfur geochemistry. Geochimica et Cosmochimica Acta **58:** 67-73.

Thamdrup, B., H. Fossing, and B. B. Jørgensen. 1994b. Manganese, iron and sulfur cycling in a coastal marine sediment, Aarhus Bay, Denmark. Geochimica et Cosmochimica Acta **58:** 5115-5129.

Thauer, R. K., K. Jungermann, and K. Decker. 1977. Energy conservation in chemotrophic anaerobic bacteria. Bacteriol. Rev. **41:** 100-180.

Treude, T. 2003. Anaerobic oxidation of methane in marine sediments. Ph.D. thesis.

Treude T. 2011. Biogeochemical reactions in marine sediments underlying anoxic water bodies, p. 18-38. *In* A. Altenbach, J. Bernhard and J. Seckbach [eds.], Anoxia: Paleontological Strategies and Evidence for Eukaryote Survival. Cellular Origins, Life in Extreme Habitats and Astrobiology (COLE) Book Series. Springer.

Treude, T. and others 2009. Biogeochemistry of a deep-sea whale fall: sulfate reduction, sulfide efflux and methanogenesis. Mar. Ecol. Prog. Ser. **382:** 1-21.

Ulloa, O., D. E. Canfield, E. F. DeLong, R. M. Letelier, and F. J. Stewart. 2012. Microbial oceanography of anoxic oxygen minimum zones. Proceedings of the National Academy of Sciences **109:** 15996-16003.

Valentine, D. L. and others 2016. Autonomous marine robotic technology reveals an expansive benthic bacterial community relevant to regional nitrogen biogeochemistry. Environmental Science & Technology **50:** 11057-11065.

Van de Graaf, A. A., A. Mulder, P. De Bruijn, M. S. M. Jetten, L. A. Robertson, and J. G. Kuenen. 1995. Anaerobic oxidation of ammoinium is a biologically mediated process. Appl. Environ. Microbiol. **61:** 1246-1251.

van de Velde, S. J. and others 2020. Elevated sedimentary removal of Fe, Mn, and trace elements following a transient oxygenation event in the Eastern Gotland Basin, central Baltic Sea. Geochimica et Cosmochimica Acta **271:** 16-32.

Van Kessel, M. A. and others 2015. Complete nitrification by a single microorganism. Nature **528:** 555-559.

Venceslau, S., Y. Stockdreher, C. Dahl, and I. Pereira. 2014. The "bacterial heterodisulfide" DsrC is a key protein in dissimilatory sulfur metabolism. Biochimica et Biophysica Acta (BBA)-Bioenergetics **1837:** 1148-1164.

Ward, B. and others 2009. Denitrification as the dominant nitrogen loss process in the Arabian Sea. Nature **461:** 78-81.

Wardlaw, G. D., and D. L. Valentine. 2005. Evidence for salt diffusion from sediments contributing to increasing salinity in the Salton Sea, California. Hydrobiologia **533:** 77-85.

Wasmund, K., M. Mußmann, and A. Loy. 2017. The life sulfuric: microbial ecology of sulfur cycling in marine sediments. Environmental microbiology reports **9:** 323-344.

Weber, K. A., L. A. Achenbach, and J. D. Coates. 2006. Microorganisms pumping iron: anaerobic microbial iron oxidation and reduction. Nature Reviews Microbiology **4:** 752-764.

Widdel, F., S. Schnell, S. Heising, A. Ehrenreich, B. Assmus, and B. Schink. 1993. Ferrous iron oxidation by anoxygenic phototrophic bacteria. Nature **362:** 834-836.

Wilkin, R., and H. Barnes. 1997. Formation processes of framboidal pyrite. Geochimica et Cosmochimica Acta **61**: 323-339.

Williams, W. D. 2002. Environmental threats to salt lakes and the likely status of inland saline ecosystems in 2025. Environmental conservation **29:** 154-167.

Wing, B. A., and I. Halevy. 2014. Intracellular metabolite levels shape sulfur isotope fractionation during microbial sulfate respiration. Proceedings of the National Academy of Sciences **111:** 18116-18125.

Wooster, W. S., T. J. Chow, and I. Barrett. 1965. Nitrite distribution in Peru Current waters.

Wyrtki, K. 1962. The oxygen minima in relation to ocean circulation, p. 11-23. Deep Sea research and oceanographic abstracts. Elsevier.

Yousavich, D. J. and others 2024. Marine anoxia initiates giant sulfur-oxidizing bacterial mat proliferation and associated changes in benthic nitrogen, sulfur, and iron cycling in the Santa Barbara Basin, California Borderland. Biogeosciences **21:** 789-809.

Zhang, X., B. B. Ward, and D. M. Sigman. 2020. Global nitrogen cycle: critical enzymes, organisms, and processes for nitrogen budgets and dynamics. Chemical reviews **120:** 5308-5351.

Chapter 2

Marine anoxia initiates giant sulfur-bacteria mat proliferation and associated changes in benthic nitrogen, sulfur, and iron cycling in the Santa Barbara Basin, California Borderland

David J. Yousavich[1], De'Marcus Robinson[2], Xuefeng Peng[3], Sebastian J. E. Krause[1,4], Frank Wenzhöfer[5,6,7], Felix Janssen[5,6], Na Liu[8], Jonathan Tarn[8], Frank Kinnaman[8], David L. Valentine[8], Tina Treude[1,2]

[1]Department of Earth, Planetary, and Space Sciences, University of California Los Angeles, 595 Charles E. Young Drive East, Los Angeles, CA 90095, USA

[2]Department of Atmospheric and Oceanic Sciences, University of California Los Angeles, Math Science Building, 520 Portola Plaza, Los Angeles, CA 90095, USA

[3]School of Earth, Ocean, and Environment, University of South Carolina, 701 Sumter Street, EWS 617, Columbia, SC 29208, USA

[4]Earth Research Institute, 6832 Ellison Hall, University of California Santa Barbara, Ca 93106

[5]HGF-MPG Joint Research Group for Deep-Sea Ecology and Technology, Alfred-Wegener-Institute, Helmholtz-Center for Polar and Marine Research, Am Handelshafen 12, 27570 Bremerhaven, Germany

[6] HGF-MPG Joint Research Group for Deep-Sea Ecology and Technology, Max Planck Institute for Marine Microbiology, Celsiusstrasse 1, 28359 Bremen, Germany

[7]Department of Biology, DIAS, Nordcee and HADAL Centres, University of Southern Denmark, 5230 Odense M, Denmark

[8]Department of Earth Science and Marine Science Institute, University of California, Santa Barbara, CA 93106, USA

Abstract

The Santa Barbara Basin naturally experiences transient deoxygenation due to its unique geological setting in the Southern California Borderland and seasonal changes in ocean currents. Long-term measurements of the basin showed that anoxic events and subsequent nitrate exhaustion in the bottom waters have been occurring more frequently and lasting longer over the past decade. One characteristic of the Santa Barbara Basin is the seasonal development of extensive mats of benthic nitrate-reducing sulfur-oxidizing bacteria, which are found at the sediment-water interface when the basin's bottom waters reach anoxia but still provide some nitrate. To assess the mat's impact on the benthic and pelagic redox environment, we collected biogeochemical sediment and benthic flux data in November 2019, after anoxia developed in the deepest waters of the basin and dissolved nitrate was depleted (down to 9.9 μM). We found that the development of mats was associated with a shift from denitrification to dissimilatory nitrate reduction to ammonium. The zone of sulfate reduction appeared near the sediment-water interface in sediment hosting these ephemeral white mats. We found that an exhaustion of iron oxides in the surface sediment was an additional prerequisite for mat proliferation. Our research further suggests that cycles of deoxygenation and reoxygenation of the benthic environment result in extremely high benthic fluxes of dissolved iron from the basin's sediment. This work expands our understanding of nitrate-reducing sulfur-oxidizing mats and their role in sustaining and potentially expanding marine anoxia.

Introduction

Naturally occurring low-oxygen waters in the ocean are commonly observed below the ocean's mixed layer where respiration consumes oxygen faster than it is produced or ventilated. When low oxygen conditions occur along the western continental shelf in regions susceptible to upwelling events and/or undergoing eutrophication, organic matter remineralization can frequently drive oxygen concentrations to hypoxic (O_2 < 63 μM) (Middelburg and Levin 2009) and/or anoxic levels (O_2 < 3 μM) (Canfield et al. 2010b; Fossing et al. 1995b). These areas are usually referred to as Oxygen Minimum Zones (OMZs). In the water column of OMZs, nitrogen reduction becomes an important mechanism for organic matter remineralization (Ward et al. 2009). OMZs within coastal basins that experience seasonal changes in upwelling can experience anoxic and nitrate reducing conditions that extend to the benthic environment, especially when high productivity and associated organic matter export coincide with seasonal patterns of physical mixing. This fundamental change in the redox conditions at the sediment-water interface encourages elevated rates of anaerobic microbial processes and can promote organic matter preservation in the sediments (Middelburg and Levin 2009; Treude 2011), though a recent study suggests a thin reactive surface layer can provide high rates of organic matter degradation in anoxic environments (van de Velde et al. 2023). Persistent anoxia in these coastal OMZ can lead to huge releases of sulfide (up to 13.7 mmol m^{-2} d^{-1}) and ammonium (up to 21.2 mmol m^{-2} d^{-1}) into the water column (Sommer et al. 2016).

The Santa Barbara Basin (SBB) is an example of one of these coastal OMZs that experiences seasonal deoxygenation. Drastic changes in water column oxygenation and seafloor redox conditions drive complex changes in benthic biogeochemistry and microbiology, evidenced most clearly by the development of thick, expansive mats of giant sulfur-oxidizing

bacteria (GSOB) on the SBB seafloor (Bernhard et al. 2003; Kuwabara et al. 1999; Prokopenko et al. 2006; Valentine et al. 2016). A 2016 survey of the basin identified a vast GSOB mat spread over 1.6 contiguous km, confined between 487 and 523 km in the SBB depocenter where conditions were anoxic but not depleted of NO_3^- (Valentine et al. 2016). These GSOB mats have been noted previously in the SBB benthos, appearing at times of anoxia and disappearing when oxygen is present in the bottom water (Kuwabara et al. 1999; Reimers et al. 1996b). Similar GSOB mats have been identified in other transiently deoxygenated OMZs such as the Peruvian/Chilean coast (Høgslund et al. 2009; Schulz et al. 1996; Sommer et al. 2016; Zopfi et al. 2001). The chemoautotrophic bacteria that constitute the bulk of GSOB mats (typically *Thioploca* and/or *Beggiatoa*) utilize sulfide as an electron donor and O_2 or NO_3^- as a terminal electron acceptor (Jørgensen and Nelson 2004). Some GSOB can hyperaccumulate NO_3^- in cell vacuoles up to 500 mM (Fossing et al. 1995a) and use this NO_3^- reserve to oxidize sulfide that diffuses from the underlying sediment to perform their metabolism. (Huettel et al. 1996; Mußmann et al. 2003; Sayama 2001).

The activity of GSOB mats contribute significantly to element cycling in benthic marine environments with large effects on biogeochemical conditions in the bottom water. Isotopic measurements of $^{15}N/^{14}N$ and $^{18}O/^{16}O$ from NO_3^- in the SBB water column suggest that benthic organisms are responsible for approximately 75% of the total NO_3^- reduction in the SBB (Sigman et al. 2003). Other studies found that GSOB mats inhibit the diffusion of NO_3^- into sediments via hyper-accumulation in vacuoles thereby creating conditions ideal for bacterial heterotrophic sulfate reduction beneath them (Fossing et al. 1995b; Zopfi et al. 2001). These studies suggest that GSOB mats in the SBB may be responsible for the majority of NO_3^- consumption in the basin rather than water-column microbes. Additionally, GSOB mats have

been reported to deplete NO_3^- via dissimilatory nitrate reduction to ammonia (DNRA) in the anoxic bottom water of the Peruvian OMZ (Dale et al. 2016) and in the hypoxic transition zone in the Eastern Gotland Basin of the Baltic Sea (Noffke et al. 2016). By contrast, benthic microbial communities in the hypoxic (42 μM) Mauritanian OMZ perform canonical denitrification instead (Dale et al. 2014). The contrast between the Peruvian and Mauritanian OMZ suggests that bottom- water anoxia triggers the appearance of GSOB mats, and that DNRA is more prevalent where GSOB mats are present.

The rapid accumulation and consumption of NO_3^- by GSOB mats has ramifications for the redox conditions in the sediment underneath. The depletion of NO_3^- and shallowing of the nitracline could promote high rates of sulfate reduction in the sediment underneath the GSOB mat. In return, the sulfate reduction zone exists close to the sediment-water interface, providing the GSOB mat with readily accessible sulfide. If a metabolic feedback loop is then established between sulfur-oxidizing bacteria at the sediment-water interface and sulfate-reducing bacteria in the sediment, increased NO_3^- loss from the water column and spreading of sulfidic conditions in SBB sediment is expected. With these mats being potentially crucial to nitrogen and sulfur cycling in sediments underlying OMZs, their biogeochemical transformations and ergo effect upon basin redox conditions are critically important to understanding element cycling in the SBB. Such gained knowledge would have additional benefits for predicting biogeochemical feedbacks to the projected expansion of oceanic oxygen deficiency, in the SBB and in OMZs more general, as a result of global change (Stramma et al. 2008).

Utilizing in-situ technologies, sediment porewater extraction, solid phase analyses, and radiotracer techniques, this study aims to answer the following overarching questions: (1) Which environmental conditions initiate and sustain the proliferation of GSOB mats? (2) Which

biogeochemical transformations occur in the sediment underneath these mats? (3) What role do the mats play in the increasingly prevalent anoxic and nitrate-depleted condition found in the SBB? These investigations represent the first basin-wide geochemical characterization of the Santa Barbara Basin which hosts the largest as-of-yet mapped GSOB mat in the world's oceans. It is the first suite of in-situ flux measurements carried out in the SBB, which is unique to other heavily studied marine settings (e.g., Eastern Gotland Basin, Peruvian upwelling zone) in that it is an oceanic basin within an upwelling zone. The results presented here also provide geochemical context for a number of other related investigations in the SBB (Peng et al. 2023; Robinson et al. 2022; Xuefeng Peng et al. 2023) as well as the first measurements in a multi-year study of biogeochemical changes in response to warming waters and increased stratification on the California coast.

2. Materials and Methods

2.1 Study Site

The Santa Barbara Basin (SBB) is a coastal basin in the California Borderland with an approximate maximum depth of 600 m characterized by a seasonally anoxic water column (Sholkovitz and Gieskes 1971; Sverdrup and Allen 1939). The transform boundary along the California Borderland heavily affects the geomorphology of basins in this region; these basins become twisted as the plates rub against each other and form a series of "bathtubs" blocked by sills and seamounts off the coast of California. The SBB is bordered by the California coast in the north, the Channel Islands in the south, the Santa Monica basin to the southeast, and the Arguello Canyon to the west. A sill to the west of the basin at around 475 m depth (Fig. 1) prohibits most water transfer between the Santa Lucia Slope and the deeper waters of the SBB (Sholkovitz and Gieskes 1971). The highly productive surface waters in the basin provide ample organic matter to the basin's water column, encouraging strong remineralization processes below the euphotic zone, which can induce anoxia below the sill depth, with typically less than 1 μmol O_2 L^{-1} (Emery et al. 1962; Emmer and Thunell 2000; Sholkovitz 1973; Thunell 1998). Benthic faunal distribution within the basin is tightly correlated with this sill depth and related oxygen conditions; below the sill, the sea snail *Alia permodesta* is the most commonly found benthic fauna, while sea stars, sea urchins, and other echinoderms increase in density above the sill (Myhre et al. 2018). During upwelling events (usually in Spring), oxygenated waters from the California Current spill over the western sill and ventilate the SBB, and reportedly increase bottom water oxygen concentrations to approximately 20 μmol O_2 L^{-1} (Goericke et al. 2015). SBB water-column oxygen and nitrogen concentrations have been evaluated through a longitudinal survey by the California Cooperative Oceanic Fisheries Investigations (CalCOFI)

with data starting in the 1950's. The data collected by this survey shows increasing durations of anoxia and fixed nitrogen loss in the basin with the SBB becoming completely nitrate-depleted below the sill at least three times between 2012 and 2017 (https://calcofi.org/data/).

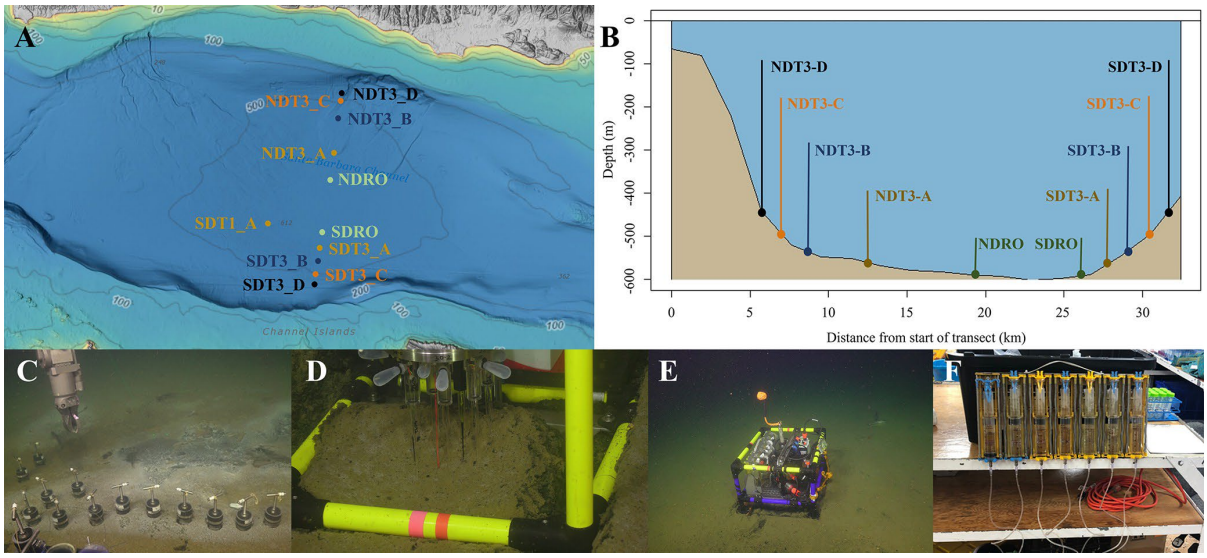

Figure 2-1. Maps of sampling locations in the Santa Barbara Basin and photographs of deployed equipment: **(a)** bathymetric map of the Santa Barbara Basin with locations of all sampled stations; **(b)** cross section of the Santa Barbara Basin with locations of all sampled stations; **(c)** sediment push coring with the ROV arm; **(d)** sediment microprofiler; **(e)** benthic flux chamber; (*F*) a close-up of a syringe system from a benthic flux chamber. The map in panel **(a)** was generated using the Bathymetric Data Viewer provided by the National Centers for Environmental Information.

2.2 Benthic sediment sampling and instrument deployment

Sediment samples were taken between 30 October and 11 November 2019 during an expedition aboard the research vessel *(R/V) Atlantis* equipped with the remote operated vehicle (ROV) Jason. Samples were taken at stations along a bimodal, north-south transect through the depocenter of the SBB, as well as one station on a separate transect. Details of sampling stations can be seen in Fig. 1A and 1B. Briefly, depocenter stations are labeled as NDRO and SDRO (northern and southern depocenter radial origin, respectively). The remaining stations are named

for the cardinal direction (north vs. south) and the transect number (e.g., SDT1-A is on transect 1 while SDT3-A is on transect 3). As station depth decreases, the alpha suffix increases (e.g., NDT3-A is deeper than NDT3-B, etc.).

ROV Jason conducted sediment push coring and deployed automated benthic flux chambers (BFC) and microprofilers at each station. Bottom water oxygen concentration was determined using an Aanderaa 4831 oxygen optode (Aanderaa Instruments, Bergen, Norway) installed on the ROV. Optical modems (Luma 250LP, Hydromea, Renens, Switzerland) installed on the ROV and the BFC and microprofilers were used to transmit deployment settings and start/terminate measurements of the instruments. Multiple push cores (polycarbonate, 30.5 cm length, 6.35 cm inner diameter) per sampling station were retrieved during ROV Jason deployments (Fig. 1C). Replicate cores from each station were transferred to an onboard 6°C cold room upon recovery aboard the ship and subsampled for either solid phase analyses, porewater geochemistry, or radiotracer experiments.

2.3 Sediment Core Sub-Sampling

Two replicate ROV push cores that were collected near each other at each station were processed under a constant argon flow to protect redox-sensitive species. Cores were sectioned in 1-cm increments in the top 10 cm followed by 2-cm increments deeper in the core. Sediments from the NDT3-B station were sliced into 2-cm increments. Sediment subsections were transferred into argon-filled 50-mL conical centrifuge tubes. Sediment samples were centrifuged at 2300 x g for 20 minutes. The centrifugate was subsampled without filtering as fast as possible

for porewater analyses, to avoid contamination with oxygen. Solid phase cores were sectioned similarly to porewater cores and sub-sampled for sediment density, porosity, and organic matter content analyses. A 10 mL cut-off plastic syringe was used to collect 6 mL of sediment into pre-weighed plastic vials (15 mL snap-cap vials) and stored in the dark at 4°C for sediment porosity and density analysis. Two-mL microcentrifuge tubes were filled with sediment from each depth interval and stored at -30°C for sediment organic matter analyses. One ROV push core per station was sub-sampled with a miniaturized push core (length 20 cm, inner diameter 2.6 cm) and taken immediately to the shipboard radioisotope van for radiotracer experiments (see section 2.5).

2.4 Sediment Porewater Geochemistry

Concentrations of porewater sulfide (Cline 1969), NH_4^+, PO_4^{3-}, and Fe^{2+} (Grasshoff et al. 1999) were determined shipboard with a Shimadzu UV-Spectrophotometer (UV-1800). Detection limits for sulfide, NH_4^+, PO_4^{3-}, and Fe^{2+} were 1 µM. Subsamples (2 mL) for porewater NO_3^- and NO_2^- concentrations were stored in 2-mL plastic vials with an O-ring, frozen shipboard at -30°C and analyzed at UCLA on the same spectrophotometer using the method following (García-Robledo et al. 2014). The detection limit for NO_3^- and NO_2^- was 0.5 µM. Samples for porewater DIC analyses were preserved shipboard with 5 µL saturated HgCl in headspace free glass vials and stored at 4°C for later analysis following the procedure of (Hall and Aller 1992). DIC detection limit was 0.1 mM. Total alkalinity was determined shipboard using direct titration of 500 µL of pore water with 0.01M Titrisol® HCl (Pavlova et al. 2008). The analysis was calibrated using IAPSO seawater standard, with a precision and detection limit of 0.05 meq L^{-1}. Subsamples (1 mL) for sulfate and chlorinity analyses were stored in 2-mL plastic vials, kept

gas-tight with an O-ring, frozen shipboard at -30°C. These were later measured in the UCLA lab using a Metrohm 761 ion chromatograph with a methodological detection limit of 30 μM (Dale et al. 2015).

2.5 Solid Phase Analyses

Porosity/Density samples were collected in pre-weighed plastic vials and dried at 50°C for up to 96 hr until the dry weight was stable. Sediment porosity was calculated by taking the difference between wet and dry sediment weight and dividing by the volume of the initial wet sediment aliquot. Sediment density was calculated by dividing the wet sediment weight by its volume. Treatment of sediment subsamples for total organic carbon (TOC), total organic nitrogen (TON), and organic carbon isotope composition ($\delta^{13}C$) were modified from the method of (Harris et al. 2001) and sent to the University of California Davis Stable Isotope Facility for analysis using Elemental Analyzer – Isotope Ratio Mass Spectrometry. TOC and TON were calculated based on the sample peak area corrected against a reference material (alfalfa flour). Limit of quantification based on peak area was 100 μg C with an uncertainty of ± 0.2 ‰ for $\delta^{13}C$.

2.6 Sulfate Reduction

To determine ex-situ microbial sulfate reduction rates, whole round sub-cores were injected with 10 μL carrier-free ^{35}S-Sulfate radiotracer (dissolved in water, 200 kBq, specific activity 37 TBq $mmol^{-1}$) into pre-drilled, silicon-filled holes at 1-cm increments according to (Jørgensen 1978). These sub-cores were incubated at 6°C in the dark for 6-8 hours. Incubations were stopped by slicing sediment cores in 1-cm increments into 50-mL centrifuge tubes filled

with 20-mL zinc acetate (20% w/w) and frozen at -20°C until analysis at the land-based laboratory. Microbial activity in controls was terminated with zinc acetate (20 mL of 20% w/w) before the addition of radiotracer and subsequent freezing. Lab-based analysis of sulfate reduction rates were determined following the cold-chromium distillation procedure (Kallmeyer et al. 2004).

2.7 Benthic In-Situ Investigations

Per station, one to three microprofiler (Fig. 1D) and three BFC (Fig. 1E) deployments were carried out by the ROV Jason at the seafloor. Construction, deployment and operation of automated microprofilers and BFCs followed those described in (Treude et al. 2009). The microprofiler deployed in this study is a modified, miniaturized version of the instrument described in (Gundersen and Jørgensen 1990) that was constructed specifically for use by ROV. Microprofilers were outfitted with three O_2-microelectrodes (Glud et al. 2000), two pH-microelectrodes (Revsbech and Jørgensen 1986), two H_2S-microelectrodes (Jeroschewsky et al. 1996), and one conductivity sensor to determine the position of the sediment-water interface relative to the tips of the microelectrodes. Concentrations of oxygen and sulfide, as well as pH were each calculated from microelectrode readings and averaged for the respective sites where replicates existed.

The BFC consisted of a frame equipped with a cylindrical polycarbonate chamber (inner diameter = 19 cm) with its lower portion sticking out of the frame. The upper side of the chamber was closed by a lid containing a stirrer (Type K/MT 11, K.U.M., Kiel, Germany), oxygen optodes (Type 4330, Aanderaa Data Instruments, Bergen Norway and Hydroflash, Contros/Kongsberg Maritime, Kongsberg, Norway), a conductivity sensor (type 5860, Aanderaa

Data Instruments), and a valve. Prior to insertion into the sediments, the chambers were held upside down by the ROV manipulating arms within approximately 10 m of the seafloor and moved back and forth to make sure that water from shallower depth that may have been trapped was replaced by bottom water. Chamber incubations lasted between 240 and 390 minutes. Each BFC was outfitted with a custom-built syringe sampler containing seven syringes that were connected by tubes to sampling ports in the upper wall of the chambers (Fig. 1F): one injection syringe and six sampling syringes that were fired at regular time intervals over the time course of the deployment. The injection syringe contained de-ionized water and the reduction in salinity in the overlaying water after salinity readings stabilized (i.e., full mixing was achieved) 10-30 min after injection was used to determine BFC volumes (Kononets et al. 2021). Samples obtained from the overlaying water of the BFC were examined for the same geochemical constituents as described above (section 2.4). Benthic fluxes of NO_3^-, NH_4^+, PO_4^{3-}, and Fe^{2+} were calculated as follows:

$$J = \frac{\Delta c}{\Delta t} * \frac{V}{A}$$

[1]

Where J is the flux in mmol m^{-2} d^{-1}, ΔC is the concentration change in mmol m^{-3}, Δt is the time interval in d, V is the overlying water volume in m^3, and A is the surface area of the sediment covered by the benthic flux chamber in m^2. An average flux within BFC's was calculated for stations of similar depth. One chamber per site contained $^{15}N\text{-}NO_3^-$ in the injection syringe for in-situ nitrogen cycling experiments. Results are reported from two of these chambers (SDRO and NDT3-D) and all $^{15}N\text{-}NO_3^-$ chambers were excluded from benthic flux calculations (see next

section).

2.8 In Situ ^{15}N Incubations

Two hundred µmol of ^{15}N-labeled potassium nitrate (99% ^{15}N; Cambridge Isotopes) was injected into the ^{15}N incubation chamber at each site to obtain a final concentration of ~50 – 100 µM ^{15}N-labeled nitrate. Nitrate was amended at this level to prevent its depletion before the last sampling time point (Valentine et al. 2016). Samples for $\delta^{15}N$ analysis were preserved by filling a pre-evacuated 12-ml exetainer vial with 0.1 ml 7M zinc chloride as a preservative. Another aliquot (~12 ml) of seawater for ammonium isotope analysis was filtered through 0.2 µm syringe filters and stored frozen. Prior to analyzing the samples in 12-ml exetainer vials, 5 mL of sample was replaced with ultra-high purity helium to create a headspace. The concentration and $\delta^{15}N$ of dissolved N_2 and N_2O was determined using a Sercon CryoPrep gas concentration system interfaced to a Sercon 20-20 isotope-ratio mass spectrometer (IRMS) at the University of California Davis Stable Isotope Facility.

2.9 Ammonium Isotope Analyses

The production of $^{15}NH_4^+$ in seawater samples was measured using a method adapted from Zhang et al. (2007) and described previously by (Peng et al. 2016). In brief, NH_4^+ was first oxidized to NO_2^- using hypobromite (BrO^-) and then reduced to N_2O using an acetic acid-azide working solution (Zhang et al. 2007). The $\delta^{15}N$ of the produced N_2O was determined using an Elementar Americas PrecisION continuous flow, multicollector, isotope-ratio mass spectrometer coupled to an automated gas extraction system as described in (Charoenpong et al. 2014). Calibration and correction were performed as described in (Bourbonnais et al. 2017). The measurement precision was ±0.2 ‰ for $\delta^{15}N$. Depending on the in-situ ammonium

concentration, the detection limit for total NH_4^+ production rates ranged between 0.006 and 0.0685 mmol m^{-2} d^{-1}.

Table 2-1. Station details and photos of representative ROV push cores taken at each station. Mat presence (Y: yes; N: no) was determined vi- sually. Station water depth and oxygen concentration were determined by sensors attached to ROV *Jason* (bdl: below detection limit, < 3 µM O_2). Anoxia was confirmed by additional methods (see discussion in Sect. 4.1). Latitude and longitude were determined by triangulation be- tween the ROV and the ship. Bottom-water nitrate concentration was derived from an average of benthic flux chamber nitrate measurements at time 0 for each station (chambers with no calculable flux and ^{15}N-nitrate addition excluded). Note that benthic flux chambers were not deployed at SDT1-A. Photographs show the sediment–water interface (SWI; top part) and each sediment core in full length (lower part).

Parameter	NDT3-D	NDT3-C	NDT3-B	NDT3-A	NDRO	SDRO	SDT1-A	SDT3-A	SDT3-B	SDT3-C	SDT3-D
Mat Present	N	N	N	Y	Y	Y	Y	Y	N	N	N
Depth (m)	447	498	537	572	580	586	573	571	536	494	447
Latitude (°)	34.363	34.353	34.333	34.292	34.262	34.201	34.212	34.184	34.168	34.152	34.142
Longitude (°)	-120.015	-120.016	-120.019	-120.026	-120.031	-120.044	-120.116	-120.047	-120.053	-120.050	-120.052
Oxygen (µM)	8.7	5.2	12.2	9.2	0.0	0.0	0.0	0.0	1.8	3.1	9.6
Nitrate (µM)	27.3	26.0	11.5	24.4	18.5	9.9		20.4	20.6	16.3	28.0

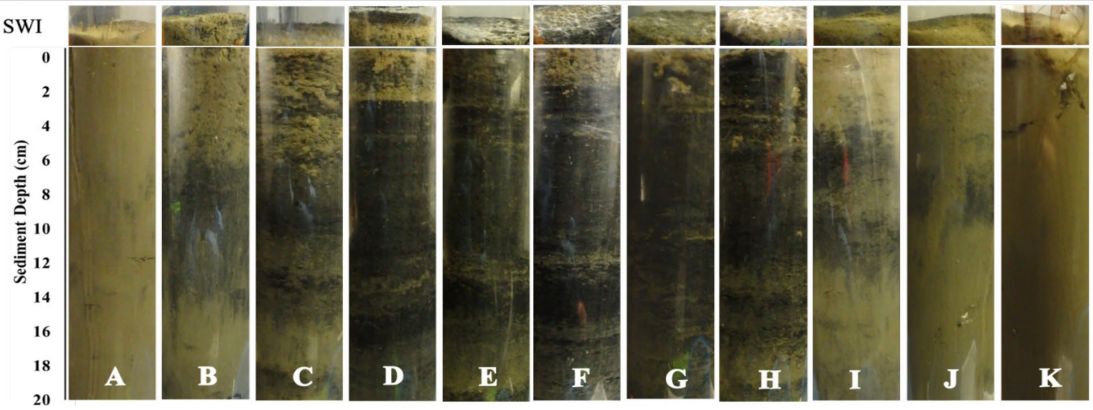

3. Results

3.1 Bottom water conditions

O_2 and NO_3^- concentrations in the bottom water along the transects can be seen in Table 1. O_2 concentrations below detection as determined by the ROV sensor could in some cases be considered to represent anoxia (0 µM O_2) based on a set of different analytical methods (see discussion section 4.1). Bottom water solute concentrations (as defined by the average T_0 concentration in BFC at each site) can be seen in Appendix A, Figs. 1-4. Bottom water NO_3^-

concentrations roughly decreased with increasing station depth (e.g., 28 μM at NDT3-D vs. 19 μM at NDRO). Bottom water NO_2^- concentrations were below detection at all stations. Bottom water NH_4^+ concentrations were 9 μM at NDRO and 13 μM at SDRO and below detection in shallower stations. Bottom water PO_4^{3-} concentrations roughly increased with increasing basin depth (e.g., 2 μM at SDT3-D vs. 7 μM at SDRO). Finally, Fe^{2+} was 2 and 5 μM at the NDRO and SDRO stations, respectively and below detection at all shallower stations.

3.2 Sediment characteristics

Photographs of sediment cores with a depth scale are shown below Table 1. Sediment colors were classified according to Hossain et al. (2014). Cores from the shallowest (D) stations were uniformly reddish in color with small pockets of black. The sediment color changed with station depth, transitioning from a reddish color in the shallowest stations to predominantly black with reddish laminations at the depocenter stations. The band of black sediment appeared at approx. 8 cm sediment depth in the C-station cores and became progressively more ubiquitous with station depth. Notably, NDT3-C sediment (Table 1B) contained black bands from approx. 6-14 cm sediment depth, while SDT3-C sediment (Table 1J) had a much narrower band around 8-10 cm. Sediment cores from shallower stations (D and C stations) contained signs of bioturbation (e.g., u-shaped burrows) and, in some cases, contained visible macrofauna, such as polychaetas and mollusks. Deeper in the basin (A and depocenter stations) no signs of bioturbation were detected, and the sediment-water interface was colonized by patches of white GSOB mats. Spherical cells (given the moniker ‘ghost balls’) were found mixed amongst giant sulfur bacteria filaments within the top 0-1 cm of sediment at NDRO (Appendix A, Fig. 7). These unknown organisms had similar morphological characteristics to the species

Thiomargarita namibiensis (Schulz et al. 1999; Schulz and Schulz 2005) containing a translucent cell with sulfur granules giving them a ghostly white appearance. A small sample of cells (n = 8) were measured, featuring diameters between 48.0 and 99.6 µm, amounting to an average biovolume of 2.5 x 10^5 μm^3, compared to *T. namibiensis* with a cell diameter usually between 100-300 µm (Schulz et al. 1999). B station cores contained sporadic GSOB filaments slightly deeper in the sediment (approx. 2-4 cm sediment depth). Sediment solid phase parameters (averaged over the entire sediment core depth) can be seen in Table 2. Average sediment porosity increased with basin depth (e.g., from 0.79 at NDT3-D to 0.88 at NDRO). TOC, TON, the C/N ratio, and the $\delta^{13}C$ isotopic signature of organic carbon remained relatively constant (2.5 – 4.5%, 0.1 – 0.4%, 8.0 – 8.7 and 21.3 – 22.4 ‰, respectively) over all stations.

3.3 Sediment porewater geochemistry

Total alkalinity (Figs. 2 A-E & 3 A-F) increased steadily with sediment depth at all stations starting with, on average, 2.4 mM in the core supernatant reaching a maximum at the respective deepest sediment sample (20 cm). Porewater alkalinity and DIC also increased with basin depth (Figs. 2 A-E & 3 A-F) indicating that total alkalinity was dominated by the carbonate system. Porewater DIC was, on average, 2.2 mM in the core supernatant and reached maximum concentrations at the deepest sediment depth (20 cm) at most stations.

Porewater PO_4^{3-} profiles (Figs. 2 A-E & 3 A-F) were markedly different between the depocenter and shallower C and D stations. Porewater PO_4^{3-} concentrations in the depocenter and A stations generally increased with sediment depth but several profiles (NDT3-C, NDT3-A, SDRO, SDT1-A) remained unchanged or decreased deeper in the sediment (starting at approx. 10 cm). The profiles in C and D stations showed a peak in PO_4^{3-} concentrations near the

sediment-water interface, particularly in the northern basin. Below 2 cm, PO_4^{3-} decreased with sediment depth, but sometimes showed a second small peak deeper in the sediment (12-14 cm at NDT3-D and 10-12 cm at SDT3-D).

Porewater NH_4^+ concentrations (Figs 2 & 3 A-E) showed trends often similar to alkalinity and DIC; NH_4^+ concentrations increased downcore and were higher at depocenter than at D stations (e.g., 370 and 91 μM at 20 cm for SDRO and SDT3-D, respectively). Porewater NO_2^- (Appendix A, Table 1) and NO_3^- (Figs. 2 F-J & F G-L) concentrations were at or near zero below 2 cm at every station, except at SDRO and NDT3-A where large peaks in NO_3^- (376 and 81 μM, respectively) and NO_2^- (37 and 5 μM, respectively) occurred in the top 1 cm.

Porewater Fe^{2+} concentrations (Figs. 2 F-J & 3 G-L) were several orders of magnitude higher at shallower D-stations (max. 722 and 395 μM at NDT3-D and SDT3-D, respectively) compared to depocenter stations (max. 13 and 51 μM at NDRO and SDRO, respectively). NDT3-C porewater Fe^{2+} concentration (Fig. 2G) peaked in the top 1 cm of sediment (similar to deeper stations) while SDT3-C porewater Fe^{2+} concentration (Fig. 3H) peaked around 5-cm sediment depth. Fe^{2+} concentrations reached a max. at 0-2 cm and declined sharply with depth in depocenter and A-station sediment. Northern basin sediment was similar, but the decline in Fe^{2+} below 0-2 cm was less pronounced.

Maximum porewater sulfide concentrations (Figs. 2 F-J & 3 G-L) were 1-2 orders of magnitude lower at the shallower D-stations (5 and 4 μM at NDT3-D and SDT3-D, respectively) compared to A stations (350 and 148 μM at NDT3-A and SDT1-A, respectively). Unlike Fe^{2+}, peaks in sulfide concentration occurred deeper in the sediment (e.g., below 5 cm depth at A stations). Porewater sulfate concentrations (Figs. 2 K-O & 3 M-R) decreased slightly with depth, but never reached values below 20 mM at any station.

3.4 In-situ microprofiling

Microprofiler O_2 and sulfide measurements are shown in Fig. 4. Oxygen was rapidly consumed within the first 0-1 cm of sediment at every station where O_2 was detected in the bottom water (i.e., at all stations except NDRO, which showed no positive signal of oxygen in the water compared to the sediment; note that no oxygen profile is available for SDRO). Sulfide concentrations from microsensors showed similar trends to spectrophotometric measurements, albeit with different absolute values (below detection in shallower B-, C- and D-stations that lacked mats and >1,000 μM at A- and depocenter stations). Microprofiler pH (Fig. 4) was near 7.5 in the bottom water at all stations, and slowly decreased to near 7.0 in the lower parts (3-5 cm) sediment at most stations except NDT3-C and SDT3-B. pH at 2.5 cm at SDT3-B reached 6.77, which was the lowest observed during this expedition.

3.5 In-situ fluxes of benthic solutes

NO_3^-, NH_4^+, PO_4^{3-}, and Fe^{2+} flux measured in the BFC revealed different patterns of uptake and release from the sediment throughout the basin (Fig. 5 and Appendix A, Figs. 1-4). BFC O_2 concentrations were compromised by O_2 release from the chamber's polycarbonate walls, which prevented an accurate calculation of O_2 fluxes from BFC sensor data. NO_3^- was consumed at all stations as indicated by a negative flux (i.e., a flux into the sediment). On the contrary, benthic release (i.e., a flux out of the sediment) was observed for all other analyzed solutes (NH_4^+, PO_4^{3-}, and Fe^{2+}), with the lowest fluxes in the shallow D and C-stations and highest fluxes in the depocenter. Ammonium fluxes were the highest of all the determined solutes and showed the largest difference between deep and shallow stations, with a flux of 1.6

mmol m^{-2} d^{-1} at NDT3-C (there were no measurable NH_4^+ fluxes in D-station chambers) and reaching 11.1 ± 3.1 mmol m^{-2} d^{-1} (n = 3) at the two depocenter stations. The depocenter ammonium flux far-outpaced the concomitant flux of nitrate into depocenter sediments (-3.2 ± 0.7 mmol m^{-2} d^{-1}, n = 3). Iron and phosphate fluxes were similar at depocenter stations (4.1 ± 0.7, n = 3, and 3.2 ± 0.7, n = 3, mmol m^{-2} d^{-1}, respectively). Alkalinity and DIC concentrations from flux chambers (Appendix A, Figs. 5 and 6) remained constant at all stations and thus no DIC flux was calculated. Results from BFCs injected with ^{15}N-NO_3^- at the SDRO and NDT3-D station are shown in Fig. 6. The rates of denitrification, anammox, and N_2O production were higher at SDRO compared to NDT3-D. $^{15}NH_4^+$ production (DNRA) was one order of magnitude higher at the SDRO station (2.67 mmol m^{-2} d^{-1}) compared to the NDT3-D station (0.14 mmol m^{-2} d^{-1}). DNRA accounted for a much higher percentage of NO_3^- reduction at SDRO (54.1%) than NDT3-D (13.3%).

Table 2-2. Sediment solid-phase data: porosity, density, total organic carbon (TOC), total organic nitrogen (TON), C : N ratio, and δ13C. All data were averaged for the top 0–19 cm of sediment except for NDT3-C (17 cm), NDT3-A (11 cm), and SDRO (7 cm), where the core length was shorter. The integrated sulfate reduction rate (SRR) values were integrated over a 0–14 cm sediment depth. No sulfate reduction rates

Station	Porosity	Density	TOC (%)	TON (%)	C : N ratio	$\delta^{13}C$ (‰)	Integrated SRR (mmol m^{-2} d^{-2})
NDT3-D	0.79 ± 0.03	1.21 ± 0.07	2.9 ± 0.5	0.3 ± 0.1	8.9 ± 0.2	−22.4 ± 0.3	2.9
NDT3-C	0.81 ± 0.04	1.16 ± 0.08	2.5 ± 0.5	0.5 ± 0.1	8.7 ± 0.5	−22.4 ± 0.4	3.8
NDT3-B	0.86 ± 0.04	1.06 ± 0.08	3.6 ± 0.5	0.4 ± 0.1	8.5 ± 0.5	−22.2 ± 0.4	
NDT3-A	0.88 ± 0.03	1.05 ± 0.04	3.1 ± 0.4	0.4 ± 0.1	8.2 ± 0.2	−22.1 ± 0.2	2.7
NDRO	0.88 ± 0.04	1.06 ± 0.03	3.3 ± 0.4	0.4 ± 0.0	8.2 ± 0.4	−22.1 ± 0.2	4.1
SDRO	0.87 ± 0.03	1.04 ± 0.03	3.5 ± 0.4	0.4 ± 0.1	8.0 ± 0.2	−22.0 ± 0.3	
SDT1-A	0.88 ± 0.03	1.11 ± 0.23	4.5 ± 0.5	1.0 ± 0.1	8.6 ± 0.8	−21.3 ± 0.7	2.9
SDT3-A	0.86 ± 0.04	1.05 ± 0.05	3.2 ± 0.0	0.4 ± 0.0	8.3 ± 0.6	−22.1 ± 0.4	
SDT3-B	0.85 ± 0.04	1.12 ± 0.06	3.6 ± 0.6	0.4 ± 0.1	8.3 ± 0.3	−22.0 ± 0.2	
SDT3-C	0.82 ± 0.04	1.22 ± 0.05	3.6 ± 0.8	0.4 ± 0.1	8.7 ± 0.3	−21.9 ± 0.2	1.7
SDT3-D	0.78 ± 0.04	1.22 ± 0.03	3.3 ± 0.5	0.4 ± 0.1	8.5 ± 0.2	−22.0 ± 0.1	1.9

3.6 Sulfate reduction rates

Vertical profiles of bacterial sulfate reduction as determined by the radioisotope

technique differed throughout the basin (Figs. 2 & 3). Peaks in sulfate reduction were seen in the top 0-1 cm of sediment at stations with a visible GSOB mat on the surface (120.2, 151.0, and 85.3 nmol cm^{-3} d^{-1} at NDRO, SDT1-A, and NDT3-A, respectively). Sediments at most shallower basin depths exhibited peaks slightly deeper in the sediment and of lower magnitude (25.5, 44.5, 22.5 nmol cm^{-3} d^{-1} at SDT3-C, NDT3-D, and SDT3-D respectively). NDT3-C had no visible GSOB mats but exhibited a peak (133.7 nmol cm^{-3} d^{-1}) in sulfate reduction at 0-1 cm depth, similar to deeper stations (e.g., NDRO in Fig. 2O), which differed from other shallow stations (e.g., SDT3-C in Fig. 3N). The integrated sulfate reduction rate (0-14 cm depth) at NDRO (4.1 mmol m^{-2} d^{-1}) was noticeably higher than most other stations with the exception of NDT3-C (3.8 mmol m^{-2} d^{-1}) (Table 2). NDT3-D and NDT3-C exhibited higher integrated rates (2.9 and 3.8 mmol m^{-2} d^{-1}) than their southern station counterparts SDT3-D and SDT3-C (1.9 and 1.7 mmol m^{-2} d^{-1})

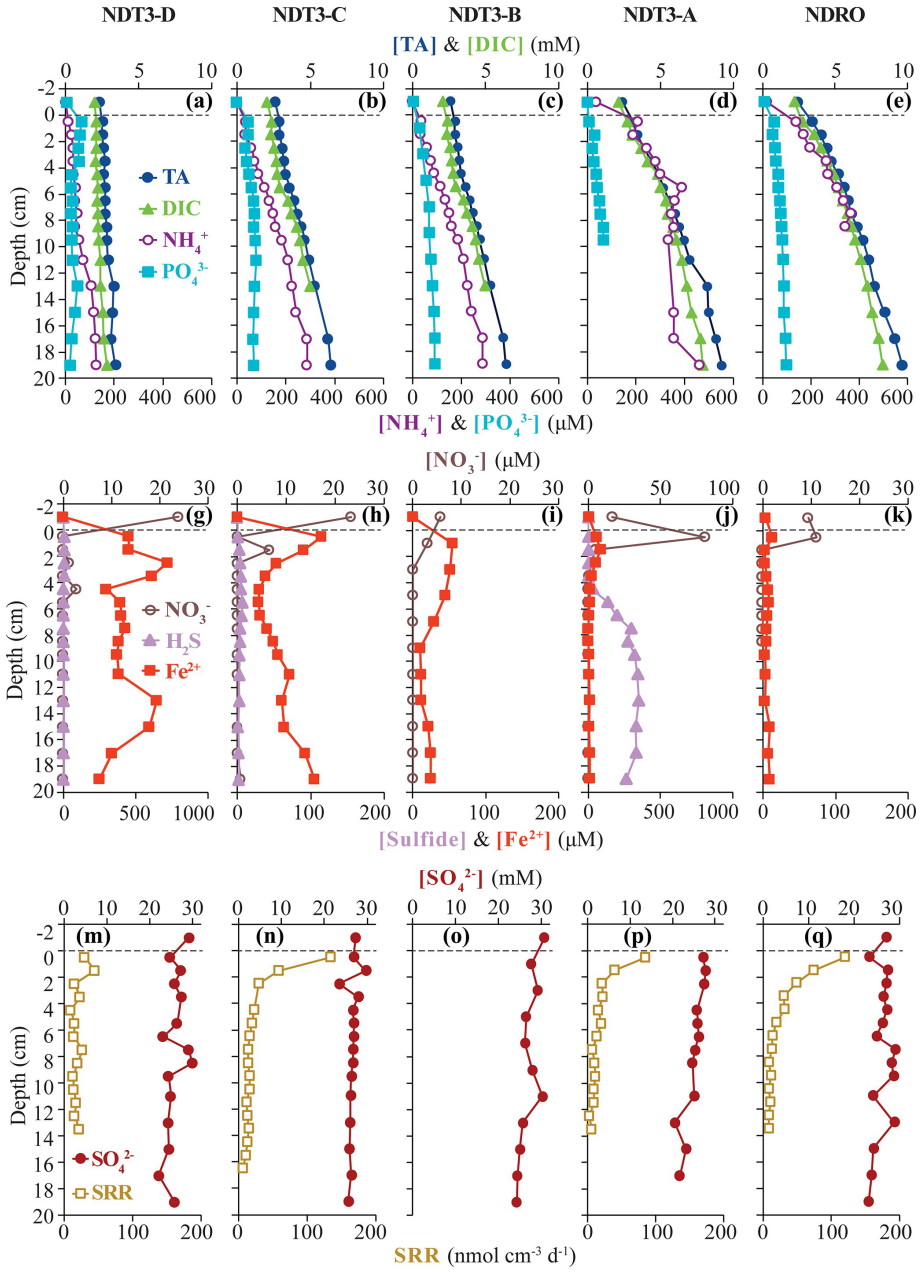

Figure 2-2. Biogeochemical data from ROV sediment push cores collected at stations on the northern transect (NDT3) and in the northern depocenter (NDRO): total alkalinity (TA), dissolved inorganic carbon (DIC), ammonium (NH_4^+), phosphate (PO_4^{3-}) in the first row; nitrate (NO_3^-), total sulfide (sulfide), and iron (II) (Fe^{2+}) in the second row; sulfate (SO_4^{2-}) and bacterial sulfate reduction rate (SRR) in the third row. Data analyzed from sediment core supernatant are plotted at -1 cm sediment depth; the dotted line connotes the sediment-water interface. Note the change in scale on the primary x-axis in panel I and the change in scale of the secondary x-axis in panels F and I. No spectrophotometric sulfide data is available for NDRO and NDT3-B and no SRR data is available for NDT3-B. For station details see Fig. 1 and Table 1.

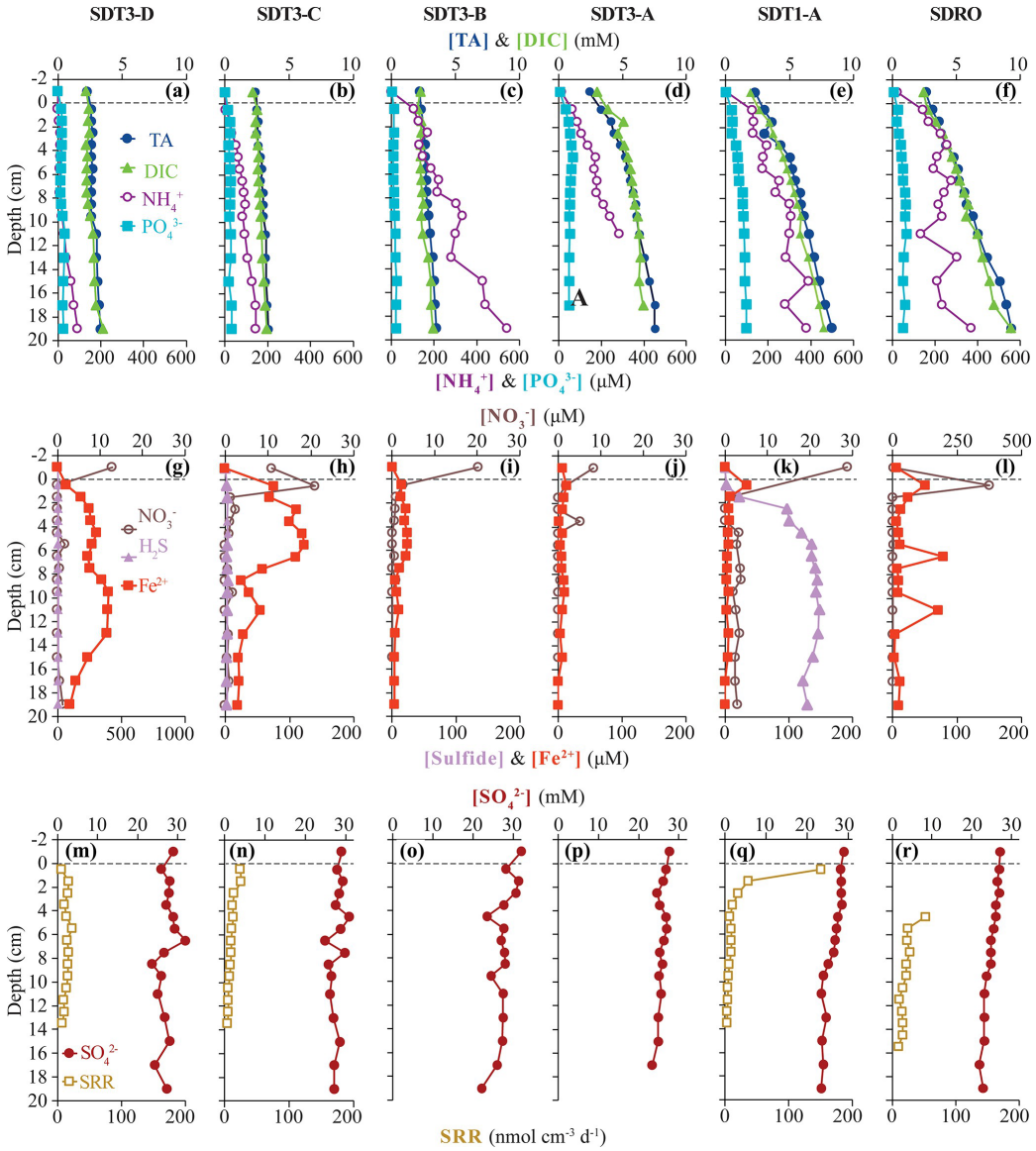

Figure 2-3. Biogeochemical data from ROV sediment push cores collected at stations on the two southern transects (SDT1 and SDT3) and the southern depocenter (SDRO): total alkalinity (TA), dissolved inorganic carbon (DIC), ammonium (NH_4^+), phosphate (PO_4^{3-}) in the first row; nitrate (NO_3^-), total sulfide (sulfide), and iron (II) (Fe^{2+}) in the second row; sulfate (SO_4^{2-}) and bacterial sulfate reduction rate (SRR) in the third row. Data analyzed from sediment core supernatant are plotted at -1 cm sediment depth; the dotted line connotes the sediment-water interface. Note the change in scale on the primary x-axis in panel L and the change in scale of the secondary x-axis in panel G. No sulfide nor SRR data are available for SDT3-B and -A; spectrophotometric sulfide and the top 0-4 cm of SRR data are not available for SDRO. For station details see Fig. 1 and Table 1.

4. Discussion

4.1 Giant sulfur-oxidizing bacterial mats proliferated in response to deoxygenation in the Santa Barbara Basin

The SBB is an ideal environment to study the effect of transient deoxygenation on benthic biogeochemistry. In Fall 2019, when this expedition took place, the SBB was undergoing a transition from oxygenated to virtually anoxic conditions (Qin et al. 2022). When the AT42-19 cruise occurred, most of the bottom water in the basin was hypoxic (A-, B-, C-, and D-stations), except for the depositional center. Separate O_2 measurements from the ROV sensor (O_2 below detection limit, Table 1), microprofilers (no signal change between water column and sediment, Fig. 4), and Winkler titration from CTD/rosette casts (uniform non-zero value below 500 m (Qin et al. 2022)) indicated full anoxia in the bottom water at the deeper stations (NDRO and SDRO). Notably, bottom water conditions revealed a slight asymmetry between the basin transects (Fig. 1); bottom water along the northern transect generally had more O_2 and NO_3^- than the southern transect (e.g., 9 μM O_2 at NDT3-A and 0 μM O_2 at SDT3-A). This asymmetry indicated differences in the circulation and/or microbial communities between the northern and southern portions of the basin. Whether this asymmetry is a permanent feature of the basin or symptomatic of the specific conditions in November 2019 is unclear; previous studies in the SBB have been restricted to the depocenter or one side of the basin (Kuwabara et al. 1999; Reimers et al. 1996a; Sholkovitz 1973). Regardless of bottom water oxidant concentration, the energetically most favorable terminal electron acceptors (O_2 and NO_3^-) disappeared in a very narrow zone below the sediment-water interface (Fig. 4 and Figs. 2 and 3, respectively), consistent with their expected rapid consumption by the benthic microbial community.

In the present study, benthic GSOB mats were primarily limited to the anoxic depocenter of the SBB. Similarly, such mats were replete in the core of the anoxic Peruvian OMZ (Levin et al. 2002; Mosch et al. 2012; Sommer et al. 2016), but absent from the seafloor below the hypoxic, i.e., slightly oxygenated, Mauritanian OMZ (Schroller-Lomnitz et al. 2019). GSOB mats in November 2019 were observed deeper in the basin than in October 2013 (Valentine et al. 2016) but in a similar location to June 1988 (Reimers et al. 1996a) and April 1997 (Kuwabara et al. 1999). During the 2013 sampling, dense GSOB mats were confined to depths between approx. 500-570 m (equivalent to the B-stations from this expedition), corresponding with anoxic conditions in the bottom water. This habitat was sandwiched between an anoxic, anitric (i.e., nitrate-free) deep and a hypoxic, nitrigenated (i.e., nitrate-rich) shallower water layer (Valentine et al. 2016). The difference in depth distribution of GSOB mats between the 2013 and 2019 expedition provides evidence that GSOB mats in the SBB are ephemeral and proliferate where the bottom water is anoxic but not anitric.

As our study represents only a snapshot of an oxygen- and nitrate-driven mat dynamic, we can only speculate how areas of the basin that did not contain GSOB mats in November 2019 fit into this dynamic. For example, mat-forming sulfur bacteria found slightly deeper in the sediment at B-stations (see section 3.2) could be progenitors to surface sediment colonization of thick GSOB mats, as has been recorded in other transiently deoxygenated environments (Jørgensen 1977). Alternatively, these subsurface colonies could also be remnants of a former surface GSOB mat that retreated under changing redox conditions. Oxygenated conditions in the water preceding the 2019 expedition would, in this context, suggest the mats migrated following a previous anoxic event (Qin et al. 2022). If deoxygenation persisted in the SBB after the AT42-19 cruise, then anitria (i.e., anitric conditions – similar to anoxia) would likely follow in the

deepest basin water. These conditions would be similar to those seen in 2013 (Valentine et al. 2016), where GSOB mats formed a contiguous "donut ring" at shallower basin depths. Interestingly, GSOB mats in the Eastern Gotland Basin of the Baltic Sea were confined to a hypoxic transition zone, where O_2 was < 30 µM but did not reach anoxia, while no mats were observed at deeper anoxic locations (Noffke et al. 2016). This difference in distribution compared to the SBB suggests that GSOB mats proliferate under different conditions (anoxic or hypoxic), potentially depending on the species of mat-forming bacteria present and whether they specialize in aerobic or anaerobic chemosynthesis.

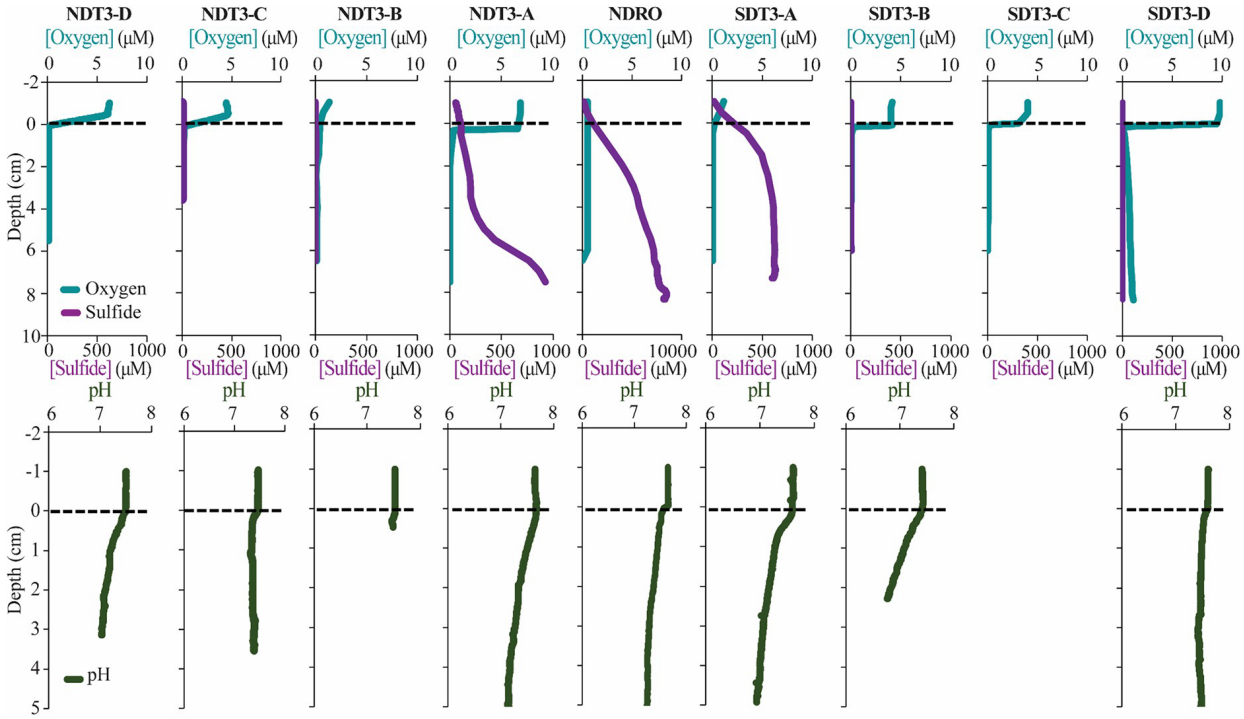

Figure 2-4. In-situ sediment microprofiler results for all stations (except SDT1-A and SDRO): oxygen (O_2) and total sulfide (sulfide) concentration in the first row; pH profiles in the second row. Note the change in scale on the secondary x-axis for NDRO sulfide. Values determined in the overlying water are plotted at negative sediment depths; the dotted line connotes the sediment-water interface.

4.2 Shift from benthic denitrification to dissimilatory nitrate reduction to ammonium in response to complete deoxygenation in the Santa Barbara Basin

Benthic uptake and release of nitrogen species by SBB sediment appeared to be affected by the presence of GSOB mats. While total benthic nitrate uptake was similar between D- and depocenter stations based on in-situ NO_3^- flux measurements (Fig. 4), NH_4^+ release from the sediment into the water column increased where GSOB mats were present (Fig. 5). This trend is supported by the porewater profiles of NH_4^+, which showed a steeper increase over sediment depth at deeper stations (Figs. 2 & 3). Incubations with $^{15}N\text{-}NO_3^-$ revealed that N_2 production (denitrification and anammox) accounted for 86% of NO_3^-/NO_2^- reduction in the shallow basin, while NH_4^+ production (DNRA) accounted for 13% and N_2O production accounted for 1% (NDT3-D, Fig. 6;(Peng et al. 2023)). In contrast, most (54%) of NO_3^- reduction at the depositional center occurred via DNRA; N_2 production accounted for 45% and N_2O production accounted for 1% of NO_3^- reduction at the SDRO (Fig. 6; Peng et al. 2023). It is important to note that these results only describe patterns of NO_3^- reduction in the basin, while other mechanisms of nitrate uptake by sediment (e.g., hyper-accumulation of nitrate into vacuoles) are more difficult to calculate accurately.

It is likely important to SBB benthic nitrogen cycling that some eukaryotic organisms can hyper-accumulate NO_3^- in benthic, anoxic environments including diatoms (Kamp et al. 2011) and foraminifera (Risgaard-Petersen et al. 2006). Additionally, meiofauna (e.g., nematodes) can enhance rates of denitrification (Bonaglia et al. 2014). Both foraminifera and meiofauna were observed in SBB depocenter and A-station sediments in November 2019, and diatoms were observed in shallower sediments in the basin (data not shown). Other studies found that benthic

foraminifera in the SBB depocenter can hyperaccumulate NO_3^- intracellularly up to 375 ± 174 mM (Bernhard et al. 2012) and host symbionts capable of performing denitrification (Bernhard et al. 2000). These foraminifera were found to be responsible for approx. 3 mM N m^{-2} d^{-1}, or 67% of the total denitrification occurring in the SBB depocenter (Bernhard et al. 2012). Additionally, fungi could reduce NO_3^- or NO_2^- to nitrous oxide in marine sediments and may contribute to denitrification in SBB sediments (Kamp et al. 2015; Lazo-Murphy et al. 2022). This opens up the possibility that the majority of denitrification we observed in the SBB depocenter is performed by eukaryotes, while prokaryotes (especially GSOB) are responsible for most of the DNRA. Elevated NO_3^- and NO_2^- concentrations that were observed in our 0-1 cm samples from NDT3-A and SDRO have been reported from SBB depocenter sediments in the past (Bernhard et al. 2003; Reimers et al. 1996a), and have been attributed to both GSOB and benthic eukaryotes. The impact of eukaryotes on SBB benthic nitrogen transformation remains to be disentangled from the mats themselves.

Our data suggests a transition from denitrification-dominated sediment in the oxygenated basin to an increasing influence of DNRA on N cycling in the deeper, anoxic basin. Placed in the context of other OMZs, Mauritanian shelf sediment was dominated by denitrification (Dale et al. 2014), similar to SBB shallow sediment (below hypoxic water) while core Peruvian OMZ sediment was dominated by DNRA, similar to sediment of the deeper SBB (below anoxic water) (Sommer et al. 2016). Nitrate reduction in sediment below the seasonally hypoxic Eckernförde Bay (Dale et al. 2011) and below the hypoxic transition zone of the Eastern Gotland Basin (Noffke et al. 2016) also showed increased DNRA where GSOB mats were present, though with an order of magnitude lower NH_4^+ flux (avg. 1.74 mmol m^{-2} d^{-1} and max. 1.10 mmol m^{-2} d^{-1}, respectively) than the SBB depocenter.

While our study suggests a shift from denitrification to DNRA during deoxygenation of SBB bottom water, other studies examined changes in benthic nitrogen cycling under reverse conditions, i.e., the reoxidation of the environment following anoxia (De Brabandere et al. 2015; Hylén et al. 2022). After a decadal oxygenation event in the Eastern Gotland Basin (Baltic Sea) in 2015-2016, sediment exhibited a slight increase in denitrification, but remained dominated by DNRA and N_2O production (Hylén et al. 2022). The lack of N_2 production via denitrification following this oxygenation event was attributed to the reoxygenation event being too weak to substantially oxidize sediments, which would favor denitrification (Hylén et al. 2022). In an engineered reoxygenation event of the By Fjord on Sweden's western coast, where dissolved O_2 and NO_3^- content of anoxic and anitric bottom water was artificially increased to approx. 130 μM O_2 and 20 μM NO_3^- over a period of roughly 2 years, denitrification rates were increased by an order of magnitude and DNRA rates were also stimulated (De Brabandere et al. 2015). Comparing our results to these two studies suggests that DNRA bacteria are more resilient to weak reoxygenation events and thrive in transiently deoxygenated systems that remain hypoxic ($O_2 < 63$ μM). The frequency and magnitude of reoxygenation and deoxygenation of SBB bottom waters, and the effect of these processes on the benthic microbial community, could be a major factor supporting some of the highest recorded total nitrate reduction rates in a natural benthic marine setting (Peng et al. 2023).

A high ratio of electron donor to electron acceptor favors DNRA over denitrification (Hardison et al. 2015; Marchant et al. 2014; Tiedje et al. 1983) and this ratio appears to be critical in determining the dominant nitrate reduction pathway in SBB sediments, similar to the Eastern Gotland Basin (Hylén et al. 2022) and the By Fjord (De Brabandere et al. 2015). Example energy yields for denitrification and DNRA are shown in Table 3. As discussed in

(Tiedje et al. 1983), heterotrophic denitrification yields more energy per mol of electron donor than DNRA. However, the reverse is true when considering energy yield per mol of electron acceptor (NO_3^-). DNRA also yields 3 more electrons per molecule of NO_3^- than denitrification. Tiedje et al. argued that in environments that are starved of powerful terminal electron acceptors, such as anoxic, organic-rich sediment, the energy yield per electron acceptor and additional electrons available for transfer could push nitrate reduction towards DNRA. Multiple laboratory and model studies have converged on an electron donor to acceptor ratio of approximately 3 to encourage DNRA over denitrification (Algar and Vallino 2014; Hardison et al. 2015) though other studies have found higher values (Kraft et al. 2014; Porubsky et al. 2009). Sulfide concentrations near the sediment-water interface at the SBB depocenter (approx. 200 μM at 0.5 cm depth; Fig. 3, NDRO) would favor chemoautotrophic DNRA over denitrification at ambient marine nitrate concentrations (approx. 28 μM). Additionally, DNRA appears to be the preferred nitrate reduction pathway for chemoautotrophs that utilize iron or sulfide as an electron donor (An and Gardner 2002; Caffrey et al. 2019; Kessler et al. 2019). As GSOB mats hyper-accumulate nitrate from the bottom water into their intracellular vacuoles, the resulting decline in electron acceptors at the sediment-water interface coupled with an elevation of the sulfate reduction zone would create an electron donor to acceptor ratio that favors DNRA. Since GSOB mats in the SBB seem to prefer DNRA, starving the bottom water of electron acceptors coupled with the high sulfate reduction rates could give them a competitive advantage and allow them to proliferate into the largest-yet mapped GSOB mat in Earth's oceans, as seen in other expeditions (Kuwabara et al. 1999; Reimers et al. 1996a; Valentine et al. 2016).

4.3 Microbial mat proliferation and benthic phosphate remineralization dependent on high

rates of organic matter degradation in the Santa Barbara Basin

Organic carbon content of the benthic environment appears to be a key control on sulfate reduction rates near the sediment-water interface as well as microbial mat proliferation. Sulfate reduction rates in the SBB depocenter are most similar in magnitude and profile (i.e., highest rates found at the sediment-water interface and decline drastically thereafter) to those found in sediments below the transiently deoxygenated portion of the Peruvian shelf (e.g., 4.1 mmol m^{-2} d^{-1} at the SBB NDRO station vs. 2.5-3.8 mmol m^{-2} d^{-1} at 128-144 m water depth on the Peruvian margin (Gier et al. 2016; Treude et al. 2021)). The TOC content of surface sediments in these two regions are both high and within the same order of magnitude (maximum recorded TOC of 5.2% at the 0-1 cm margin at the SDT1-A station compared with 7.6% in the Peruvian margin 145 m depth (Noffke et al. 2012)). In comparison, sulfate reduction rates in the SBB were at least one order of magnitude lower than found in sediment below the OMZ on the Namibian Shelf, which has much higher TOC contents of >10% (Bremner 1981; Brüchert et al. 2003). Sulfate reduction rates in the shelf sediments below the Eastern Arabian OMZ were much lower (0.18 – 1.27 mmol m^{-2} d^{-1}) than rates in the SBB depocenter (Naik et al. 2017) despite similar hypoxic to anoxic bottom water conditions. These lower sulfate reduction rates were attributed to the relatively low amount of pelagic primary productivity and ergo benthic organic matter delivery in the Eastern Arabian OMZ compared to other upwelling systems (Naik et al. 2017). The organic matter content of the sediment appears to be important in the proliferation of GSOB mats; too much TOC could result in toxic levels of sulfide at the sediment-water interface (*Beggiatoa* exhibit an aversion to sulfidic sediments but toxicity has not been quantified) (Preisler et al. 2007), whereas too little sulfide would not provide enough electron donor for the GSOB's chemoautotrophic metabolism.

The profiles of several indicators for benthic anaerobic organic matter remineralization (total alkalinity, DIC, PO_4^{3-}, NH_4^+) increased in steepness with increasing water depth (Figs. 2 A-E & 3A-F). One divergence from this trend can be seen in PO_4^{3-} profiles from the shallow C- and D-stations, which also featured low rates of sulfate reduction. PO_4^{3-} profiles in these sediments track closely to Fe^{2+} profiles; both solutes dip in concentration in areas with visible iron sulfide formation (e.g., 5-11 cm in NDT3-D as seen in Fig. 2A). Additionally, several stations that exhibited high sulfate reduction rates in surface sediment (e.g., SDT1-A) showed almost no change in PO_4^{3-} at depths below 5 cm (e.g., Fig. 2 K-O compared to Fig. 2 A-E). This phenomenon has been previously documented in SBB sediment and is attributed to the precipitation of carbonate fluorapatite (Reimers et al. 1996a). The confinement of these flat PO_4^{3-} profiles to stations with >100 nmol cm^{-3} d^{-1} sulfate reduction in surface sediment suggests that this mineralogical sink of PO_4^{3-} in SBB sediment may be dependent on high sulfate reduction rates, owing to the bicarbonate produced by sulfate reduction (Reimers et al. 1996a), and is not found throughout the basin. Flat PO_4^{3-} profiles were also reported from the transiently deoxygenated portion of the Peruvian OMZ, where phosphate mineral precipitation has been documented (Noffke et al. 2012). Similar to the shallow margins of the SBB, PO_4^{3-} in Mauritanian OMZ porewater tracks closely with changes in porewater Fe^{2+} (Schroller-Lomnitz et al. 2019), indicating that iron mineralization/dissolution mechanisms hold a greater influence on PO_4^{3-} concentrations under hypoxic bottom waters.

Table 2-3. Example reactions of nitrate reduction pathways with associated energy yield in respect to the electron donor (H_2 or HS^-) and electron acceptor (NO_3^-) and electron accepting capacity. Modified from Table 2 in (Tiedje et al. 1983).

Reaction	ΔG0' (kcal mol^{-1})		Electrons per NO_3^-
	H_2/HS^-	NO_3^-	
Chemoheterotrophic Denitrification $2NO_3^- + 5H_2 + 2H^+ \rightarrow N_2 + 6H_2O$	-53.6	-133.9	5
Chemoautotrophic Denitrification $8NO_3^- + 5HS^- + 3H^+ \rightarrow 5SO_4^{2-} + 4N_2 + 4H_2O$	-177.9	-111.2	5
Chemoheterotrophic DNRA $NO_3^- + 4H_2 + 2H^+ \rightarrow NH_4^+ + 3H_2O$	-35.8	-143.4	8
Chemoautotrophic DNRA $NO_3^- + HS^- + H^+ + H_2O \rightarrow NH_4^+ + SO_4^{2-}$	-107.0	-107.0	8

4.4 Iron oxide exhaustion is critical for raising the sulfate reduction zone close to the sediment-water interface in Santa Barbara Basin sediment.

The hyper-accumulation of NO_3^- by GSOB mats potentially facilitates sulfate reduction close to the sediment-water interface in the SBB (e.g., NDRO and NDT3-A as seen in fig. 2N and 2O) by starving the sediment of this more powerful electron acceptor. The rise of the sulfate reduction zone at NDT3-C (fig. 2L) further suggests that the exhaustion of iron oxides and the formation of iron sulfide below the sediment-water interface may play a crucial role in controlling the distribution of sulfate reduction as well. SBB sediments showed a wide vertical and horizontal heterogeneity of redox states based on visual appearance (Fig. 1A-K). Sediment beneath the hypoxic bottom water at the shallowest D-stations was reddish, consistent with a high content of iron oxides. Interestingly, porewater Fe^{2+} concentrations in shallower parts of the basin (e.g., NDT3-D, max. ~700 μM Fe^{2+}) were an order of magnitude larger than those found in both the Peruvian (max ~60 and ~30 μM Fe^{2+}, respectively; (Noffke et al. 2012; Plass et al. 2020) and Mauritanian (max. ~50 μM Fe^{2+}; Schroller-Lomnitz et al 2019) OMZ. It should be noted that porewater samples for geochemical analyses were unfiltered and hence reported iron

concentrations include aqueous, colloidal, and nanoparticulate species. Regardless, all these components represent bioavailable sources of iron. Further, since filtering through 0.45 or 0.2 μm filters only removes a fraction of colloidal particles and no nanoparticles (Raiswell and Canfield 2012), potential surplus porewater iron in SBB samples in comparison to studies that applied filtering was likely minimal.

Deeper in the basin, bands of black sediment that appear mid-core at NDT3-C (6-14 cm) and SDT3-C (6-10 cm) indicate the formation of iron sulfides as a result of sulfide produced by sulfate reduction (Canfield 1989a). Both D-stations had similar bottom water conditions (Table 1), sulfate reduction rates (Fig. 3W-AG), porewater concentrations of solutes (Figs. 2 and 3), and visual sediment characteristics (Section 3.1). On the contrary, there are some noticeable differences in the porewater geochemistry between the two C-stations. At the C-stations, peaks in sulfate reduction were in the surface sediment, above the iron sulfide layers, and declined below approximately 4 cm, indicating a discrepancy between observed peak sulfate reduction activity and the mineralogical clues left behind by the process. Comparing NDT3-C and SDT3-C, iron sulfide formation (Table 1B compared to 1J), porewater Fe^{2+} profiles (Fig. 2G compared to Fig. 3H), and sulfate reduction rates (Fig. 2L compared to Fig. 3N) show that NDT3-C sediment appears to be in transition towards a more sulfidic state, while SDT3-C sediments still mimic the shallow D-station ferruginous state. While sulfate reduction rates for B-stations are not available due to technical issues during sample processing, porewater Fe^{2+} profiles show a similar difference between the north and south basin (Fig. 2H compared to Fig. 3I) as did visual sediment characteristics (Table 1C compared to 1I). This difference in biogeochemical profiles and apparent minerology between the north and south C- and B-stations could be a result of hydrographic and/or bathymetric differences in the basin (Bograd et al. 2002; Sholkovitz and

Gieskes 1971), but a discernable link between the differences in sediment biogeochemistry and the differences in bottom water oxygen (Table 1) need to be further explored.

Deeper in the basin (depocenter and A-stations), porewater Fe^{2+} concentrations in sediment beneath anoxic bottom water (max. 84 μM Fe^{2+}) were similar to concentrations found below the Peruvian OMZ in 2008 under anoxic bottom water conditions (78 m water depth, max. 80 μM Fe^{2+}) (Noffke et al. 2012). These deep basin porewater Fe^{2+} concentrations were, however, an order of magnitude larger than those found at a similar site on the Peruvian shelf (75 m water depth, max. 1 μM Fe^{2+}) in 2017 during a kelvin-wave-associated "Coastal El Niño" event that created oxygenated bottom waters during the sampling and the disappearance of previously observed dense GSOB mats (Plass et al. 2020). As the SBB water column was undergoing rapid deoxygenation in the weeks preceding this study (Qin et al. 2022), the sediments below the sill appeared to be actively shifting from a ferruginous state to a sulfidic state, with this change starting around the C-stations and being complete in the depocenter. Comparing apparent iron sulfide formation with dips in porewater Fe^{2+} concentrations in C-station profiles (Fig. 1B compared to Fig. 2G and Fig. 1J compared to Fig. 3H) signals a shift away from a ferruginous state occurring just below the SBB sill.

C-station porewater Fe^{2+} concentrations and sulfate reduction rates indicate that migration of the sulfate reduction zone towards the sediment-water interface is associated with iron sulfide formation deeper in the sediment. The activity (or lack thereof) of cable bacteria, which are able to bridge the gap between the oxidized sediment-water interface and reduced sediment below using a biofilament (Pfeffer et al. 2012), could explain the interplay between sulfate reduction and iron cycling in SBB sediments. Cable bacteria, such as *Ca. Electronema* sp., contain genes involved in DNRA (Kjeldsen et al. 2019) and can perform nitrate reduction in

incubation experiments (Marzocchi et al. 2014), but their direct transformation of NO_3^- in the environment appears limited (Kessler et al. 2019) and they appear to be inactive in anoxic aquatic environments (Hermans et al. 2019; Marzocchi et al. 2018; Seitaj et al. 2015). Cable bacteria primarily conduct aerobic sulfide oxidation (Pfeffer et al. 2012), though they can also utilize Fe^{2+} as an electron donor (Seitaj et al. 2015). The maximum recorded filament length of cable bacteria is 7 cm (Van De Velde et al. 2016), though typically they are not stretched completely vertically through the sediment. The appearance of black sediment in the SBB C-station sediments, starting at approx. 5 cm depth, could be an indication that cable bacteria are oxidizing iron sulfides at that sediment depth and prevent their formation at shallower depths. Further, cable bacteria have been found to directly compete with GSOB in transiently deoxygenated systems, with cable bacteria active under oxygenated conditions and GSOB active in anoxic conditions (Seitaj et al. 2015). Cable bacteria can also prevent the benthic release of sulfide, which is toxic to many pelagic animals, via the creation of an iron-oxide buffer (formed through Fe^{2+} oxidation) in near-surface sediments (Seitaj et al. 2015). Therefore, if cable bacteria activity in the SBB decreased with declining oxygen concentrations below the sill, the iron oxide buffer they create could have been reduced, encouraging the sulfate reduction zone to migrate towards the sediment surface (as seen at NDT3-C). Cable bacteria can sometimes be detected in sediments via a slight pH increase (typically pH > 8) (Schauer et al. 2014) which was not reflected in our pH results, but this phenomenon is more typically seen in the laboratory and not the field (Hermans et al. 2019).

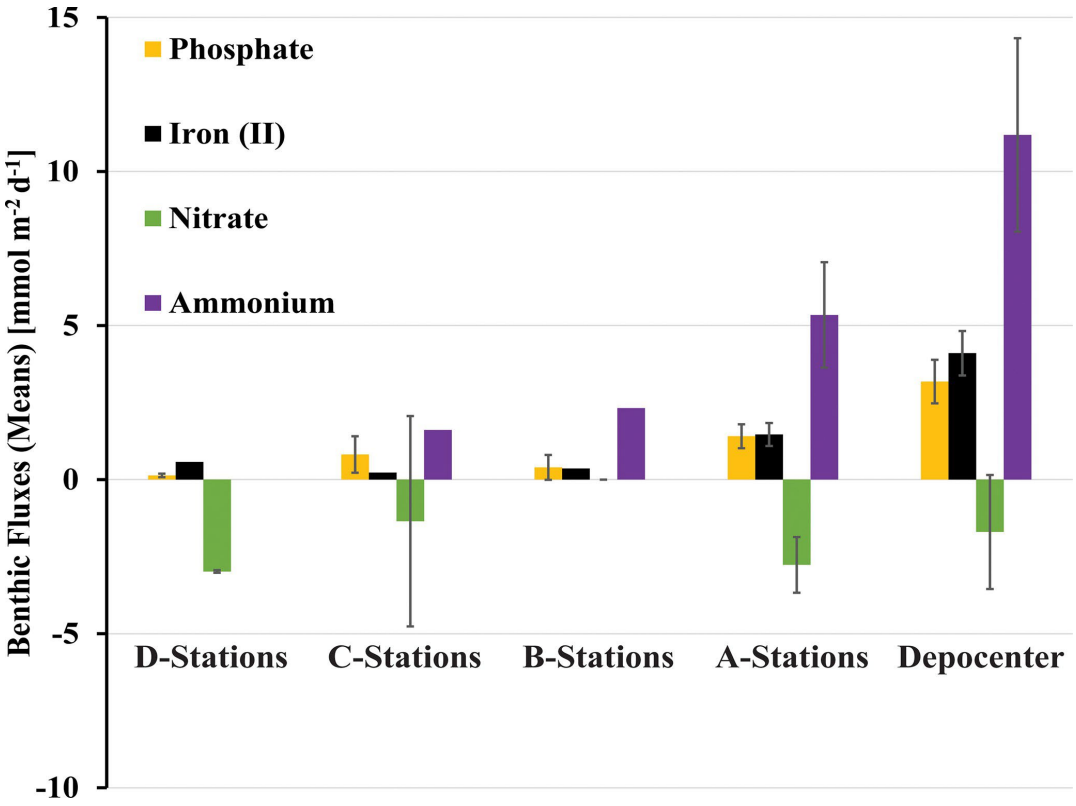

Figure 2-5. Benthic fluxes of solutes (positive flux = release from the seafloor; negative flux = uptake by the seafloor) determined with in-situ benthic flux chambers. Rates were averaged for stations of same depth from the northern and southern transect and the depocenter (NDRO and SDRO). Note, giant sulfur-oxidizing bacterial mats were found at depocenter and A-stations. Error bars represent standard errors.

4.5 Iron and phosphate flux into SBB bottom water is a feature of transient deoxygenation.

Release of dissolved iron and phosphate from sediment below anoxic waters is a well-documented phenomenon (e.g., (Mortimer 1941; Noffke et al. 2012; Van Cappellen and Ingall 1994; van de Velde et al. 2020a)) and this phenomenon is seen in the SBB as well. As postulated previously (Kuwabara et al. 1999), basin flushing oxidizes iron sulfides at the sediment-water interface, providing ample substrate for microbial iron reduction once anoxia returns. This iron reduction initiates high rates of Fe^{2+} release from SBB depocenter sediment (Fig. 5). Iron reduction further releases iron-bound PO_4^{3-} (Mortimer 1941) as seen by high benthic fluxes of

PO_4^{3-} at the depocenter (Fig. 5), although notably some of this PO_4^{3-} release is likely attributed to organic matter degradation (Van Cappellen and Ingall 1994). High benthic Fe^{2+} and PO_4^{3-} fluxes were also seen on the Peruvian shelf during transient anoxia (Noffke et al. 2012). The release of these solutes was interpreted to be sourced from a layer of reactive iron hydroxides existing near the sediment surface, likely established during a recent oxygenation event. Similar conditions, i.e., visibly oxidized (reddish) sediment laminae and a thin zone of iron reduction apparent from a peak in Fe^{2+} at the sediment-water interface, were found in sediment from the SBB depocenter. Deeper in the persistently anoxic core of the Peruvian OMZ, sediment appears to have little to no flux of $Fe^{2+}$and PO_4^{3-} into the bottom water (Noffke et al. 2012). Here, iron at the sediment-water interface is hypothesized to be locked up in iron sulfides, which are rarely re-oxidized due to persistent anoxia.

In a different study from the Eastern Gotland Basin in the Baltic Sea, enhanced elemental fluxes were observed during a decadal oxygen flushing event (van de Velde et al. 2020a), which was attributed to enhanced elemental recycling, or cycles of mineral precipitation in the water column followed by mineral dissolution once those minerals sink to the sediment. Notably, the iron flux observed in the Eastern Gotland Basin (max. 0.08 mmol m^{-2} d^{-1}) (van de Velde et al. 2020a) was two orders of magnitude lower than the flux observed in the anoxic depocenter of the Santa Barbara Basin (max. 4.9 mmol m^{-2} d^{-1}). It is further notable that benthic fluxes of PO_4^{3-} in the SBB depocenter were also an order of magnitude higher than fluxes in the Eastern Gotland Basin's hypoxic transition zone (3.6 vs. 0.23 mmol PO_4^{3-} m^{-2} d^{-1}) - both of which contained GSOB mats, but while the SBB was anoxic and the Eastern Gotland Basin was hypoxic (Noffke et al. 2016). These differences in Fe^{2+} and PO_4^{3}- flux between the SBB and the Eastern Gotland Basin suggest that reoxidation of the sediment-water interface during basin flushing, as opposed

to water-column-associated reoxidation, appears to encourage higher benthic iron fluxes.

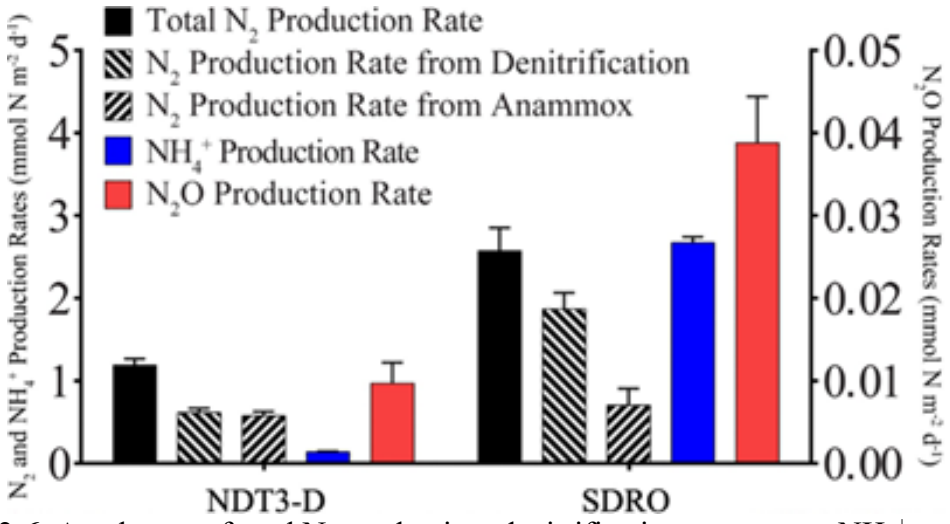

Figure 2-6. Areal rates of total N_2 production, denitrification, anammox, NH_4^+ production (DNRA), and N_2O production.

Fe^{2+} and PO_4^{3-} flux from the SBB depocenter were also approximately five times higher (Fig. 5) compared to the anoxic Peruvian shelf (4.9 vs. 0.9 mmol Fe^{2+} m^{-2} d^{-1} and 3.6 vs. 0.8 mmol PO_4^{3-} m^{-2} d^{-1}, respectively) (Noffke et al. 2012). Based on Fe^{2+} profiles, the zone of iron reduction in Peruvian shelf sediments extended down to approx. 10 cm, while the zone appeared to be much shallower and narrower (less than the top 5 cm) in the SBB depocenter. These differences in magnitude of Fe^{2+} concentration and Fe^{2+} and PO_4^{3-} flux between the SBB depocenter and the Peruvian shelf could be attributed to differences in the recency and magnitude of reoxygenation events. The release of Fe^{2+} from sediment into the bottom water could create a buffer against reoxygenation in transiently deoxygenated systems, giving a competitive advantage to anaerobic benthic metabolisms (Dale et al. 2013; Wallmann et al. 2022). Additionally, both Fe^{2+} and PO_4^{3-} release from the SBB sediment could allow for higher rates of primary productivity if those constituents diffused into the photic zone (Robinson et al. 2022). The fate of Fe^{2+} and PO_4^{3-} diffusing into SBB waters from the sediment-water interface is

a focus of ongoing work within the basin.

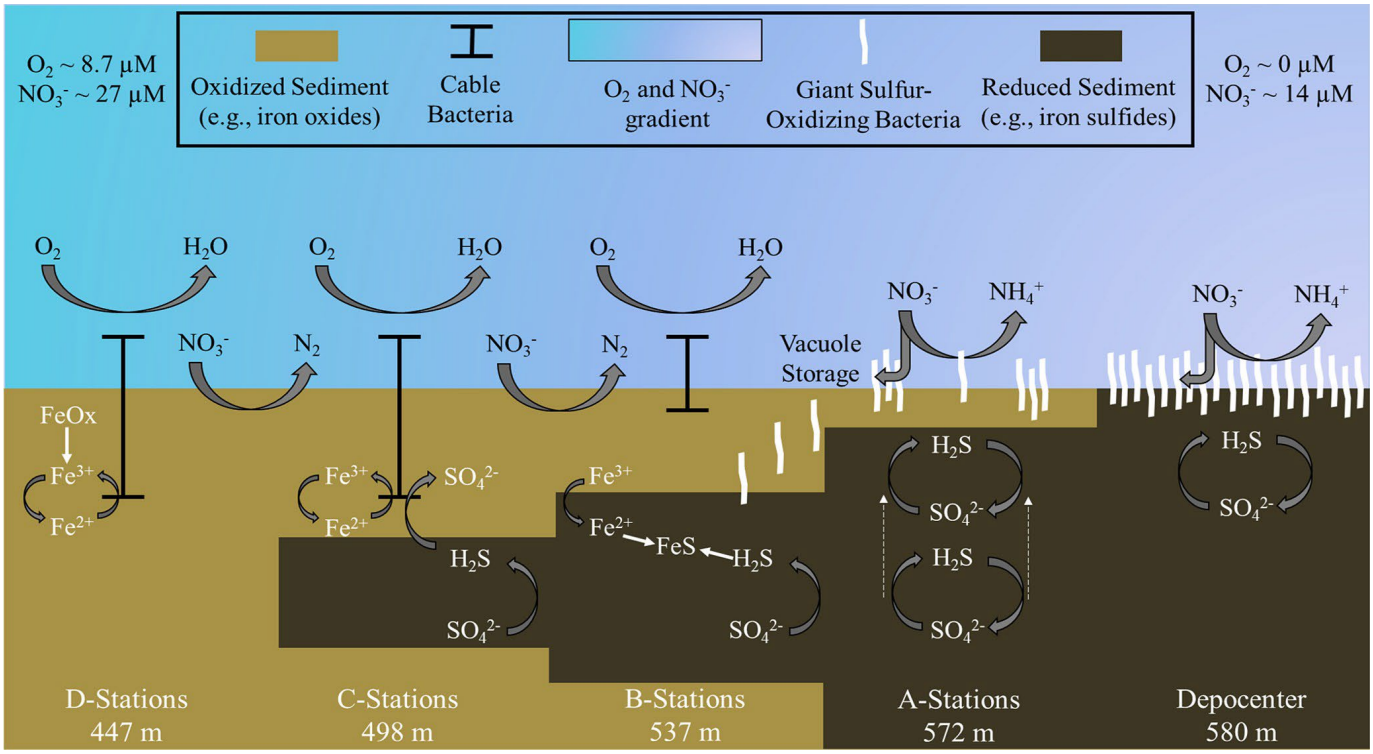

Figure 2-7: Schematic of biogeochemical processes in the Santa Barbara Basin along the depth gradients studied in October/November 2019. Teal to lavender gradient represents a decline in O_2 and NO_3^- concentrations with basin depth. In the shallower, hypoxic basin (D-stations), denitrification and iron reduction are dominant and reduced iron is rapidly re-oxidized in near-surface sediment by cable bacteria. Deeper in the basin (A-stations and depocenter), nitrogen cycling shifts towards dissimilatory nitrate reduction to ammonia (DNRA). Reduced iron combines with sulfide, produced by sulfate reduction, diffusing from deeper sediment layers to form iron sulfides. As oxygen concentration approaches zero between the A-stations and the basin's depocenter, giant sulfur-oxidizing bacteria hyper-accumulate nitrate in their intracellular vacuoles. Nitrate removal combined with the exhaustion of available iron oxides in the near-surface sediments allows the zone of sulfate reduction to migrate towards the surface (see dashed arrows at A-stations), providing the giant sulfur-oxidizing bacteria with sufficient reduced sulfur to proliferate into thick, contiguous mats. Note: Table is not to scale, and processes are simplified to illustrate main concepts.

5 Conclusions

This research expands upon the wealth of science already conducted in the SBB and other transiently deoxygenated environments by examining changes in benthic biogeochemistry

promoted by the onset of anoxia. Our main interpretations are summarized in Fig. 7. We found that GSOB mats proliferate in the SBB where the bottom water is anoxic and nitrate concentrations are declining (Fig. 7, A- and depocenter stations). Nitrate uptake by SBB sediment is similar regardless of GSOB mat presence, but these mats appear to initiate a shift from denitrification to DNRA as the primary nitrate reduction pathway (Fig. 7, beginning at B-stations). The zone of sulfate reduction rises to the sediment-water interface where GSOB mats are present (Fig. 7, A-stations), possibly because the hyper-accumulation of nitrate into their intracellular vacuoles starves the environment of this more powerful electron acceptor. However, following the natural order of electron acceptor utilization (Boudreau and Jorgensen 2001), iron oxides near the sediment-water interface must be exhausted before sulfate reduction can dominate surface sediments and GSOB mats can proliferate in the SBB (Fig. 7, depocenter stations). If anoxic events become longer and more frequent in the SBB because of global warming (see, e.g., (Qin et al. 2022; Stramma et al. 2008)), the iron oxide buffer built up in shallower basin depths could be exhausted, allowing for surface sulfate reduction and the proliferation of GSOB mats in shallower margins of the basin than currently seen. Further, the same transient deoxygenation that allows for these mats to re-stablish themselves also allows for a high Fe^{2+} and PO_4^{3-} flux into the SBB water column. In order to fully understand the complex changes in the benthic environment in response to deoxygenation, genomic and molecular work of the upper sediment community needs to be characterized. Overall, the insights gleaned from this research will aid in the understanding of fundamental biogeochemical changes that occur when marine environments become anoxic.

Acknowledgements

We thank the captain, crew, and scientific party of the R/V Atlantis, and the crew of the ROV Jason for their technical and logistical support during the research expedition AT42-19. We also thank Q. Qin, E. Arrington, M. O'Beirne, A. Mazariegos, X. Moreno, A. Eastman, and K. Gosselin for assisting with shipboard analyses. We thank J. Liu for assistance in reviewing the data processing for this manuscript. We further thank M. Alisch from the Max-Planck-Institute in Bremen, Germany for DIC analyses. We thank G. Eickert-Grötzschel, V. Hübner, A. Niclas, I. Schröder, and C. Wigand from the Max-Planck-Institute in Bremen, Germany for constructing the microsensors. We acknowledge J. Matthews from the UC Davis Stable Isotope facility for assisting with solid phase analyses. Funding for this work was provided by the US National Science Foundation, NSF OCE-1756947 and OCE-1830033 (to DLV) and OCE-1829981 (to TT), and a Simons Foundation Postdoctoral Fellowship in Marine Microbial Ecology (No. 547606 to XP). Further support was provided by the Max Planck Society and the Alfred Wegener Institute for Polar and Marine Research.

Data availability.

Biogeochemical data presented in this manuscript are accessible through the Biological & Chemical Oceanography Data Management Office (BCO-DMO) at the following landing pages: https://www.bco-dmo.org/dataset/867007; https://www.bco-dmo.org/dataset/867113; https://www.bco-dmo.org/dataset/867221; https://www.bco-dmo.org/dataset/896706

Author contributions.

TT, DV, FK, NL, and JT designed the project. DJY, SK, JT, DR, and TT processed sediment cores at sea. DJY conducted geochemical analyses of sediment porewater and benthic flux chamber water. DJY prepared TOC and TON samples. DR and SK analyzed sediment porosity and density. TT and SK performed shipboard sulfate reduction incubations. DJY and DR conducted sulfate reduction analyses. DJY, NL, and JT transformed and interpreted ROV Jason data. FJ and FW operated BFC and microprofilers and analyzed associated data. XP conducted ^{15}N experiments and analyses. All authors reviewed and edited the manuscript.

Competing interests.

At least one of the (co-)authors is a member of the editorial board of Biogeosciences.

References

Algar, C. K. and Vallino, J. J.: Predicting microbial nitrate reduction pathways in coastal sediments, Aquatic Microbial Ecology, 71, 223-238, 2014.

An, S. and Gardner, W. S.: Dissimilatory nitrate reduction to ammonium (DNRA) as a nitrogen link, versus denitrification as a sink in a shallow estuary (Laguna Madre/Baffin Bay, Texas), Marine Ecology Progress Series, 237, 41-50, 2002.

Bernhard, J. M., Visscher, P. T., and Bowser, S. S.: Submillimeter life positions of bacteria, protists, and metazoans in laminated sediments of the Santa Barbara Basin, Limnology and Oceanography, 48, 813-828, 2003.

Bernhard, J. M., Buck, K. R., Farmer, M. A., and Bowser, S. S.: The Santa Barbara Basin is a symbiosis oasis, Nature, 403, 77-80, 2000.

Bernhard, J. M., Casciotti, K. L., McIlvin, M. R., Beaudoin, D. J., Visscher, P. T., and Edgcomb, V. P.: Potential importance of physiologically diverse benthic foraminifera in sedimentary nitrate storage and respiration, Journal of Geophysical Research: Biogeosciences, 117, 2012.

Bograd, S. J., Schwing, F. B., Castro, C. G., and Timothy, D. A.: Bottom water renewal in the Santa Barbara Basin, Journal of Geophysical Research: Oceans, 107, 9-1-9-9, 2002.

Bonaglia, S., Nascimento, F. A., Bartoli, M., Klawonn, I., and Brüchert, V.: Meiofauna increases bacterial denitrification in marine sediments, Nature communications, 5, 5133, 2014.

Boudreau, B. P. and Jorgensen, B. B.: The benthic boundary layer: Transport processes and biogeochemistry, 2001.

Bourbonnais, A., Letscher, R. T., Bange, H. W., Echevin, V., Larkum, J., Mohn, J., Yoshida, N., and Altabet, M. A.: N2O production and consumption from stable isotopic and concentration data in the Peruvian coastal upwelling system, Global Biogeochemical Cycles, 31, 678-698, 2017.

Bremner, J.: Biogenic sediments on the South West African continental margin, 1981.

Brüchert, V., Jørgensen, B. B., Neumann, K., Riechmann, D., Schlösser, M., and Schulz, H.: Regulation of bacterial sulfate reduction and hydrogen sulfide fluxes in the central Namibian coastal upwelling zone, Geochim. Cosmochim. Acta, 67, 4505-4518, 2003.

Caffrey, J. M., Bonaglia, S., and Conley, D. J.: Short exposure to oxygen and sulfide alter nitrification, denitrification, and DNRA activity in seasonally hypoxic estuarine sediments, FEMS microbiology letters, 366, fny288, 2019.

California Cooperative Oceanic Fisheries Investigations: https://www.calcofi.org/ccdata.html, last

Canfield, D. E.: Reactive iron in marine sediments, Geochimica et cosmochimica acta, 53, 619-632, 1989.

Canfield, D. E., Stewart, F. J., Thamdrup, B., De Brabandere, L., Dalsgaard, T., Delong, E. F., Revsbech, N. P., and Ulloa, O.: A cryptic sulfur cycle in oxygen-minimum–zone waters off the Chilean coast, Science, 330, 1375-1378, 2010.

Charoenpong, C. N., Bristow, L. A., and Altabet, M. A.: A continuous flow isotope ratio mass spectrometry method for high precision determination of dissolved gas ratios and isotopic composition, Limnology and Oceanography: Methods, 12, 323-337, 2014.

Cline, J. D.: Spectrophometric determination of hydrogen sulfide in natural waters, Limnol. Oceanogr., 14, 454-458, 1969.

Dale, A. W., Bertics, V. J., Treude, T., and Wallmann, K.: Modeling benthic-pelagic nutrient exchange processes and porewater distributions in a seasonally hypoxic sediment: evidence for massive phosphate release by Beggiatoa?, Biogeosciences, 10, 629-651, 2013.

Dale, A. W., Sommer, S., Lomnitz, U., Bourbonnais, A., and Wallmann, K.: Biological nitrate transport in sediments on the Peruvian margin mitigates benthic sulfide emissions and drives pelagic N loss during stagnation events, Deep Sea Research Part I: Oceanographic Research Papers, 112, 123-136, 2016.

Dale, A. W., Sommer, S., Ryabenko, E., Noffke, A., Bohlen, L., Wallmann, K., Stolpovsky, K., Greinert, J., and Pfannkuche, O.: Benthic nitrogen fluxes and fractionation of nitrate in the Mauritanian oxygen minimum zone (Eastern Tropical North Atlantic), Geochimica et Cosmochimica Acta, 134, 234-256, 2014.

Dale, A. W., Sommer, S., Bohlen, L., Treude, T., Bertics, V. J., Bange, H. W., Pfannkuche, O., Schorp, T., Mattsdotter, M., and Wallmann, K.: Rates and regulation of nitrogen cycling in seasonally hypoxic sediments during winter (Boknis Eck, SW Baltic Sea): Sensitivity to environmental variables, Estuar. Continent. Shelf Sci., 95, 14-28, 2011.

Dale, A. W., Sommer, S., Lomnitz, U., Montes, I., Treude, T., Liebetrau, V., Gier, J., Hensen, C., Dengler, M., Stolpovsky, K., Bryant, L. D., and Wallmann, K.: Organic carbon production, mineralisation and preservation on the Peruvian margin, Biogeosciences, 12, 1537-1559, 2015.

De Brabandere, L., Bonaglia, S., Kononets, M. Y., Viktorsson, L., Stigebrandt, A., Thamdrup, B., and Hall, P. O.: Oxygenation of an anoxic fjord basin strongly stimulates benthic denitrification and DNRA, Biogeochemistry, 126, 131-152, 2015.

Emery, K., Hülsemann, J., and Rodolfo, K.: Influence of turbidity currents upon basin waters, Limnology and Oceanography, 7, 439-446, 1962.

Emmer, E. and Thunell, R. C.: Nitrogen isotope variations in Santa Barbara Basin sediments: Implications for denitrification in the eastern tropical North Pacific during the last 50,000 years, Paleoceanography, 15, 377-387, 2000.

Fossing, H., Gallardo, V. A., Jørgensen, B. B., Hüttel, M., Nielsen, L. P., Schulz, H., Canfield, D. E., Forster, S., Glud, R. N., and Gundersen, J. K.: Concentration and transport of nitrate by the mat-forming sulphur bacterium Thioploca, Nature, 374, 713-715, 1995.

García-Robledo, E., Corzo, A., and Papaspyrou, S.: A fast and direct spectrophotometric method for the sequential determination of nitrate and nitrite at low concentrations in small volumes, Marine Chemistry, 162, 30-36, 2014.

Gier, J., Sommer, S., Löscher, C. R., Dale, A. W., Schmitz, R. A., and Treude, T.: Nitrogen fixation in sediments along a depth transect through the Peruvian oxygen minimum zone, Biogeosciences, 13, 4065–4080, 2016.

Glud, R. N., Gundersen, J. K., and Ramsing, N. B.: Electrochemical and optical oxygen microsensors for in situ measurements, in: In situ monitoring of aquatic systems: Chemical analysis and speciation, edited by: Buffle, J., and Horvai, G., Wiley, 2000.

Goericke, R., Bograd, S. J., and Grundle, D. S.: Denitrification and flushing of the Santa Barbara Basin bottom waters, Deep Sea Research Part II: Topical Studies in Oceanography, 112, 53-60, 2015.

Grasshoff, K., Ehrhardt, M., and Kremling, K.: Methods of seawater analysis, Wiley-VCH Verlag GmbH, Weinheim1999.

Gundersen, J. K. and Jørgensen, B. B.: Microstructure of diffusive boundary layers and the oxygen uptake of the sea floor, Nature, 345, 604-607, 1990.

Hall, P. O. J. and Aller, R. C.: Rapid small-volume flow injection analysis for ∑ CO2 and NH4+ in marine and fresh waters, Limnol. Oceanogr., 37, 1113-1119, 1992.

Hardison, A. K., Algar, C. K., Giblin, A. E., and Rich, J. J.: Influence of organic carbon and nitrate loading on partitioning between dissimilatory nitrate reduction to ammonium (DNRA) and N2 production, Geochimica et Cosmochimica Acta, 164, 146-160, 2015.

Harris, D., Horwáth, W. R., and Van Kessel, C.: Acid fumigation of soils to remove carbonates prior to total organic carbon or carbon-13 isotopic analysis, Soil Science Society of America Journal, 65, 1853-1856, 2001.

Hermans, M., Lenstra, W. K., Hidalgo-Martinez, S., van Helmond, N. A., Witbaard, R., Meysman, F. J., Gonzalez, S., and Slomp, C. P.: Abundance and biogeochemical impact of cable bacteria in Baltic Sea sediments, Environmental science & technology, 53, 7494-7503, 2019.

Hossain, M., Bhattacharya, P., Frape, S. K., Jacks, G., Islam, M. M., Rahman, M. M., von Brömssen, M., Hasan, M. A., and Ahmed, K. M.: Sediment color tool for targeting arsenic-safe aquifers for the installation of shallow drinking water tubewells, Science of the Total Environment, 493, 615-625, 2014.

Huettel, M., Forster, S., Kloser, S., and Fossing, H.: Vertical migration in the sediment-dwelling sulfur bacteria Thioploca spp. in overcoming diffusion limitations, Applied and Environmental Microbiology, 62, 1863-1872, 1996.

Hylén, A., Bonaglia, S., Robertson, E., Marzocchi, U., Kononets, M., and Hall, P. O.: Enhanced benthic nitrous oxide and ammonium production after natural oxygenation of long-term anoxic sediments, Limnology and Oceanography, 67, 419-433, 2022.

Høgslund, S., Revsbech, N. P., Kuenen, J. G., Jørgensen, B. B., Gallardo, V. A., Vossenberg, J. v. d., Nielsen, J. L., Holmkvist, L., Arning, E. T., and Nielsen, L. P.: Physiology and behaviour of marine Thioploca, The ISME journal, 3, 647-657, 2009.

Jeroschewsky, P., Steuckart, C., and Kuehl, M.: An amperometric microsensor for the determination af H2S in aquatic environments, Anal. Chem., 68, 4351-4357, 1996.

Jørgensen, B.: Distribution of colorless sulfur bacteria (Beggiatoa spp.) in a coastal marine sediment, Marine Biology, 41, 19-28, 1977.

Jørgensen, B. B.: A comparison of methods for the quantification of bacterial sulphate reduction in coastal marine sediments: I. Measurements with radiotracer techniques, Geomicrobiol. J., 1, 11-27, 1978.

Jørgensen, B. B. and Nelson, D. C.: Sulfide oxidation in marine sediments: Geochemistry meets microbiology, Geological Society of America, Special Paper 379, 63-81, 2004.

Kallmeyer, J., Ferdelman, T. G., Weber, A., Fossing, H., and Jørgensen, B. B.: A cold chromium distillation procedure for radiolabeled sulfide applied to sulfate reduction measurements, Limnol. Oceanogr. Methods, 2, 171-180, 2004.

Kamp, A., Høgslund, S., Risgaard-Petersen, N., and Stief, P.: Nitrate storage and dissimilatory nitrate reduction by eukaryotic microbes, Frontiers in microbiology, 6, 1492, 2015.

Kamp, A., de Beer, D., Nitsch, J. L., Lavik, G., and Stief, P.: Diatoms respire nitrate to survive dark and anoxic conditions, Proceedings of the National Academy of Sciences, 108, 5649-5654, 2011.

Kessler, A. J., Wawryk, M., Marzocchi, U., Roberts, K. L., Wong, W. W., Risgaard-Petersen, N., Meysman, F. J., Glud, R. N., and Cook, P. L.: Cable bacteria promote DNRA through iron sulfide dissolution, Limnology and Oceanography, 64, 1228-1238, 2019.

Kjeldsen, K. U., Schreiber, L., Thorup, C. A., Boesen, T., Bjerg, J. T., Yang, T., Dueholm, M. S., Larsen, S., Risgaard-Petersen, N., and Nierychlo, M.: On the evolution and physiology of cable bacteria, Proceedings of the National Academy of Sciences, 116, 19116-19125, 2019.

Kononets, M., Tengberg, A., Nilsson, M., Ekeroth, N., Hylén, A., Robertson, E. K., Van De Velde, S., Bonaglia, S., Rütting, T., and Blomqvist, S.: In situ incubations with the Gothenburg benthic chamber landers: Applications and quality control, Journal of Marine Systems, 214, 103475, 2021.

Kraft, B., Tegetmeyer, H. E., Sharma, R., Klotz, M. G., Ferdelman, T. G., Hettich, R. L., Geelhoed, J. S., and Strous, M.: The environmental controls that govern the end product of bacterial nitrate respiration, Science, 345, 676-679, 2014.

Kuwabara, J. S., van Geen, A., McCorkle, D. C., and Bernhard, J. M.: Dissolved sulfide distributions in the water column and sediment pore waters of the Santa Barbara Basin, Geochimica et Cosmochimica Acta, 63, 2199-2209, 1999.

Lazo-Murphy, B. M., Larson, S., Staines, S., Bruck, H., McHenry, J., Bourbonnais, A., and Peng, X.: Nitrous oxide production and isotopomer composition by fungi isolated from salt marsh sediments, Frontiers in Marine Science, 9, 1098508, 2022.

Levin, L. A., Gutierrez, D., Rathburn, A. E., Neira, C., Sellanes, J., Munoz, P., Gallardo, V. A., and Salamance, M.: Bethic processes on the Peru margin: a transect across the oxygen minimum zone during the 1997-98 El Nino, Prog. Oceanog., 53, 1-27, 2002.

Marchant, H. K., Lavik, G., Holtappels, M., and Kuypers, M. M.: The fate of nitrate in intertidal permeable sediments, PloS one, 9, e104517, 2014.

Marzocchi, U., Bonaglia, S., van de Velde, S., Hall, P. O., Schramm, A., Risgaard-Petersen, N., and Meysman, F. J.: Transient bottom water oxygenation creates a niche for cable bacteria in long-term anoxic sediments of the Eastern Gotland Basin, Environmental microbiology, 20, 3031-3041, 2018.

Marzocchi, U., Trojan, D., Larsen, S., Louise Meyer, R., Peter Revsbech, N., Schramm, A., Peter Nielsen, L., and Risgaard-Petersen, N.: Electric coupling between distant nitrate reduction and sulfide oxidation in marine sediment, The ISME journal, 8, 1682-1690, 2014.

Middelburg, J. and Levin, L.: Coastal hypoxia and sediment biogeochemistry, Biogeosciences, 6, 1273-1293, 2009.

Mortimer, C. H.: The exchange of dissolved substances between mud and water in lakes, Journal of ecology, 29, 280-329, 1941.

Mosch, T., Sommer, S., Dengler, M., Noffke, A., Bohlen, L., Pfannkuche, O., Liebetrau, V., and Wallmann, K.: Factors influencing the distribution of epibenthic megafauna across the Peruvian oxygen minimum zone, Deep Sea Research Part I: Oceanographic Research Papers, 68, 123-135, 2012.

Mußmann, M., Schulz, H. N., Strotmann, B., Kjær, T., Nielsen, L. P., Rosselló-Mora, R. A., Amann, R. I., and Jørgensen, B. B.: Phylogeny and distribution of nitrate-storing Beggiatoa spp. in coastal marine sediments, Environmental Microbiology, 5, 523-533, 2003.

Myhre, S. E., Pak, D., Borreggine, M., Kennett, J. P., Nicholson, C., Hill, T. M., and Deutsch, C.: Oxygen minimum zone biotic baseline transects for paleoceanographic reconstructions in Santa Barbara Basin, CA, Deep Sea Research Part II: Topical Studies in Oceanography, 150, 118-131, 2018.

Naik, R., Naqvi, S., and Araujo, J.: Anaerobic carbon mineralisation through sulphate reduction in the inner shelf sediments of eastern Arabian Sea, Estuaries and Coasts, 40, 134-144, 2017.

Noffke, A., Sommer, S., Dale, A., Hall, P., and Pfannkuche, O.: Benthic nutrient fluxes in the Eastern Gotland Basin (Baltic Sea) with particular focus on microbial mat ecosystems, Journal of Marine Systems, 158, 1-12, 2016.

Noffke, A., Hensen, C., Sommer, S., Scholz, F., Bohlen, L., Mosch, T., Graco, M., and Wallmann, K.: Benthic iron and phosphorus fluxes across the Peruvian oxygen minimum zone, Limnol. Oceanogr., 57, 851-867, 2012.

Pavlova, G. Y., Tishchenko, P. Y., Volkova, T., Dickson, A., and Wallmann, K.: Intercalibration of Bruevich's method to determine the total alkalinity in seawater, Oceanology, 48, 438-443, 2008.

Peng, X., Ji, Q., Angell, J. H., Kearns, P. J., Yang, H. J., Bowen, J. L., and Ward, B. B.: Long-term fertilization alters the relative importance of nitrate reduction pathways in salt marsh sediments, Journal of Geophysical Research: Biogeosciences, 121, 2082-2095, 2016.

Peng, X., Yousavich, D. J., Bourbonnais, A., Wenzhoefer, F., Janssen, F., Treude, T., and Valentine, D. L.: The fate of fixed nitrogen in Santa Barbara Basin sediments during seasonal anoxia, EGUsphere, 2023, 1-26, 2023.

Pfeffer, C., Larsen, S., Song, J., Dong, M., Besenbacher, F., Meyer, R. L., Kjeldsen, K. U., Schreiber, L., Gorby, Y. A., and El-Naggar, M. Y.: Filamentous bacteria transport electrons over centimetre distances, Nature, 491, 218-221, 2012.

Plass, A., Schlosser, C., Sommer, S., Dale, A. W., Achterberg, E. P., and Scholz, F.: The control of hydrogen sulfide on benthic iron and cadmium fluxes in the oxygen minimum zone off Peru, Biogeosciences, 17, 3685-3704, 2020.

Porubsky, W., Weston, N., and Joye, S.: Benthic metabolism and the fate of dissolved inorganic nitrogen in intertidal sediments, Estuarine, Coastal and Shelf Science, 83, 392-402, 2009.

Preisler, A., De Beer, D., Lichtschlag, A., Lavik, G., Boetius, A., and Jørgensen, B. B.: Biological and chemical sulfide oxidation in a Beggiatoa inhabited marine sediment, ISME Journal, 341-351, 2007.

Prokopenko, M., Hammond, D., Berelson, W., Bernhard, J., Stott, L., and Douglas, R.: Nitrogen cycling in the sediments of Santa Barbara basin and Eastern Subtropical North Pacific: Nitrogen isotopes, diagenesis and possible chemosymbiosis between two lithotrophs (Thioploca and Anammox)—"riding on a glider", Earth and Planetary Science Letters, 242, 186-204, 2006.

Qin, Q., Kinnaman, F. S., Gosselin, K. M., Liu, N., Treude, T., and Valentine, D. L.: Seasonality of Water Column Methane Oxidation and Deoxygenation in a Dynamic Marine Environment, Geochimica et Cosmochimica Acta, 2022.

Raiswell, R. and Canfield, D. E.: The iron biogeochemical cycle past and present, Geochemical perspectives, 1, 1-2, 2012.

Reimers, C. E., Ruttenberg, K. C., Canfield, D. E., Christiansen, M. B., and Martin, J. B.: Porewater pH and authigenic phases formed in the uppermost sediments of Santa Barbara Basin, Geochim. Cosmochim. Acta, 60, 4037-4057, 1996.

Revsbech, N. P. and Jørgensen, B. B.: Microelectrodes: their use in microbial ecology, in: Adv. Microb. Ecol., edited by: Marshall, K. C., Plenum, New York, 293-352, 1986.

Risgaard-Petersen, N., Langezaal, A. M., Ingvardsen, S., Schmid, M. C., Jetten, M. S. M., Op den Camp, H. J. M., Derksen, J. W. M., Pina-Ochoa, E., Eriksson, S. P., Nielsen, L. P., Revsbech, N. P., Cedhagen, T., and Zwaan van der, G. J.: Evidence for complete denitrification in a benthic foraminifer, Nature, 443, 93-96, 2006.

Robinson, D. M., Pham, A. L., Yousavich, D. J., Janssen, F., Wenzhöfer, F., Arrington, E. C., Gosselin, K. M., Sandoval-Belmar, M., Mar, M., and Valentine, D. L.: Iron "Ore" Nothing: Benthic iron fluxes from the oxygen-deficient Santa Barbara Basin enhance phytoplankton productivity in surface waters, Biogeosciences Discussions, 1-36, 2022.

Sayama, M.: Presence of nitrate-accumulating sulfur bacteria and their influence on nitrogen cycling in a shallow coastal marine sediment, Applied and Environmental Microbiology, 67, 3481-3487, 2001.

Schauer, R., Risgaard-Petersen, N., Kjeldsen, K. U., Tataru Bjerg, J. J., B Jørgensen, B., Schramm, A., and Nielsen, L. P.: Succession of cable bacteria and electric currents in marine sediment, The ISME journal, 8, 1314-1322, 2014.

Schroller-Lomnitz, U., Hensen, C., Dale, A. W., Scholz, F., Clemens, D., Sommer, S., Noffke, A., and Wallmann, K.: Dissolved benthic phosphate, iron and carbon fluxes in the Mauritanian upwelling system and implications for ongoing deoxygenation, Deep Sea Research Part I: Oceanographic Research Papers, 143, 70-84, 2019.

Schulz, H. N. and Schulz, H. D.: Large sulfur bacteria and the formation of phosphorite, Science, 307, 416-418, 2005.

Schulz, H. N., Jorgensen, B. B., Fossing, H. A., and Ramsing, N. B.: Community structure of filamentous, sheath-building sulfur bacteria, Thioploca spp., off the coast of Chile, Applied and Environmental Microbiology, 62, 1855-1862, 1996.

Schulz, H. N., Brinkhoff, T., Ferdelman, T. G., Hernández Mariné, M., Teske, A., and Jørgensen, B. B.: Dense populations of a giant sulfur bacterium in Namibian shelf sediments, Science, 284, 493-495, 1999.

Seitaj, D., Schauer, R., Sulu-Gambari, F., Hidalgo-Martinez, S., Malkin, S. Y., Burdorf, L. D., Slomp, C. P., and Meysman, F. J.: Cable bacteria generate a firewall against euxinia in seasonally hypoxic basins, Proceedings of the National Academy of Sciences, 112, 13278-13283, 2015.

Sholkovitz, E.: Interstitial water chemistry of the Santa Barbara Basin sediments, Geochimica et Cosmochimica Acta, 37, 2043-2073, 1973.

Sholkovitz, E. R. and Gieskes, J. M.: A PHYSICAL-CHEMICAL STUDY OF THE FLUSHING OF THE SANTA BARBARA BASIN 1, Limnology and Oceanography, 16, 479-489, 1971.

Sigman, D. M., Robinson, R., Knapp, A., Van Geen, A., McCorkle, D., Brandes, J., and Thunell, R.: Distinguishing between water column and sedimentary denitrification in the Santa Barbara Basin using the stable isotopes of nitrate, Geochemistry, Geophysics, Geosystems, 4, 2003.

Sommer, S., Gier, J., Treude, T., Lomnitz, U., Dengler, M., Cardich, J., and Dale, A. W.: Depletion of oxygen, nitrate and nitrite in the Peruvian oxygen minimum zone cause an imbalance of benthic nitrogen fluxes, Deep-Sea Res. I, 112, 113–122, 2016.

Stramma, L., Johnson, G. C., Sprintall, J., and Mohrholz, V.: Expanding oxygen-minimum zones in the tropical oceans, Science, 320, 655-658, 2008.

Sverdrup, H. and Allen, W.: Distribution of diatoms in relation to the character of water masses and currents off Southern California in 1938, J. mar. Res, 2, 131-144, 1939.

Thunell, R. C.: Particle fluxes in a coastal upwelling zone: sediment trap results from Santa Barbara Basin, California, Deep Sea Research Part II: Topical Studies in Oceanography, 45, 1863-1884, 1998.

Tiedje, J. M., Sexstone, A. J., Myrold, D. D., and Robinson, J. A.: Denitrification: ecological niches, competition and survival, Antonie van Leeuwenhoek, 48, 569-583, 1983.

Treude, T.: Biogeochemical reactions in marine sediments underlying anoxic water bodies, in: Anoxia: Paleontological Strategies and Evidence for Eukaryote Survival, edited by: Altenbach, A., Bernhard, J., and Seckbach, J., Cellular Origins, Life in Extreme Habitats and Astrobiology (COLE) Book Series, Springer, Dordrecht, 18-38, 2011.

Treude, T., Hamdan, L. J., Lemieux, S., Dale, A. W., and Sommer, S.: Rapid sulfur cycling in sediments from the Peruvian oxygen minimum zone featuring simultaneous sulfate reduction and sulfide oxidation, Limnology and Oceanography, 66, 2661-2671, 2021.

Treude, T., Smith, C. R., Wenzhoefer, F., Carney, E., Bernardino, A. F., Hannides, A. K., Krueger, M., and Boetius, A.: Biogeochemistry of a deep-sea whale fall: sulfate reduction, sulfide efflux and methanogenesis, Mar. Ecol. Prog. Ser., 382, 1-21, 2009.

Valentine, D. L., Fisher, G. B., Pizarro, O., Kaiser, C. L., Yoerger, D., Breier, J. A., and Tarn, J.: Autonomous marine robotic technology reveals an expansive benthic bacterial community relevant to regional nitrogen biogeochemistry, Environmental science & technology, 50, 11057-11065, 2016.

Van Cappellen, P. and Ingall, E. D.: Benthic phosphorus regeneration, net primary production, and ocean anoxia: A model of the coupled marine biogeochemical cycles of carbon and phosphorus, Paleoceanography, 9, 677-692, 1994.

Van De Velde, S., Lesven, L., Burdorf, L. D., Hidalgo-Martinez, S., Geelhoed, J. S., Van Rijswijk, P., Gao, Y., and Meysman, F. J.: The impact of electrogenic sulfur oxidation on the biogeochemistry of coastal sediments: A field study, Geochimica et Cosmochimica Acta, 194, 211-232, 2016.

van de Velde, S. J., Hylén, A., Eriksson, M., James, R. K., Kononets, M. Y., Robertson, E. K., and Hall, P. O.: Exceptionally high respiration rates in the reactive surface layer of sediments underlying oxygen-deficient bottom waters, Proceedings of the Royal Society A, 479, 20230189, 2023.

van de Velde, S. J., Hylén, A., Kononets, M., Marzocchi, U., Leermakers, M., Choumiline, K., Hall, P. O., and Meysman, F. J.: Elevated sedimentary removal of Fe, Mn, and trace elements following a transient oxygenation event in the Eastern Gotland Basin, central Baltic Sea, Geochimica et Cosmochimica Acta, 271, 16-32, 2020.

Wallmann, K., José, Y. S., Hopwood, M. J., Somes, C. J., Dale, A. W., Scholz, F., Achterberg, E. P., and Oschlies, A.: Biogeochemical feedbacks may amplify ongoing and future ocean deoxygenation: a case study from the Peruvian oxygen minimum zone, Biogeochemistry, 159, 45-67, 2022.

Ward, B., Devol, A., Rich, J., Chang, B., Bulow, S., Naik, H., Pratihary, A., and Jayakumar, A.: Denitrification as the dominant nitrogen loss process in the Arabian Sea, Nature, 461, 78-81, 2009.

Zhang, L., Altabet, M. A., Wu, T., and Hadas, O.: Sensitive measurement of NH4+ 15N/14N (δ15NH4+) at natural abundance levels in fresh and saltwaters, Analytical Chemistry, 79, 5297-5303, 2007.

Zopfi, J., Kjær, T., Nielsen, L. P., and Jørgensen, B. B.: Ecology of Thioploca spp.: nitrate and sulfur storage in relation to chemical microgradients and influence of Thioploca spp. on the sedimentary nitrogen cycle, Applied and Environmental Microbiology, 67, 5530-5537, 2001.

Chapter 3

Increased bottom water anoxia leads to a loss of sedimentary iron content and an associated shift to a sulfidic sediment state in the Santa Barbara Basin, California.

David J. Yousavich[1], Felix Janssen[5,6], Jiarui Liu[1], Emily Klonicki[1], Kira Homola[1], De'Marcus Robinson[2], Peter Girguis[7], David L. Valentine[8], Joan M. Bernhard[9], Tina Treude[1,2]

[1]Department of Earth, Planetary, and Space Sciences, University of California Los Angeles, 595 Charles E. Young Drive East, Los Angeles, CA 90095, USA

[2]Department of Atmospheric and Oceanic Sciences, University of California Los Angeles, Math Science Building, 520 Portola Plaza, Los Angeles, CA 90095, USA

[3]School of Earth, Ocean, and Environment, University of South Carolina, 701 Sumter Street, EWS 617, Columbia, SC 29208, USA

[4]Earth Research Institute, 6832 Ellison Hall, University of California Santa Barbara, Ca 93106-3060

[5]HGF-MPG Joint Research Group for Deep-Sea Ecology and Technology, Alfred-Wegener-Institute, Helmholtz-Center for Polar and Marine Research, Am Handelshafen 12, 27570 Bremerhaven, Germany

[6]HGF-MPG Joint Research Group for Deep-Sea Ecology and Technology, Max Planck Institute for Marine Microbiology, Celsiusstrasse 1, 28359 Bremen, Germany

[7]Department of Organismic and Evolutionary Biology, Harvard University, 16 Divinity Avenue, Cambridge, MA 02138, USA

[8]Department of Earth Science and Marine Science Institute, University of California, Santa Barbara, CA 93106, USA

[9]Geology & Geophysics Department, Woods Hole Oceanographic Institution, Woods Hole, MA 02543, USA.

Abstract

The Santa Barbara Basin within the Southern California Bight experiences anoxic events below the Basin's sill, which is situated at ~475 m depth. These anoxic events have increased in duration, frequency, and strength, corresponding to an increase in El Niño conditions in the Pacific Ocean. The sediment below the Basin sill experiences vast swings in redox state at the sediment-water interface, and previous expeditions in the Basin over the past several decades have shown the benthic microbiology and chemistry can be vastly different depending on the redox conditions in the bottom water. Using a combination of long-term water column chemistry observations, analyses from sediment samples, and in-situ experiments, we investigated how increasing anoxia in the Basin is affecting early diagenesis of iron and sulfide minerals in the sediment. We found there is a shift in redox conditions from a ferruginous to sulfidic state in the sediment below the sill. This geochemical shift is evidenced by high rates of biological sulfate reduction (>200 nmol cm^{-3} d^{-1}) with concomitant high concentrations of porewater sulfide (>100 μM) in the Basin Depocenter, yet the accumulation of iron sulfides below the sill is well below what is expected in sulfidic marine sediment. The sediment below the sill appears to be losing highly reactive iron content to the anoxic water column and does not appear to regain this iron upon re-oxygenation events. Additionally, in summer 2023 we documented a flux of more than 1

mmol m^{-2} d^{-1} hydrogen sulfide into the water column that replaced the iron flux seen in fall 2019. This work demonstrates how increased deoxygenation in the Santa Barbara Basin associated with increasing El Niño events in the Pacific Ocean has drastic impacts on sediment near the sediment-water interface.

Introduction

Oxygen minimum zones, naturally occurring areas in the ocean where organic matter remineralization in the water column drives down dissolved oxygen concentrations, are intensifying due to global warming and eutrophication (Stramma et al. 2008). Anoxia (zero-oxygen condition) development is facilitated when low oxygen waters occur within semi-enclosed oceanic basins with extended deep-water residence times (e.g., the Baltic Sea (Almroth-Rosell et al. 2021)) and coastal upwelling environments (e.g., the Peruvian margin (Demaison and Moore 1980)). The Santa Barbara Basin (hereafter 'Basin') is located in the Southern California Borderland and features a sill at 475m which forms a layer of poorly mixed water between the sill and its maximum depth at approx. 590 m. Historically, annual upwelling events in the winter and spring can introduce a flushing event in the Basin (Bograd et al. 2002; Sholkovitz and Gieskes 1971), although these events do not happen every year (McWilliams et al. 2024; Reimers et al. 1990). Due to a relatively high sedimentation rate in the Basin (1-10 mm yr^{-1}), these shifts in bottom water redox regime have been well documented in the varved sediments of the Basin's depositional center (hereafter, 'Depocenter') (Schimmelmann and Lange 1996). One predominant feature of the Basin's sedimentary record are lighter-colored, diatom-rich laminae that correspond to late summer/early fall in the Basin. These laminae also correspond to periods when the Basin's bottom waters stagnate, allowing anoxia and the

subsequent development of expansive mats of giant sulfur-oxidizing bacteria (hereafter 'mats') in the Basin's Depocenter (Bernhard et al. 2003; Kuwabara et al. 1999; Reimers et al. 1996a; Valentine et al. 2016; Yousavich et al. 2024). To perform their chemoautotrophic metabolism, i.e., nitrate reduction coupled to sulfide oxidation, the mats hyper-accumulate nitrate from the bottom water in intracellular vacuoles, enabling them to migrate deeper into sulfidic sediment for access to their electron donor (Fossing 1995; McHatton et al. 1996).

Mats in the Basin are concomitant with high fluxes of NH_4^+, Fe^{2+}, and PO_4^{3-} from sediment and require a depletion in iron oxides so that free hydrogen sulfide can reach the sediment-water interface and allow the mats to proliferate (Yousavich et al. 2024). Previous benthic surveys showed that mats disappear from the Basin Depocenter after complete nitrate depletion in the water column and appear further upslope where anoxic water still contains nitrate (Valentine et al. 2016). Studies from oxygen minimum zones on the Peruvian margin (Sommer et al. 2016) and in the Baltic Sea (Seitaj et al. 2015) have further shown that bottom waters turn euxinic, i.e., accumulate hydrogen sulfide in the water, once the sulfide-oxidizing mats vacate an area in response to nitrate deficiency. A long-term study in the Basin's water column conducted by the California Cooperative Oceanic Fisheries Investigations (CalCOFI, https://calcofi.org/data/) has shown that Basin flushing is becoming less frequent, while periods of anoxia and nitrate deficiency below the sill have increased in frequency, duration, and distribution since the 1950's (Qin et al. 2022). Additionally, the Basin's sedimentary record suggests annual flushing events with oxygenated water until the 1970's, after which changes in the California Current System weakened upwelling in the North Pacific, in turn weakening flushing events in the Basin (Palacios et al. 2004). Accordingly, increasing anoxia and nitrate deficiency in the Basin may push sediments towards a sulfidic state, beginning in the Basin's

Depocenter and dispersing to shallower depths concertedly with an increase in the magnitude and duration of anoxic events. If sulfidic conditions became present in the bottom water, this euxinia would create an environment that is hostile to larger benthic organisms such as cephalopods and crustaceans; pulses of sulfide from anoxic waters have been implicated in fish kills off the coast of Africa (Hamukuaya et al. 1998).

Here we present results from four expeditions to the Santa Barbara Basin between 2019 and 2023, reporting a distinct geochemical shift in the sedimentary redox environment in response to increasing marine anoxia. We collected sediment and conducted in-situ experiments on the seafloor along Basin depth transects characterized by different redox regimes. Through a combination of biogeochemical analyses, in-situ observations, and extensive historical data, we report evidence that the benthic environment of the Basin is shifting towards a sulfidic state, which is associated with a loss of highly reactive iron in the Basin's upper sediments in response to increased deoxygenation. The data presented here expands our knowledge on early sediment diagenesis, particularly the formation and preservation of iron and sulfide mineral phases, in transiently deoxygenated environments and provides a glimpse into potential future shifts in their redox state.

Shift from a ferruginous to a sulfidic state in the Basin's sediment in response to persistent deoxygenation

To assess the effect of increasing deoxygenation in coastal California bottom waters through the late 20th and early 21st century, it was imperative to analyze long-term trends in the water column and sediment in tandem. The Depocenter sediment of the Basin has been sampled

and analyzed for porewater Fe^{2+}, porewater sulfide, and sulfate reduction rates at several occasions since the 1980's: February, June, and October of 1988 in Reimers et al. (1996a) ; February and November of 1995 in Kuwabara et al. (1999) and Zheng et al. (2000) ; November 2019; July 2021; June 2022; and June 2023. All results from 2019 (aside from iron mineral speciation) were reported initially in Yousavich et al. (2024); results from the last three sampling campaigns (2021-2023) are reported here for the first time and compared to previous data. Depocenter profiles for 2019 and 2023 were reported from the NDRO station, which was our closest sampling location to the sites sampled in 1988 and 1995. Details of the Depocenter and other sampling stations can be found in Appendix B, Fig. 1 & Table 4.

Our analyses indicate that concentrations of porewater Fe^{2+}, a product of benthic iron reduction, decreased in recent years, displaying only a weak peak at the sediment-water interface (< 20 μM since 2019 in the top 1 cm layer) and near-zero values below (Fig. 3-1c & 1f). These declines in porewater Fe^{2+} in the Basin Depocenter sediment are accompanied by an increase in porewater sulfide (Fig. 3-1d & 1g) particularly near the sediment-water interface. This shift from a ferruginous sedimentary state to a sulfidic sedimentary state coincides with the appearance of periodic total nitrate depletion below the Basin's sill (Fig. 3-1c) and a weakening in the intensity of flushing events in the Basin (Bograd et al. 2002; Zheng et al. 2000).

The most intense flushing events appear to correspond with transitions from El Niño to La Niña climate patterns, when the California Current System is strengthened and warm surface waters in the California Bight are replaced with cooler waters (Bograd et al. 2002; McWilliams et al. 2024). El Niño events, which are increasing in frequency along with global temperatures(Cai et al. 2014), coincide with the most extreme anoxic conditions that have been observed in the Basin. The presence of authigenic molybdenum minerals in the Basin's

sediments, which require anoxia in the bottom waters and at least 10 μM porewater sulfide near the sediment-water interface to form, indicate El Niño-related anoxia in the Basin in 1972, 1982 and 1990 (Zheng et al. 2000). Predictions of oxygen conditions in basins off the coast of California from coupled physical-chemical models are inaccurate at predicting the duration and intensity of anoxia due to inadequate spatial and temporal resolution (McWilliams et al. 2024). It is thus important to resolve the frequency and duration of these anoxic events, and how it changed over time, in order to understand the effects of expanding anoxia on sediment biogeochemistry.

Using DIVA (Data-Interpolating Variational Analysis) gridded values in the Ocean Data Viewer, we determined that anoxic events in the Basin have increased in frequency; 17% of days between 1985-1990 had an estimated $[O_2] < 2$ μM and 55% of days between 2015 and 2020 had an estimated $[O_2] < 2$ μM. These periods of anoxia also lasted an average of 185 days longer (Appendix B, Fig. 2). Our results indicate that as El Niño events become more frequent and stronger, and as Basin flushing becomes weaker, the Basin will continue to shift towards a sulfidic sediment state. A shift towards sulfidic sediment is further suggested by our Spearman rank correlation, which shows that porewater Fe^{2+} in the Basin is positively correlated ($\rho = 0.62$) while porewater sulfide is negatively correlated with bottom water oxygen concentration ($\rho = -0.61$, Appendix B, Table 1). Additionally, several products of organic matter degradation like alkalinity ($\rho = 0.63$), ammonium ($\rho = 0.70$), and phosphate ($\rho = 0.34$) correlate positively with water depth (Fig. 3-2), indicating that organic matter degradation increases towards the Basin's Depocenter, where this shift from ferruginous to sulfidic sediment state is occurring.

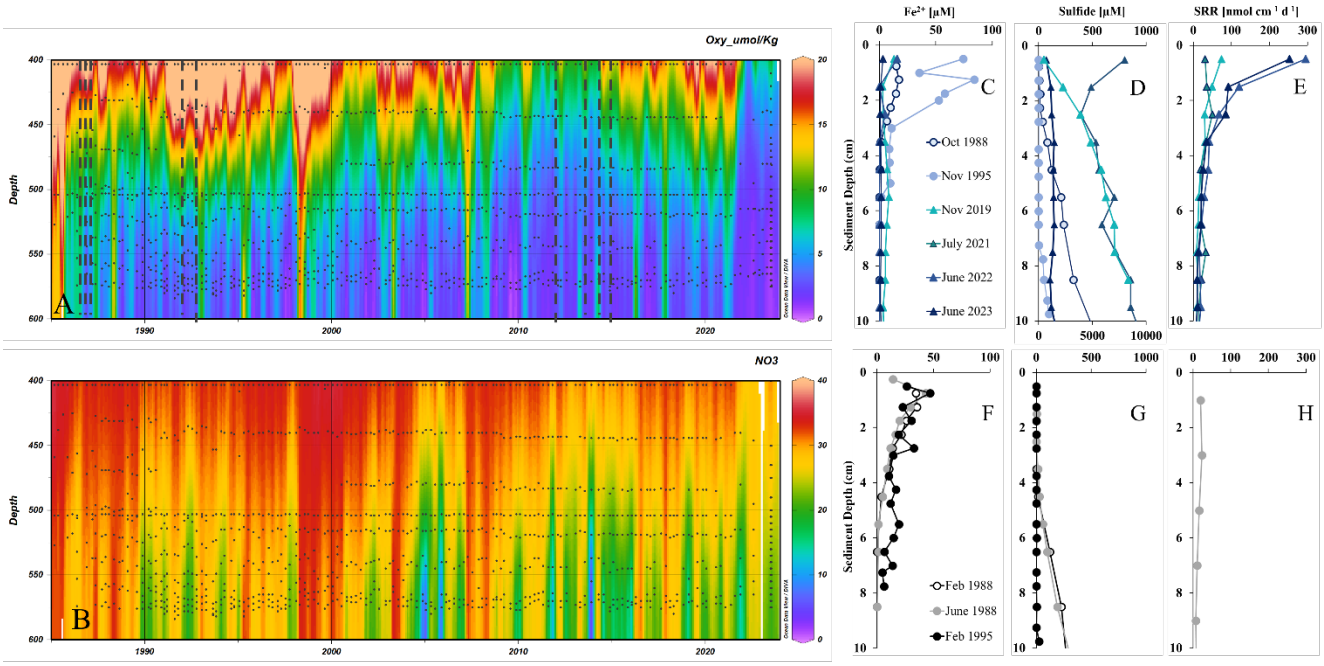

Figure 3-1: Bottom water and sediment redox over time in the Basin Depocenter. **A.** Oxygen concentration (µmol Kg^{-1}) below 400 m depth in the Basin from 1985-2023. Vertical dashed lines represent sampling time-points represented in d-h. **B.** Nitrate concentration (µmol Kg^{-1}) below 400 m depth in the Basin from 1985-2023. (**C, D & E).** Sediment porewater Fe^{2+} concentrations and sulfide concentrations, and microbial sediment sulfate reduction rates (SRR) in the Depocenter during anoxic bottom water conditions (**F, G & H).** Sediment porewater Fe^{2+} concentrations and sulfide concentrations, and microbial sulfate reduction rates in the Depocenter during oxygenated bottom water conditions. (**A**) and (**B**) were created using DIVA gridding in the Ocean Data Viewer and are based off of CalCOFI observations. Black dots in (**A**) and (**B**) represent discrete samples from CalCOFI and Winkler titrations from May 1970 (Sholkovitz and Gieskes 1971) as well as oxygen optodes on CTD casts from 2022, and 2023. Sediment porewater profiles and microbial rates from 1988 taken from (Reimers et al. (1990) and Reimers et al. (1996a) and profiles from 1995 taken from Kuwabara et al. (1999). Full oxygen and nitrate profiles since 1956 in the Basin can be seen in Appendix B, Fig. 3.

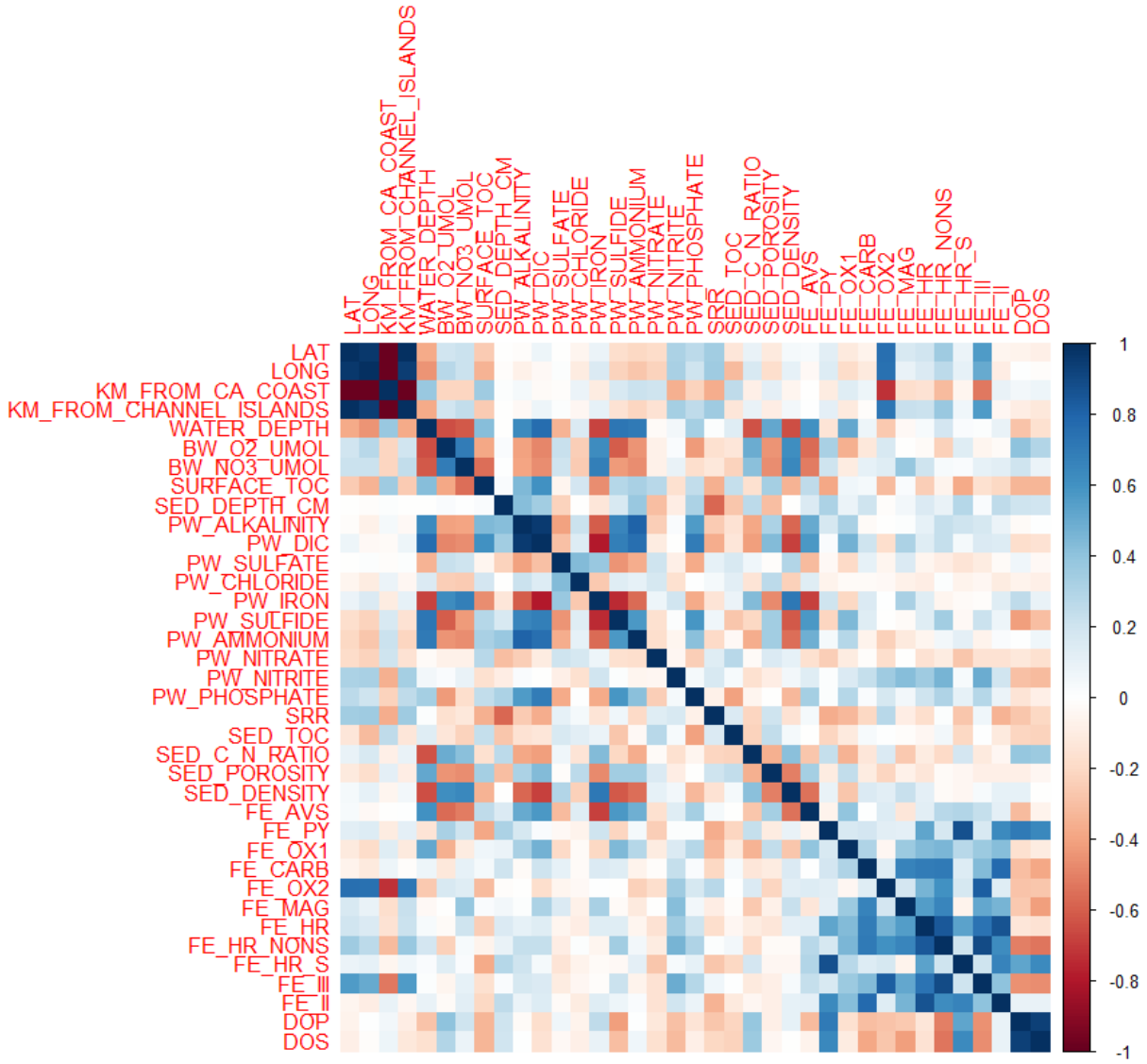

Figure 3-2. Relationship of geochemical parameters in the Basin benthic environment.

Results of the Spearman Rank Correlation test on measured parameters in 2019 (Yousavich et al. 2024) and 2023 in a heatmap. Red corresponds to a negative correlation of two parameters and blue corresponds to a positive correlation of two parameters. The darker the color, the stronger the correlation. Parameters that start with BW, PW, and SED represent bottom water, porewater, and sediment solid phase, respectively. "LAT" is latitude, "LONG" is longitude, KM is kilometers, CM is centimeters, SRR is sulfate reduction rate, TOC is total organic carbon, FE_AVS is iron mono-sulfides, FE_PY is pyrite, FE_CARB is iron carbonates, FE_OX1 is poorly crystalline iron oxides, FE_OX2 is highly crystalline iron oxides, and FE_MAG is magnetite. FE_HR is the sum of these fractions. FE_HR_NONS is the sum of these fractions except FE_AVS and FE_PY. FE_III is the sum of FE_OX1, FE_OX2, and FE_MAG. FE_II is the sum of FE_AVS, FE_PY, and FE_CARB. DOP and DOS are degree of pyritization (Fe_{py}/Fe_{HR}) and degree of sulfidation ($Fe_{py} + Fe_{AVS}/Fe_{HR}$), respectively. Correlation coefficients

and p-values are presented in Appendix B, Tables 1 & 2.

Extended anoxia leads to a loss of sedimentary iron in the Basin.

The waters below the Basin sill and up to approx. 400 m water depth are enriched in Fe^{2+} during times of anoxia (Robinson et al. 2022; Shiller et al. 1985). Additionally, seasonal transitions from an Fe^{2+}-dominated sediment-water interface to a sulfide-dominated sediment-water interface have been observed in the Basin's Depocenter sediment (Reimers et al. 1990). To evaluate changes in early diagenesis of iron and sulfide minerals throughout the Basin, we utilized geochemical sediment porewater analyses, radiotracer studies of bacterial sulfate reduction, and a sequential extraction protocol designed for iron and sulfide mineral speciation in modern sediments (Poulton 2021). We applied these analyses to sediment samples taken on a transect from the Depocenter (580 m) to just above the sill (450 m) in 2019 and in 2023 (Appendix B, Fig. 1).

We found that highly crystalline iron oxide content (Fe_{ox2}) in Basin sediment was negatively correlated (ρ = -0.72, Fig. 3-2) to distance from the California coast (defined as distance from the outlet of San Jose Creek, the closest stream outlet to the study site). The primary delivery of sedimentary iron to the Basin is via turbidity currents through submarine canyons along the coast (Schimmelmann and Lange 1996), thus decreased highly reactive iron content (Fe_{HR}) towards the southern end of the Basin is likely explained by physical distance from the California coast. Acid volatile sulfides (predominantly in the form of iron mono-sulfides, therefore here termed Fe_{AVS}) was negatively correlated with bottom water oxygen (ρ = -0.56), nitrate (ρ = -0.52), and porewater iron (ρ = -0.68). Fe_{py} (elemental sulfur and pyrite) showed no strong correlations with any measured constituents, except a slight negative relationship with sulfate reduction rate (ρ = -0.36) and surface organic carbon (ρ = -0.38).

Similarly, the degree of pyritization (DOP in Fig. 3-2), the ratio of Fe_{py}/Fe_{HR}, was negatively correlated with surface TOC and sulfate reduction rate. DOP was also negatively correlated with porewater sulfide despite sulfide being necessary for Fe_{py} formation (ρ = -0.41). This negative relationship between DOP and sulfate reduction rate agrees with previous findings (Hardisty et al. 2018). Results from our sulfate reduction determinations suggest this negative relationship is caused by Fe^{2+} sequestration into Fe_{carb} (iron carbonates): bicarbonate is a byproduct of sulfate reduction (Jørgensen et al. 2019), and we detected a build-up of Fe_{carb} where sulfate reduction rates were high (Fig. 3-4).

Just above the Basin sill (NDT3-D, 450 m) we found an accumulation of Fe_{py} within 3-cm of the sediment-water interface 2019 (Fig. 3-3B), which was not present in 2023 (Fig. 3-3E) nor was this Fe_{py} detected directly below the sill at 500 m in both years (NDT3-C, Fig. 3-3H & K). Sediment at NDT3-C showed a depletion in Fe_{py} content near the sediment-water interface from 2019 to 2023 (Fig. 3-3H compared to 3-3K), albeit with a slight growth in Fe_{AVS} (metal mono-sulfide) content. Fe_{ox1} (poorly crystalline iron oxides), Fe_{ox2} (highly crystalline iron oxides), and Fe_{mag} (magnetite), the sum of which constitute iron oxide content in the sediment, were similar in magnitude in 2019 and 2023, above (NDT3-D) and below (NDT3-C) the sill. The iron oxide content at 500 m was markedly depleted just below the sediment-water interface in 2023 (Fig. 3-3J compared to 2G), coinciding with a depression in the porewater Fe^{2+} (Fig. 3-3L compared to 3-3I), but more replication is needed to determine if local-scale heterogeneity could explain those differences.

Deeper in the Basin (NDT3-A, 570 m), there was a slight build-up of Fe_{AVS} near the sediment-water interface in 2023 that was absent in 2019 (Fig. 3-4E) along with an increase in sulfate reduction rates (3-3F). The Depocenter (NDRO, 580 m) exhibits a high Fe(II) content

relative to iron oxide content. Fe(II) is primarily in the form of iron carbonates, not iron sulfides (Figs. 3-3H & K). Integrated sulfate reduction rates (0-10 cm sediment depth) were high below the sill, peaking at ~560 m (10.6 mmol m^{-2} d^{-1}, Appendix B, Table 5). Despite these high rates of sulfate reduction in the deeper Basin, the degree of pyritization (Fe_{py}/Fe_{HR}) was low throughout the entire Basin (0.16 ± 0.15), only approaching 0.5 near the sediment-water interface at the shallowest station below the sill. This degree of pyritization is commonly used to distinguish between sediments deposited in ferruginous and euxinic bottom water conditions, with values below 0.7 indicating ferruginous conditions and values above 0.7 indicating euxinia (Hancock et al. 2019; Liu et al. 2020; Poulton 2021).

As previously reported, the Fe_{PY}/Fe_{HR} ratio in Santa Barbara Basin sediments are anomalously low (<0.7) for sediments with high amounts of sulfide detected in the porewater (Hardisty et al. 2018; Raven et al. 2016; Reimers et al. 1996a). This low ratio has been attributed to high organic matter delivery rates and high rates of ongoing organoclastic sulfate reduction (which produces bicarbonate as a byproduct) in sediments where iron sulfides are accumulating (Hardisty et al. 2018). Our results indicate that reduced forms of iron are primarily shunted into iron carbonates below the Basin sill, especially in the Depocenter of the Basin where sulfate reduction rates are highest. These iron carbonates could be transformed to pyrite later in diagenesis via the polysulfide pathway, which is preferred in alkaline sediments (Kamyshny Jr and Ferdelman 2010). This pathway, however, requires sufficient elemental sulfur to react with Fe(II) minerals (Liu et al. 2020). While we did not assess elemental sulfur separate of pyrite in the Basin sediment, the low ratio of Fe_{py} to Fe_{carb}, particularly below the Basin sill, indicates that deeper pyrite formation would require deeper elemental sulfur formation as well. Interestingly, the highest pyrite content in the sediment was measured at both NDT3-D (Fig. 3-3B) and SDT3-

D (Appendix B, Fig. 3) in 2019, both of which are the only stations that lie above the Basin sill. The presence of sulfur-oxidizing bacteria below the sill could interfere with the production of Fe_{Py} and Fe_{AVS}, and encourage Fe(II) to instead form iron carbonates, or flux out of the sediment entirely.

The sediment iron content measured in 2023 revealed a relatively steady highly crystalline iron oxide content in Depocenter sediment, but a loss of Fe(II) (-30.3 ± 8.2 μmol Fe/g) and poorly crystalline iron oxides (-66.4 ± 64.5 μmol Fe/g) in the upper 3 cm of sediment (Fig. 3-4J & K, respectively). Additionally, the high flux of Fe^{2+} seen from the sediment to the water in the deep Basin in 2019 (Robinson et al. 2022), which was absent in 2023 (Fig. 3-6), could explain why surface sediment appears relatively depleted in highly reactive iron content compared to shallower sediment in the Basin. This decrease in sedimentary iron content and change in Fe^{2+} flux could indicate that deeper stations below the sill, which experience frequent deoxygenation, are losing their iron content due to cycles of deoxygenation and reoxygenation. In contrast, the nearby Santa Monica Basin rarely (if ever) experiences full anoxia and has an enrichment of iron oxide content in the deep Basin surface sediment due (in part) to upward diffusive flux and re-oxidation of porewater Fe^{2+} in the hypoxic bottom waters (Figueroa et al. 2023).

It is commonly believed that Fe^{2+} that fluxes into the water column during anoxia is re-precipitated as poorly crystalline iron oxides once it reaches the oxycline (as it was the case, for example, at around 500 m water depth in July 2023 in the Basin, Fig. 3-1B) or once oxygenated waters return (Reimers et al. 1990; van de Velde et al. 2020a). It is possible that Basin Fe^{2+} is rather transported in particulate form by bottom water or mid-water currents upslope and potentially out of the Basin entirely. This hypothesis is supported by the presence of currents

along the Basin's northern slope that carry water down the California Coast in-between Basin flushing events (Bograd et al. 2002; McWilliams et al. 2024). The overall depletion of both oxidized and reduced forms of iron near the sediment-water interface below the sill could be indicative of a net loss of highly reactive iron from sediments below transiently deoxygenated systems.

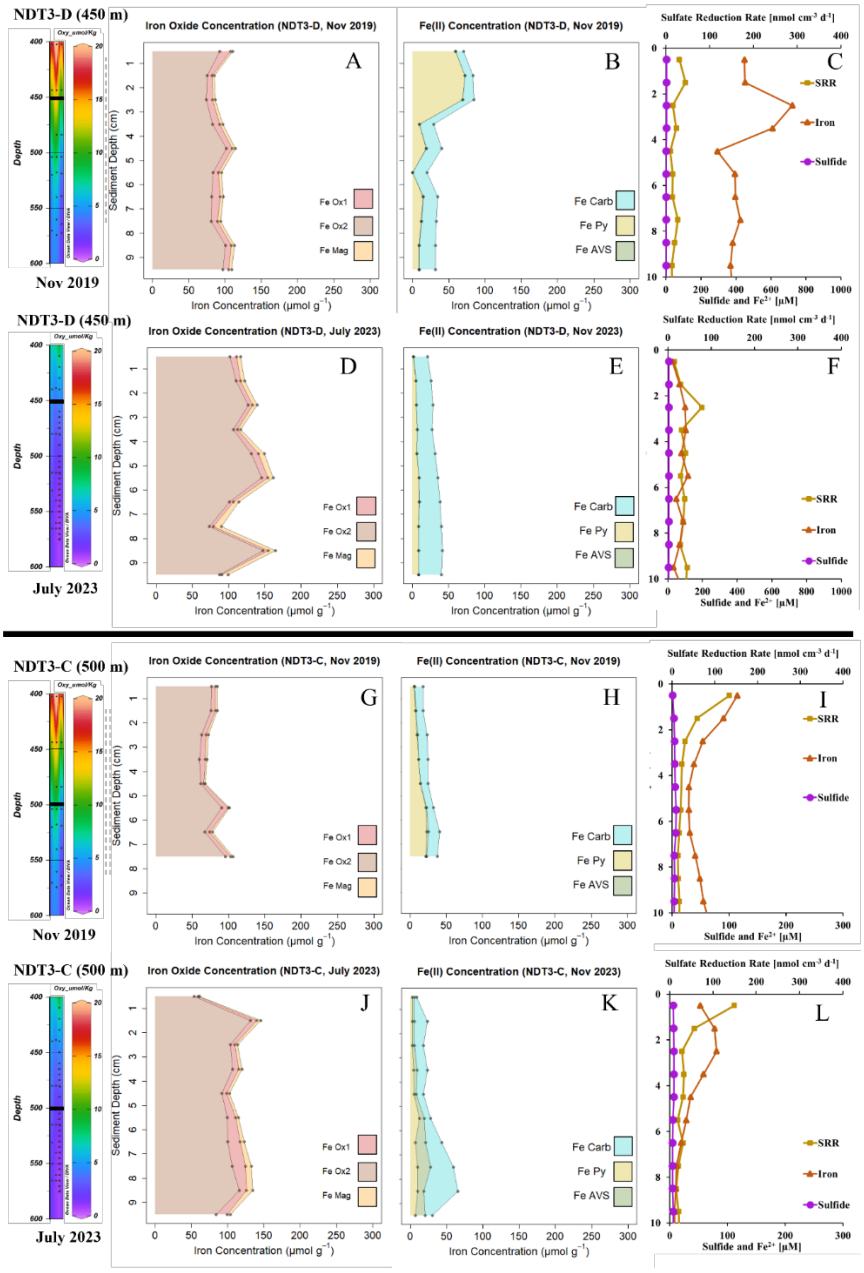

Figure 3-3: Sediment iron minerals and parameters relevant for their formation. Results from sediment taken from NDT3-D station in 2019 (**A-C**) and in 2023 (**D-F**).**:** Results from sediment taken from NDT3-C station in 2019 (**G-I**) and in 2023 (**J-L**)**. A, D, G and J** represent iron oxide content while **B, E, H, and K** represent iron sulfide content. **C, F, I, and L** show porewater iron, sulfide, and sulfate reduction rate activity. Note the change in scale of the x-axis between NDT3-D and NDT3-C. Definitions for each iron fraction can be found in the methods section. Briefly, Fe_{AVS} is iron monosulfides, Fe_{Py} is pyrite, Fe_{carb} is iron carbonates, Fe_{Ox1} is poorly crystalline iron oxides, Fe_{Ox2} is highly crystalline iron oxides, and Fe_{mag} is magnetite. An excerpt from the water column oxygen concentration during both timepoints is provided on the left side of the Table, with the horizontal black bar representing the sampling

depth. Sediment core photos are provided to allow visual comparison of sediment in November 2019 vs. July 2023.

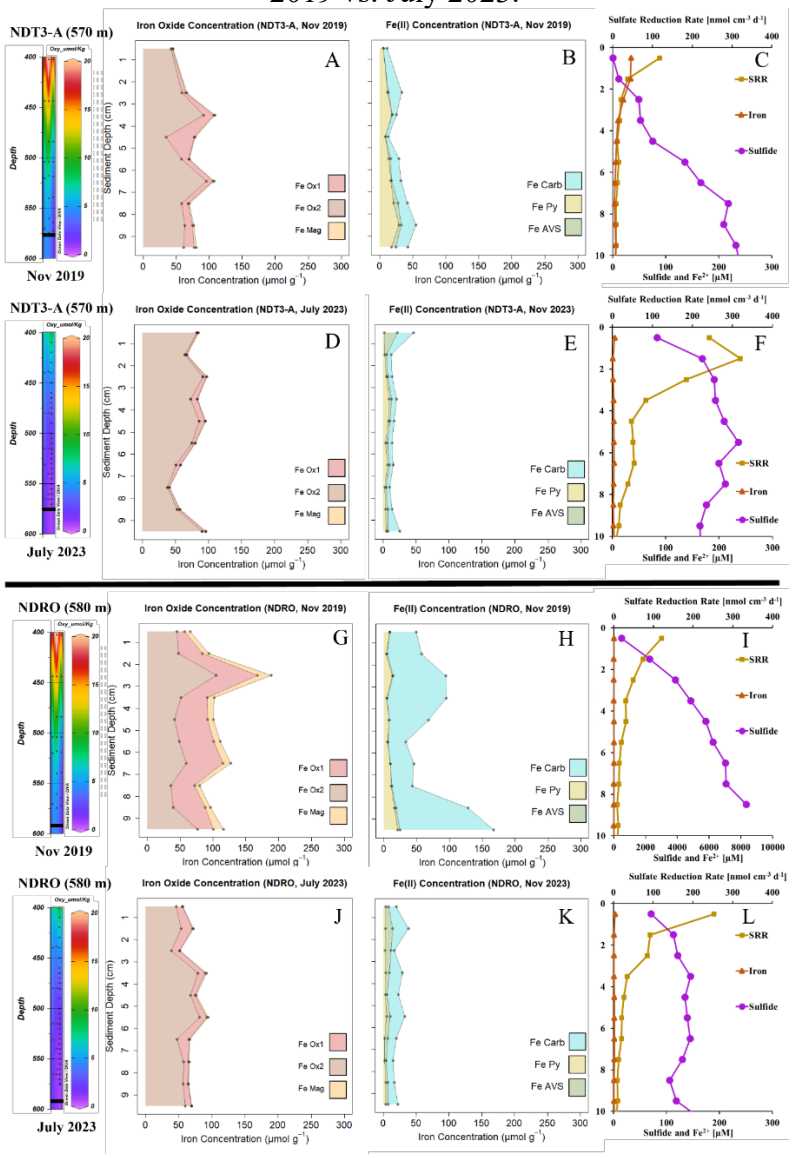

Figure 3-4: Sediment iron minerals and parameters relevant for their formation. Results from sediment taken from NDT3-A station in 2019 (**A-C**) and 2023 (**D-F**). **g-i:** Results from sediment taken from NDRO station in 2019 and in 2023 (**J-L**). **A, D, G, and J** represent iron oxide content while **B, E, H, and K** represent iron sulfide content. **C, F, I, and L** show porewater iron, sulfide, and sulfate reduction rate activity. Note the change in scale of the x-axis in (**i**) compared to other porewater profiles. Definitions for each iron fraction can be found in the methods section. Briefly, Fe_{AVS} is iron mono-sulfides, Fe_{Py} is pyrite, Fe_{carb} is iron carbonates, Fe_{Ox1} is poorly crystalline iron oxides, Fe_{Ox2} is highly crystalline iron oxides, and Fe_{mag} is magnetite. An excerpt from the water column oxygen concentration during both timepoints is provided on the left side of the Table, with the horizontal black bar representing the sampling depth. Sediment core photos are provided as an inset of the first panel to allow visual comparison of sediment in November 2019 vs. July 2023.

Pulses of sulfide into the water column follow iron exhaustion.

Extended anoxia leads to a loss of sedimentary iron in the Basin.

We deployed in-situ benthic flux chambers (hereafter 'chambers') to quantify benthic fluxes of solutes, which captured changes in temporal and spatial distribution of Fe^{2+} fluxes in the Basin depending on bottom water anoxia. We also recorded a Basin flushing event using a benthic lander ('ABISS') equipped with sensors that recorded pH, dissolved oxygen, and temperature at 570 m depth from July 2021 through June 2022.

Sensors aboard the ABISS lander recorded an increase of oxygen (up to 11.5 μM) from November-December 2021 alongside an increase in pH and a decrease in bottom water temperature (Fig. 3-5). These changes indicate that cooler, oxygenated water came over the sill during this time, reoxygenating the Basin's bottom waters as is typical during winter/spring upwelling season in the Southern California Bight. While the oxygen sensor was programmed to stop recording near the end of 2021, the pH and temperature logs continued through June of 2022. Assuming the in-situ measurements recorded on the ABISS lander between November 2021 – January 2022 (Figure 3-5) are representative of a typical flushing event, we estimate these events last approx. sixty days before anoxia is re-established in the Basin's Depocenter.

Notably, there are distinct periods in March 2022 and May-June 2022 where oscillations in the pH meter similar to November 2021 were recorded, but there was no discernible coinciding change in bottom water temperature. The absence of a temperature change suggests that the pH disturbances were either caused by isothermal intrusion of oxygenated water, or by changes within the bottom water chemistry originating from the sediment. Oxygen measurements by CalCOFI (April 2022) and during our one-day field trip (July 2022) do not

indicate a large-scale influx of oxygenated water into the Basin occurring in either March or May 2022, but as anoxia is quickly re-established (flushing events last approx. 60 days), the possibility cannot be ruled out. Absent an influx of oxygenated water, it is also possible that these pH perturbations are due to a flux of bicarbonate ions into the bottom water, which are the byproduct of anaerobic organic carbon remineralization (e.g., sulfate reduction). In 2023 we detected an alkalinity release from the Depocenter sediment (0.09 mmol m^{-2} d^{-1}, Appendix B, Fig. 6). Similarly, an increase in alkalinity in response to benthic bicarbonate release has also been reported from the Baltic Sea (van de Velde et al. 2023).

Additionally, organoclastic sulfate reduction (e.g., acetate oxidation, Eq. 1) consumes protons and produces bicarbonate which raises pH. Sulfide oxidation coupled with nitrate reduction (Eq. 2), and anabolic CO_2 fixation done by chemoautotrophic organisms such as those that populate the Basin's mats (Teske and Nelson 2006), consume protons which also raises pH.

$$CH_3COO^- + SO_4^{2-} + H^+ \rightarrow 2HCO_3^- + H_2S$$

[1]

$$HS^- + 1.6NO_3^- + 0.6H^+ \rightarrow SO_4^{2-} + 0.8N_2 + 0.8H_2O$$

[2]

$$6CO_2 + 24H^+ \rightarrow C_6H_{12}O_6 + 6H_2O$$

[3]

Given the high porewater sulfide measured at the sediment-water interface in July 2022 (800 µM, Fig. 3-1G), and the presence of mats in the Basin's Depocenter along with nitrate in the bottom water in July 2022, the pH oscillations observed could be due to a sulfide oxidation

either at the sediment-water interface or in the bottom water. Additionally, fluxes of sulfide into the bottom water were documented in July 2023 based on chamber incubations from 520 – 580 m water depth in the Basin (Fig. 3-6). These measurements represent the first directly-measured sulfide flux into the Basin from the sediment. A flux of sulfide from the Basin's sediment during anoxic water column conditions has been previously postulated based on diffusion estimates from porewater profiles (Kuwabara et al. 1999). The largest flux recorded in our study was 1.33 ± 1.09 mmol m^{-2} d^{-1} in the Basin's Depocenter. The observed fluxes of sulfide coincided with strong dampening of iron fluxes (4.1 compared to 0.1 mmol m^{-2} d^{-1} in 2019 and 2023, respectively), which further re-enforces the hypothesis that reactive iron content in the deepest parts of the Basin is being exhausted over time (Yousavich et al. 2024).

The trend in increasing deoxygenation in the oceans has been mostly attributed to increased stratification and lower dissolved oxygen solubility due to warmer surface water temperatures (Stramma et al. 2008) and eutrophication leading to higher primary productivity (Stramma et al. 2010). One of the largest extinctions of marine metazoan life happened at the Triassic-Jurassic boundary (Dunhill et al. 2018). This mass extinction is largely ascribed to localized de-oxygenation and pulses of euxinia in shallow marine environments (Bond et al. 2023). These changes in marine redox environments followed increases in atmospheric carbon concentrations due to volcanic activity and increased nutrient input to the oceans (Ruhl et al. 2011). Atmospheric carbon (CO_2) concentrations have been increasing on Earth since at least the beginning of the 20th century (Hansen et al. 1981). Small increases in organic matter delivery to marine sediment can cause a semi-irreversible shift from ferruginous to sulfidic sediment state, allowing for a flux of sulfide into the water (van de Velde et al. 2020b). Fe_{Py}/Fe_{HR} ratios from the Naples Beach outcrop (sediment age ~18-7 Ma), suggest that bottom water euxinia occurred

several times in the pre-cursor of the Santa Barbara Basin during the Miocene Epoch (Hancock et al. 2019). The patterns of alternating oxygenated, ferruginous and euxinic bottom waters interpreted from these Fe_{Py}/Fe_{HR} ratios suggest transient deoxygenation associated with upwelling systems. The frequency of deoxygenation suggested by the Naples Beach outcrop (approx. 18% of observations over the 11 Ma indicated oxygenated conditions) is much greater than modern upwelling systems, however. Given the apparent exhaustion of iron oxide content in near-surface sediments in the Basin's deep waters, and the apparent shift away from a ferruginous sediment state below the sill, the Santa Barbara Basin could develop semi-permanent euxinia (i.e., lasting years at a time with only occasional oxygenation events) in the bottom water in the future, as was seen in its pre-cursor during the Miocene epoch (Hancock et al. 2019). The Basin appears to have developed nitrate depletion, a pre-requisite to euxinia, under the sill at least three times since 1985, thus given our measured sulfide flux it is likely that the Basin has experienced euxinia recently and that this may become a frequent phenomenon in the future.

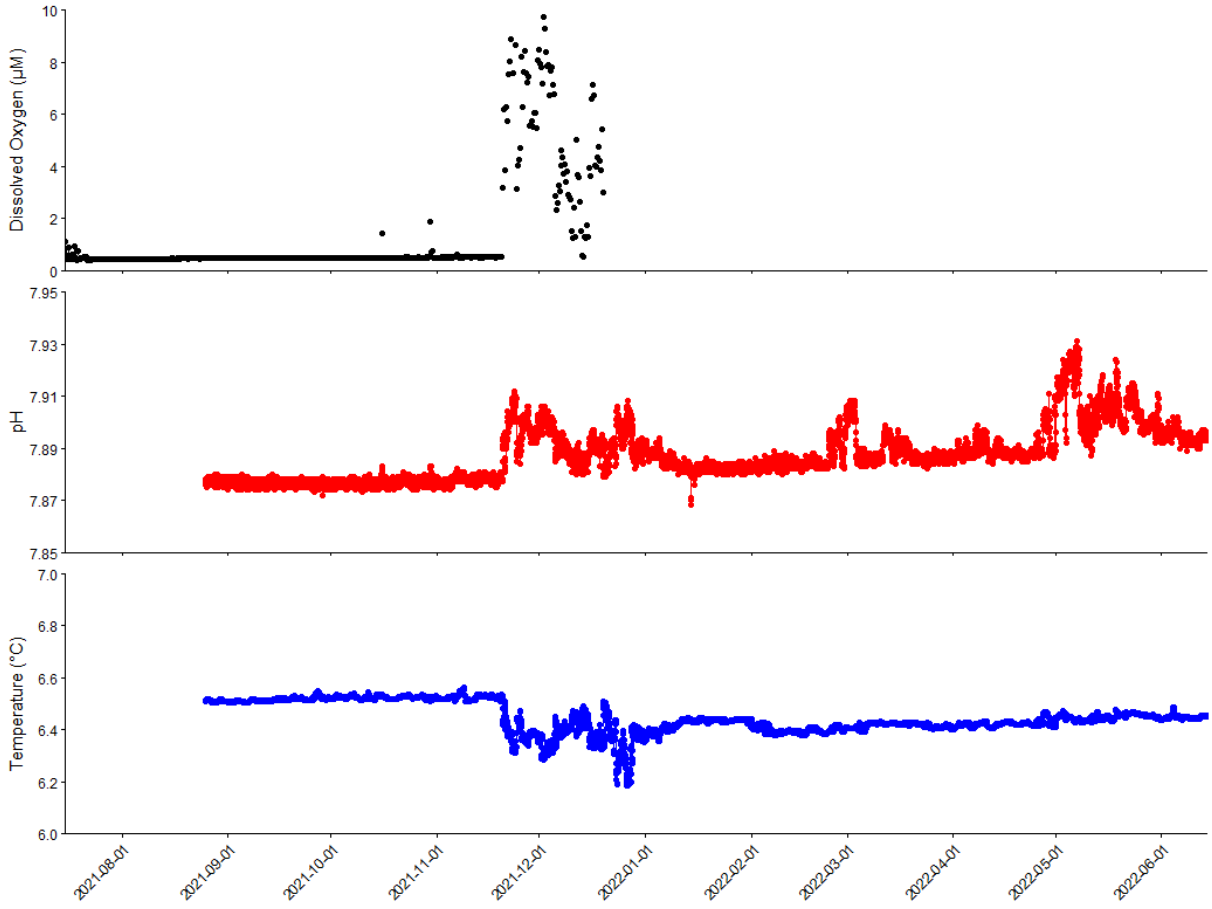

Figure 3-5. Dissolved oxygen, pH, and Temperature from the ABISS lander. Dissolved oxygen concentrations from sensors aboard the ABISS lander are in the top panel (black dots), pH is in the middle panel (red), and temperature in degrees Celsius is in the bottom panel (blue).

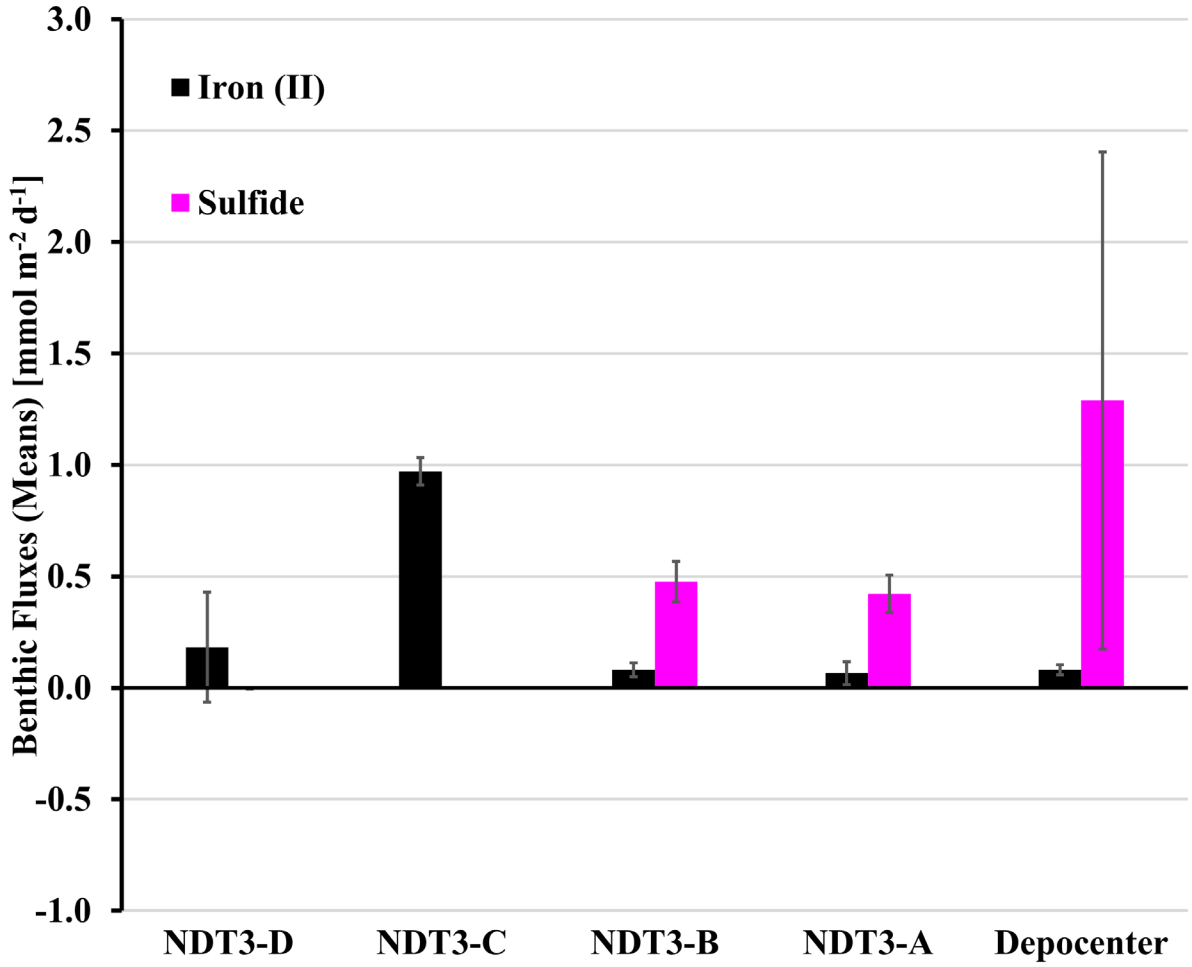

Figure 3-6. Benthic fluxes of sulfide and Fe^{2+} from June-July 2023.
Sulfide and Fe^{2+} fluxes calculated from changes in concentrations in benthic flux chambers. Error bars represent standard deviation from multiple benthic flux chamber deployments per site. Details of changes in concentration for each chamber can be found in Appendix B, Fig. 5.

Methods

Study Site and Sampling Procedures

Samples from the Santa Barbara Basin were collected in 2019, 2021, 2022, and 2023 at several stations along a depth transect traversing different water and sediment redox conditions (Appendix B, Table 3). Sampling details (dates, vessels, stations, equipment, parameters) are shown in Appendix B, Table 3. Sediment cores (push cores or multicorer cores) were immediately transferred to 6°C and sub-sampled for porewater analyses, solid phase analyses,

and radiotracer experiments. Sediment processing prior to analyses is described in detail in Yousavich et al. (2024).

Solid Phase Analyses

Porosity/Density samples from 2023 were collected and analyzed the same as described in Yousavich et al. (2024). Sediment sampled in 2019 for sequential extractions was collected in Whirl-Packs™ during core slicing and immediately frozen. Sediment samples were taken from the middle of the bag once thawed for sequential extraction. Sediment sampled in 2023 for sequential extractions was weighed into two separate, argon-flushed 2-mL plastic vials (one aliquot for sulfide extractions, one aliquot for iron extractions) and immediately frozen. Extractions of 2019 and 2023 sediments were both performed in 2023.

One aliquot of wet sediment was treated with a standard two-step sulfide extraction (Fossing and Jørgensen 1989). First, sediment was incubated with 6 N HCl to release the acid volatile sulfur (AVS, mainly Fe mono-sulfide) and then with a chromium(II) chloride solution to release the chromium reducible sulfur (CRS, pyrite and elemental sulfur). These two solid-phase sulfur species were recovered in separate 6-mL 5% zinc acetate traps. The contents of AVS and CRS were analyzed after dilution spectrophotometrically by the methylene blue method (Cline 1969). Fe_{AVS} was calculated from the measured AVS content of each sample assuming 1:1 Fe:S stoichiometry. Fe_{py} was calculated from the measured CRS content of each sample assuming negligible elemental sulfur content and a 1:2 Fe:S stoichiometry.

Sequential iron extractions followed the protocol of Poulton (2021). These extractions consisted of: (i) anoxic 0.5 N HCl (Fe^{2+} and total Fe measured separately), (ii) sodium dithionite/citrate, and (iii) ammonium oxalate/oxalic acid. The Fe(II) concentration of (i) was

determined spectrophotometrically by the ferrozine assay (Stookey 1970) ; while total Fe concentration of (i) was determined via the ferrozine assay after complexing with hydroxylamine hydrochloride. Total Fe from (ii) and (iii) were determined via the ferrozine assay.

The above procedure leads to four operationally-defined, distinct fractions. Fe_{carb}: Fe(II) from extraction (i), targeting AVS and carbonate; Fe_{ox1}: Fe(III) from extraction (i), targeting poorly crystalline iron oxides (e.g., ferrihydrite, lepidocrocite); Fe_{ox2}: total Fe from extraction (ii), targeting highly crystalline iron oxides (e.g., goethite, hematite); and total Fe from extraction (iii), targeting magnetite (Fe_{mag}). Final Fe(II) concentration for Fe_{carb} is the measured value for $Fe_{carb} - Fe_{AVS}$. Final Fe(III) concentration of Fe_{ox1} is the measured value of total Fe for $Fe_{ox1} - Fe_{carb}$. "Highly Reactive Iron" (Fe_{HR}) is defined by $Fe_{ox1} + Fe_{ox2} + Fe_{mag} + Fe_{AVS} + Fe_{pyr} + Fe_{carb.}$ Highly Reactive Fe(III) is defined as $Fe_{ox1} + Fe_{ox2} + Fe_{mag}$. Highly Reactive Fe(II) is defined as $Fe_{AVS} + Fe_{pyr} + Fe_{carb}$. Degree of pyritization is Fe_{py} / Fe_{HR} while degree of sulfidation is $(Fe_{Py} + Fe_{AVS}) / Fe_{HR}$. Note, in Poulton (2021) Fe_{carb} is referred to as $Fe(II)_{unsulf}$.

Sulfate Reduction

To determine ex-situ microbial sulfate reduction rates, whole round sub-cores were injected at 1-cm increments with 10 µL carrier-free ^{35}S-Sulfate radiotracer via pre-drilled, silicon-filled holes according to Jørgensen (1978). Details of the radiotracer injections and incubation procedures were identical to Yousavich et al. (2024). Lab-based analysis of sulfate reduction rates was accomplished following the cold-chromium distillation procedure (Kallmeyer et al. 2004).

Porewater Geochemistry

Concentrations of porewater total sulfide (Cline 1969), NH_4^+, PO_4^{3-}, and Fe^{2+} (Grasshoff et al. 1999) were determined with a Shimadzu UV-Spectrophotometer (UV-1800) immediately after core sectioning. Detection limits for total sulfide, NH_4^+, PO_4^{3-}, and Fe^{2+} were 1 µM. The detection limit for NO_3^- and NO_2^- was 0.5 µM. The analysis was calibrated using IAPSO seawater standard, with a precision and detection limit of 0.05 meq L^{-1}. Subsamples (1 mL) for sulfate (used to calculate sulfate reduction rates) were stored in O-ring sealed 2-mL plastic vials, frozen at -30°C and measured later using a Metrohm 761 ion chromatograph with a methodological detection limit of 30 µM (Dale et al. 2015).

Benthic In-Situ Investigations

Per station, two benthic flux chambers deployments were carried out by the HOV *Alvin* on the seafloor and recovered on the subsequent dive. Construction, deployment and operation of automated chambers followed those described in Yousavich et al. (2024) modified from Treude et al. (2009). Different than in previous deployments in the SBB (Yousavich et al., 2024), chambers were kept on their side during descent on the underwater elevator to avoid capture of surface water inside the chamber rather than shaking the chambers manually once they reached the seafloor. Chamber incubations lasted approx. 20h. Samples obtained from the overlaying water of the chambers were examined for the same geochemical constituents as described above (Porewater geochemistry). Benthic fluxes of sulfide, and Fe^{2+} were calculated as follows:

$$J = \frac{\Delta c}{\Delta t} * \frac{V}{A}$$

[4]

Where J is the flux in mmol m^{-2} d^{-1}, ΔC is the concentration change in mmol m^{-3}, Δt is the time interval in d, V is the overlying water volume in m^3, and A is the surface area of the sediment covered by the benthic flux chamber in m^2. An average flux within chambers was calculated for stations of similar depth.

ABISS Lander

The ABISS lander is an autonomous biogeochemical observatory, which is built upon a 2 m x 2m seafloor lander. For the Basin deployment, the lander was equipped with 2 oxygen optodes (Aanderaa™ 4330W with ultra-stable foils), a PyroScience™ AquapHOx-LX optical pH and temperature datalogger, an osmotic sampling system for microbial and geochemical sampling (e.g, as in Robidart et al. (2013), and a custom low-light camera system. The lander frame is anodized aluminum, with syntactic foam floatation and an EdgeTech™ acoustic release, which drops the steel ballast for ascent. Deployment of the ABISS lander occurred aboard the *R/V Nautilus* on July 15, 2021 with visual confirmation of its successful deployment undertaken by *ROV Hercules*. Recovery of the ABISS lander occurred on August 5, 2023 during dive 5211. Exact lander coordinates and water depth can be seen in Appendix B, Table 4. One oxygen optode was located on the top of the 2 meter tall floatation mast, but no data were recovered due to memory corruption. The other oxygen, pH, and temperature sensors were all located approximately 1 m above the seafloor on the lander's main deck.

Time-series oxygen and nitrate data

Time series maps were generated using Ocean Data View version 5.6.7–64 bit. All data is from CalCOFI except 1969/1970 oxygen data (Sholkovitz 1973) and from an oxygen optode

deployed on a CTD cast during our 2023 expedition. CalCOFI data after June 2021 is considered preliminary and may be subject to future changes. Gridded fields were calculated using DIVA gridding algorithm, with X scale-length of 5 and Y scale-length of 300.

Spearman Rank Correlation

2019 and 2023 station metadata (e.g., depth, latitude, longitude), bottom water chemistry, sediment solid phase, porewater, and microbial rate data were used to calculate the Spearman Rank Correlation Values for the Santa Barbara Basin. This analysis was conducted in R Studio (R 4.3.2) using the "cor" function with method set to "spearman". Significance testing at a 95% confidence interval was conducted and only correlations with a significant correlation ($p < 0.05$) were further examined and reported upon here.

Acknowledgements

We thank the captain, crew, and scientific party of the R/V *Atlantis*, R/V *Nautilus*, and R/V *Shearwater* as well as the crew of ROV Jason, HOV Alvin, and ROV Hercules for their technical and logistical support during the research expeditions. Special thanks go to T. Anders and S. Krause for supporting benthic flux chamber deployments and the Alvin basket coordination in 2023, respectively. We thank Tessa Holzmann, Alexandra Fowler, George Vetushko, Zoe Collins, Nick Leong, Ashley Huh, Sara Matsumara, Eleanor Arrington, Kyla Murphy, Hailie Kittner, Jacob Schmidt, Kelsey Gosselin, Chiara Corbo, Julianne McHenry, and Frank Kinnaman for assisting with shipboard and shore-based analyses. We thank Brooke Travis, Christopher Powers, Sarah Lott, and Virginia Edgcomb for their assistance in deploying the ABISS lander and collecting sediment in 2021. Funding for this work was provided by the

US National Science Foundation, OCE-1829981 (to TT) and NSF OCE-1756947 and OCE-1830033 (to DLV). Funding for 2021 sample collection and ABISS lander deployment was provided by NASA 80NSSC21K0478 (to JMB). Funding for the ABISS lander was supported by the National Aeronautics and Space Administration under Grant No. NNX17AB31G (to PRG), issued through the Planetary Science and Technology Through Analog Research program, The Gordon and Betty Moore Foundation grant #9208 (to PRG), and the National Science Foundation via NSF OCE-1635365 (to PRG). Further support was provided by the Max Planck Society/ Max Planck Institute for Marine Microbiology Bremen and the Helmholtz Association / Alfred-Wegener-Institute for Polar and Marine Research.

Data availability.

Data will be available upon publication of the manuscript.

Author contributions.

TT, DV, and DJY designed the project. FJ designed the benthic flux chambers. PG designed the ABISS lander. DJY and JMB collected sediments aboard R/V Nautilus in 2021. DJY, JMB, and PG transformed and interpreted ABISS lander and ROV Hercules data from 2021. TT and DV coordinated the 2022 expedition with the R/V Shearwater. TT, DV, DJY, and DR collected sediments aboard the R/V Shearwater in 2022. DJY and DR conducted geochemical and sulfate reduction rate analyses from the 2021 and 2022 samplings. TT and DV coordinated the 2023 expedition with the R/V Atlantis. TT, DV, FJ, DJY, DR, EK, JL and KH collected sediment and deployed/recovered benthic flux chambers using ALVIN in 2023. EK, JL and KH processed sediment cores at sea in 2023. DJY conducted geochemical analyses of

sediment porewater and benthic flux chamber water at sea in 2023. EK, JL, and TT performed sulfate reduction incubations at sea in 2023. DJY, EK, JL, and KH analyzed sulfate reduction rates from the 2023 sampling. DJY conducted solid phase analyses and sequential extractions. DJY and JL analyzed sequential extraction results. FJ and DJY analyzed benthic flux chamber data. DJY and TT wrote the manuscript with input from all co-authors.

Competing interests.

The authors declare no competing interests.

References.

Almroth-Rosell, E. *et al.* A regime shift toward a more anoxic environment in a eutrophic Sea in northern Europe. *Frontiers in Marine Science* **8**, 799936 (2021).

Bernhard, J. M., Visscher, P. T. & Bowser, S. S. Submillimeter life positions of bacteria, protists, and metazoans in laminated sediments of the Santa Barbara Basin. *Limnology and Oceanography* **48**, 813-828 (2003).

Bograd, S. J., Schwing, F. B., Castro, C. G. & Timothy, D. A. Bottom water renewal in the Santa Barbara Basin. *Journal of Geophysical Research: Oceans* **107**, 9-1-9-9 (2002).

Bond, A. D., Dickson, A. J., Ruhl, M., Bos, R. & van de Schootbrugge, B. Globally limited but severe shallow-shelf euxinia during the end-Triassic extinction. *Nature Geoscience* **16**, 1181-1187 (2023).

Cai, W. *et al.* Increasing frequency of extreme El Niño events due to greenhouse warming. *Nature climate change* **4**, 111-116 (2014).

Cline, J. D. Spectrophometric determination of hydrogen sulfide in natural waters. *Limnol. Oceanogr.* **14**, 454-458 (1969).

Dale, A. W. *et al.* Organic carbon production, mineralisation and preservation on the Peruvian margin. *Biogeosciences* **12**, 1537-1559 (2015).

Demaison, G. J. & Moore, G. T. Anoxic environments and oil source bed genesis. *Organic geochemistry* **2**, 9-31 (1980).

Dunhill, A. M., Foster, W. J., Sciberras, J. & Twitchett, R. J. Impact of the Late Triassic mass extinction on functional diversity and composition of marine ecosystems. *Palaeontology* **61**, 133-148 (2018).

Figueroa, M. C. *et al.* Early diagenetic processes in an iron-dominated marine depositional system. *Geochimica et Cosmochimica Acta* **341**, 183-199 (2023).

Fossing, H. & Jørgensen, B. B. Measurements of bacterial sulphate reduction in sediments: evaluation of a single-step chromium reduction method. *Biogeochemistry* **8**, 205-222 (1989).

Fossing, H. in *Geochemical transformations of sedimentary sulfur* Vol. 612 (eds M. A. Vairavamurthy & M. A. A. Schoonen) 348-364 (American Chemical Society Symposium Series, 1995).

Grasshoff, K., Ehrhardt, M. & Kremling, K. *Methods of seawater analysis*. (Wiley-VCH Verlag GmbH, 1999).

Hamukuaya, H., O'Toole, M. & Woodhead, P. Observations of severe hypoxia and offshore displacement of Cape hake over the Namibian shelf in 1994. *South African Journal of Marine Science* **19**, 57-59 (1998).

Hancock, L. G., Hardisty, D. S., Behl, R. J. & Lyons, T. W. A multi-basin redox reconstruction for the Miocene Monterey Formation, California, USA. *Palaeogeography, palaeoclimatology, palaeoecology* **520**, 114-127 (2019).

Hansen, J. *et al.* Climate impact of increasing atmospheric carbon dioxide. *Science* **213**, 957-966 (1981).

Hardisty, D. S. *et al.* An evaluation of sedimentary molybdenum and iron as proxies for pore fluid paleoredox conditions. *American Journal of Science* **318**, 527-556 (2018).

Jørgensen, B. B. A comparison of methods for the quantification of bacterial sulphate reduction in coastal marine sediments: I. Measurements with radiotracer techniques. *Geomicrobiol. J.* **1**, 11-27 (1978).

Jørgensen, B. B., Findlay, A. J. & Pellerin, A. The biogeochemical sulfur cycle of marine sediments. *Frontiers in microbiology* **10**, 436320 (2019).

Kamyshny Jr, A. & Ferdelman, T. G. Dynamics of zero-valent sulfur species including polysulfides at seep sites on intertidal sand flats (Wadden Sea, North Sea). *Marine Chemistry* **121**, 17-26 (2010).

Kallmeyer, J., Ferdelman, T. G., Weber, A., Fossing, H. & Jørgensen, B. B. A cold chromium distillation procedure for radiolabeled sulfide applied to sulfate reduction measurements. *Limnol. Oceanogr. Methods* **2**, 171-180 (2004).

Kuwabara, J. S., van Geen, A., McCorkle, D. C. & Bernhard, J. M. Dissolved sulfide distributions in the water column and sediment pore waters of the Santa Barbara Basin. *Geochimica et Cosmochimica Acta* **63**, 2199-2209 (1999).

Liu, J. *et al.* Early diagenesis of iron and sulfur in Bornholm Basin sediments: The role of near-surface pyrite formation. *Geochimica et Cosmochimica Acta* **284**, 43-60 (2020).

McHatton, S. C., Barry, J. P., Jannash, H. W. & Nelson, D. C. High nitrate concentrations in vacuolate, autotrophic marine Beggiatoa spp. *Appl. Environ. Microbiol.* **62**, 954-958 (1996).

McWilliams, J. C., Damien, P. & Kessouri, F. Vol. Submitted (Progress in Oceanography, 2024).

Palacios, D. M., Bograd, S. J., Mendelssohn, R. & Schwing, F. B. Long-term and seasonal trends in stratification in the California Current, 1950–1993. *Journal of Geophysical Research: Oceans* **109** (2004).

Poulton, S. W. *The iron speciation paleoredox proxy*. (Cambridge University Press, 2021).

Qin, Q. *et al.* Seasonality of Water Column Methane Oxidation and Deoxygenation in a Dynamic Marine Environment. *Geochimica et Cosmochimica Acta* (2022).

Raven, M. R., Sessions, A. L., Fischer, W. W. & Adkins, J. F. Sedimentary pyrite δ34S differs from porewater sulfide in Santa Barbara Basin: Proposed role of organic sulfur. *Geochimica et Cosmochimica Acta* **186**, 120-134 (2016).

Reimers, C. E., Lange, C. B., Tabak, M. & Bernhard, J. M. Seasonal spillover and varve formation in the Santa Barbara Basin, California. *Limnology and Oceanography* **35**, 1577-1585 (1990).

Reimers, C. E., Ruttenberg, K. C., Canfield, D. E., Christiansen, M. B. & Martin, J. B. Porewater pH and authigenic phases formed in the uppermost sediments of Santa Barbara Basin. *Geochim. Cosmochim. Acta* **60**, 4037-4057 (1996).

Robidart, J. *et al.* Characterizing microbial community and geochemical dynamics at hydrothermal vents using osmotically driven continuous fluid samplers. *Environmental science & technology* **47**, 4399-4407 (2013).

Robinson, D. M. *et al.* Iron "Ore" Nothing: Benthic iron fluxes from the oxygen-deficient Santa Barbara Basin enhance phytoplankton productivity in surface waters. *Biogeosciences Discussions*, 1-36 (2022).

Ruhl, M., Bonis, N. R., Reichart, G.-J., Damsté, J. S. S. & Kürschner, W. M. Atmospheric carbon injection linked to end-Triassic mass extinction. *Science* **333**, 430-434 (2011).

Schimmelmann, A. & Lange, C. B. Tales of 1001 varves: a review of Santa Barbara Basin sediment studies. *Geological Society, London, Special Publications* **116**, 121-141 (1996).

Seitaj, D. *et al.* Cable bacteria generate a firewall against euxinia in seasonally hypoxic basins. *Proceedings of the National Academy of Sciences* **112**, 13278-13283 (2015).

Shiller, A. M., Gieskes, J. M. & Price, N. B. Particulate iron and manganese in the Santa Barbara Basin, California. *Geochimica et Cosmochimica Acta* **49**, 1239-1249 (1985).

Sholkovitz, E. R. & Gieskes, J. M. A PHYSICAL-CHEMICAL STUDY OF THE FLUSHING OF THE SANTA BARBARA BASIN 1. *Limnology and Oceanography* **16**, 479-489 (1971).

Sholkovitz, E. Interstitial water chemistry of the Santa Barbara Basin sediments. *Geochimica et Cosmochimica Acta* **37**, 2043-2073 (1973).

Sommer, S. *et al.* Depletion of oxygen, nitrate and nitrite in the Peruvian oxygen minimum zone cause an imbalance of benthic nitrogen fluxes. *Deep-Sea Res. I* **112**, 113–122 (2016).

Stookey, L. L. Ferrozine---a new spectrophotometric reagent for iron. *Analytical chemistry* **42**, 779-781 (1970).

Stramma, L., Johnson, G. C., Sprintall, J. & Mohrholz, V. Expanding oxygen-minimum zones in the tropical oceans. *Science* **320**, 655-658 (2008).

Stramma, L., Schmidtko, S., Levin, L. A. & Johnson, G. C. Ocean oxygen minima expansions and their biological impacts. *Deep-Sea Research I* **57**, 587-595 (2010).

Teske, A. & Nelson, D. C. The genera beggiatoa and thioploca. *Prokaryotes* **6**, 784-810 (2006).

Treude, T. *et al.* Biogeochemistry of a deep-sea whale fall: sulfate reduction, sulfide efflux and methanogenesis. *Mar. Ecol. Prog. Ser.* **382**, 1-21 (2009).

Valentine, D. L. *et al.* Autonomous marine robotic technology reveals an expansive benthic bacterial community relevant to regional nitrogen biogeochemistry. *Environmental science & technology* **50**, 11057-11065 (2016).

van de Velde, S. J., Reinhard, C. T., Ridgwell, A. & Meysman, F. J. Bistability in the redox chemistry of sediments and oceans. *Proceedings of the National Academy of Sciences* **117**, 33043-33050 (2020).

van de Velde, S. J. *et al.* Elevated sedimentary removal of Fe, Mn, and trace elements following a transient oxygenation event in the Eastern Gotland Basin, central Baltic Sea. *Geochimica et Cosmochimica Acta* **271**, 16-32 (2020).

van de Velde, S. J. *et al.* Exceptionally high respiration rates in the reactive surface layer of sediments underlying oxygen-deficient bottom waters. *Proceedings of the Royal Society A* **479**, 20230189 (2023).

Yousavich, D. J. *et al.* Marine anoxia initiates giant sulfur-oxidizing bacterial mat proliferation and associated changes in benthic nitrogen, sulfur, and iron cycling in the Santa Barbara Basin, California Borderland. *Biogeosciences* **21**, 789-809 (2024).

Zheng, Y., Anderson, R. F., Van Geen, A. & Kuwabara, J. Authigenic molybdenum formation in marine sediments: a link to pore water sulfide in the Santa Barbara Basin. *Geochimica et Cosmochimica Acta* **64**, 4165-4178 (2000).

Chapter 4

Microbial sulfur, nitrogen, and methane metabolisms in the water column and sediment of the Salton Sea - A seasonally anoxic, holomictic saline lake

David J. Yousavich[1*], Charles Diamond[2], Caroline Hung[2], George Vetushko[1], Xuefeng Peng[3], Tim Lyons[2], Tina Treude[1,4*]

[1]Department of Earth, Planetary, and Space Sciences, University of California Los Angeles, 595 Charles E. Young Drive East, Los Angeles, CA 90095, USA

[3]School of Earth, Ocean, and Environment, University of South Carolina, 701 Sumter Street, EWS 617, Columbia, SC 29208, USA

[4]Department of Atmospheric and Oceanic Sciences, University of California Los Angeles, Math Science Building, 520 Portola Plaza, Los Angeles, CA 90095, USA

Abstract

The Salton Sea is a large, shallow, inland lake that is marked by hypersaline conditions and rapid desiccation. Sulfate concentration in the Salton Sea exceed five times seawater concentrations, and the lake's seasonal hypolimnion reaches anoxia during the summer and fall resulting in extreme euxinia (>2 mM sulfide). The maximum depth of the lake has shallowed by over 3 m since 2003, with the remaining lake water becoming increasingly more saline. The lake has also frequently experienced many harmful algal and dinoflagellate blooms. While geochemical and metagenomic studies have been done of the lake's water column and sediments,

these studies pre-date drastic reductions to the lake's inflow since 2018, and further, microbial metabolic rates have not been determined in either the lakes water column or sediments. Between January 2020 and November 2023, we conducted geochemical analyses and microbial rate determinations in the water column and sediment of the Salton Sea during five sampling campaigns to assess how desiccation is affecting the lake's biogeochemistry. We found that the lake no longer contains an intensely stratified thermocline though it does develop an anoxic bottom layer during summer months. We detected are high rates of ex-situ and potential sulfate reduction in both the sediment (>3 mmol m^{-2} d^{-1}) and water column (up to 2,200 nmol L^{-1} d^{-1}), including under oxygenated conditions near the lake's surface. We also present potential rates for denitrification and anaerobic ammonium oxidation, and ex-situ rates of methane oxidation in the lake's water column. This work furthers our understanding of how the biogeochemistry of inland endorheic lakes changes as desiccation drives their salinity higher.

Introduction

Inland saline lake habitats around the world, which are considered critical habitats for migrating birds, are desiccating, thereby creating increasingly saline habitats that can be toxic for aquatic life (Jellison et al. 2004). These lakes are primarily endorheic (i.e., the basin is not connected to the world's oceans) and exist in arid climates around the world. Human development in these water-scarce regions has reduced the inflow to these inland lakes, causing them to desiccate over time (Williams 2002). As the lake water level decreases, it exposes areas of lakebed to the air, which can release dust that contains toxic chemicals (e.g., recalcitrant pesticides) that were once complexed in the lakes sediments (Frie et al. 2017). Additionally, as the lake shallows, wind-driven mixing patterns can penetrate closer to the lakebed.

Most lakes around the world have some degree of mixing, particularly when air temperatures cool and/or wind can induce mixing within the lake (i.e., holomictic lakes). During the summer, holomictic lakes can develop thermal stratification and a hypolimnion, or a bottom layer below the thermocline that does not mix with upper waters. This stratification can lead to chemical changes, such as anoxia and euxinia, in the hypolimnion, restricting fish and larger organisms to the upper waters of the lake, and potentially leading to mass fish-kills (Marti-Cardona et al. 2008). Some lakes (such as Hot Lake, WA) are meromictic, where permanent stratification prohibits mixing year-round, ergo these lakes have a permanent hypolimnion (Anderson 1958). Meromictic lakes are usually stratified based on salinity, with brackish to hypersaline bottom waters, such as Green Lake, NY (Brunskill and Ludlam 1969). The biogeochemistry above and below the pycnocline in both holomictic and meromictic lakes is usually quite different. With restricted mixing in the hypolimnion a negative oxidative reductive potential (ORP) is common, indicative of anaerobic metabolisms like sulfate reduction and anaerobic methane oxidation (Ingvorsen et al. 1981; Joye et al. 1999).

Endorheic salt lakes constitute nearly half of all standing inland water volume on Earth (Williams 1996). Both freshwater and saline lake biogeochemistry and microbial community composition varies between the hypolimnion and epilimnion (Diao et al. 2017; Phillips et al. 2021). Changes in mixing patterns can bring about drastic changes in saline lake community composition and biogeochemical cycling, particularly in the hypolimnion of these lakes (Bjorndahl et al. 2022; Phillips et al. 2021). Additionally, once anoxia is established in a lake's hypolimnion, the sediments below the lake act as a seed for anaerobic microbial communities to migrate into the water column, particularly sulfate reducing bacteria (Phillips et al. 2021). Sediments below saline lakes can contain vastly different microbial community structures

depending on salinity and relative ion concentration, with archaeal lineages becoming prevalent and more diverse with increasing salinity in some salt lakes (Liu et al. 2023; Swan et al. 2010a). In particular, both fermentation and sulfate reduction are dominant metabolic pathways in anoxic sediments and hypolimnions of saline lakes (Liu et al. 2023; Phillips et al. 2021; Swan et al. 2010a).

The Salton Sea is an endorheic, holomictic lake that has developed an extremely euxinic seasonal hypolimnion, with sulfide concentrations exceeding 2 mM between May and November 2006 at maximum lake depth of 15 m (Reese et al. 2008). In fall, the Santa Ana winds usually mix the lake, causing the sulfide that built up in the euxinic hypolimnion to oxidize to sulfate and leading to gypsum blooms that can be seen from satellite images (Tiffany et al. 2007b). The Salton Sea has been progressively desiccating, since its formation but especially since both agricultural runoff was reduced in 2003 and periodic Colorado river discharge was stopped in 2018 (Fogel et al. 2021). The high salt concentrations are thought to be due to connections to underlying evaporite layers (Wardlaw and Valentine 2005). Additionally, as the lake has dried, fumaroles containing high levels of ammonium sulfate salts that are connected to geothermal brines below the Salton Sea have been uncovered, allowing the possibility that some of the sulfate in the lake is geothermally sourced (Adams et al. 2017). The sulfide in the Salton Sea is thought to be a result of biological sulfate reduction in the sediments (Reese et al. 2008). Microbial sulfate reduction rates for the Salton Sea sediments have been assessed once (Swan 2009) but water column sulfate reduction has not been quantified. As the Salton Sea is rapidly desiccating, there is an urgent need to quantify the biogeochemical changes that coincide with the lake's drying process to assess the future of the lake and its surrounding community, which include the Coachella and Imperial valleys, one of the United States most important agricultural

regions (Fogel et al. 2021).

In order to quantify microbial metabolic activities and associated geochemical signatures of the Salton Sea since the state of California stopped diverting Colorado River water to the lake in 2018, we conducted five sampling campaigns between January 2020 and November 2023. We collected water column and sediment samples for geochemical and microbial respiration rate determinations. We set out to quantify the relative contribution of sediment and water column sulfate reduction to the extreme euxinia seen in the Salton Sea. We also sought to understand biological oxidation and reduction of nitrogen species and the oxidation of methane in the lake water. In combination, our analyses provide a first glance at the biogeochemistry of the Salton Sea and may aid the understanding of biogeochemical processes of other drying inland lakes, such as the Aral Sea (Micklin 2007), as well as past mass-drying events in Earth's history, such as the Messinian Salinity Crisis (Krijgsman et al. 1999).

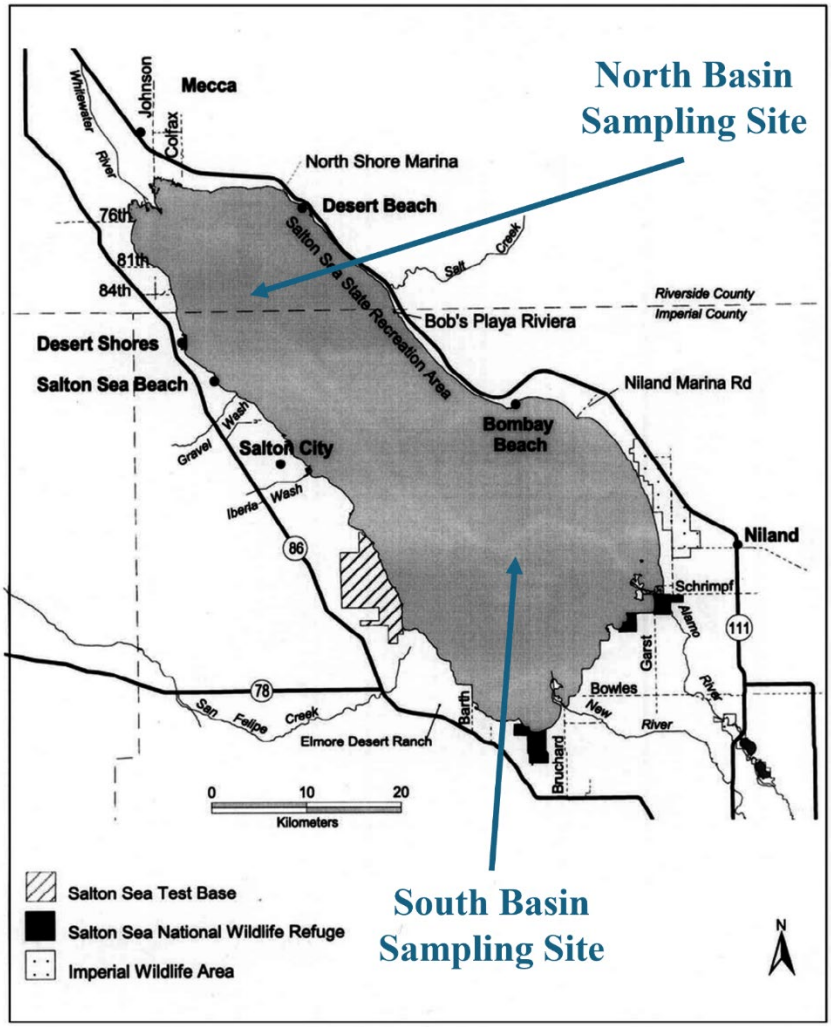

Figure 4-1. Map of the Salton Sea with sampling locations in the North and South Basin. Map taken from Shuford et al. (2002).

Study Site

The Salton Sea is an inland lake in California's Coachella Valley with two basins, centered approx. at 33.26093° latitude, -115.742° longitude (South basin) and 33.44454° latitude, -115.9628° longitude (North basin). The Salton Sea is evaporating at a rate of 0.3 m yr^{-1} and the maximum depth of the Salton Sea in both basins during the sampling period was approx. 10.5 m. The modern Salton Sea formed when a levee on the Colorado River broke in 1905 and diverted water for two years into the Coachella valley, where it settled in the Salton Sink, the lowest point

(approx. 64 m below sea level) of the Salton Trough. The Salton Trough lies above the San Andreas fault, an active transform boundary, which contains a geothermal field roughly below the Salton Sink (Younker et al. 1982). The Salton Trough was connected to the Gulf of California in the early Pleistocene and was progressively cut off by the formation of the Colorado River Delta, creating a shallow marine inland sea that eventually evaporated (Tompson 2016). Over the course of the late Pleistocene and into the Holocene epoch, a lake would form in the Salton Trough, occasionally connecting with the Gulf of California, due to meandering of the Colorado River, before re-desiccating, with the most recent incarnation (before the Salton Sea) being Lake Cahuilla between 1600-1700 AD (Waters 1983). These cycles of marine evaporation, re-flooding and subsequent dissolution of evaporites, and re-desiccation have led to the salinity of the current day Salton Sea (47 PSU as of 2006, (Reese et al. 2008)).

The biology of the Salton Sea has changed rapidly with the lake's decline. While the lake still provides a crucial habitat for migrating birds (Lyons et al. 2018), larger aquatic organisms that used to populate the lake such as the hybrid Tilapia *Oreochromis mossambicus x O. urolepis hornorum* (Riedel et al. 2002) and even meiofauna such as the polychaete *Neanthes succinea* (Dexter et al. 2007) are now restricted to riparian wetlands on the lakes perimeter (Fogel et al. 2021). The Salton Sea has experienced many massive fish kills, particularly in later summer months when wind mixes the lakes hypolimnion with waters above the thermocline (Marti-Cardona et al. 2008). Ecosystem models of the Salton Sea have shown that harmful algal blooms, salinity increase, heat spikes, and sulfide toxicity have all contributed to these fish kills (Kjelland and Swannack 2018).

The microbiology of the Salton Sea water column is characterized by organisms that can tolerate the hypersaline, alkaline, and anoxic/euxinic conditions present in the lake (Freund et al.

2022). *Proteobacteria* and *Bacteroidetes* constituted >60% of phyla detected in the water column in late summer 2009, while *Rhodobactareles* (an order within *Alphaproteobacteria* known for anoxygenic photosynthesis) were also prevalent; only 5% of the taxa found belonged to Cyanobacteria lineages (Dillon et al. 2009). Additionally, seasonal variation in geochemistry of the lake seems to heavily impact relative bacterioplankton abundance, with strongest species diversity in the spring and much lower species richness in summer and fall (Dillon et al. 2009). Species diversity within the Salton Sea appears to be tightly correlated to sulfide concentrations, with chemoautotrophic and anoxygenic photosynthesizers being most prevalent during euxinic conditions (Swan et al. 2010b). Archaea were found to be the dominant micro-organisms at all depths in the Salton Sea sediment (Swan et al. 2010a). Bacterial communities of the surface sediment are dominated by aerobic organisms such as *Rosebacter* spp. when the hypolimnion is oxygenated, while sulfate-reducing Deltaproteobacteria become dominant when the hypolimnion is anoxic/euxinic (Dillon et al. 2009; Swan et al. 2010a).

Materials and Methods

Sample collection and processing

Water column samples from the Salton Sea were collected using a small, motorized boat on 8 January 2020, 11 August 2020, 22 September 2021, and 16 November 2023. Sediment samples were collected using the same small, motorized boat on 24 August 2021. Samples from 2020 and 2021 were collected at the depositional center (hereafter depocenter) of the southern basin. Due to logistical complications with launching the boat in the southern basin in 2023, samples from 2023 were collected at the depocenter of the northern basin. Samples from 2020 and 2021 were collected using a Niskin bottle that was lowered to depth and closed by dropping

a weight that activated two tension wires, which snapped the ends of the bottle closed. Samples from 2023 were collected using a hydraulic pump with in-line filtration at 5 microns (Alexis® 12 volt peristaltic pump from Proactive Environmental Products® at 500 mL per minute). In all samplings, a calibrated YSI EXO2 multi-parameter sonde (YSI Incorporated, Yellow Springs, OH, USA) equipped with temperature, conductivity, pH, turbidity, dissolved oxygen, dissolved organic matter, salinity, and oxidation-reduction potential (ORP) sensors was lowered at each site before water column samples were collected. Sediment samples were taken from the southern basin depocenter on 24 August 2021.

Water column samples for sulfate reduction rate determinations were collected in 30-mL glass serum vials and were immediately closed bubble free with a stopper and crimped on the boat. Water column samples collected for geochemical parameters were collected in 15-mL plastic centrifuge tubes. Samples for total sulfide concentration determinations were collected in separate 15-mL conical centrifuge tubes or 30-mL serum vials, each of which contained 2 mL of 5% zinc acetate to preserve sulfide. Sediment samples were taken with a large bore sediment sampler unit with stainless steel core head and one-way check valve and ball valve vacuum release. Two replicate sediment cores (polycarbonate core tube, length ~ 40 cm length, internal diameter ~ 9.5 cm, outer diameter ~ 10 cm) during the August 2021 field campaign were taken back to the home lab. One core was sub-sampled with two smaller push cores (polycarbonate, length = 20 cm, diameter = 2.6 cm) for sulfate reduction rate incubations. The other core was stored at the home lab at room temperature for approx. 1 week (with overlying supernatant and a taped plastic stopper on top), until it was sliced in 1-cm increments under a constant argon flow into argon-filled 50-mL plastic centrifuge tubes. Sediment was centrifuged at 2300 *xg* for 20 minutes and the centrifugate was immediately subsampled for geochemical parameters.

Geochemical analyses

Concentrations of porewater and water column sulfide (Cline 1969), NH_4^+, PO_4^{3-}, and Fe^{2+} (Grasshoff et al. 1999) were determined in the lab with a Shimadzu UV-Spectrophotometer (UV-1800). Detection limits for sulfide, NH_4^+, PO_4^{3-}, and Fe^{2+} were 1 µM. Water column and porewater subsamples (2 mL) were taken in the laboratory, stored in 2-mL plastic vials with an O-ring, frozen at -30°C and analyzed for NO_3^- and NO_2^- concentrations on the same spectrophotometer using the method following (García-Robledo et al. 2014). The detection limit for NO_3^- and NO_2^- was 0.5 µM. Subsamples (1 mL from both porewater and water column samples) for sulfate and chlorinity were taken in the laboratory, stored in 2-mL plastic vials with an O-ring, frozen at -30°C and later measured using a Metrohm 761 ion chromatograph with a methodological detection limit of 30 µM (Dale et al. 2015). Samples for water column methane concentration were collected in 125-mL serum vials bubble free and then injected with 7.5 mL of 50% sodium hydroxide solution and 2.5 ml air to stop microbial activity and force the gas into the headspace. Methane was determined in headspace samples using a Shimadzu Gas Chromatograph (GC-2014) with a packed Haysep-D column and a flame ionization detector. The column temperature was 80 ºC with helium as the carrier gas at 12 mL per min. Methane concentrations were calibrated against methane standards (Scotty Analyzed Gases) with a ± 5% precision.

Sulfate Reduction

To determine ex-situ microbial sulfate reduction rates in the water column, water samples were collected into 30-mL glass serum vials and closed bubble-free with blue butyl stoppers

(Bellco). Five replicate samples (three in August 2020) were collected per water column depth. If a sample had a large bubble in it, we did not use it for rate determinations, thus 7 m depth in September 2021 and 1 m depth in November 2023 constitute four replicates instead of five. Additionally, five samples to produce killed controls were collected per sampling campaign. ^{35}S-Sulfate radiotracer (15-20 µl, dissolved in water, specific activity 37 TBq mmol^{-1}, was injected activity: 0.8, 1.7, and 2.3 MBq in 2020, 2021, and 2023) was injected through the stopper and the samples were incubated for 21-23 days. After incubation, the vials were opened, and the water was poured into 50-mL centrifuge tubes pre-filled with 10-mL zinc acetate (20% w/w) and frozen at -20°C until analysis. Microbial activity in controls was terminated by injecting either 4.2 mL 37% formaldehyde (2020, 2021) or 300 µl 25% H_2SO_4 (2023) before injection of the radiotracer. Approx. 1g of bentonite clay was added to centrifuge tubes to ensure a pellet would form upon centrifugation. In 2023, water samples were amended with sulfide (final concentration 40 µM) to remove traces of oxygen. Sulfate reduction rates determined from this incubation should therefore be considered potential rates.

To determine ex-situ microbial sulfate reduction rates in the sediment, whole round sub-cores were injected with 10 µL carrier-free ^{35}S-sulfate radiotracer (dissolved in water, 222 kBq, specific activity 37 TBq mmol^{-1}) into pre-drilled, silicon-filled holes at 1-cm increments according to (Jørgensen 1978). These sub-cores were incubated at room temperature for 7.5 hours. Incubations were stopped by slicing sediment cores in 1-cm increments into 50-mL centrifuge tubes filled with 20-mL zinc acetate (20% w/w) and frozen at -20°C until analysis. Microbial activity in controls was terminated with zinc acetate (20 mL of 20% w/w) before the addition of radiotracer and subsequent freezing. Lab-based analysis of both water column and sediment sulfate reduction rates were determined following the cold-chromium distillation

procedure (Kallmeyer et al. 2004).

Methane Oxidation

Water samples for ex-situ methane oxidation rate determinations were collected only in 2023. Three replicate water samples were collected from 1 and 10.5 m water depth into 30-mL serum glass vials and closed bubble free with a blue butyl rubber stopper (Bellco) shipboard and injected with 10 µl ^{3}H-methane radiotracer (gaseous, 55 kBq, specific activity 0.37-0.74 TBq mmol^{-1}) in the home laboratory. Microbial activity in control samples was terminated by the addition of 300 µL 25% H_2SO_4 prior to radiotracer injection. Samples were incubated at room temperature, in the dark, for 94 hrs. After incubation, the sample vials were opened, and 2 mL water (^{3}H-CH_4 + ^{3}H-H_2O sample) was removed and analyzed directly by liquid scintillation counting. After that, another 2 mL water was removed and bubbled with air for 5 min to degas methane (^{3}H-H_2O sample), followed by liquid scintillation counting. Calculation of the methane oxidation rates was according to (Bussmann et al. 2015).

Ammonium Oxidation Rate Determination

Samples for potential ammonium oxidation rate determination were collected in 60-mL serum vials shipboard and pre-incubated with 150 µM sodium dithionite for three days to ensure anoxia. After three days, ammonium oxidation samples were injected with ^{15}N-NH_4^+. Three replicate ammonium oxidation incubations were stopped at 0, 12, 24, and 36 hours. All incubations were done in discrete glass vials in parallel (i.e., 16 total incubations, four replicates and four time-points) and each incubation was sacrificed after sampling. Approx. 20-mL of each ammonium oxidation sample was transferred to a 50-mL plastic centrifuge tube and immediately

frozen at -30°C. An additional approx. 12 mL of each incubation was transferred to a 15-mL plastic centrifuge tube and frozen at -30°C for subsequent nitrogen species concentration determination.

Samples for ammonium oxidation were treated using the cadmium-azide method following (McIlvin and Altabet 2005). Briefly, 100 mg of MgO and 0.75 g of pre-treated cadmium were added to 20-mL of subsample from each ammonium oxidation incubation in a 50-mL centrifuge tube and incubated on a shaking table (set to low) for 17 hours. The MgO is used to stabilize pH and the Cd is used to transform NO_3^- to NO_2^-. 2.5 mL of each sample was transferred into an exetainer using a plastic syringe and needle, purged with helium for 5 minutes, and then injected with 0.4 mL of a 1:1 sodium azide, acetic acid solution to convert NO_2^- to N_2O. After 10 minutes, 0.3 mL of 10M NaOH was injected into each exetainer to neutralize the hydrazoic acid. In-house NO_3^- concentration and stable isotope standards were prepared for the analysis and treated through the sodium-azide procedure.

The concentration and stable isotope composition of N_2O produced from the cadmium-azide method were analyzed at the UC Davis Stable Isotope Facility using elemental analyzer–isotope ratio mass spectrometry. The detection limit was 0.2 nmol of N and the precision of $\delta^{15}N$ was 0.2‰. The inclusion of in-house NO_3^- concentration and stable isotope standards resulted in standard curves that enable the calculation of sample NO_3^- concentration and stable isotope compositions (Appendix C, Fig. 4-1). $^{15}N\text{-}NO_3^-$ concentration in each sample was calculated by multiplying the concentration of NO_3^- by the measured $\delta^{15}N\text{-}NO_3^-$. A linear regression was performed to calculate the production rate of $^{15}N\text{-}NO_3^-$ (Appendix C, Fig. 2). Ammonium oxidation rates were then calculated using the following equation:

$$V_{NH_4^+} = \frac{\Delta[15_{NO_3^-}]}{f^{15}NH_4^+ \, x \, T}$$

Where $\Delta[^{15}NO_3^-]$ is the change in concentration of $^{15}NO_3^-$ between the start and end of the incubation as a result of ammonium oxidation, $f^{15}NH_4^+$ is the fraction of NH_4^+ that was labeled with ^{15}N at the beginning of the incubation and T is the length (in days) of the incubation.

Denitrification Rate Determination

Samples for potential denitrification rate determination were collected similar to ammonium oxidation standards (see previous section). Except denitrification samples were injected with ^{15}N-NO_3^- to a final concentration of 5 µM each and two replicate denitrification incubations were stopped at 0, 12, 24, and 36 hours. Seven mL of each denitrification sample was pulled through the stopper using a plastic syringe and immediately injected into a gas-tight exetainer vial that was pre-filled with 0.1 mL of 7 M zinc chloride. An additional approx. 12 mL of each incubation was transferred to a 15-mL plastic centrifuge tube and frozen at -30°C for subsequent nitrogen species concentration determination.

Exetainers with denitrification and ammonium oxidation subsamples were sent to the UC Davis Stable Isotope Facility for analysis using elemental analyzer–isotope ratio mass spectrometry. The concentration of N_2O and ratio of $^{45}N_2O/^{44}N_2O$ were determined for ammonium oxidation rates and the concentration of N_2 and ratio of $^{29}N_2/^{28}N_2$ were determined for denitrification rates.

Subsamples were sent to the UC Davis Stable Isotope Facility for analysis using elemental analyzer–isotope ratio mass spectrometry. Concentration of N_2 and ratio of $^{29}N_2/^{28}N_2$ were determined for denitrification rates. The detection limit was 0.2 nmol of N and the precision of $\delta^{15}N$ was 0.2‰. Total amount of ^{15}N-N_2 of each sample was calculated using an

average of the measured amount of N_2 multiplied by the measured $\delta^{15}N$- N_2 of each sample. Only incubations from 0 and 36 hours were used for the calculation (concentrations for every incubation can be seen in Appendix C, Fig. 2).

Table 4-1: Physical attributes of the Salton Sea water column. Parameters are averaged over approx. 10.5 m water depth; n represents number of measurements averaged for each date. Peak measured chlorophyll values were at 1 m water depth for all the sampling campaigns. November 2023 sampling campaign occurred in the north basin depocenter while all other sampling campaigns occurred in the south basin depocenter. TDS is Total Dissolved Solids.

Date	n	Average Water Temp	Average pH	Average TDS	Average Chlorophyll	Peak Chlorophyll
		° C		mg L^{-1}	RFU	RFU
8/11/2020	38	30.1 ± 0.8	8.1 ± 0.1	53544 ± 84	2.62 ± 1.59	7.42
8/24/2021	11	30.4 ± 0.3	8.0 ± 0.0	53245 ± 110	3.02 ± 0.77	4.44
9/22/2021	13	29.8 ± 0.5	8.0 ± 0.0	56788 ± 52	1.30 ± 0.25	1.84
11/16/2023	9	19.7 ± 0.1	8.6 ± 0.0	8218 ± 243	3.52 ± 0.46	4.36

Results

Physical and chemical parameters in the water column

The water temperature in the lake varied between seasons but was constant over all depths for each sampling campaign: approx. 30°C in 2020 and 2021, and 20°C in 2023 (Table 1). Average pH in the water column remained near 8 in August 2020, August 2021, and September 2021, but was 8.6 in November 2023. Chlorophyll peaked near 1 m depth in all sampling campaigns, with a maximum measured value of 7.42 RFU (relative fluorescence units) in August 2020. While overall salinity was not assessed, sulfate and chloride concentrations decreased slightly with depth during all sampling campaigns (e.g., from 176 to 168 mM sulfate and from 845 to 811 mM chloride between 1 and 10.5 m in August 2020, Fig. 4-2B), except in

September 2021. Surface sulfate concentration increased with every sampling; the lowest value (163 mM) was found in January 2020 (Appendix C, Table 1) and the highest (210 mM) in November 2023.

Dissolved water column oxygen peaked near 1-2 m depth and decreased with depth in all sampling campaigns, reaching anoxic conditions at approx. 8 m depth in August 2020 and at 9 m depth in September 2021 (Fig. 4-2). Oxygen was >100 µM at all sampled depths in 2023. Sulfide concentrations ranged between 0 – 5 µM, except for one sample in August 2020 at 10.5 m (57 µM). Phosphate concentrations stayed constant over depth at approx. 4 µM in September 2021 and November 2023 (Fig. 4-2). Nitrate concentrations remained near zero in all measured samples (Fig. 4-2). Ammonium concentrations decreased slightly between 1 and 10.5 m depth in September 2021 (from 22.0 to 21.3 µM) and November 2023 (from 31.5 to 25.3 µM) (Fig. 4-2). Nitrite and Fe^{2+} concentrations were not found above detection limit in the Salton Sea at any sampling campaign (data not shown).

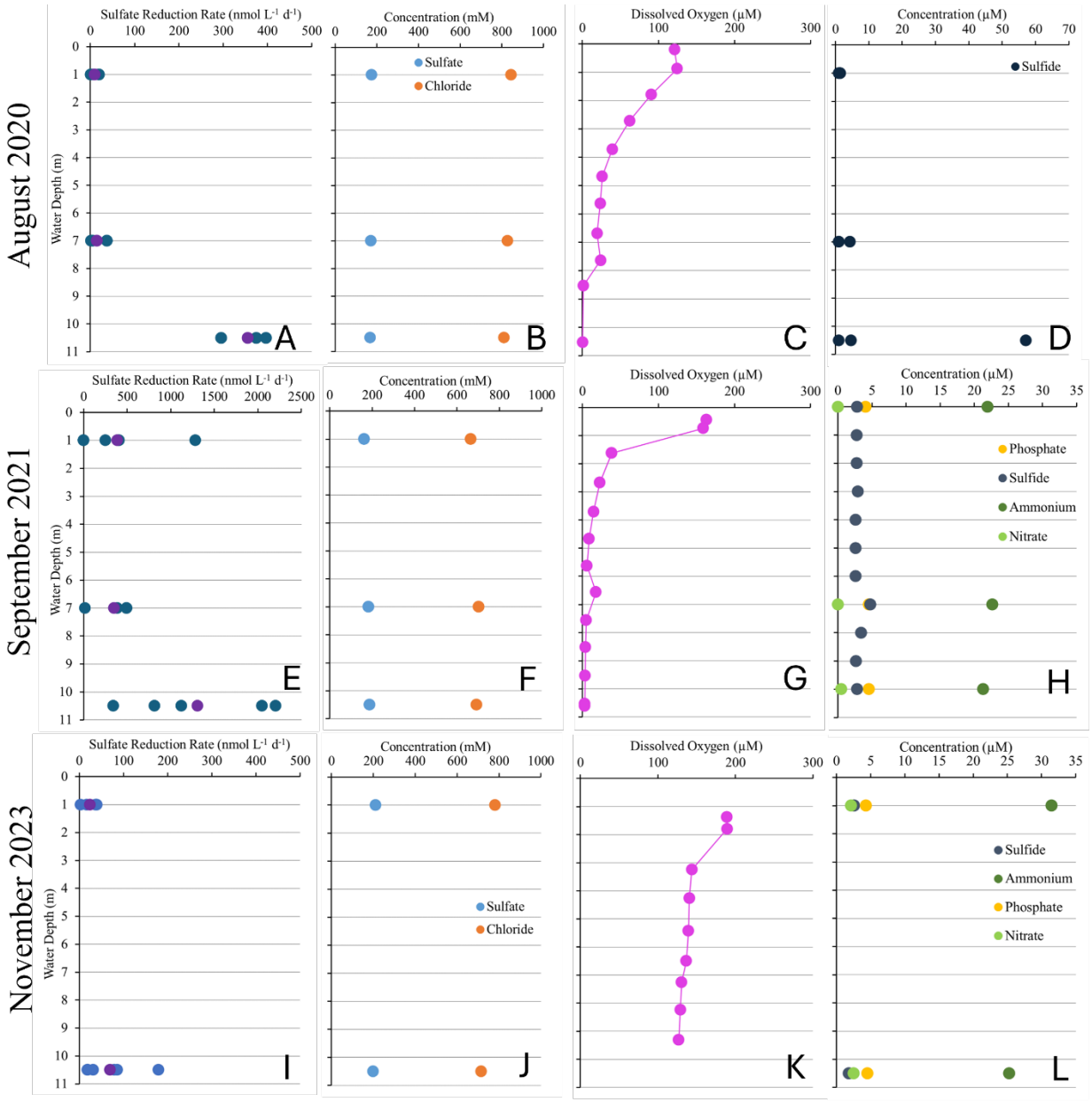

Figure 4-2. Biogeochemistry of the Salton Sea water column during three sampling campaigns (top: August 2020, middle: September 2021, bottom: November 2023). **(A, E, I)**: Sulfate reduction rates. Blue dots represent individual measurements while purple dots represent the average. Note the change in scale for E compared to A & I. **(B, F, J)**: Sulfate and chloride concentrations. **(C, G, K)**: Dissolved oxygen concentrations. **(D, H, L)**: Phosphate, sulfide, ammonium, and nitrate concentrations. Note the change in scale for D compared to H & L.

Microbial metabolic rates in the water column

We detected sulfate reduction in the water column during every sampling campaign and in at least one sample at every depth (Fig. 4-2) except at 1 m depth in January 2020 (Appendix C, Table 1). Sulfate reduction rates were generally higher at 10.5 m water depth than 1 m during all sampling campaigns (e.g., 10 vs. 356 nmol L^{-1} d^{-1} at 1 and 10.5 m water depth in August 2020). Sulfate reduction rates were highest at 10 m depth in September 2021 (1,310 nmol L^{-1} d^{-1}) and lowest in November 2023 (69 nmol L^{-1} d^{-1}). Water column methane in November 2023 was 22 nmol L^{-1} at 1 m depth and 47 nmol L^{-1} at 10 m depth (Fig.4-4). Methane oxidation rates at 1 m depth ranged from 0.036 – 0.053 nmol L^{-1} d^{-1} and from 0.062 to 0.088 nmol L^{-1} d^{-1} at 10 m depth (Fig. 4-4). The potential anaerobic ammonium oxidation (annamox) rate at 10 m depth was 0.001 nmol NO_3^- L^{-1} d^{-1} (Fig. 4-4), while the potential denitrification rate at the same depth was 93 nmol L^{-1} d^{-1} (Fig. 4-4).

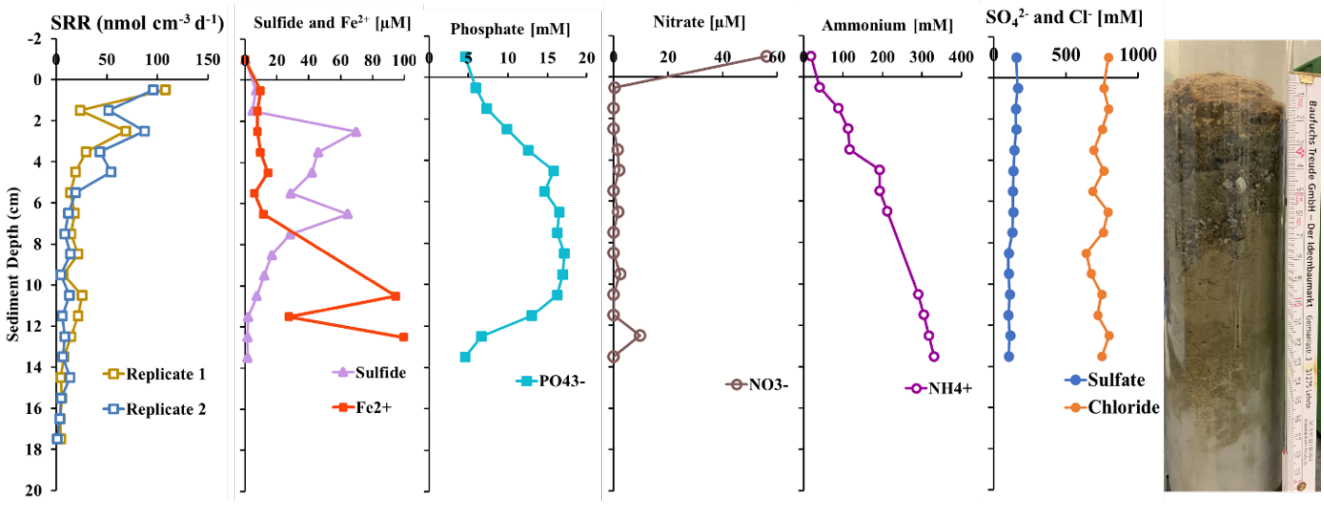

Figure 4-3. Biogeochemical parameters in Salton Sea sediment from the sampling campaign to the south basin depocenter in August 2021. Starting from left to right: sulfate reduction rate (SRR); sulfide and iron concentrations; phosphate concentrations; nitrate concentrations; ammonium concentrations; sulfate and chloride concentrations; and a photo of the core used for sulfate reduction rates. The two SRR replicates represent different sub-cores from the same core.

Negative depths indicate samples collected from the core supernatant water.

Sediment characteristic, geochemistry, and sulfate reduction

The top approx. 2 cm of the sediment consisted of brown sludge, likely dead algae. From 2 cm to approx. 10 cm, the sediment consisted of biogenic skeletal material (e.g., fish and barnacle skeletons) along with loosely consolidated sand. Between approx. 10 cm and 17 cm, the core was composed of a brown clay or silt-like sediment, and below 17 cm the sediment was composed of sticky grey clay (e.g., bentonite). Sulfate reduction rates in the Salton Sea sediment peaked just below the sediment-water interface (102 nmol cm^{-3} d^{-1} in the 0-1 cm section) and steadily decreased with depth (Fig. 4-3). Sediment porewater sulfide concentrations were 7 μM at 0-1 cm, peaked at 2-3 cm (70 μM), and declined to >2 μM below 11 cm (Fig. 4-3). Sediment porewater Fe^{2+} concentrations increased with depth, reaching a maximum (100 μM) at 12-13 cm (the deepest measured section, Fig. 4-3). Nitrate and nitrite were near-zero in the entire sediment core (except 7 μM nitrite at 0-1 cm and 10 μM nitrate at 12-13 cm); however, core supernatant nitrate and nitrite were 56 and 35 μM, respectively (Fig. 4-3). Phosphate concentrations increased with sediment depth peaking with 17 μM at 8-9 cm depth and decreasing in deeper sediments (Fig. 4-3).

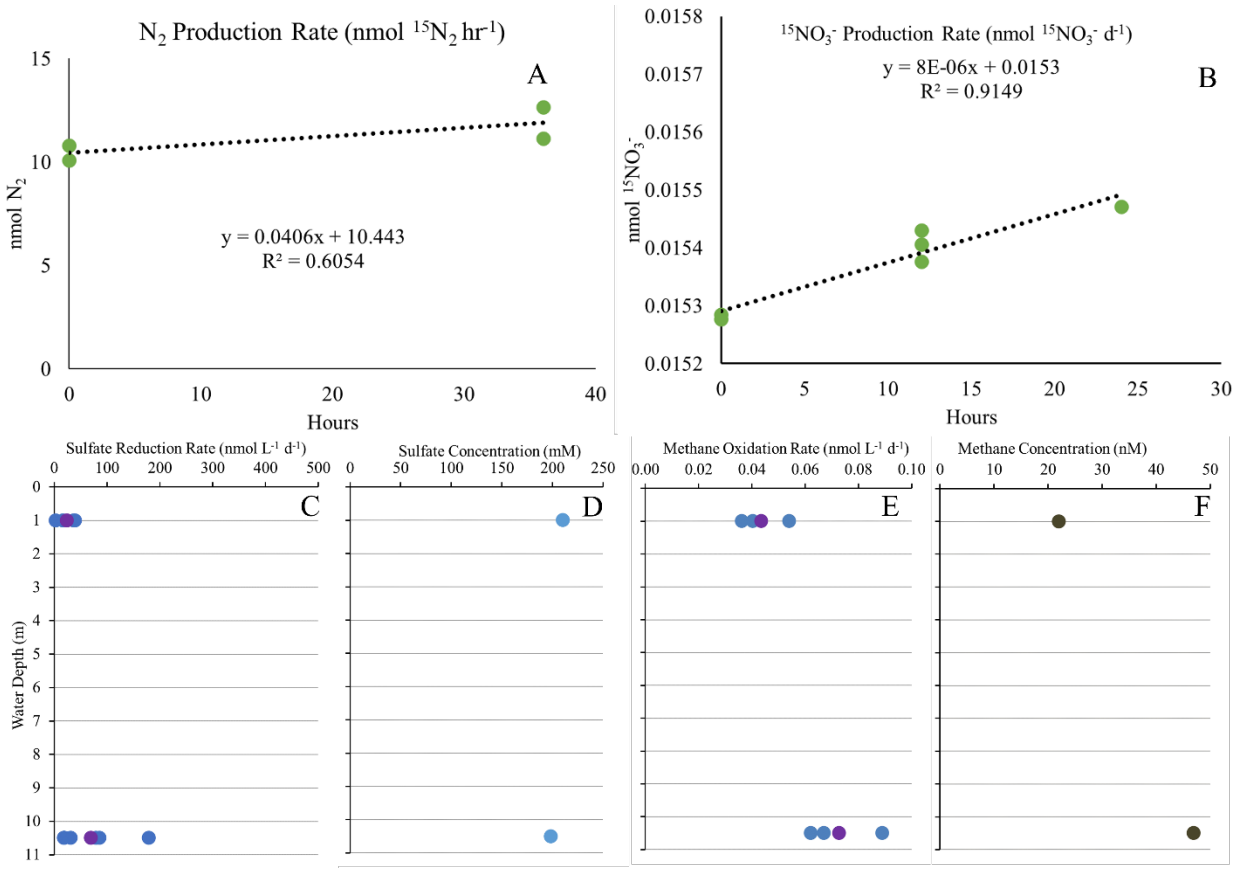

Figure 4-4. Microbial respiration rates from the November 2023 sampling campaign. **(A)** N_2 production rate at 10.5 m depth in the lake, used to calculate denitrification rates. **(B)** NO_3^- production rate at 10.5 m depth in the lake, used to calculated annamox rates. **(C)** Sulfate reduction rates at 1 m and 10.5 m depth (same as Fig.4-2I). **(D)** Sulfate concentrations at 1 m and 10.5 m depth (same as 2J). **(E)** Methane oxidation rates at 1 m and 10.5 m depth. Blue dots represent discrete samples while purple dots represent average per depth. **(F)** Methane concentrations at 1 m and 10.5 m depth.

Discussion

In this study, we set out to quantify microbial metabolisms and associated geochemistry near the surface and near the lakebed of the Salton Sea when a hypolimnion was present and when there was no stratification. Ex-situ sulfate reduction rates (measured in 2020, 2021) from oxygenated waters above the chemocline indicate that small rates of sulfate reduction (<500 nmol SO_4^{2-} L^{-1} d^{-1}) are possible even in oxygenated waters of the Salton Sea. Potential sulfate

reduction rates (measured in 2023 in artificially deoxygenated samples) indicate that water column sulfate reduction is quickly established upon onset of anoxia, in contrast to studies in Mono Lake where sulfate reducers appeared in the hypolimnion approx. one year after the onset of anoxia (Phillips et al. 2021). An order of magnitude higher rates of water column sulfate reduction were detected below the chemocline (where O_2 reaches 0 μM) in September 2021. While the oxidation-reduction potential was not as low as August 2020, when much lower sulfate reduction rates were recorded, the chemocline in September 2021 was located approx. 2 m higher during the 2021 sampling. This discrepancy indicates that anoxia was more established in the bottom waters in September 2021 compared to August 2020. Salton Sea water column sulfate reduction is likely particle-associated, similar to sulfate reduction in the marine water column (Bianchi et al. 2018; Raven et al. 2021). Future studies of sulfate reduction in the Salton Sea water column would benefit from monthly sampling events including biogeochemical analyses of the particles in the water column.

Sediment sulfate reduction rates were similar (~100 nmol cm^{-3} d^{-1}) to those measured in 2005 at the sediment-water interface (Swan 2009). Despite the high rates of both sediment (measured in August 2021) and water column (measured in September 2021) sulfate reduction, sulfide did not accumulate above 5 μM in the water column. Sediment porewater sulfide peaked between 2 and 7 cm sediment depth while sulfate reduction was highest in the top layer (0-1 cm). The lower concentration of sulfide in the top 0-1 cm layer, could be caused by either (1) chemical oxidation, introduced through oxygenation of the supernatant water during sampling and core storage, (2) microbial sulfide oxidation, or (3) fast short-distance diffusion into the water column. Regardless the cause, based on the integrated (0-10 cm) sulfate reduction rates calculated from our sediment incubations (3.58 mmol m^{-2} d^{-1}) and a southern depocenter area of

102 km^2 (from Table 3.1 in (Cook 2000)) the Salton Sea south basin depocenter sediment could provide up to 3.6 x 10^5 moles sulfide d^{-1} to the water column during anoxic bottom water conditions. Some of this sulfide would likely be oxidized by microbes (e.g., by anoxygenic photosynthesis) at the sediment-water interface, and some of this sulfide would react with Fe^{2+} in the porewater, however the excess would diffuse into the water column. This sulfide would contribute to an estimated 7,700 metric tons of iron sulfides formed per year in the Salton Sea, much of which forms as framboidal pyrite in the water column (de Koff et al. 2008). The rest of this sulfide likely oxidizes to elemental sulfur and eventually sulfate when it comes in contact with oxygen.

Over four sampling campaigns from 2020 – 2023, a hypolimnion in the Salton Sea was never observed, as evidenced by temperature (Table 1) and salinity (Fig. 4-2) data, including in summer months when air temperatures above the lake were over 40°C. Despite the lack of a hypolimnion, dissolved oxygen concentrations at the bottom of the lake and oxidation-reduction potential (Appendix C, Fig. 4-3) indicate anoxic conditions near the lakebed in August 2020 and September 2021. The low concomitant sulfide concentrations, however, indicate that the intense euxinia that characterized the lake in the past, where sulfide concentrations in the lake exceeded 2 mM from May- November (Reese et al. 2008), was not present in summer 2021 or 2022. The low sulfide accumulation in the lake's bottom waters could be because the lake is now too shallow to develop a thermocline (Table 1); daily wind-driven mixing may reach the lake's maximum depths now. Spontaneous mixing could also be a factor; with an annual evaporation rate of approx. 0.3 m H_2O yr^{-1} (Fogel et al. 2021), and the salinity in the lake (as shown by sulfate and chloride concentrations) being slightly higher at the lake's surface than at the maximum depth in August 2020 and September 2021, higher saline waters in contact with the air

could sink to the bottom of the lake at night. This daily delivery of oxygenated waters, and the lack of a discernable thermocline, could prevent a euxinic hypolimnion from developing in summer months, like has been described in the past at the Salton Sea (Reese et al. 2008).

While organic carbon delivery to sediment was not assessed during these sampling campaigns, our TDS measurements (Table 1) along with visual evidence (Appendix C, Fig. 4-4) of green mats and thick green-brown sludge on the shores of the lake indicate high amounts of primary production during our sampling campaigns. Algal and dinoflagellate blooms have been noted in both winter and summer months in the Salton Sea (Carmichael and Li 2006; Tiffany et al. 2007a; Tiffany et al. 2007c). These blooms are fed by the high flux of nutrients into the Salton Sea from agricultural and wastewater runoff (Fogel et al. 2021). Total phosphorus and nitrogen are notably depleted in the Salton Sea water column compared to the streams (e.g., 1.11 and 0.069 mg L^{-1} Total P in the New River and Salton Sea, respectively) that feed the lake (Holdren and Montaño 2002). Opposite to previous studies (Holdren and Montaño 2002) our results indicate that the Salton Sea is limited in respect to nitrogen (1:7.2 ratio of PO_4^{3-} to $NO_3^- + NO_2^- + NH_4^+$ in November 2023). One possibility for a shift from phosphorus to nitrogen limitation is that macro-organisms that would incorporate phosphate into their shells/bones (e.g., barnacles) can no longer live in the lake due to the salinity, temperature, harmful algal blooms, and sulfide toxicity (Kjelland and Swannack 2018). Nitrate in the Salton Sea did not exceed 3 µM in any of our sampling campaigns, however, ammonium concentrations in the sea exceed 20 µM in both September 2021 and November 2023 (Fig. 4-2), and sediment ammonium concentrations exceeded 100 µM below 2 cm in the sediment porewater, likely due to organic matter degradation (Fig. 4-3).

Our potential denitrification rates are similar to other saline lakes (e.g., 93 and 74 nmol

N_2 L^{-1} d^{-1} produced in the Salton Sea and Lake Rassnitzer, Germany, respectively (Hamersley et al. 2009)). Our potential annamox rate for the deep Salton Sea is several orders of magnitude smaller by comparison (0.001 nmol L^{-1} d^{-1}). This low activity was likely a result of the fully oxygenated water column in the November 2023 sampling, which forced us to induce anoxic incubations to measure potential rates. Our potential denitrification and annamox rates however do suggest that organisms capable of anaerobic metabolisms are present in oxygenated waters of the Salton Sea and rapidly begin cycling nitrogen species at the onset of anoxia. Similar to sulfate reducers, these organisms may even be active in particle associated micro-environments in oxygenated waters of the lake. Molecular studies (e.g., gene sequencing and fluorescence in situ hybridization) should be undertaken in conjunction with more metabolic rate determinations in the Salton Sea water in both summer and winter months to identify and quantify the anaerobic microbes that populate the water column under different redox regimes.

Conclusion

In this study, we present the first measured microbial metabolic rates (sulfate reduction, denitrification, and methane oxidation) in the Salton Sea water column. We show that sulfate reduction appears to be active in the Salton Sea water column even when oxygen is present, and that anaerobic ammonium oxidation and denitrification are initiated quickly after the onset of anoxia. We further show that the sediments and anoxic waters (when present) of the Salton Sea produce > 1 x 10^5 moles of sulfide per day, though our highest recorded sulfide concentration in the water column was less than 100 μM and all other measurements were near-zero. We show that the lake appears to have become too shallow for a thermocline to develop. Our data suggests that evaporation-driven salinity increases in surface waters may contribute to regular oxygen

delivery to the bottom waters, preventing the intense euxinia (>2 mM) that once characterized the lake's hypolimnion. Our results indicate that drying endorheic lakes are subject to changes in their biogeochemistry due to changes in mixing patterns brought on by their shallowing. Future studies of the lake's biogeochemistry would benefit from monthly samplings that aim to correlate changes anaerobic metabolisms in the water column to changes in the lake's physical and chemical properties. Additionally, the particle micro-environments within the Salton Sea water column would be an excellent candidate to study anaerobic organisms that thrive under oxygenated conditions.

Acknowledgements

We thank Christopher Tino for assistance in the 2020 sampling campaigns. We thank Alexandra Fowler, Tessa Holzmann, and Sebastian Krause for their help with processing the sediment samples. We thank Marcus Lin for assistance with sulfate reduction analyses. Special thanks to the UC Davis Stable Isotope Facility for their assistance in measuring $\delta^{15}N$ in our incubations.

Data availability.

Data will be available once the manuscript is published.

Author contributions.

TT, TL, and DJY conceived of the project. DJY, CH, CD, and GV collected water column samples. DJY, CH, CD, and GV performed geochemical analyses for water column samples. TT, TL, CH, and CD collected sediment samples. DJY and TT performed ^{35}S

incubations and analyses. DJY processed and analyzed sediment samples. DJY, GV, and XP performed ^{15}N incubations and analyses. DJY and TT wrote the manuscript with input from all co-authors.

References

Adams, P. M., D. K. Lynch, K. N. Buckland, P. D. Johnson, and D. M. Tratt. 2017. Sulfate mineralogy of fumaroles in the salton sea geothermal field, Imperial County, California. Journal of Volcanology and Geothermal Research **347:** 15-43.

Anderson, G. 1958. Some limnological features of a shallow saline meromictic lake. Limnology and Oceanography **3:** 259-270.

Bianchi, D., T. S. Weber, R. Kiko, and C. Deutsch. 2018. Global niche of marine anaerobic metabolisms expanded by particle microenvironments. Nature Geoscience **11:** 263-268.

Bjorndahl, J. A. and others 2022. Abrupt changes in the physical and biological structure of endorheic upland lakes due to 8-m lake-level variation during the 20th century. Limnology and Oceanography **67:** 1022-1039.

Brunskill, G., and S. Ludlam. 1969. Fayetteville Green Lake, New York. I. Physical and chemical limnology 1. Limnology and Oceanography **14:** 817-829.

Bussmann, I., A. Matousu, R. Osudar, and S. Mau. 2015. Assessment of the radio 3H-CH4 tracer technique to measure aerobic methane oxidation in the water column. Limnology and Oceanography: Methods **13:** 312-327.

Carmichael, W. W., and R. Li. 2006. Cyanobacteria toxins in the Salton Sea. Saline systems **2:** 1-13.

Cline, J. D. 1969. Spectrophometric determination of hydrogen sulfide in natural waters. Limnol. Oceanogr. **14:** 454-458.

Cook, C. B. 2000. Internal dynamics of a terminal basin lake: a numerical model for management of the Salton Sea. University of California, Davis.

Dale, A. W. and others 2015. Organic carbon production, mineralisation and preservation on the Peruvian margin. Biogeosciences **12:** 1537-1559.

de Koff, J. P., M. A. Anderson, and C. Amrhein. 2008. Geochemistry of iron in the Salton Sea, California, p. 111-121. The Salton Sea Centennial Symposium: Proceedings of a Symposium Celebrating a Century of Symbiosis Among Agriculture, Wildlife and People, 1905–2005, held in San Diego, California, USA, March 2005. Springer.

Dexter, D. M., J. S. Dainer, P. M. Detwiler, M. F. Moreau, and S. H. Hurlbert. 2007. Decline of springtime abundance of the pileworm Neanthes succinea in relation to hydrographic conditions at the Salton Sea, California. Lake and Reservoir Management **23:** 570-581.

Diao, M., R. Sinnige, K. Kalbitz, J. Huisman, and G. Muyzer. 2017. Succession of bacterial communities in a seasonally stratified lake with an anoxic and sulfidic hypolimnion. Frontiers in Microbiology **8:** 266042.

Dillon, J. G., L. M. McMath, and A. L. Trout. 2009. Seasonal changes in bacterial diversity in the Salton Sea. Hydrobiologia **632:** 49-64.

Fogel, M. and others 2021. Crisis at the Salton Sea: The Vital Role of Science.

Freund, H. and others 2022. Microbiome interactions and their ecological implications at the Salton Sea. California Agriculture **76**.

Frie, A. L., J. H. Dingle, S. C. Ying, and R. Bahreini. 2017. The effect of a receding saline lake (the Salton Sea) on airborne particulate matter composition. Environmental science & technology **51:** 8283-8292.

García-Robledo, E., A. Corzo, and S. Papaspyrou. 2014. A fast and direct spectrophotometric method for the sequential determination of nitrate and nitrite at low concentrations in small volumes. Marine Chemistry **162:** 30-36.

Grasshoff, K., M. Ehrhardt, and K. Kremling. 1999. Methods of seawater analysis. Wiley-VCH Verlag GmbH.

Hamersley, M. R., D. Woebken, B. Boehrer, M. Schultze, G. Lavik, and M. M. Kuypers. 2009. Water column anammox and denitrification in a temperate permanently stratified lake (Lake Rassnitzer, Germany). Systematic and applied microbiology **32:** 571-582.

Holdren, G. C., and A. Montaño. 2002. Chemical and physical characteristics of the Salton Sea, California. Hydrobiologia **473:** 1-21.

Ingvorsen, K., J. G. Zeikus, and T. D. Brock. 1981. Dynamics of bacterial sulfate reduction in a eutrophic lake. Appl. Environm. Microbiol. **42:** 1029-1036.

Jellison, R. and others 2004. Conservation and management challenges of saline lakes: a review of five experience briefs. Lake Basin Management Initiative: Thematic Paper.

Joye, S. B., T. L. Connell, L. G. Miller, R. S. Oremland, and R. S. Jellison. 1999. Oxidation of ammonia and methane in an alkaline, saline lake. Limnology and oceanography **44:** 178-188.

Jørgensen, B. B. 1978. A comparison of methods for the quantification of bacterial sulphate reduction in coastal marine sediments: I. Measurements with radiotracer techniques. Geomicrobiol. J. **1:** 11-27.

Kallmeyer, J., T. G. Ferdelman, A. Weber, H. Fossing, and B. B. Jørgensen. 2004. A cold chromium distillation procedure for radiolabeled sulfide applied to sulfate reduction measurements. Limnol. Oceanogr. Methods **2:** 171-180.

Kjelland, M. E., and T. M. Swannack. 2018. Salton Sea days of future past: Modeling impacts of alternative water transfer scenarios on fish and bird population dynamics. Ecological Informatics **43:** 124-145.

Krijgsman, W., F. J. Hilgen, I. Raffi, F. J. Sierro, and D. Wilson. 1999. Chronology, causes and progression of the Messinian salinity crisis. Nature **400:** 652-655.

Liu, Y.-H. and others 2023. Sediment prokaryotic microbial community and potential biogeochemical cycle from saline lakes shaped by habitat. Microbiological Research **270:** 127342.

Lyons, D. E., A. G. Patterson, J. Tennyson, T. J. Lawes, and D. D. Roby. 2018. The Salton sea: critical migratory stopover habitat for Caspian terns (Hydroprogne caspia) in the North American Pacific Flyway. Waterbirds **41:** 154-165.

Marti-Cardona, B., T. Steissberg, S. G. Schladow, and S. Hook. 2008. Relating fish kills to upwellings and wind patterns in the Salton Sea, p. 85-95. The Salton Sea Centennial Symposium: Proceedings of a Symposium Celebrating a Century of Symbiosis Among Agriculture, Wildlife and People, 1905–2005, held in San Diego, California, USA, March 2005. Springer.

McIlvin, M. R., and M. A. Altabet. 2005. Chemical conversion of nitrate and nitrite to nitrous oxide for nitrogen and oxygen isotopic analysis in freshwater and seawater. Analytical Chemistry **77:** 5589-5595.

Micklin, P. 2007. The Aral sea disaster. Annu. Rev. Earth Planet. Sci. **35:** 47-72.

Phillips, A. A. and others 2021. Microbial succession and dynamics in meromictic Mono Lake, California. Geobiology **19:** 376-393.

Raven, M., R. Keil, and S. Webb. 2021. Microbial sulfate reduction and organic sulfur formation in sinking marine particles. Science **371:** 178-181.

Reese, B. K., M. A. Anderson, and C. Amrhein. 2008. Hydrogen sulfide production and volatilization in a polymictic eutrophic saline lake, Salton Sea, California. Science of the total environment **406:** 205-218.

Riedel, R., L. Caskey, and B. A. Costa-Pierce. 2002. Fish biology and fisheries ecology of the Salton Sea, California, p. 229-244. The Salton Sea: Proceedings of the Salton Sea Symposium, held in Desert Hot Springs, California, 13–14 January 2000. Springer.

Shuford, W. D., N. Warnock, K. C. Molina, and K. K. Sturm. 2002. The Salton Sea as critical habitat to migratory and resident waterbirds. Hydrobiologia **473:** 255-274.

Swan, B. K. 2009. Diversity, abundance and activity of microbial communities associated with anoxia in a hypersaline lake, the Salton Sea, California. University of California, Santa Barbara.

Swan, B. K., C. J. Ehrhardt, K. M. Reifel, L. I. Moreno, and D. L. Valentine. 2010a. Archaeal and bacterial communities respond differently to environmental gradients in anoxic sediments of a California hypersaline lake, the Salton Sea. Applied and environmental microbiology **76:** 757-768.

Swan, B. K., K. M. Reifel, and D. L. Valentine. 2010b. Periodic sulfide irruptions impact microbial community structure and diversity in the water column of a hypersaline lake. Aquatic Microbial Ecology **60:** 97-108.

Tiffany, M. A., M. R. González, B. K. Swan, K. M. Reifel, J. M. Watts, and S. H. Hurlbert. 2007a. Phytoplankton dynamics in the Salton Sea, California, 1997–1999. Lake and Reservoir Management **23:** 582-605.

Tiffany, M. A., S. L. Ustin, and S. H. Hurlbert. 2007b. Sulfide irruptions and gypsum blooms in the Salton Sea as detected by satellite imagery, 1979–2006. Lake and Reservoir Management **23:** 637-652.

Tiffany, M. A., J. Wolny, M. Garrett, K. Steidinger, and S. H. Hurlbert. 2007c. Dramatic blooms of Prymnesium sp.(Prymnesiophyceae) and Alexandrium margalefii (Dinophyceae) in the Salton Sea, California. Lake and Reservoir Management **23:** 620-629.

Tompson, A. F. 2016. Born from a flood: The Salton Sea and its story of survival. Journal of Earth Science **27:** 89-97.

Wardlaw, G. D., and D. L. Valentine. 2005. Evidence for salt diffusion from sediments contributing to increasing salinity in the Salton Sea, California. Hydrobiologia **533:** 77-85.

Waters, M. R. 1983. Late Holocene lacustrine chronology and archaeology of ancient Lake Cahuilla, California. Quaternary Research **19:** 373-387.

Williams, W. D. 1996. What future for saline lakes? Environment: Science and Policy for Sustainable Development **38:** 12-39.

Williams W.D. 2002. Environmental threats to salt lakes and the likely status of inland saline ecosystems in 2025. Environmental conservation **29:** 154-167.

Younker, L. W., P. W. Kasameyer, and J. D. Tewhey. 1982. Geological, geophysical, and thermal characteristics of the Salton Sea Geothermal Field, California. Journal of Volcanology and Geothermal Research **12:** 221-258.

Chapter 5

Conclusions and Future Directions

The novel research presented in this thesis details the exploration of transiently deoxygenated environments and expands our collective knowledge of sulfur and nitrogen biogeochemistry, the benthic response to expanding oxygen minimum zones, and microbial metabolisms in drying inland lakes.

The findings in chapter 2 elucidated questions involving the proliferation of the largest yet-mapped mat of giant sulfur-oxidizing bacterial (GSOB) mats in Earth's oceans. The ephemeral nature of these mats in the Santa Barbara Basin have been well documented (Kuwabara et al. 1999; Reimers et al. 1996a), requiring anoxia but not total nitrate depletion to proliferate (Valentine et al. 2016). Our new studies found that the GSOB that comprise the mats require an exhaustion of iron oxides in surface sediments, which leads to the elevation of the sulfate reduction zone to the sediment-water interface, in order to proliferate into thick, contiguous mats on the seafloor of the Santa Barbara Basin. Similar to other transiently deoxygenated environments (Dale et al. 2016; Noffke et al. 2016), these bacteria conduct dissimilatory nitrate reduction to ammonium. Additionally, the wealth of geochemical parameters published in chapter 2 are a foundation for other manuscripts that have been published, submitted, and are currently in preparation for publication. In totality, this work shows that expanding oxygen minimum zones, when they interact with the benthic environment, lead to the proliferation of chemoautotrophic microbial mats on the seafloor and the flux of reduced compounds into the pelagic environment.

Chapter 3 combines our data from chapter 2 with data gathered from three additional expeditions in the Santa Barbara Basin, historical geochemical data from the sediment

(Kuwabara et al. 1999; Reimers et al. 1996a; Sholkovitz 1973; Zheng et al. 2000), and long-term water column monitoring from the California Cooperative Oceanic Fisheries Investigation (CalCOFI) to explore the interplay between iron and sulfur cycling in transiently deoxygenated aquatic environments. We found that sustained anoxia within the basin is concomitant with a shift from a ferruginous to sulfidic sediment state, a net loss of highly reactive iron from surface sediment, and the first-documented sulfide flux from the sediment into the Santa Barbara Basin water column. The extensive amount of in-situ data collected from the ABISS benthic lander allowed us to constrain the duration and intensity of a flushing event within the Santa Barbara Basin, which will help inform biogeochemical modeling in the Southern California Bite and hopefully other transiently deoxygenated marine systems.

We presented the first measured microbial rates (sulfate reduction, denitrification, and methane oxidation) in the water column of the Salton Sea in Chapter 4. We found that sulfate concentrations within the lake have increased over time (to above 200 mM) and that as the lake has shallowed from 15 m to 10.5 m maximum depth, a thermocline no longer appears to develop and the extreme euxinia (>2 mM) seen in the past (Reese et al. 2008) is no longer present. The lake still develops anoxia during the summer months, however, and sulfate reduction rates appears active in the water column in both oxygenated and anoxic conditions. Additionally, we found that denitrification is quickly established, at high rates, upon the onset of anoxia in the lake. These results represent a pilot study within the Salton Sea and offer a blueprint for future research in endorheic lakes.

Going forward, the work presented within this dissertation offers several avenues of future exploration into oxygen minimum zones, the benthic marine environment, and drying inland lakes. The contribution of aerobic sulfide oxidizers, especially cable bacteria, within these

transiently deoxygenated environments needs to be further constrained. Previous work within the Baltic Sea has showed that as anoxia develops, colonies of cable bacteria yield their biogeochemical niche to giant sulfur-oxidizing bacterial mats (Marzocchi et al. 2018; Schauer et al. 2014). The exact geochemical conditions that accompany this shift still need to be constrained, as does the contribution of other sulfur-oxidizing bacteria, such as the "ghost balls" we documented in the basin in 2019. A combination of metagenomics, molecular biology, and further geochemistry within the Santa Barbara Basin will help elucidate changes in the benthic chemoautotrophic communities in these transiently deoxygenated environments, what geochemical parameters accompany these shifts, and how these organisms modulate their surrounding environment.

Additionally, further work into iron mineral speciation in these transiently deoxygenated environments will help guide the understanding of early diagenesis in both current environments, and our interpretations of past marine anoxia from iron and sulfide mineral paleo-proxies. In particular, elucidating the geochemical conditions at the sediment-water interface that preface reduced iron to be shunted into iron carbonates vs. iron sulfides would greatly expand our understanding of how reduced iron is processed during early diagenesis. Recent developments in in-situ sulfur isotope fractionation by the use of black & white photographic film coupled to secondary ion mass spectrometry (Gomes et al. 2022) should be applied to the sediment in Santa Barbara Basin in oxygenated, anoxic, and nitrate-depleted conditions to understand how sulfur isotope fractionation during early diagenesis is effected by transient deoxygenation. The exact causes of deoxygenation within the Santa Barbara Basin remain elusive; further investigations into organic matter delivery to the basin sediment should elucidate whether anoxia is becoming more of a permanent fixture within the basin. Further in-situ observations, particularly of sulfide,

should be conducted in the benthic environment to monitor whether euxinia develops within the basin's bottom waters and how this effects benthic animal populations within the basin.

The Salton Sea offers a dynamic environment to study sulfur-driven metabolisms, and especially how these metabolisms interplay with desiccation of saline environments. The high sulfate content within the water column of the Salton Sea, transient anoxia in the lake's bottom waters, and apparent ammonium flux from the sediment into the water allows for a natural environment to study the newly documented metabolism of sulfate reduction coupled with ammonium oxidation (Dominika et al. 2021). Additionally, further constraining the sulfate reduction rate in the sediment porewaters and water column of the Salton Sea will allow for estimations of sulfide content within the lake, and whether gypsum irruptions (Tiffany et al. 2007b) and sulfide flux into the air surrounding the lake (Reese et al. 2008) that have characterized the lake in the past will continue in the future.

I have been extremely privileged to contribute to our understanding of marine and lacustrine environments. In conducting fieldwork aboard ships large and small, going down to the seafloor in a submersible, and guiding remote operated vehicles on sample collection and in-situ experimentation on the seafloor, I have found the mantra that "limitations breed creativity" to be especially true. These environments are technologically difficult to study, and I have been incredibly inspired by the teamwork, ingenuity, gumption, and gusto necessary to make this work possible. There are exciting outstanding research questions in this work, some I have detailed here, and many others yet to be pontificated upon. I look forward to guiding future investigations into marine and lacustrine chemistry and microbiology to enhance our collective understanding of Earth's past, present, and future.

Appendix A

Supplementary Material: Marine anoxia initiates microbial mat proliferation and associated changes in benthic nitrogen, sulfur, and iron cycling in the Santa Barbara Basin, California Borderland.

Table 1: Porewater nitrite concentrations taken from sediment cores at SDRO and SDT3-A. Nitrite was below detection in sediment cores for all other stations.

Sediment Depth	SDRO [NO_2^-]	SDT3A [NO_2^-]
[cm]	[µmol L^{-1}]	[µmol L^{-1}]
-1	1.1	0.0
0.5	36.6	5.2
1.5	1.4	1.7
2.5	1.1	0.7
3.5	1.1	0.0
4.5	1.2	0.0
5.5	0.0	0.0
6.5	6.1	0.0
7.5	4.3	0.0
8.5	0.0	0.0
9.5	0.0	0.0
11	0.0	
13	0.0	
15	0.0	0.0
17	0.0	0.0
19		0.0

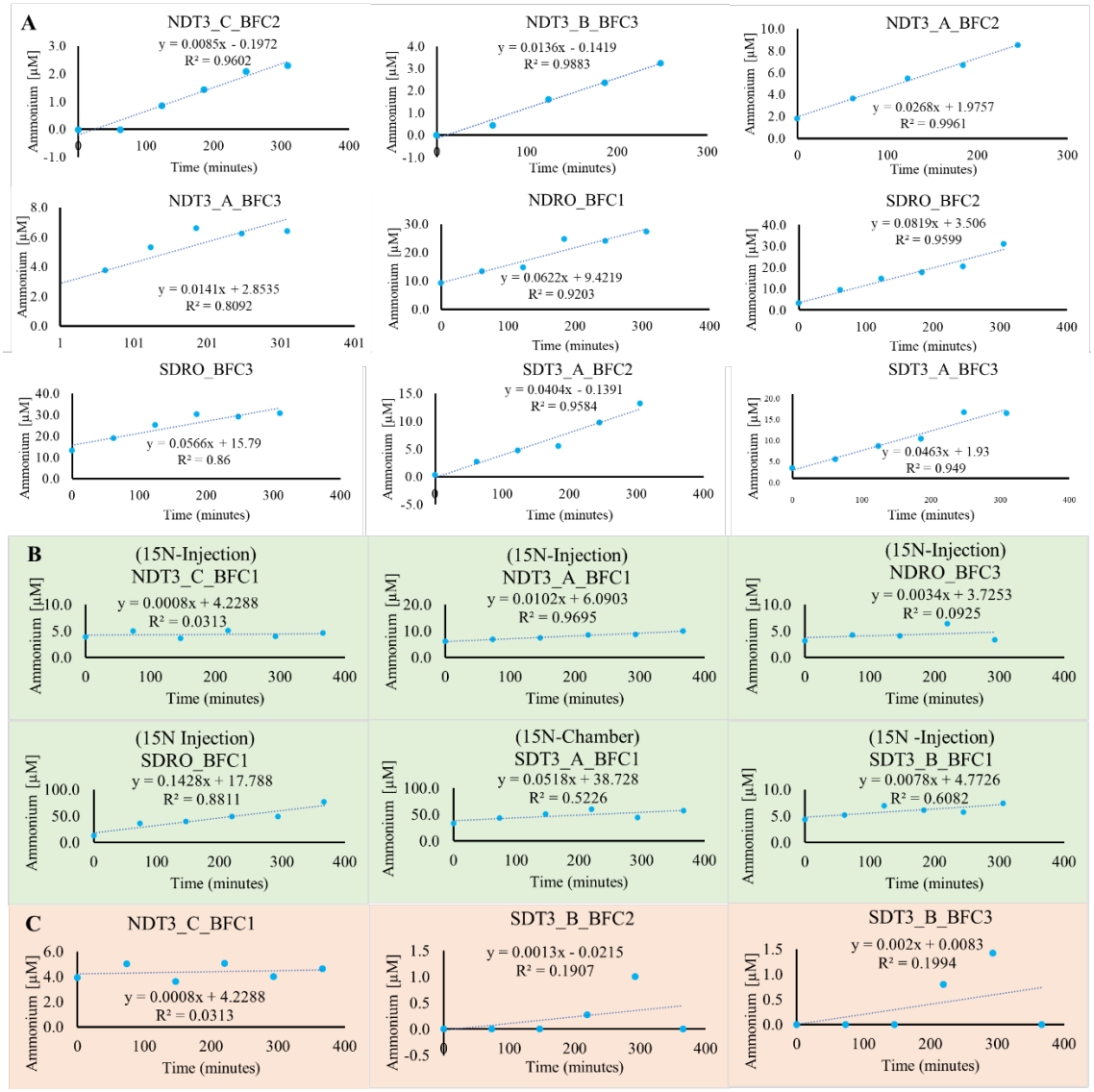

Figure 1: A) Ammonium concentration changes over time from benthic flux chamber (BFC1, BFC2, BFC3) incubations. B) Ammonium concentration changes over time from 15N-Nitrate benthic flux chamber incubations. Note these chambers were not used to calculate benthic fluxes. C) Ammonium concentration changes over time from benthic flux chamber incubations where there was no calculatable flux. No data are shown from chambers if there was a mechanical failure with the deployment or ammonium concentrations were all below detection. For station abbreviation definitions please refer to the main manuscript.

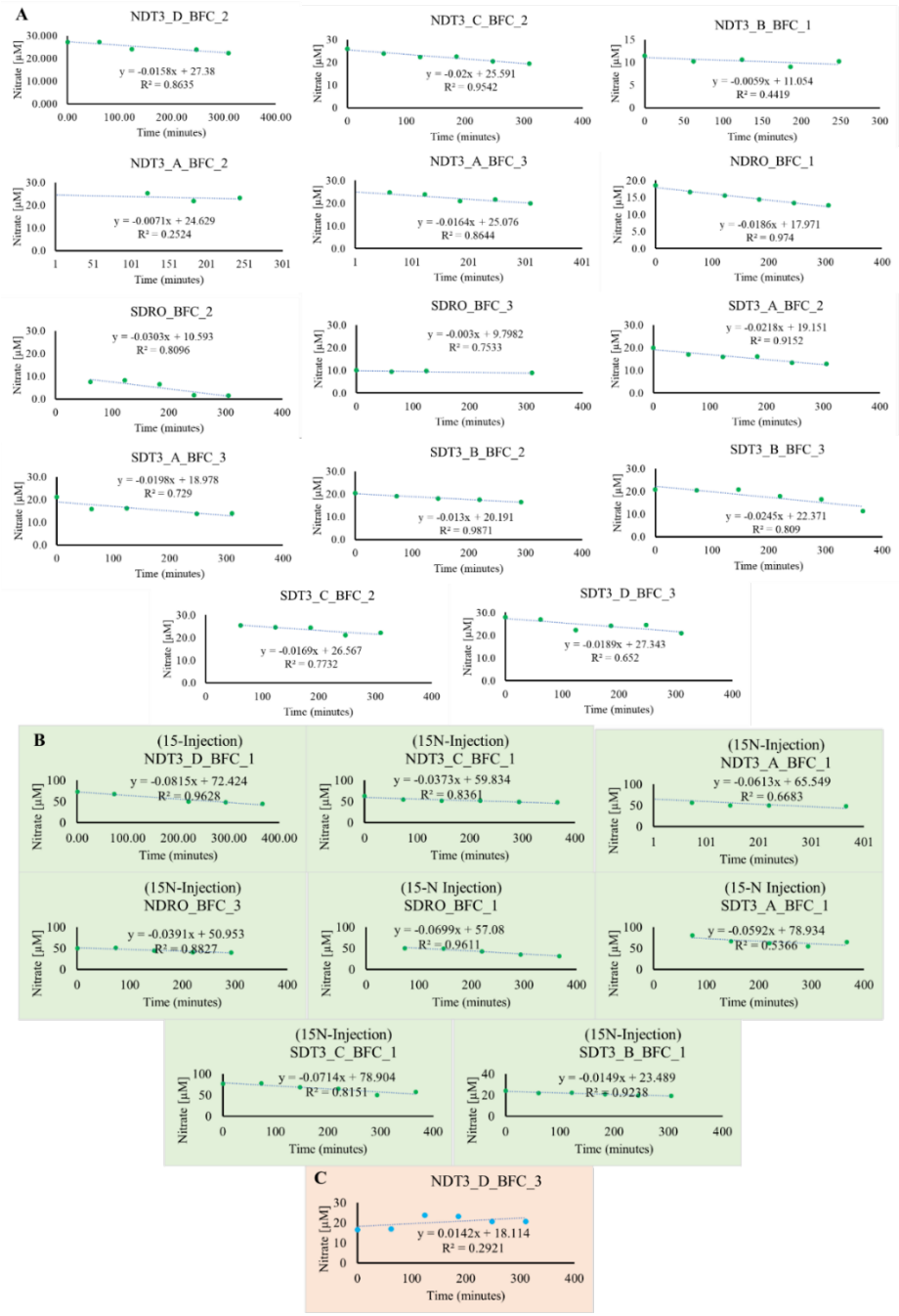

Figure 2: Nitrate concentration changes over time from benthic flux chamber (BFC1, BFC2, BFC3) incubations. B) Nitrate concentration changes over time from ^{15}N-Nitrate benthic flux chamber incubations. Note these chambers were not used to calculate benthic fluxes. C) Nitrate concentration changes over time from benthic flux chamber incubations where there was no calculatable flux. No data are shown from chambers if there was a mechanical failure with the deployment. For station abbreviation definitions please refer to the main manuscript.

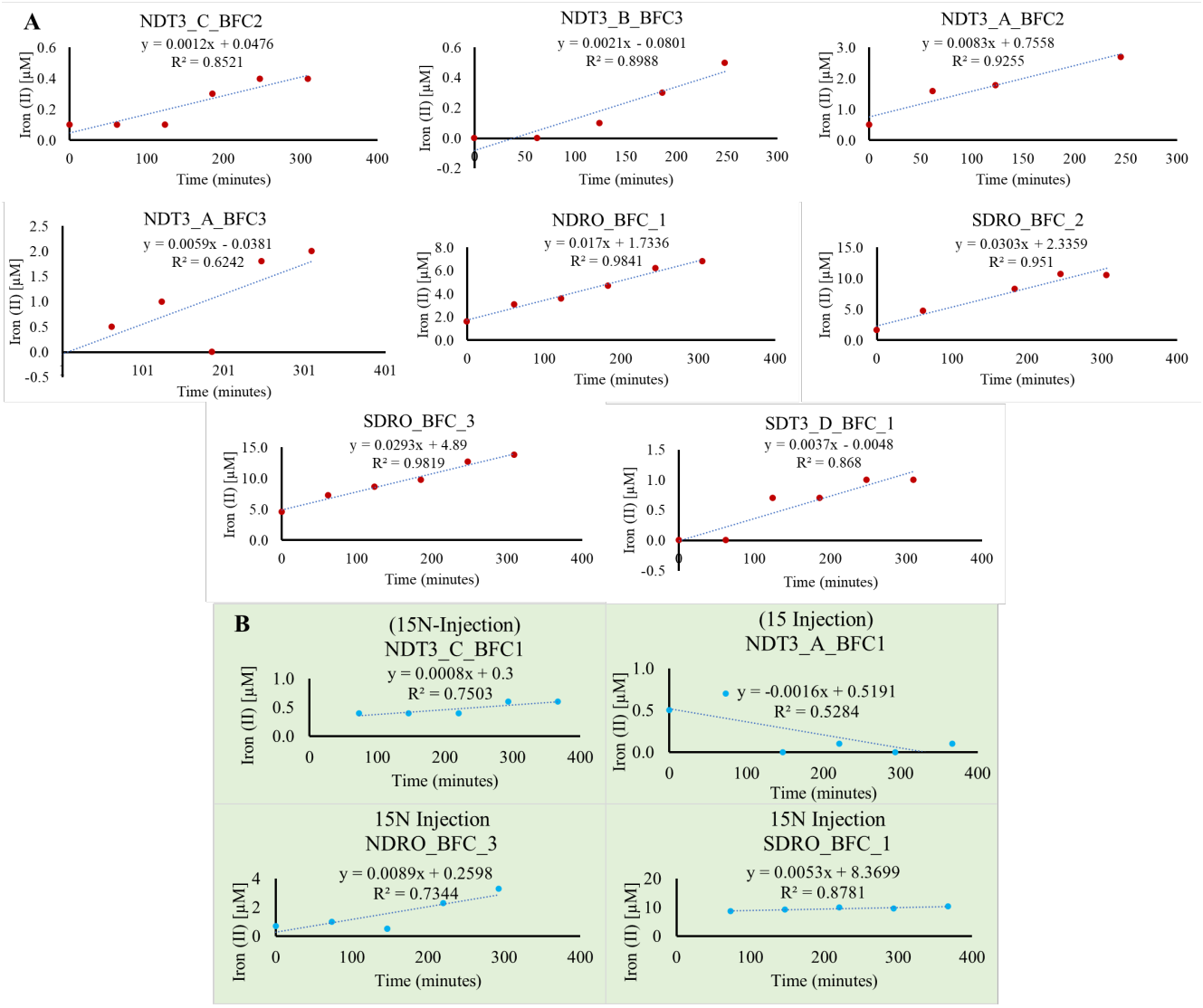

Figure 3: Iron (II) concentration changes over time from benthic flux chamber (BFC1, BFC2, BFC3) incubations. B) Iron (II) concentration changes over time from ^{15}N-Nitrate benthic flux chamber incubations. Note these chambers were not used to calculate benthic fluxes. No data are shown from chambers if there was a mechanical failure with the deployment or concentrations were all below detection. For station abbreviation definitions please refer to the main manuscript.

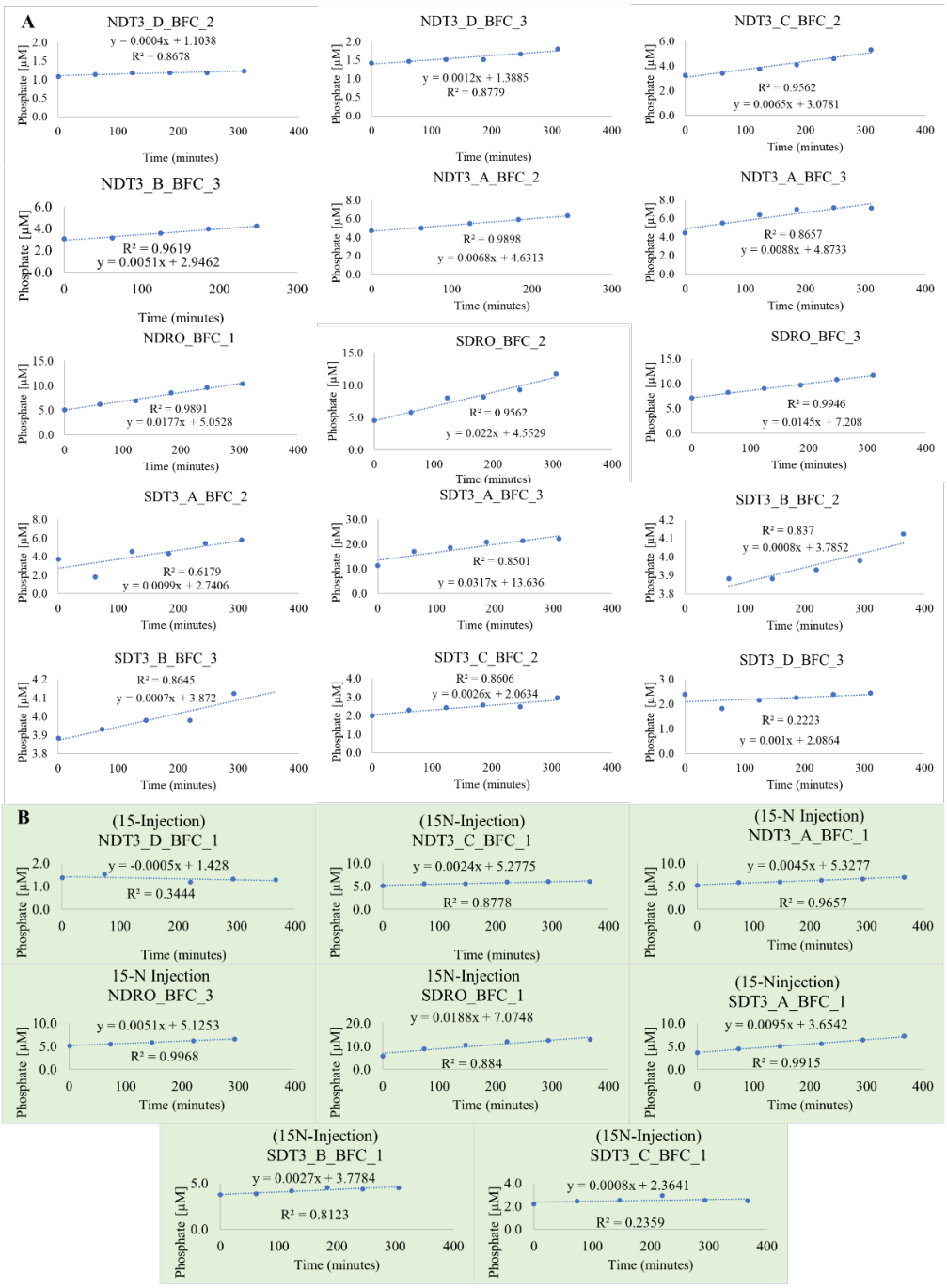

Figure 4: Phosphate concentration changes over time from benthic flux chamber (BFC1, BFC2, BFC3) incubations. B) Phosphate concentration changes over time from 15N-Nitrate benthic flux chamber incubations. Note these chambers were not used to calculate benthic fluxes. No data are shown from chambers if there was a mechanical failure with the deployment or concentrations were all below detection. For station abbreviation definitions please refer to the main manuscript.

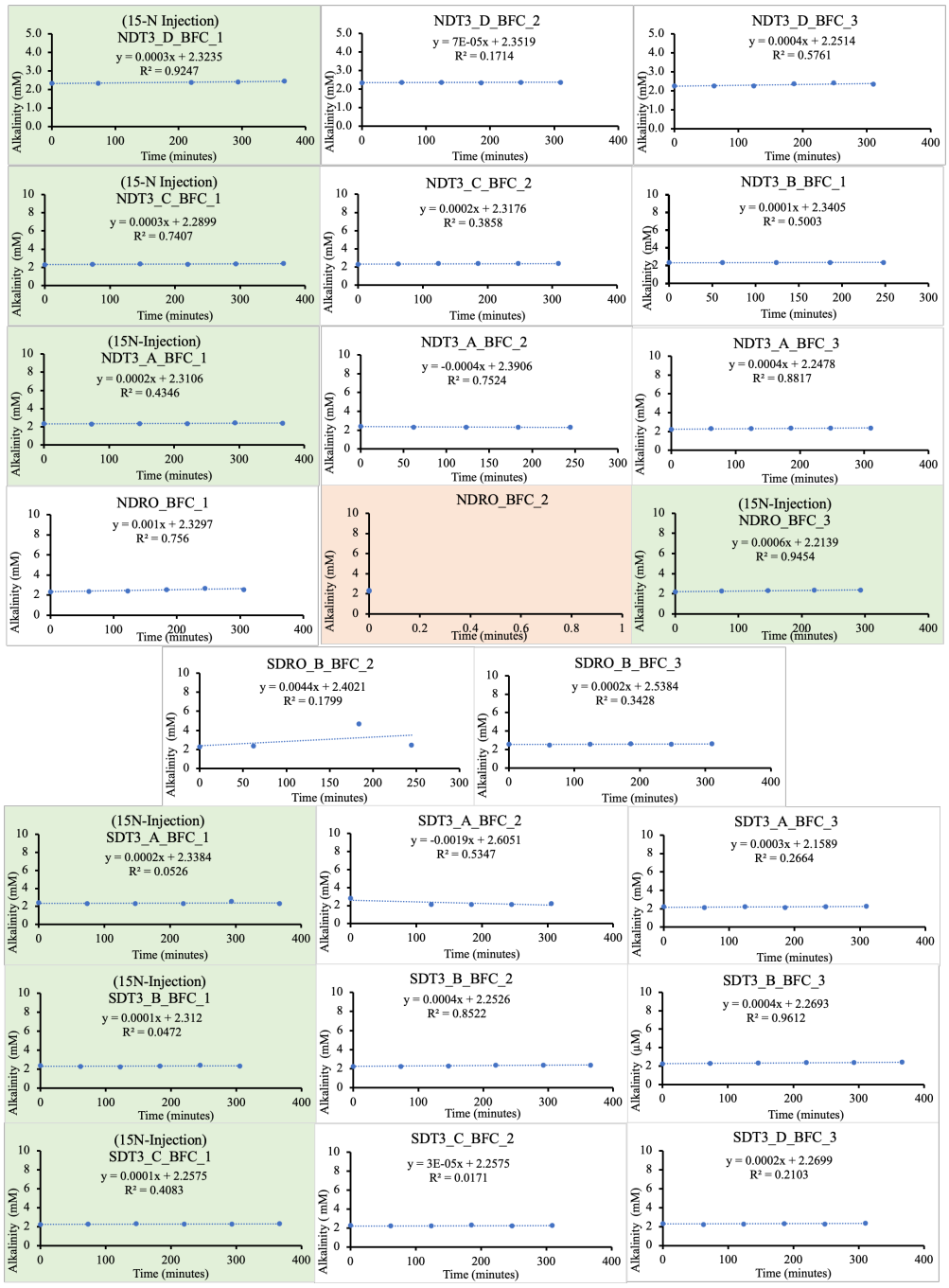

Figure 5: Total Alkalinity changes over time from benthic flux chamber (BFC1, BFC2, BFC3) incubations. No data are shown from chambers if there was a mechanical failure with the deployment or concentrations were all below detection. For station abbreviation definitions please refer to the main manuscript.

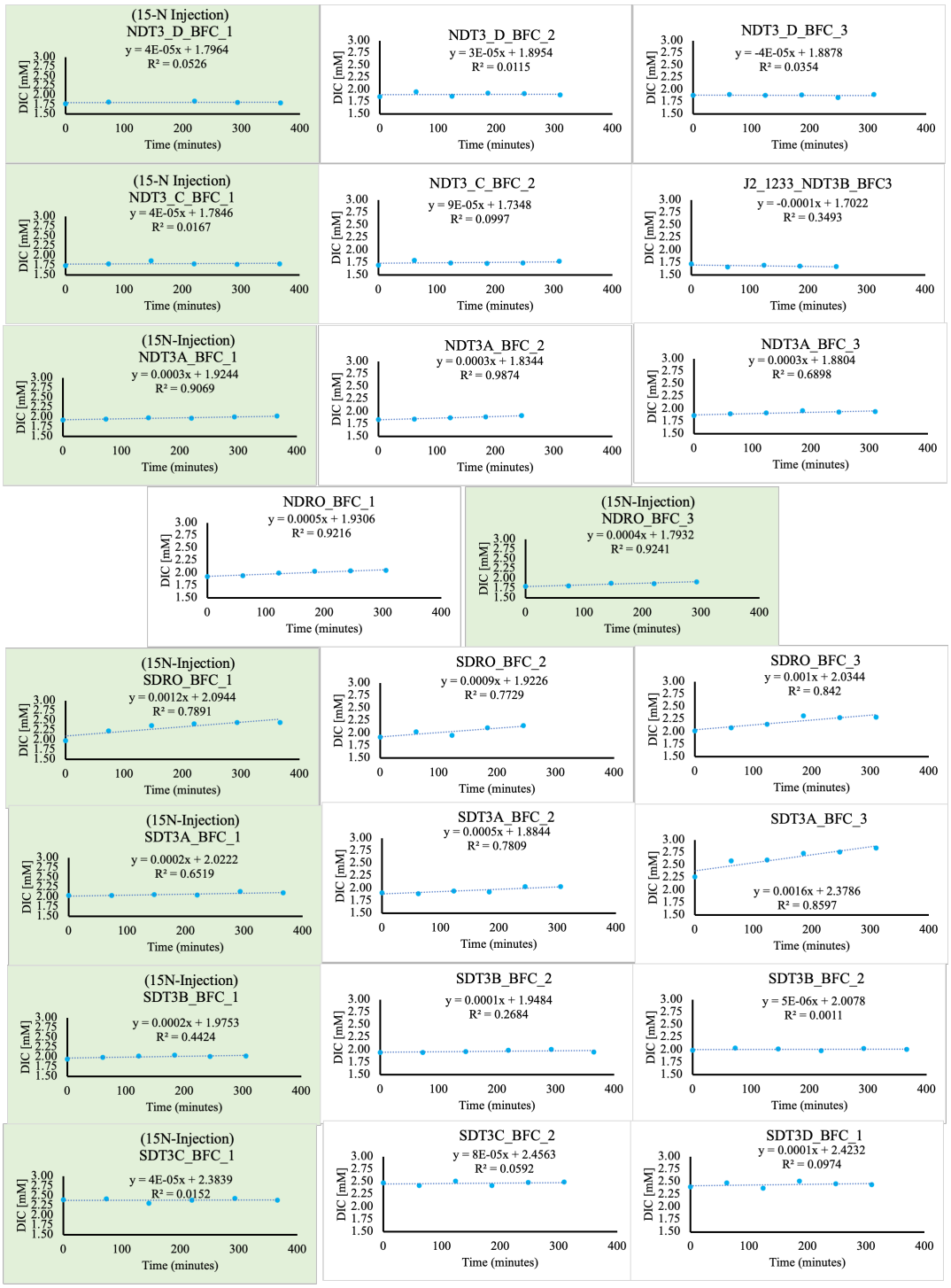

Figure 6: Dissolved Inorganic Carbon (DIC) changes over time from benthic flux chamber (BFC1, BFC2, BFC3) incubations. No data are shown from chambers if there was a mechanical failure with the deployment or concentrations were all below detection. For station abbreviation definitions please refer to the main manuscript.

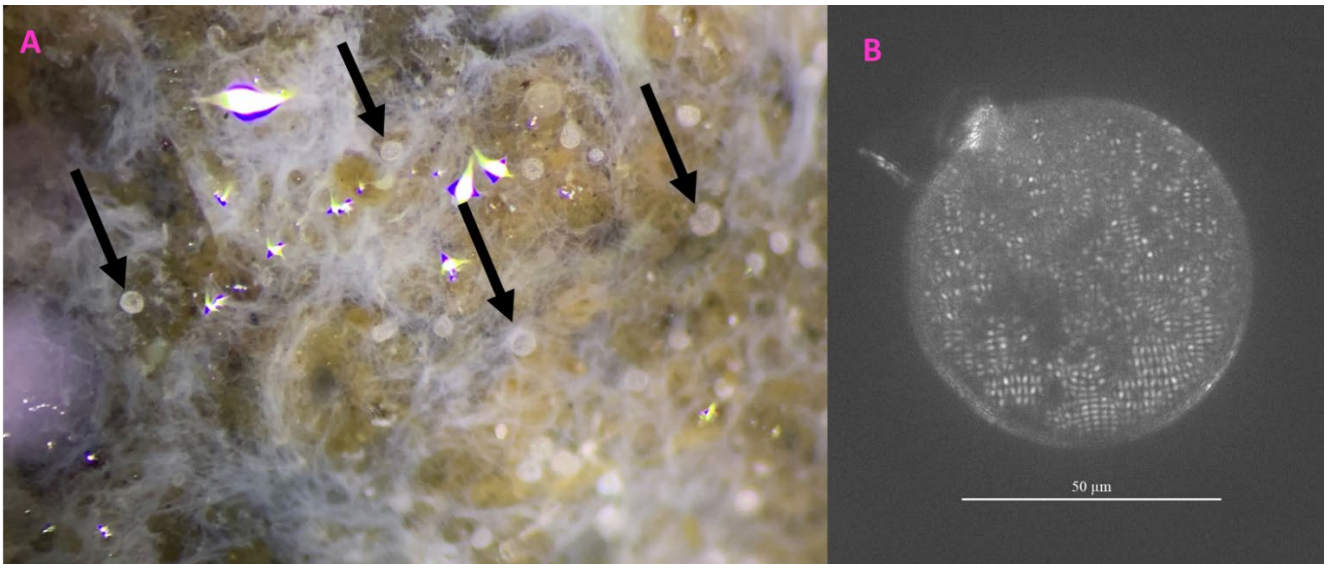

Figure 7: A) Photograph of spherical sulfur bacteria (nicknamed 'ghost balls') within a mat of filamentous sulfur bacteria as seen through a dissection microscope. Black arrows point to a few of the ghost balls. The size of the ghost ball radius ranges between 24.0 – 49.8 µm (n = 8). B) Light Microscopy image of representative ghost ball with a scale bar. Ghost Balls were sampled from the 0-1 cm section of a core collected from station NDRO.

Appendix B

Supplemental Material: Increased bottom water anoxia leads to a loss of sedimentary iron content and an associated shift to a sulfidic sediment state in the Santa Barbara Basin.

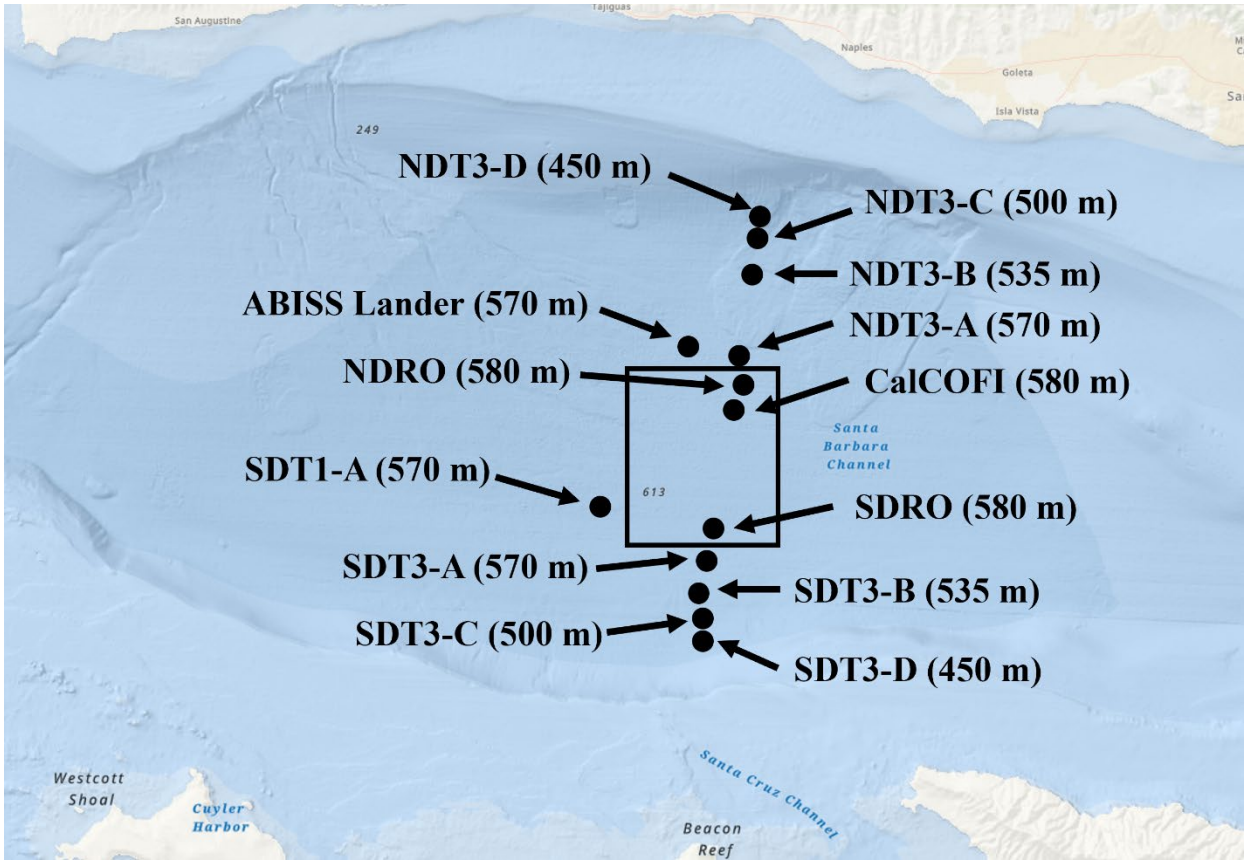

Figure 1. Map of the Santa Barbara Channel with sampling stations and approximate depths labeled. Black box represents the area in which "Depocenter" stations have been sampled in the present study (NDRO, SDRO) and previous studies. The CalCOFI sampling site and location of the ABISS lander are also highlighted. The map was created using the National Oceanographic and Atmospheric Administration bathymetric viewer.

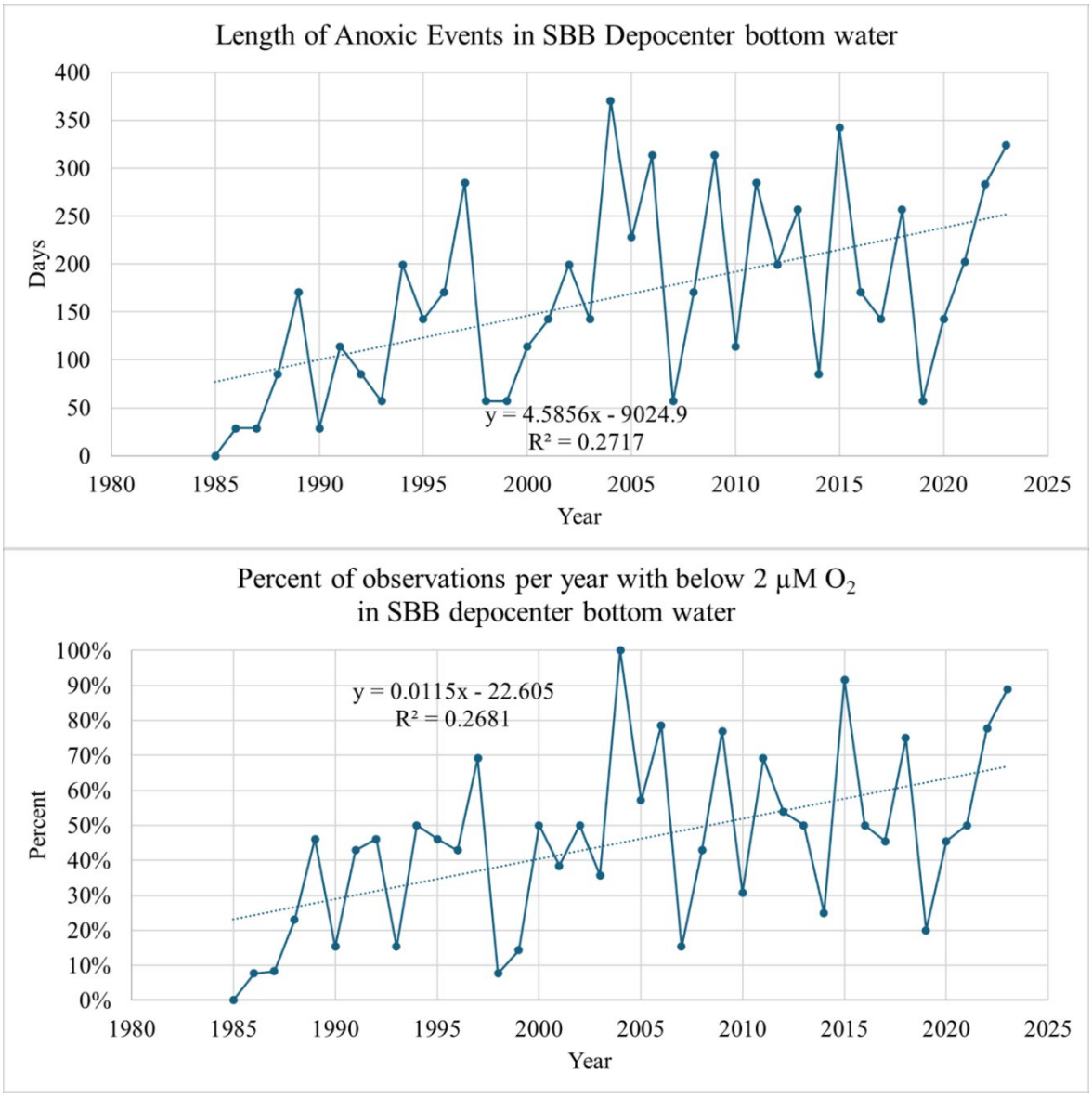

Figure 2. Length in anoxic events (top) and percent time of anoxia within the Depocenter (bottom) over time. Values were exported from Ocean Data Viewer and represent DIVA gridding at a scale of x=5 and y=300.

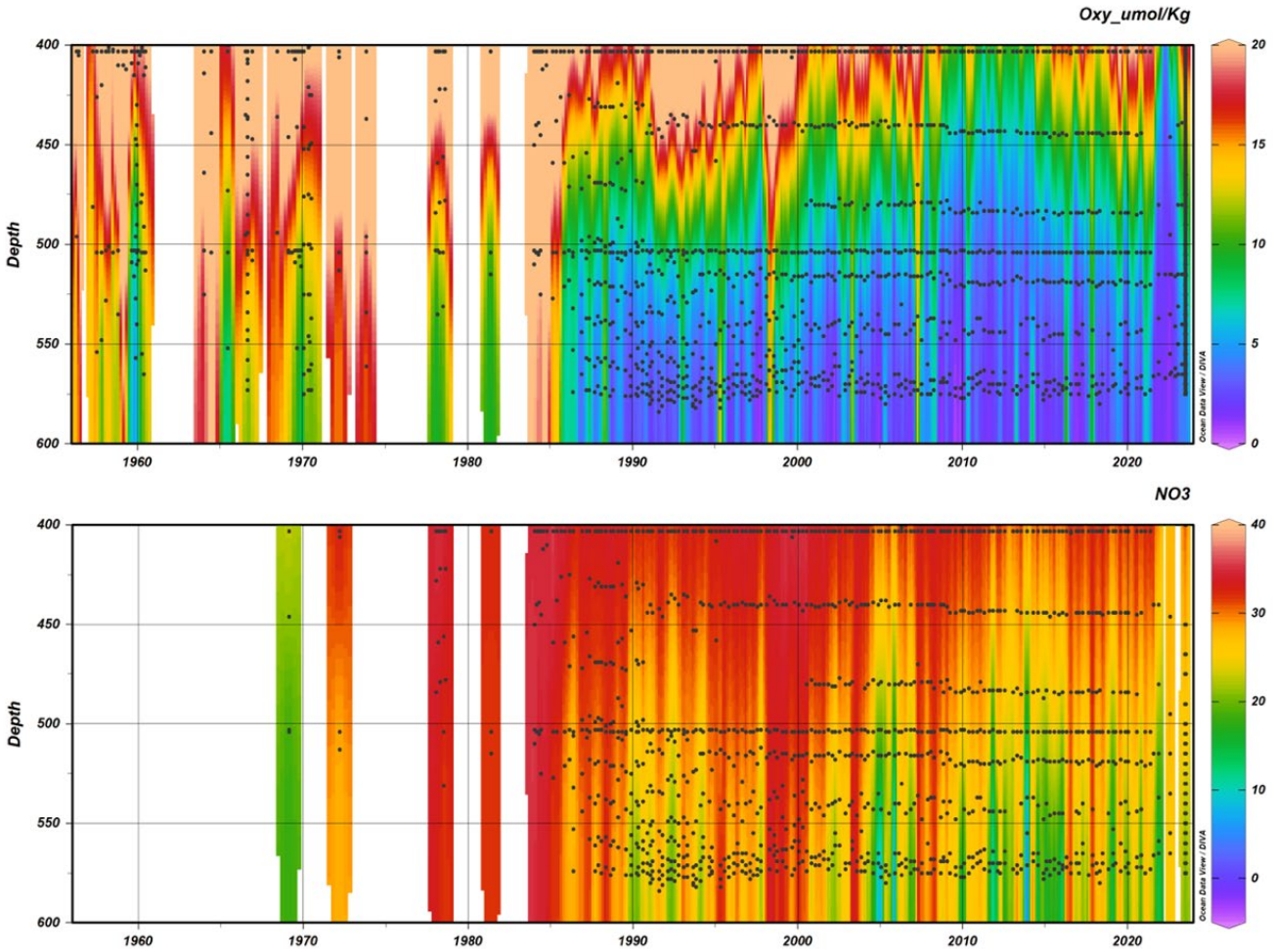

Figure 3. Dissolved oxygen (top) and Nitrate (bottom) concentrations in the Santa Barbara Basin from 1956-2023. All data is from CalCOFI except data from 1969/1970 Sholkovitz et al. (1973) and July 2023.

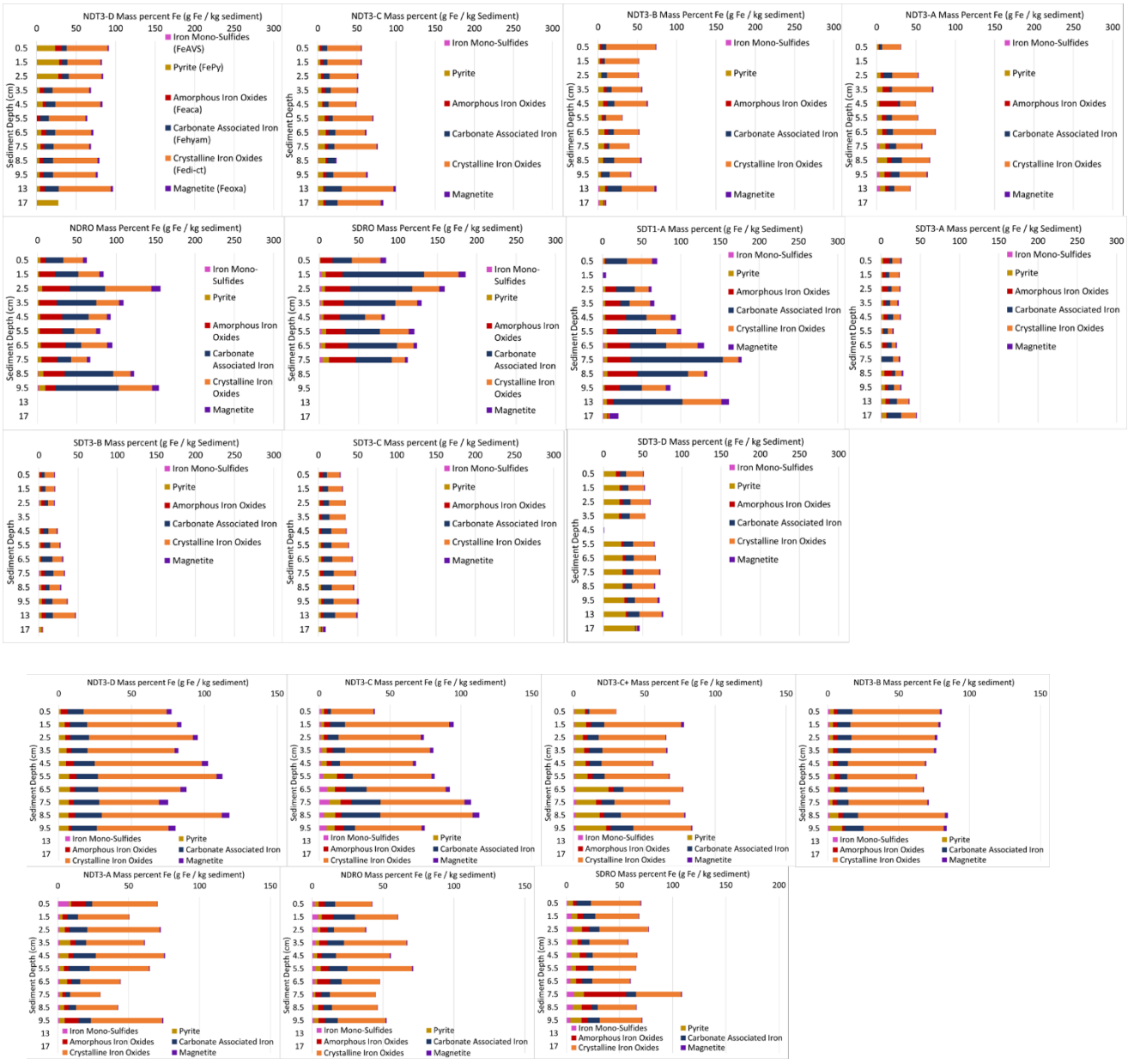

Figure 4. Sediment digestions from 2019 (top cluster) and 2023 (bottom cluster). Each bar represents a discrete depth. Iron concentrations are shown as g Fe per kg of sediment.

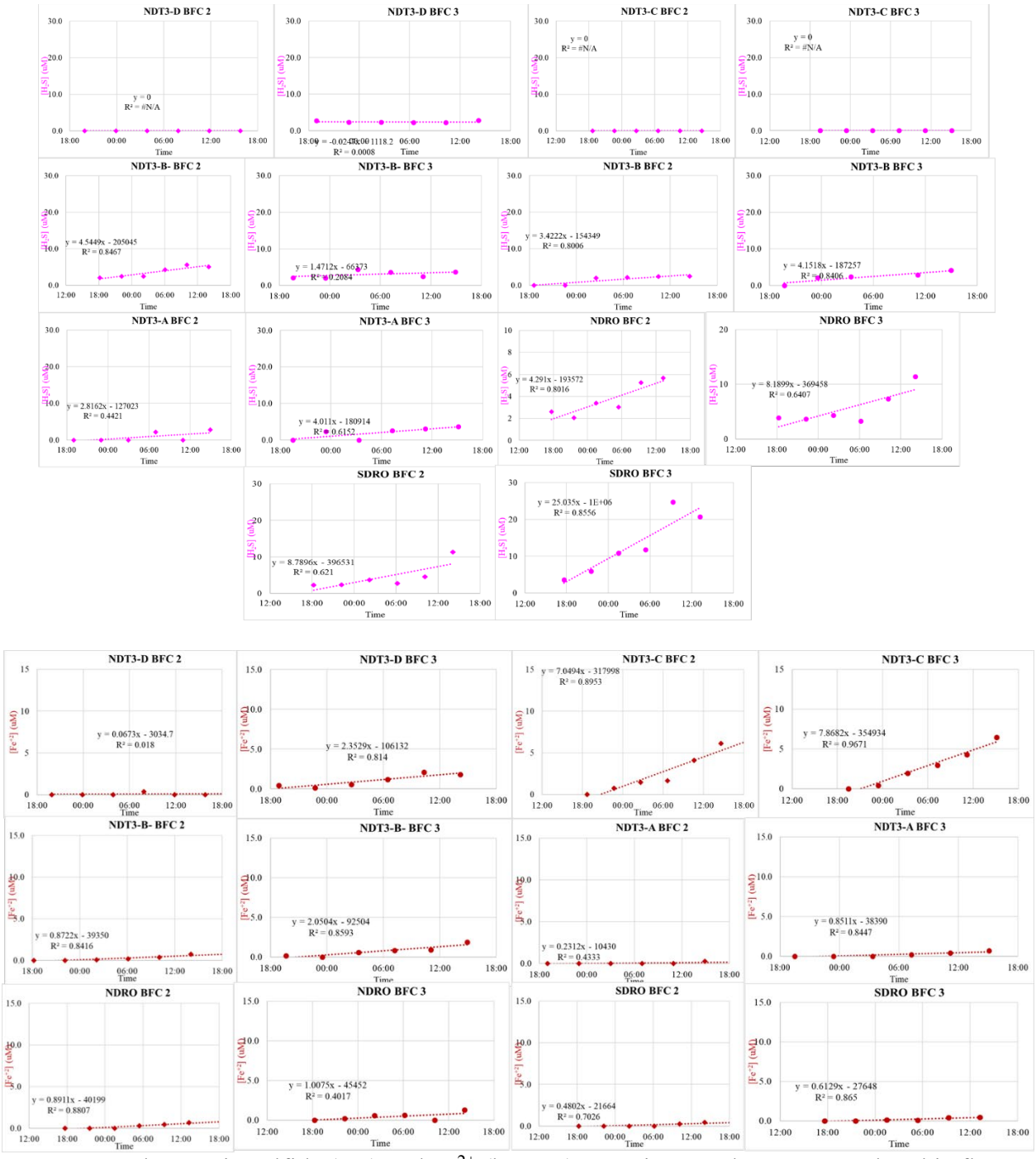

Figure 5. Changes in sulfide (top) and Fe^{2+} (bottom) over time used to construct benthic fluxes from individual chambers in 2023.

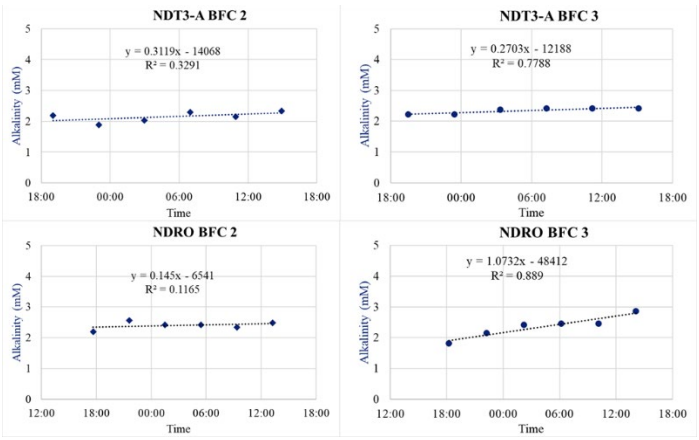

Figure 6. Changes in alkalinity over time used to construct benthic fluxes from individual chambers in 2023. Concentrations are only reported for two of the deepest stations (NDRO and NDT3-A).

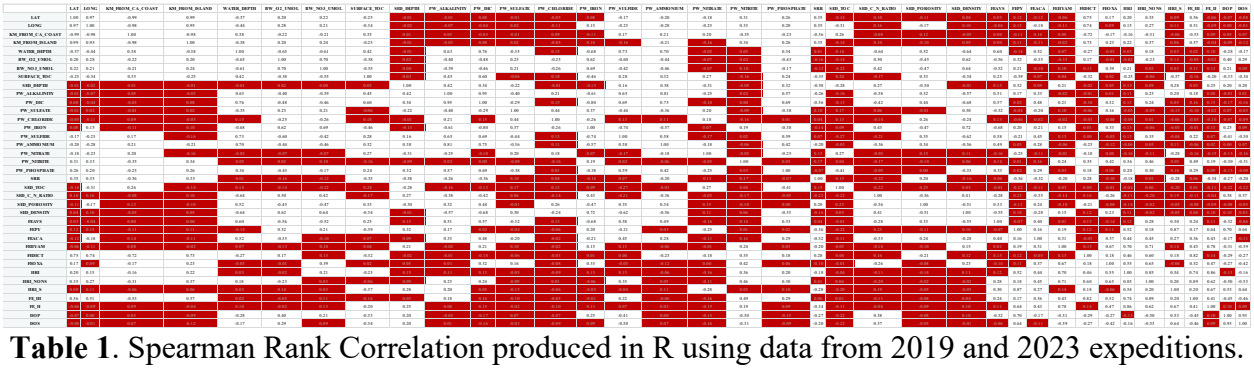

Table 1. Spearman Rank Correlation produced in R using data from 2019 and 2023 expeditions. Cells in red have p values above 0.05 and the relationship between those variables is considered insignificant.

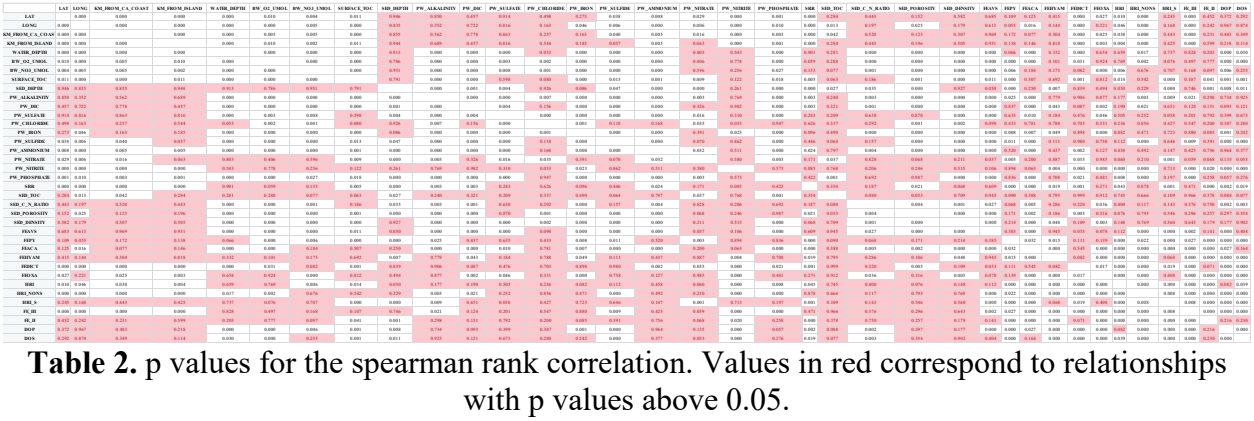

Table 2. p values for the spearman rank correlation. Values in red correspond to relationships with p values above 0.05.

Sampling Date	Sampling Stations	Vessel	Sampling Device and Type	Parameters Measured
October - November 2019	NDT3-D, NDT3-C, NDT3-B, NDT3-A, NDRO, SDRO, SDT1-A, SDT3-A, SDT3-B, SDT3-C, SDT3-D	R/V Atlantis	Benthic Flux Chamber water	Nitrate, Nitrite, Sulfide, Fe2+, phosphate, ammonium, sulfate chloride, DIC, Alkalinity
			Porewater from ROV Jason push cores	Nitrate, Nitrite, Sulfide, Fe2+, phosphate, ammonium, sulfate chloride, DIC, Alkalinity
			Sediment from ROV Jason push cores	Sulfate reduction rate, TOC, TON, density, porosity, Fe Mineral phases
			Sensor data from microprofilers	Dissolved oxygen, sulfide
July 2021	Depocenter, NDT3-A, NDT3-C, NDT3-D	R/V Nautilus	Porewater from ROV Hercules push cores	Sulfate reduction rate, nitrate, nitrite, sulfide, Fe2+, phosphate, ammonium, sulfate, chloride
July-Dec 2021	SDT1-A	ABISS Lander	Sensor data from ABISS	pH, temperature, dissolved oxygen
July 2022	NDRO	R/V Sheerwater	Porewater from Multicorer	Sulfate reduction rate, nitrate, nitrite, sulfide, Fe2+, phosphate, ammonium, sulfate, chloride
June - July 2023	NDRO, SDRO, NDT3-A	R/V Atlantis	Benthic Flux Chamber water	Nitrate, Nitrite, Sulfide, Fe2+, phosphate, ammonium, sulfate, chloride, Alkalinity
			Porewater from ALVIN push cores	Nitrate, Nitrite, Sulfide, Fe2+, phosphate, ammonium, sulfate, chloride, Alkalinity
			Sediment from ALVIN push cores	Sulfate reduction rate, TOC, TON, density, porosity, Fe Mineral phases

Table 3. Details of sampling stations in the Basin.

Station	Lat	Long	Depth (m)
NDT3_D	34.36270433	-120.0147509	447
NDT3_C	34.35260657	-120.016166	498
NDT3_B	34.33341481	-120.0194757	537
NDT3_A	34.29228292	-120.0256272	572
NDRO	34.26216872	-120.0305491	580
SDRO	34.20101741	-120.0441367	586
SDT1_A	34.21173835	-120.1164661	573
SDT3_A	34.18391621	-120.0472195	571
SDT3_B	34.16759993	-120.0530042	536
SDT3_C	34.15158674	-120.0504786	494
SDT3_D	34.14209313	-120.0515394	447
ABISS	34.299182	-120.05943	567

Table 4. Latitude, Longitude, and water column depth for stations that were sampled in this study.

Station	Depth (m)	Integrated SRR (mmol/m2/d)
NDT3-D	447	3.72
NDT3-C	498	4.02
NDT3-C+	511	3.63
NDT3-B-	515	5.64
NDT3-B	537	3.55
NDT3-A	563	10.60
NDT3-A+	572	2.78
NDRO	580	6.15
SDRO	580	5.38

Table 5. Depth integrated sulfate reduction rates (SRR) from June/July 2023. Rates are integrated over the top 10-cm of sediment.

Appendix C

Supplemental Material: Anaerobic metabolisms active during anoxia and oxygenation in the water column and sediments of the Salton Sea, a holomictic saline lake.

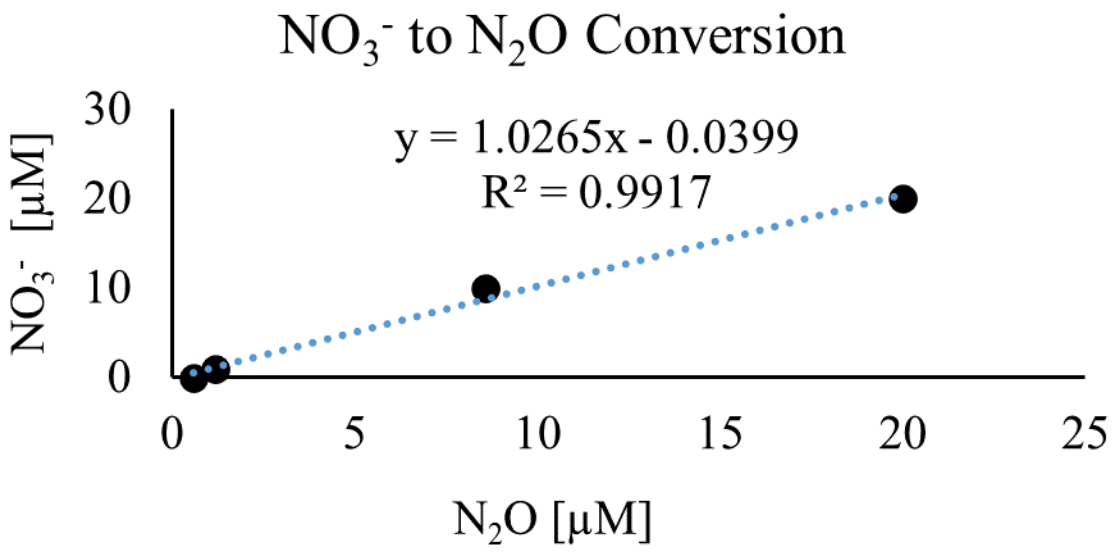

Figure 1. Standard curve of NO_3^- to N_2O conversion used in ammonium oxidation rate determination.

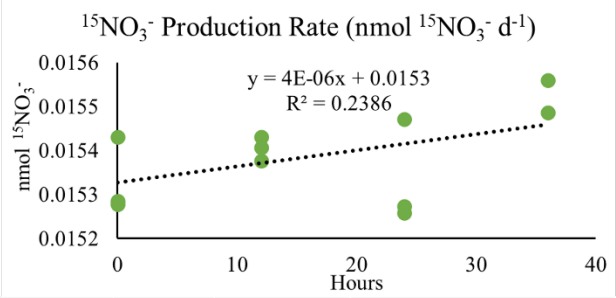

Sample Name	Time (hr)	Total NO_3^- (uM)	$^{15}NO_3^-$ (nM) based on average [NO_3^-]
SS_NoMo_R1_T0	0	4.77	0.01528
SS_NoMo_R1_T1	12	3.53	0.01541
SS_NoMo_R1_T2	24	4.73	0.01526
SS_NoMo_R1_T3	36	0.74	0.01549
SS_NoMo_R2_T0	0	4.12	0.01543
SS_NoMo_R2_T1	12	4.60	0.01538
SS_NoMo_R2_T2	24	3.23	0.01547
SS_NoMo_R2_T3	36	0.70	0.01556
SS_NoMo_R3_T0	0	4.75	0.01528
SS_NoMo_R3_T1	12	3.27	0.01543
SS_NoMo_R3_T2	24	4.52	0.01527
SS_NoMo_R3_T3	36	0.51	0.01562

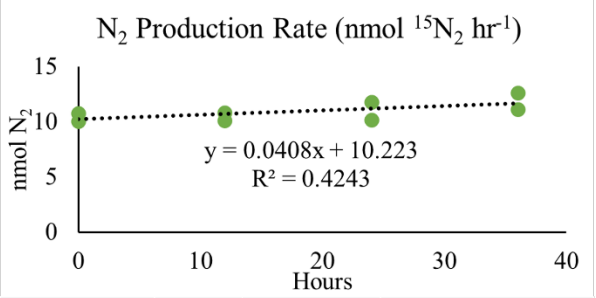

Sample Name	Time (hr)	N_2 (µmoles/vial)	$^{15}N_2$ (nmol) based on 29/28
SS_Denit_R1_T0	0	2.5	10.8
SS_Denit_R1_T1	12	2.7	10.8
SS_Denit_R1_T2	24	4.8	10.2
SS_Denit_R1_T3	36	1.5	11.2
SS_Denit_R2_T0	0	1.5	10.1
SS_Denit_R2_T1	12	6.4	10.2
SS_Denit_R2_T2	24	1.3	11.8
SS_Denit_R2_T3	36	1.3	12.7

Figure 2. Full dataset of ^{15}N incubations used for anaerobic ammonium oxidation (left) and Denitrification (right).

Table 1. Sulfate concentrations and sulfate reduction rate determination from January 2020. Note, the ^{35}S-Sulfate incubations for January 2020 were done in 70-mL serum vials rather than 30-mL vials like our other incubations. * connotes that the rate measured was not above 3x the standard deviation of controls.

Depth (m)	Sulfate [mM]	SRR (nmol L^{-1} d^{-1})
1.0	163	1*
1.0	163	0
10.5	166	0
10.5	166	23
10.5	166	242

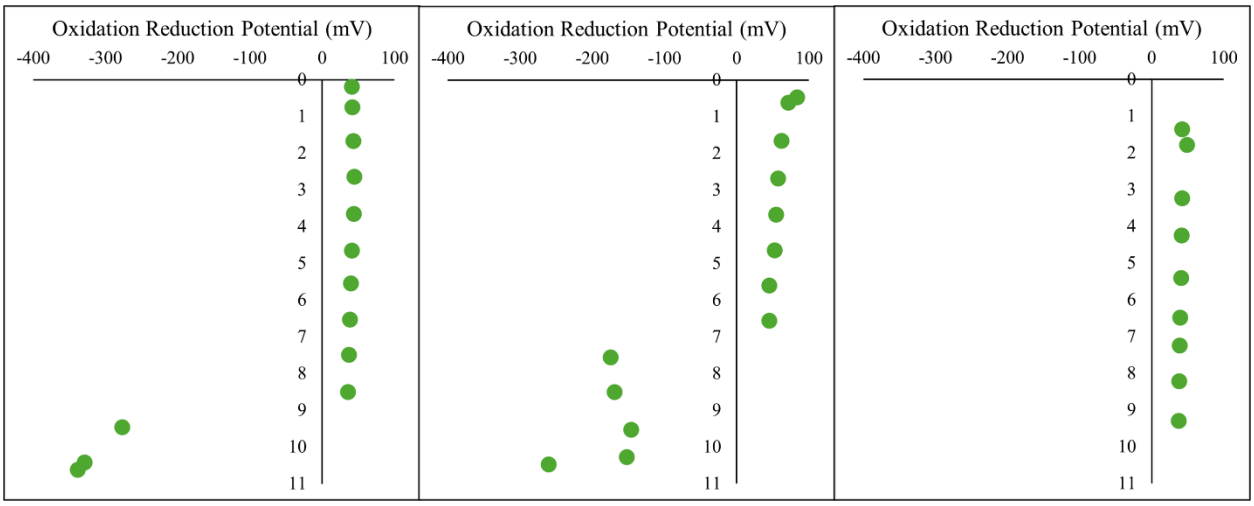

Figure 3. Oxidation reduction potential from the Salton Sea water column in August 2020 (left), September 2021 (middle), and November 2023 (right). Y-axis represents water column depth in all graphs.

Figure 4. Pictures from August 2020 (left) and September 2021 (middle, right) sampling campaigns at the Salton Sea. All three pictures show the dense cyanobacteria mat and/or organic-rich detrital sludge found on the margins of the lake.

References

Dale, A. W., S. Sommer, U. Lomnitz, A. Bourbonnais, and K. Wallmann. 2016. Biological nitrate transport in sediments on the Peruvian margin mitigates benthic sulfide emissions and drives pelagic N loss during stagnation events. Deep Sea Research Part I: Oceanographic Research Papers **112:** 123-136.

Dominika, G., M. Joanna, and M. Jacek. 2021. Sulfate reducing ammonium oxidation (SULFAMMOX) process under anaerobic conditions. Environmental Technology & Innovation **22:** 101416.

Gomes, M. L. and others 2022. Sedimentary pyrite sulfur isotope compositions preserve signatures of the surface microbial mat environment in sediments underlying low-oxygen cyanobacterial mats. Geobiology **20:** 60-78.

Kuwabara, J. S., A. van Geen, D. C. McCorkle, and J. M. Bernhard. 1999. Dissolved sulfide distributions in the water column and sediment pore waters of the Santa Barbara Basin. Geochimica et Cosmochimica Acta **63:** 2199-2209.

Marzocchi, U. and others 2018. Transient bottom water oxygenation creates a niche for cable bacteria in long-term anoxic sediments of the Eastern Gotland Basin. Environmental microbiology **20:** 3031-3041.

Noffke, A., S. Sommer, A. Dale, P. Hall, and O. Pfannkuche. 2016. Benthic nutrient fluxes in the Eastern Gotland Basin (Baltic Sea) with particular focus on microbial mat ecosystems. Journal of Marine Systems **158:** 1-12.

Reese, B. K., M. A. Anderson, and C. Amrhein. 2008. Hydrogen sulfide production and volatilization in a polymictic eutrophic saline lake, Salton Sea, California. Science of the total environment **406:** 205-218.

Reimers, C. E., K. C. Ruttenberg, D. E. Canfield, M. B. Christiansen, and J. B. Martin. 1996a. Porewater pH and authigenic phases formed in the uppermost sediments of Santa Barbara Basin. Geochim. Cosmochim. Acta **60:** 4037-4057.

Schauer, R. and others 2014. Succession of cable bacteria and electric currents in marine sediment. The ISME journal **8:** 1314-1322.

Sholkovitz, E. 1973. Interstitial water chemistry of the Santa Barbara Basin sediments. Geochimica et Cosmochimica Acta **37:** 2043-2073.

Tiffany, M. A., S. L. Ustin, and S. H. Hurlbert. 2007b. Sulfide irruptions and gypsum blooms in the Salton Sea as detected by satellite imagery, 1979–2006. Lake and Reservoir Management **23:** 637-652.

Valentine, D. L. and others 2016. Autonomous marine robotic technology reveals an expansive benthic bacterial community relevant to regional nitrogen biogeochemistry. Environmental science & technology **50:** 11057-11065.

Zheng, Y., R. F. Anderson, A. Van Geen, and J. Kuwabara. 2000. Authigenic molybdenum formation in marine sediments: a link to pore water sulfide in the Santa Barbara Basin. Geochimica et Cosmochimica Acta **64:** 4165-4178.